# CHARACTERISATION AND PROPERTIES OF RECTORITE AND RECTORITE-BASED CLAY FILMS AND BIONANOCOMPOSITES

by

## Maria Todorova Atanasova

A dissertation submitted in partial fulfilment
of the requirements for the degree

## Doctor of Philosophy

in the

**Department of Chemical Engineering**

**Faculty of Engineering, Built Environment and Information Technology**

**University of Pretoria**

Pretoria

December 2017

# Characterisation and properties of rectorite and rectorite-based clay films and bionanocomposites

Author:            Maria T. Atanasova

Supervisor:        Prof. Walter W. Focke

Department:        Chemical Engineering

University:        University of Pretoria

Degree:            PhD (Philosophiae Doctor)

## ABSTRACT

This research aimed to characterise the physico-chemical and structural properties of rectorite from a local deposit, the Beatrix Gold Mine in South Africa and to investigate its unique material properties. The ultimate research target was to explore the capability of natural and ion-exchanged mixed-layer clay rectorite to form binderless, non-isotropic (i.e. two-dimensionally oriented), self-standing, and mechanically strong clay-only films as a precursor to bionanocomposites with very high clay loading. The primary goal was to develop a facile "green" method, i.e. an energy-efficient, environmentally-friendly process without organic modifications, binders, plasticisers, thermal pre-treatments or other property enhancers. At these conditions the extent of process and product limitations was evaluated via statistical analysis to estimate the limits for the ultimate material performance.

Three rectorite-rich samples from the Beatrix Gold Mine, South Africa, were obtained, purified to > 90 % rectorite content and characterised. Structurally and chemically, the purified materials from the three samples were very similar and were categorised as rectorite, except where applicable specifics are highlighted. Based on chemical composition by X-ray fluorescence spectroscopy (XRF), X-ray diffraction (XRD) and

nuclear magnetic resonance (NMR) evidence, the rectorite from Beatrix Mine was identified as Na-Ca-rectorite, a dioctahedral regular interstratification of mica-smectite type. Scanning electron microscopy (SEM) revealed a layered morphology. High resolution transmission microscopy (TEM) showed well distinguished light and dark layers of about 2.20 nm consistent with the 1:1 interstratified mica-smectite nature. XRD measurements confirmed the basal spacing $d_{001}$ of 2.20 nm, indicating a one-water-layer structure. Unit cell parameters, for a monoclinic unit cell with primitive lattice, refined to $a$ = 5.177 Å; $b$ = 8.980 Å; $c$ = 22.489 Å and $\beta$ = 97.335 °, with a mean crystallite size around 14 nm and a calculated cell volume of 1045 $Å^3$. The Greene-Kelly test suggested that the expandable smectite layers have montmorillonite-beidellite composition. NMR indicated a high degree of Al substitution and the presence of different Al sites corresponding to six- and four-fold octahedral and tetrahedral aluminium respectively. The chemical composition and diffraction data suggest that the mica is Na-Ca-rich, i.e. of paragonite-margarite series. The fixed interlayer regions (mica interlayers) contain proportionally dominant $Na^+$ and $Ca^{2+}$ and minor amounts of $K^+$. The exchangeable smectitic interlayers contain almost equal amounts of $Na^+$ and $Ca^{2+}$ ions. The distribution of the interlayer $Na^+$ ions was quantified by $^{23}Na$ solid-state NMR spectroscopy. It points to a three component mixed–layer structure with considerable variation in the composition of the mica layer of the different samples.

Rectorite clay-only films (RecF) were prepared by the simple device of allowing slow evaporation of aqueous dispersions. In this process the exfoliated natural clay sheets self-assembled into cohesive films. The inorganic films from neat and ion-exchanged rectorite clay were translucent and flexible, with a layered microstructure and they featured excellent mechanical properties. The multi-layered films consist of continuous layers of well-aligned clay platelets parallel to the casting surface. Layers overlapped randomly in the lateral direction (plane) and joined vertically in an irregular manner by edge to face cross-links (bridging) forming coherent multi-

layered sheets organised in platelet-void nanostructured films. The films with highest mechanical performance had thickness below 30 μm. Overall films from rectorite clay with monovalent interlayer content exhibited highest strength ranging from 10 - 44 MPa and Young's Modulus 2 - 56 GPa. The corresponding experimental values for films with divalent interlayer cations were 8 - 23 MPa and modulus 11 - 25 GPa. The neat Na-Ca-rectorite films had strength 12 - 34 MPa and modulus 3 - 9 GPa. Of all cation-exchanged modifications, only $NH_4$-Rec films showed increased tensile strength compared to the neat material used for the exchange. Ultimate strength and modulus values were estimated via extreme-value statistical analysis. Some of these values compare favourably with values featured by polymer films.

Using the ion-exchanged clay modification with the best performance, i.e. $NH_4$-rectorite, the possibility of producing mixed-layer biopolymer-based nanocomposites with high clay loading was investigated. $NH_4$-rectorite-chitosan nanocomposites ($NH_4$-Rec/CS NCF) were prepared over the complete compositional range (100 - 0 %) clay, i.e. 0 - 100 % chitosan respectively). Bionanocomposite films were successfully prepared from rectorite clay and chitosan without pre-modifications, binders, plasticisers, thermal pre-treatments or other property enhancers. The bionanocomposite films featured enhanced mechanical strength and optical transparency compared to the two starting materials. The strength of 80/20 films, (denoting 80 % rectorite and 20 % chitosan), already exceeded the maximum values measured for both the neat clay films and the neat chitosan films. Films in the mid-compositional range showed a tensile strength increase of up to 227 % and 108 % relative to the neat clay films and chitosan films respectively, with the maximum measured for the 60/40 composition. The Young's modulus followed a similar trend, with the highest values occurring over a broad compositional range (80/20 to 30/70) and gradually decreasing with a decrease of clay proportion in the mix. The composite films showed a gradual improvement in transparency with decreasing clay content. The rectorite films had an off-white colour with a subtle blue-grey tint and a pearly

lustre on the smooth underside. The neat chitosan films had a smoky yellow-grey appearance often with a wavy top surface. The enhanced mechanical and optical properties of the $NH_4$-Rec/CS NCF indicated good compatibility between the two end-components. It demonstrated the feasibility of the ion-exchange method for the preparation of strong clay-chitosan nanocomposite films with high clay loading in the absence of organic modifications, binders, plasticisers, thermal pre-treatments or other property enhancers.

The excellent mechanical strength of rectorite-only films, and the enhanced performance and optical properties of derived bionanocomposites with high clay loadings, open new opportunities for clay minerals in materials science. It is worth pursuing further these unique lamellar, "hybrid"-type mixed-layer structures that resemble other natural ordered composites such as nacre. The statistical predictions indicated a strong potential for realising similar superior mechanical properties that paired with the clay ability to spontaneously self-assemble into cohesive films further encourages such endavor.

## ACKNOWLEDGEMENTS

Geoscience, the University of Pretoria, South Africa, the Leibniz-Institut für Polymerforschung, Dresden and the Institut für Experimentelle Physik, Technische Universität Bergakademie, Freiberg, Germany, for technical support in allowing the use of specilised instrumentation for this research.

## DECLARATION

I, Maria T. Atanasova, declare that the thesis, which I hereby submit for the degree Doctor of Philosophy (PhD) in the Department of Chemical Engineering, Faculty of Engineering, Built Environment and Information Technology at the University of Pretoria, is my own work and has not previously been submitted by me for a degree at this or any other tertiary institution.


24 July 2018

……………………………………

…………………………………..

## THESIS OUTLINE

The thesis is presented in six chapters:

**Chapter 1** is an **introduction** to the significance of natural layered aluminosilicates in multifunctional, hybrid nanomaterials and outlines the aims and the methodology applied in the present research work.

**Chapter 2** contains a comprehensive **literature review** on clay minerals, with emphasis on mixed-layer clay structures and sections on smectite group minerals, mica group minerals and rectorite. It includes a brief history of research on rectorite, i.e. geological settings and origin, structure and physico-chemical properties. An overview of existing research on biopolymers, chitosan and rectorite-biopolymer composites is given, with a summary of the diverse scope of applications reported to date. The chapter also deals with the theoretical aspects of the analytical techniques and instrumentation widely applied in materials science.

**Chapter 3** presents a description of the specific **experimental and analytical methodology** and procedures used for the preparation and characterisation of rectorite clay, rectorite films and rectorite-biopolymer composites. It includes the purification of the raw material and rectorite modifications, i.e. inorganic cation exchange and organic modifications. It also covers rectorite structure modelling and refinement, and describes validation aspects of the quantitative phase analysis.

**Chapter 4** reports the **results** of the present investigation discussed under four major headings. Section 4.1 deals with characterisation of neat and cation-exchanged rectorite; reports the results of the purification of the raw material and rectorite modifications by inorganic cation exchange; provides detailed characterisation of rectorite from the Beatrix Gold Mine, including crystallography and the structure of rectorite based on XRD and NMR study, the thermal behaviour studied by

thermogravimetric analysis (TGA) and differential thermal analysis (DTA) and XRD, microscopy, chemical composition and the Fourier transform infrared spectroscopy (FTIR) investigations. Characterisation was aimed at understanding how the crystallographic make-up of rectorite determines its unique properties which, in many respects, are different from those of its mixed-layer constituents, mica and smectite. In Section 4.2 the results of organic modifications by intercalation of organic surfactants are reported. Section 4.3 discusses the preparation, characterisation and properties of rectorite clay films. It contains a thorough report on the investigation into the effects of clay concentration, dispersion and exfoliation methodology on the microstructure and tensile strength of the clay films. In similar manner, Section 4.4 presents the results of the preparation, characterisation and properties of rectorite/chitosan bionanocomposite films (Rec/CS NCF). Here parameters such as clay-chitosan concentration, degree of dispersion, exfoliation and mixing methodology and pH were closely controlled and tuned to achieve the best mechanical strength of the films.

**Chapter 5** contains a summary of the key findings, with an extended **discussion** on rectorite clay film formation.

**Chapter 6** presents the final conclusions.

Graphical abstract



Flexible, mechanically strong rectorite clay only ceramic films

# Table of Contents

# LIST OF FIGURES

# LIST OF TABLES

# LIST OF ABBREVIATIONS

| AD | Air-dry |
|---|---|
| AFM | Atomic force microscopy |
| AIPEA | Association Internationale pour l Étude des Argiles |
| ASTM | American Society for Testing and Materials |
| ATR | Attenuated total reflectance |
| BET | Brunauer–Emmett–Teller |
| BNCF | Bionanocomposite films |
| BSE | Backscatter electrons |
| CCS | Central Control Standard |
| CEC | Cation exchange capacity |
| CGS | Council for Geoscience |
| CHN | Carbon-hydrogen-nitrogen |
| CMS | Clay Mineral Society |
| CNMMN | Commission on new minerals and mineral names |
| CRM | Certified reference material |
| CV | Coefficient of variation |
| DC10 | N,N′-dodecyldimethylammonium chloride |
| DLS | Dynamic light scattering |
| DLVO | Derjaquin, Landau, Verwey and Overbeek theory |
| DSC | Differential scanning calorimetry |
| DTA | Differential thermal analysis |
| DTG | Derivative thermogravimetry |
| EDS | Energy-dispersive spectrometry (system) |
| EG | Ethylene glycol |
| FESEM | Field emission scanning electron microscopy |
| FETEM | Field emission transmission microscopy |

| G | Glycerol |
|---|---|
| GEV | Generalised extreme value |
| gMLE | Generalised maximum likelihood |
| FPA | Fundamental parameters approach |
| FTIR | Fourier transform infrared spectroscopy |
| HE | Hydration energy |
| JNCs | Joint nomenclature committees |
| ICDD | International centre for diffraction data |
| ICP-OES | Inductively coupled plasma–optical emission spectrometer |
| ICSD | Inorganic crystal structure database |
| IMA | International mineralogical association |
| IR | Infrared spectrometer/spectroscopy |
| ISO | International Organisation for Standardisation |
| IUCr | International Union of Crystallography |
| LD | Laser diffraction |
| LDH | Layered double hydroxides |
| LOI | Loss on ignition |
| MAS NMR | Magic angle spinning NMR |
| MMT | Montmorillonite |
| NMR | Nuclear magnetic resonance |
| $NH_4$-Rec/CS NCF | $NH_4$-rectorite-chitosan nanocomposite films |
| PCS | Photon correlation spectroscopy |
| PDF | Powder diffraction file |
| PDI | Polydispersity index |
| PONKCS | Phases with partial or not known crystal structures |
| ppm | Parts per million |
| PSD | Particle size distribution |

| | | |
|---|---|---|
| pXRD | Powder X-ray diffraction | |
| QELS | Quasi-elastic light scattering | |
| QPA | Quantitative phase analysis | |
| RecF | Rectorite clay films | |
| RH | Relative humidity | |
| SDD | Silicon drift detector | |
| SE | Secondary electrons | |
| SEM | Scanning electron microscopy | |
| TGA | Thermogravimetric analysis/analyser | |
| TEM | Transmission electron microscopy | |
| TMS | Tetramethylsilane | |
| TS | Tensile strength | |
| UV-Vis | Ultraviolet-visible spectrophotometry | |
| vol.% | Volume percentage | |
| WDS | Wavelength-dispersive spectrometry | |
| XRD | X-ray diffraction | |
| XRF | X-ray fluorescence | |
| wt.% | Weight percentage | |

# CHAPTER 1      INTRODUCTION

## 1.1    Background

Natural phyllosilicate minerals, and clay minerals in particular, are among the most suitable inorganic substitutes and property enhancers in a growing array of applications (Lopes et al., 2014). Suitably modified clays can dramatically improve the physical properties of polymers, even at low concentration levels (ca. 5 vol.%). However, for best affinity it is a prerequisite that the clay is well dispersed in extensively exfoliated form. The smectite group clay minerals, e.g. montmorillonites are the most preferred reinforcement agents in nanocomposites. Because of their unique exchange capacity, reactive surface properties, lamellar crystallographic make-up and favourable particle size and aspect ratio, clay minerals can be easily modified towards target functionality (Tjong, 2006; Zhang and Evans, 2012). They are structurally analogous to some organic crystalline systems with similar lamellar arrangements, i.e. polyethylene (Ballard et al., 1980). Both organic and inorganic crystalline lamellae have comparable dimensions and due to the large aspect ratio, tend naturally to form oriented structures as coatings, membranes (Ballard and Rideal, 1983) and thin films. Clay-containing films and the hybridisation of inorganic materials is a trending topic in materials science and clay minerals research (Fernandes et al., 2014; Schoonheydt, 2014; Zhou et al., 2011). The physico-chemical properties of clay minerals, especially expandable species, define their specific behaviour in the aqueous dispersion crucial for film formation. Upon evaporation from suspensions, the dispersed clay platelets are highly susceptible to the formation of brick-like microstructures similar to that of nacre (Bennadji-Gridi et al., 2006; Sellinger et al., 1998).

While montmorillonite is the most studied and industrially utilised of the clay minerals, less attention has been given to mixed-layer clay structures such as rectorite. Illite-smectite (I/S) mixed-layer clay minerals are the most abundant and compositionally diverse in nature, and are most important in the study of diagenetic earth processes.

Generally, illite-smectites are of clay-fraction size, being dioctahedral 2:1 phyllosilicates consisting of two corner-sharing tetrahedral sheets with an octahedral sheet in-between. Regular, i.e. ordered, structures are usually given a mineral name and International Mineralogical Association (IMA) approved status, whereas random or irregularly structured sequences are generally described as I/S interstratifications. Rectorite is a regularly interstratified clay mineral with 1:1 alternating mica-like and smectite-like layers. The structure is built-up of pairs of dioctahedral 2:1 layers linked by Ca, Na or K cations. "Pure" rectorite from Beatrix Gold Mine, South Africa, features a platy-leafy morphology with translucent to transparent individual thin flakes. However, it is commonly found in layers of heterogeneous material known at the mine as "swelling clay". This clay contains between 45 % and 72 % rectorite, associated with calcite (12–14 %), quartz (8–49 %), muscovite (2–4 %), chlorite (2–6 %) and pyrophyllite (~3 %). Powdered rectorite swells in water, forming a gelatinous mass. The swelling of the structure is caused by the hydration of the exchangeable cations of the montmorillonite-like layers. The mixed-layer structure of rectorite consisting of alternating non-expandable (mica) and expandable (smectite) layers defines a set of unique properties that differ from those of mica and smectite alone. For example, the mica layer is temperature resistant and the smectite layer has cation-exchange capacity. This allows certain undesirable properties of the clay to be modified to suit specific applications, such as organoclays for polymer compatibility and the modification of thermoplastics. Rectorite dispersions facilitate the synthesis of ultralight gels that may be useful as adsorbents. Using organically modified rectorite in polymer-based nanocomposites has been found to impart desirable mechanical properties, e.g. improving the ductility of poly(lactic acid)(Li et al., 2009). However, it seems that to date no significant mechanical properties for binder-free, clay-only films have been reported.

## 1.2    Research objectives

This research aimed to characterise the physico-chemical, structural and material properties of rectorite clay from a local deposit, the Beatrix Gold Mine in South Africa. Preliminary characterisation based on results from XRD, electron microscopy (SEM, Field emission SEM (FESEM), and Field emission TEM (FETEM), thermal analysis (DSC/TGA), FTIR and Raman spectroscopy showed that this is an unusual material with unique and interesting properties. For instance, the ability of wet rectorite to increase in volume forming a gelatinous mass could be an effective rheological property with applications as rheological modifier and paint thickener. It was observed that the casting of slurries of fine rectorite-rich material results in the formation of relatively strong cohesive films. When subjected to direct flame, the thin clay film transforms into a silvery foil-like sheet which could be promising for use as a fire-retardant and for various specialised coatings.

The use of clay minerals to obtain hybrid multifunctional nanomaterials with new and improved properties is a prospect of growing technological interest and investigating the use of rectorite for this purpose became the main objective of this research. It was a prerequisite to use a "green" approach of a simple, energy-efficient, economical and environmentally friendly process to develop mechanically robust clay-only films and bionanocomposites with enhanced performance. The first step towards this goal was to investigate the capability of natural purified rectorite and its ion-exchanged modifications to form self-standing, mechanically strong clay films.

The ultimate research target was to explore the possibility of using rectorite clay to prepare non-isotropic (i.e. two-dimensionally oriented) nature-inspired bionanocomposites with very high clay loadings, i.e. tested over the complete compositional range of 100 - 0 % clay, i.e. 0 - 100 % chitosan respectively.

Major activities to achieve the main objectives of this research should include: development of an optimum purification procedure for maximum recovery of rectorite

from raw rectorite-rich material; ion-exchange modification of purified rectorite to prepare enough material for clay films and bionanocomposite preparation. The method development should focus on refining the process parameters and conditions for optimisation of the film preparation methodology for ultimate product performance. The film preparation process should be experimentally verifyed to ensure reproducibility of high performance films. The effect of texture, microstructure and other relevant parameters on the mechanical properties of the films should be considered in order to understand the mechanism of film formation and how it can be tuned towards maximum performance. Rectorite-only films and bionanocomposite films will be tested for their mechanical performance, and their light absorption and transparency. Statistical analysis of the available experimental data should be performed to determine and evaluate the limits for the ultimate mechanical performance of the films.

## 1.3    Research methodology

The research presented here was executed through the following major steps, determined by the set project objectives:

### 1.3.1  Purification, modification and characterisation of rectorite clay

- **Purification of raw material**

The aim was to remove major impurities, i.e. calcite, quartz and possibly the minor chlorite, mica and pyrophyllite. *Method:* Sieving, dispersion, sedimentation, chemical treatment. *Product:* ~2 kg high-purity rectorite-rich material to be used for further tests. *Characterisation methodology:* Electron microscopy – SEM, TEM; Structure and Crystallography – XRD, NMR; Spectroscopy – XRF, FTIR; Thermal analysis – TGA, DTA; Particle size analysis.

- **Modifications of purified rectorite**

  ⇒ **Inorganic cation exchange:** $Li^+$, $Na^+$, $NH_4^+$, $K^+$, $Cs^+$, $Mg^{2+}$, $Ca^{2+}$, $Sr^{2+}$ and $Ba^{2+}$. *Method:* Saturation with respective chloride; *Product:* Sufficient material to carry out the necessary characterisation tests.

  ⇒ **Organics modification:** different long-chain (carbon) organic surfactants. *Method:* Intercalation. *Product:* Sufficient material for tests.

## 1.3.2 Rectorite clay films (RecF): preparation, characterisation and functional properties

Investigation of the effect of clay concentration, dispersion and exfoliation methodology on the microstructure and tensile strength of the clay films. *Method:* Casting aqueous dispersions and self-assembly of exfoliated purified natural clay from aqueous dispersions during slow evaporation. *Product:* RecF for characterisation and the evaluation of properties. *Characterisation methodology:* Electron microscopy – SEM, TEM; Structure and Crystallography – XRD; Spectroscopy – XRF, FTIR; UV-Vis, BET; Mechanical properties.

## 1.3.3 Rectorite/chitosan nanocomposite films (Rec/CS NCF): preparation, characterisation and functional properties

Investigation of the effect of clay-chitosan proportions, degree of dispersion, exfoliation, mixing methodology and pH. Parameters were to be closely controlled and tuned to achieve the best mechanical strength of the film product. *Method:* Casting and self-assembly of intercalated rectorite-chitosan composites from aqueous dispersions during slow evaporation. *Product:* Rec/CS NCF films for characterisation and testing of properties. *Characterisation methodology:* Electron microscopy – SEM; Structure and Crystallography – XRD; Elemental analysis – CHN; Spectroscopy – XRF, FTIR; UV-Vis. Mechanical properties.

# CHAPTER 2    LITERATURE OVERVIEW

The following pages present a concise overview of clay science in general, and fundamental research into clays and clay minerals, with more comprehensive elaboration on the crystal chemistry of mixed-layer structures and rectorite, and mica and smectite group species as component layers in the structure of rectorite. The state of applied research on nanoclays (rectorite), biopolymers (chitosan) and nanocomposites is given, with emphasis on clay films and bionanocomposite films (NCF), specifically rectorite/chitosan composites. A literature review on all major analytical and experimental techniques relevant to this study is also presented.

## 2.1    Clays, clay minerals and mixed-layer structures

The study of clays and clay minerals dates back several centuries with a series of scientific and technological advances published in an impressive volume of knowledge available today. Among others, some of the fundamentals of clay science are set out in well-known books authored by (Bergaya and Lagaly, 2013; Bergaya et al., 2006; Brindley and Brown, 1984; Grim, 1962; Moore and Raynolds, 1997; Newman, 1987; Velde, 1985). It is a common belief that clays and clay minerals are the materials of the 21st century because they are environmentally friendly, naturally abundant and relatively inexpensive. Both fundamental and applied research are driven by a multi-disciplinary and multi-scale approach linking materials science and engineering with colloid science at macro-, micro- and nano-scale.

### 2.1.1  Definitions and terminology

The word "clays" was first assigned to fine-grained material found in geological formations by Agricola (1494–1555) almost five centuries ago in 1546 (Guggenheim and Martin, 1995), but was only identified as a mineral species at the beginning of the 19th century in the production of ceramic materials. The working bodies dealing with nomenclature and definitions of clay and clay minerals are the Joint Nomenclature

Committee (JNCs) of the Association Internationale pour l'Etude des Argiles (AIPEA) and the Clay Mineral Society (CMS). Because clay research, fundamental or applied, is such a dynamic field of science, there is an ongoing debate about and numerous revisions of clay nomenclature and definitions. These constantly evolve due to the expanding multidisciplinary approach to the study and the use of these unique materials. However, the distinction between clays and clay minerals is commonly accepted across all fields and the two terms should not be used interchangeably (Guggenheim and Martin, 1995). In essence, clay minerals are defined as naturally occurring, or synthetic, phyllosilicates or non-phyllosilicates, primarily fine-grained porous materials that impart plasticity when wet and harden upon drying and firing (Brindley, 1966; Brindley et al., 1968; Guggenheim et al., 2006; Guggenheim and Martin, 1995; Martin et al., 1991).

For clarity, the following terminology and definitions are defined here and will be applied as such throughout this document:

➢ *Lattice*: to be used in a strict crystallographic sense for a uniform distribution of points in space. There are 14 standard types of lattice, known as Bravais lattices. Phyllosilicates are based mainly on monoclinic and triclinic lattices.

➢ *Plane, sheet, layer, interlayer and structure unit*: to be used in the following manner: a *plane* of atoms, a tetrahedral or octahedral *sheet*, a 1:1 or 2:1 *layer, interlayer* space. In this order they refer to increasingly thicker arrangements, i.e. a sheet is a combination of planes and a layer is composed of sheets. Layers may be separated by *interlayer* space occupied by cations, hydrated cations, hydroxide octahedral groups or organic molecules (Brindley et al., 1968). An arrangement of a *layer* plus an *interlayer* is referred to as a *structure unit*. It may contain one or more chemical formula units (Z) (Bailey, 1984).

➢ *Unit cell, lattice constants and Miller indices* (usage of the terms is as agreed by the IUCr (International Union of Crystallography)): a *unit cell* is the parallelepiped

built on the vectors **a**, **b**, **c** of a crystallographic basis of the direct lattice. A *unit cell* is defined by lattice constants *a, b* and *c*, lattice vectors and interaxial angles $\alpha$, $\beta$, and $\gamma$ (always given in italic font). There are 7 different types of unit cell defined as crystal systems and 14 standard (Bravais) unit cells that describe all possible lattice networks. *Miller indices* (hkl) for crystallographic planes – these are the reciprocals of the fractional intercepts that the plane makes with the x, y, and z axes of the three nonparallel edges of the cubic unit cell.

➤ *Particles, aggregates and assembly:* clay particle is a generalised term also referred to as a crystallite, crystal or tactoid. It is defined as an assembly of layers; an assembly of particles is referred to as an aggregate (Figure 2-1). An arrangement of particles and aggregates results in different morphologies, i.e. plates, laths or fibres, and the formation of interlayer, interparticle and interaggregate spaces or pores (Bergaya and Lagaly, 2013).
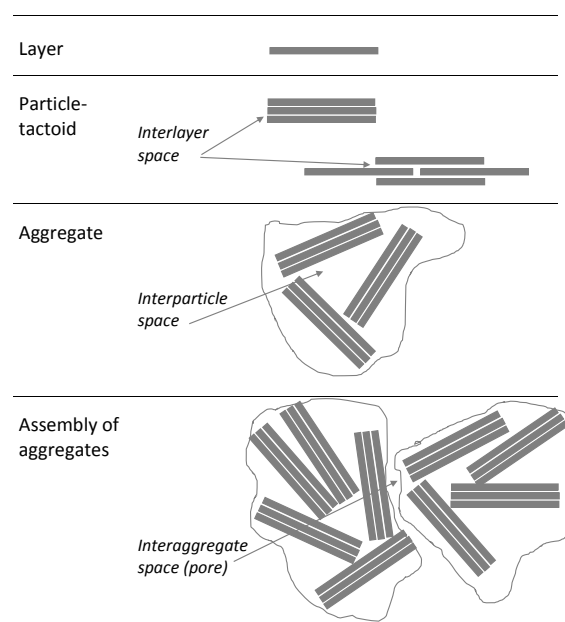


Figure 2-1. Schematic diagram showing the relationship of layer–particle-aggregate (Adapted from (Bergaya and Lagaly, 2013)

➤ *Delamination and exfoliation:* these occur in aqueous dispersions when intercalated water molecules cause the separation of two successive layers. When interaction

between the separating layers is sufficient enough to maintain some crystallographic integrity in the system, the separation is called *delamination*. With increasing separation no further interaction between the delaminated units is possible and eventually they cease to exist as a structure unit but become independently mobile in the liquid media, i.e. layers are completely *exfoliated* (Bergaya and Lagaly, 2013).

## 2.1.2  Structure and crystal chemistry of clay minerals

Clay minerals are hydrous layered silicates and belong to the larger group of phyllosilicates. The elementary structural unit is the Si-O tetrahedral linkage extending in continuous two-dimensional tetrahedral sheets (T) of composition $T_2O_5$ in a hexagonally symmetric network along the *a-b* crystallographic directions. All phyllosilicates contain silicate or aluminosilicate layers in which sheets of tetrahedrally coordinated cations (T – usually $Si^{4+}$, $Al^{3+}$ or $Fe^{3+}$) link through shared oxygens to adjacent sheets of octahedrally coordinated cations (O – most commonly $Al^{3+}$, $Fe^{3+}$, $Fe^{2+}$ or $Mg^{2+}$). Each tetrahedron links to adjacent tetrahedra in a lateral direction by three corner oxygens (the basal oxygens), while the fourth corner oxygen (the apical oxygen) is positioned in a direction normal to the tetrahedral basal plane and is shared with a neighbouring octahedral sheet. The Si-O bond distance is about 1.62 Å and the O-O distance about 2.64 Å. Up to half of the $Si^{4+}$ atoms may be replaced by the larger $Al^{3+}$ atom, causing an increase in sheet dimensions as the Al-O distance is about 1.77 Å (Moore and Raynolds, 1997). Each octahedron consists of a cation coordinated by six oxygens or hydroxyl groups and links to adjacent octahedra by sharing edges. The resulting sheets of edge-shared octahedra have a hexagonal or pseudo-hexagonal symmetry. There are two configurations of octahedra depending on the crystallographic position of the $OH^-$ group, i.e. a *cis*-oriented octahedron with $OH^-$ along the edge and a *trans*-oriented octahedron with $OH^-$ along the diagonal. When one tetrahedral sheet (T) is linked to one octahedral sheet (O), a 1:1 (TO) layer is formed as in kaolinites. Respectively there are six

octahedral sites and four tetrahedral sites in the unit cell of a 1:1 (TO) layer structure (Figure 2-2). The 1:1 layer is approximately 0.7 nm thick.
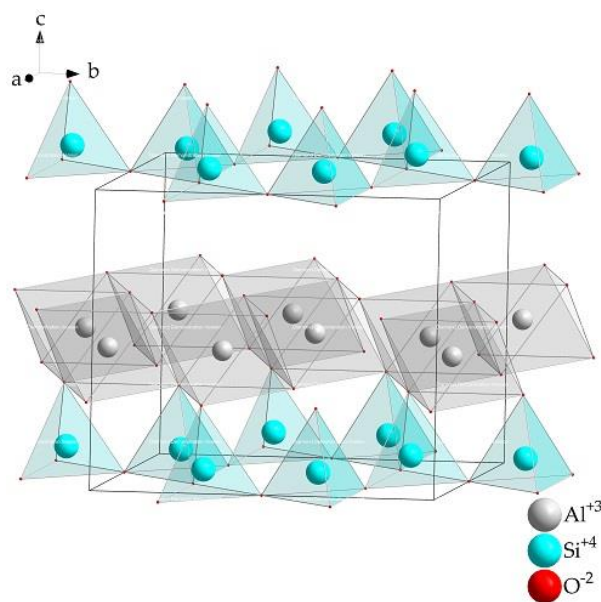


Figure 2-2. Graphical representation of the 1:1 structure of kaolinite, ICSD 31135 (Brindley and Robinson, 1946) (view down the crystallographic *a*-axis)

When one octahedral sheet (O) is linked to two tetrahedral sheets (T), i.e. one on each side, a 2:1 layer structure (TOT) is produced as in smectites and micas (Figures 2-3 and 2-4). This configuration results in six octahedral and eight (four on each side) tetrahedral sites in the 2:1 (TOT) layer unit cell. The two tetrahedral sheets are in inverted orientation to each other, i.e. they are both oriented with their apical oxygens (tips) towards the central octahedral sheet (Figures 2-3 and 2-4). Furthermore, two-thirds of the hydroxyl groups are replaced by tetrahedral apical oxygen atoms. The remaining third hydroxyl ion fits into the hole (gallery) in the hexagonal ring made by the apical oxygens of the tetrahedral sheet. Thus, the surfaces on both sides of the 2:1 layer consist of basal oxygens. The thickness of a 2:1 layer varies, depending on interlayer occupancy, from 0.91 - 0.95 nm in talc and pyrophyllite (empty interlayer space) to 1.40 - 1.45 nm in chlorite. The higher value for chlorites is ascribed to the additional octahedral interlayer sheet of cations, i.e. showing a $TOTO_{int}$ configuration (Brindley and Brown, 1984). For

simplicity, the structural formula is usually reported based on half the unit cell content, i.e. three octahedral sites. Structures with all three octahedral sites occupied by a divalent cation ($R^{2+}$, usually $Mg^{2+}$ or $Fe^{2+}$ or $Mn^{2+}$) are defined as trioctahedral or brucite-like $Mg(OH)_2$, whereas those with two of the three sites filled with a trivalent cation ($R^{3+}$, usually $Al^{3+}$ or $Fe^{3+}$) are denoted as dioctahedral or gibbsite-like $Al(OH)_3$. In these configurations structures maintain electrical neutrality until (i) substitution of $Al^{3+}$ for $Si^{4+}$ in tetrahedral sites occurs; (ii) substitution of $Al^{3+}$ for $Si^{4+}$ or other lower charge cations in octahedral sites occurs; or (iii) there are vacancies in trioctahedral species. As a result, a negative layer charge arises that is balanced by a positively charged interlayer. The most common interlayer cations are $Na^+$, $K^+$ and $Ca^{2+}$ as in smectites and micas, whereas $Mg^{2+}$, $Fe^{2+}$ and $Fe^{3+}$ are typical for chlorite and vermiculite. The interlayer cations can be exchangeable as in smectites or non-exchangeable ("fixed") as in mica species. Respectively interlayer cations are hydrated in the former and non-hydrated in the latter group. Ammonium ions $NH_4^+$ and organic molecules may replace some of the cations in the interlayer space and by electrostatic bonding neutralise the negative charge of the silicate layer. The net negative charge per layer is calculated on the basis of the structural formula, i.e. half the unit cell, and ranges from 0.2 in smectites to 2.0 in brittle micas for 2:1 clay species, whereas for 1:1 minerals the charge is close to zero. The sheets and layers can be either negatively charged as in majority of clay minerals, positively charged in the case of layered double hydroxides (LDH) or neutral or uncharged as in talc and pyrophyllite. The basic 2:1 network contains a fixed $O_{10}(OH)_2$ and the hydroxyls are uniquely in octahedral coordination. The layer charge density may have different locations in the layer depending on the origin of isomorphous substitution, e.g. octahedral or tetrahedral which affects the hydration state and the nature of the charge-balancing cation in the interlayer.

When tetrahedral and octahedral sheets join to form a 1:1 or 2:1 structural arrangement, certain adjustments and distortions take place in one or both of the sheets in order for them to combine at a common plan of oxygens. Although the O-O (oxygen-to-oxygen)

and OH-OH (hydroxyl-to-hydroxyl) ionic dimensions in the tetrahedral and octahedral sheets respectively are approximately equal at ~2.64 Å for the former and ~2.70 Å for the latter, the lateral dimensions of the tetrahedral sheet are usually larger than those of octahedral sheet (Brindley and Brown, 1984; Moore and Raynolds, 1997). Thus the sheets have to adjust by either rotation or tilting to accommodate a fit between them, creating a layer distortion typical of layered silicates. Stacking of the layers in the direction along the *c*-axis is a source of additional stacking disorder, the most extreme disorder being known as turbostratic disorder. It is manifested by displacements/rotations or translations of layers in the *a-b* plane and is most common in smectite minerals (Brindley and Brown, 1984; Moore and Raynolds, 1997).

Polytypism occurs when a compound exists in several different structural modifications, i.e. when structurally and compositionally identical layers are stacked in different ways. The most typical case is the mica minerals in which six theoretically possible polytypes exist; these are described in more detail in Section 2.3.

### 2.1.3  Mixed-layer clay minerals

Mixed-layering, interlayering and interstratification describe layered silicate structures consisting of two or more kinds of layer stacked in a vertical sequence along the *c*-axis, i.e. normal to (001) direction (Moore and Raynolds, 1997). The stacking sequence can be random, partially regular or regular.

Special names are assigned only to the regular interstratifications with components present in a fixed ratio (Bailey et al., 1982). The criterion for a regular sequence is to have at least ten 00l reflections of the same width with coefficient of variation CV < 0.75 to demonstrate adequate regularity of alternation. The coefficient of variation is defined as $CV = 100s/\bar{X}$ , where the s is the standard deviation for at least ten individually observed d(00l) values Xi, and $\bar{X}$ is the mean of the Xi values.

Mixed layering, where the expandable component is half or less of the mixture, is more susceptible to ordering than random stacking. Illite/smectite interstratifications are the most common mixed-layer clay minerals, even more common than the discrete end members (Reynolds, 1984). Generally, illite/smectites form in the process of transition from smectite to illite in suitable geological conditions (Hower, 1967, 1981; Srodon et al., 2000) and occur in clay-fraction size. They are dioctahedral 2:1 phyllosilicates consisting of two inverted corner-sharing tetrahedral sheets with an octahedral sheet in-between. Random or irregularly structured sequences are very common in nature and are usually designated as I/S interstratifications.

Although each layer maintains its structural and chemical identity, the sequence of layers scatters X-rays as one coherent unit (Reynolds, 1984). X-ray diffraction from a mixed-layer structure gives average values for the whole crystal, i.e. intermediate diffraction characteristics relative to the two component layer types. Stacking of two component layers A and B in a random sequence results in a disordered or irregular mixed-layer structure with irrational basal spacing that would not comply with Bragg's law. Ordered or regular stacking produces a supercell along the c-axis with diffracting basal spacing d00l equal to the sum of the thicknesses of each individual layer within the superstructure, i.e. dAB = dA + dB.

Structures of mixed-layer clay minerals are usually characterised by comparing experimental XRD patterns with computer-simulated mathematical models such as in the NEWMOD computer program (Reynolds, 1985). The Reichweite parameter (R) is used to characterise the range of order and the interaction between the layers (Drits, 2003; Reynolds, 1985). It is based on the probability of finding layer B after layer A or layer A after layer B and on the influence of the preceding layer has on this probability. Thus R0 describes random interstratification or lack of ordering; R1 denotes an ordered sequence where each A layer is followed by a B layer, e.g. ABABAB; R2 and R3 respectively denoting AA and AAA sequences is followed by a B layer. The R parameter is purely

statistical and can be an integer or a fraction. It describes the degree of ordering in an interstratified layer sequence using experimental d-values of basal reflections.

The crystallographic nature of I/S minerals is interpreted by two competing theories, both concerned with defining the mixed-layer structure unit. These are the MacEwan crystallite theory (MacEwan and Amil, 1958; MacEwan, 1956, 1957) based on Fourier transform methods, and X-ray scattering and the fundamental particles model (Nadeau et al., 1984) using transmission electron microscopy (TEM) of thin crystallites. According to the MacEwan model, one I/S unit is a sequence of illite and smectite layers stacked along the *c*-axis with individual structure units centred at the interlayer, i.e. the division between layers is through the centre of an octahedral sheet (Figure 2-8). An illite layer contains a dehydrated K-rich interlayer with an Al-rich tetrahedral sheet, whereas smectite has a hydrated Na-Ca-interlayer with a mainly Si-rich tetrahedral sheet. The stacking of such two layers is called "MacEwan crystallite". This model was later used to calculate the XRD patterns of I/S (Reynolds and Hower, 1970) and for modelling the computer program NEWMOD (Reynolds, 1985).

The fundamental particles model of Nadeau and co-workers describes an I/S structure made of "fundamental particles" with the dimension along the *c*-axis an integral with multiples of 10 Å. The 10 Å thick particle is seen as an isolated 2:1 layer termed a "fundamental smectite particle". Particles ≥ 20 Å are considered to be two or more 2:1 layers linked by K atoms and are termed "fundamental illite particles".

Following NMR studies on the crystallographic characteristics of I/S, (Altaner et al., 1988; Barron et al., 1985a, b; Jakobsen et al., 1995; Lausen et al., 1999) presented evidence in support of the MacEwan's crystallite model before the fundamental particles theory. ^{29}Si-NMR data convincingly differentiates signals of Si atoms in smectite layers from Si atoms in mica layers because relative to smectite, tetrahedral sites in illite have less Si and more Al as a result of predominantly tetrahedral Al for Si substitution in micas compared with smectite (Altaner et al., 1988).

The regular interstratification of dioctahedral mica and smectite is called **rectorite** (Bailey, 1982). The structure is built-up of pairs of dioctahedral 2:1 layers linked by Ca, Na or K cations. The alternating layers are mica-like and montmorillonite-like (Brown and Weir, 1963). Depending on the dominant cation, Ca-, Na- or K-rectorite varieties have been described. The swelling of the structure is similar to that of montmorillonites and is due to hydration of the exchangeable cations of the montmorillonite-like layers.

### 2.1.4  Nomenclature and classification

Based on the *charge of the interlayer content,* clay minerals are categorised into two broad classes, i.e. cationic clays which are widespread in nature, and anionic clays or mixed metal hydroxides, which are commonly synthesised.

*The layer type* and *charge per formula unit* are the classic main criteria used for the most widely accepted classification of clay minerals (Brindley et al., 1968) into the following major groups:

- Layer type 1:1

  o Serpentine-kaolin group: $x$~0 ($x$ – net layer charge)

- Layer type 2:1

  o Talc-pyrophyllite group: $x$~0

  o Smectite group: $x$~0.2–0.6

  o Vermiculite group: $x$~0.6–0.9

  o Mica group:

    - True (flexible mica): $x$~0.6–1.0

    - Brittle mica: $x$ ~1.8–2.0

- o Chlorite group: variable charge

- o Sepiolite-palygorskite group: variable charge

- o **Regularly interstratified 2:1 clay minerals: variable charge

*Note: It was only in 1982 when a group for Regularly Interstratified clay minerals was added to the 1:2 layered silicates (Bailey, 1982; Bailey et al., 1982) and recommendation criteria for species names were given. Among other reasons, the name "rectorite" is also justified here for a 1:1 regular interstratification of a dioctahedral mica and a dioctahedral smectite.

Species from the smectite, vermiculite, mica and chlorite groups are additionally divided into dioctahedral and trioctahedral subgroups. This basic classification remains at the core of subsequent reviews and upgrades which evolved as knowledge on clay minerals increased (Martin et al., 1991).

In summary, clay minerals can be generally categorised as: (i) 1:1 (T:O) or 2:1 (TOT) based on sheet configuration; (ii) dioctahedral or trioctahedral based on octahedral site occupancy; (iii) cationic or anionic based on the charge of the interlayer content; (iv) low ~0, medium ~0.2–0.6 and ~0.6–0.9, or high charge ~0.9–1.0 and 2.0 based on the charge per formula unit; and (v) hydrated or non-hydrated based on the hydration state of the interlayer content.

### 2.1.5 Properties of clay minerals

The *structural features* of clay minerals, i.e. sheet configuration or type of silicate layer and *chemical characteristics* such as magnitude of net layer charge and type of interlayer material, define the range of specific properties responsible for the growing preferential use of clays in industrial and environmental applications. On the other hand, the *fundamental properties* of clay minerals, such as layered structure with one dimension in the nanometre range, anisotropy of the layers and particles, lamellar crystallographic

make-up and favourable particle size and aspect ratio, unique exchange capacity, reactive surface properties at external (basal), internal (interlayer) and edge surfaces, allow them to be easily modified towards target functionality.

Because by definition clay minerals are fine-grained particles, generally accepted by clay mineralogists to occur in the fraction size < 2 μm, they exhibit large and variable surface areas that can significantly affect their properties. There are external and internal surface areas depending on the mean crystallite size and morphology for the former and the mineral's structural make-up and degree of dispersion/aggregation for the latter (Table 2-1). The edge surfaces contribute to the overall external surface area.

Table 2-1. Surface area of some clay minerals groups (Van Olphen and Fripiat, 1979)

| | Approximate Surface Area. $m^2/g$ | | |
|---|---|---|---|
| | Internal | External | Total |
| Smectite | 750 | 50 | 800 |
| Illite (mica) | 5 | 25 | 30 |
| Chlorite | 0 | 15 | 15 |
| Kaolinite | 0 | 15 | 15 |

The internal surface areas include the interlayer surface area and depend on the sheet configuration, i.e. the 2:1 minerals will have some internal surfaces, whereas 1:1 structures such as kaolinite will show only external surfaces. The chlorite exception is due to the additional octahedral sheet occupying the interlayer space.

The property of ion exchange is of fundamental and practical significance for clay minerals since it has a direct effect on their physical properties. It is defined as a stoichiometric and reversible replacement by exchange of ions between two electrolytes,

or as a diffusion process between electrostatic surface ions and a solution (Grim, 1962; Harland, 1994). Cation–exchange capacity (CEC) is a measure for ion exchange usually expressed as mEq/100 g. It is defined as the average quantity of cations available for exchange, usually at pH 7. The CEC is given in range per mineral and shows significant variation within the different clay minerals. For instance, the CEC of kaolinite is in the range 1–5 mEq/100 g, for micas it is 10–40 mEq/100 g, for montmorillonite it is 70–130 mEq/100 g and for vermiculite it is 130–200 mEq/100g. It is created in two main ways: (i) by substitutions in the tetrahedral or octahedral sheets that create the charge deficit, i.e. layer charge known as permanent charge; and (ii) by adsorption or dissociation of protons at the particle edges, referred to as "broken bonds" with the charge being non-permanent or pH-dependent (Bergaya and Lagaly, 2013; Grim, 1968). The layer charge is balanced by the interlayer cations' "counterions", namely $H^+$, $Li^+$, $Na^+$, $K^+$, $Mg^{2+}$ and $Ca^{2+}$, which are usually easily exchangeable as in smectite species. Thus the CEC is strongly dependent on the type of exchangeable cation, pH, temperature, particle size, morphology and surface area. The nature and ionic radius of the exchangeable cation defines the crucial properties of smectite minerals such as hydration state, unit cell dimensions (d-values) and rheological behaviour. For example, the most common naturally occurring Ca-montmorillonite is usually exchanged with $Na^+$ due to the more desirable properties of Na-montmorillonite in industrial applications.

Ionic dimensions for some of the cations relevant to the rectorite study in this work are given in Table 2-2. Ionic potential is a measure of charge density and the strength of the ionic bond. It is derived as a ratio of the ion's electrical charge (cation valence) to its ionic radius. It is also called hydration energy (HE) or hydration power and is closely related to the hydration properties of smectite minerals (Ferrage et al., 2005a; Ferrage et al., 2005b; Ferrage et al., 2007; Morodome and Kawamura, 2011).

Another critical property of clay minerals and smectites in particular is their ability to expand in the *c*-axis direction when water and other polar molecules or certain organic

molecules enter between the layers. The hydration state and the size of the interlayer cation determine the layer thickness or spacing in the $c$-axis direction, i.e. the basal spacing. Smectite and vermiculite contain hydrated alkaline or alkaline earth cations in the interlayer space, with an average spacing around 15.5 Å. The number of water layers depends on the nature of the exchangeable cations at a given water-vapour pressure. Thus Na-exchanged montmorillonite usually has one molecular water layer and a basal spacing about 12.5 Å, whereas in the Ca-montmorillonite structure there are two molecular water layers with a spacing of about 15.5 Å. In mica and illite the non-hydrated alkaline and alkaline earth cations in the interlayer result in a periodicity of around 1.0 nm (Bergaya and Lagaly, 2013). The expansion in glycerol is considerably less than in water and similar d-spacing is usually a result of the different size and shape of the molecules in the interlayer space (Barshad, 1950). Thus the physico-chemical factors for expansion are the size and charge of the interlayered ion, the nature of the interlayered substance, i.e. water, organic matter, and the total excess negative charge per unit cell, e.g. low charge smectites are expanding and high-charge micas are non-expanding but have similar interlayer content.

The ability of clay minerals to swell/expand, or the lack of this ability, is controlled by the balance of attractive and repulsive forces between adjacent 2:1 layers. The main attractive force is the electrostatic interaction between the negatively charged layers and the balancing positively charged interlayer content of alkali or alkaline earth cations. The magnitude of this force depends on the surface charge density and the layer separation in the $c$-direction (Newman, 1987). When layers are in contact or almost in contact, there are van der Waals' attractive forces between atoms in the layer surfaces and some residual electrostatic forces between charged atoms in adjacent layers. The main repulsive force arises from the hydration of interlayer cations in natural clay minerals. In addition, repulsive forces exist between the hydrogens of the hydroxyl groups bonding to the octahedrally coordinated cations in the 2:1 layer and the interlayer cations. This

repulsive force depends on the proximity of the hydroxyl hydrogen to the interlayer cation and is largest when the O-H dipole is normal to the 2:1 layer plane.

Table 2-2. Ionic radii and derived ionic potentials for some relevant cations (compiled from (Conway and Ayranci, 1999; Shannon, 1976; Volkov et al., 1997)

| Ion | Ionic Radii, nm | Hydrated Ionic Radii, nm | Ionic potential, $[z/r]$ (-) |
|---|---|---|---|
| $Li^+$ | 0.09 | 0.38 | 10.64 |
| $Na^+$ | 0.12 | 0.36 | 8.55 |
| $NH_4^+$ | 0.15 | 0.33 | 6.76 |
| $K^+$ | 0.15 | 0.33 | 6.71 |
| $Cs^+$ | 0.19 | 0.33 | 5.38 |
| $Mg^{2+}$ | 0.07 | 0.43 | 27.78 |
| $Ca^{2+}$ | 0.10 | 0.41 | 20.00 |
| $Sr^{2+}$ | 0.13 | n.a. | 15.87 |
| $Ba^{2+}$ | 0.14 | 0.88 | 13.99 |

## 2.2 Smectite group

Smectite group minerals are 2:1 (TOT) clay minerals with hydrated exchangeable alkaline or alkaline earth cations in the interlayer space and a net layer charge per formula unit in the range 0.2–0.6. The species according to octahedral occupancy are (Martin et al., 1991):

- dioctahedral – beidellite, montmorillonite, nontronite, volkonskoite
- trioctahedral – hectorite, saponite, sauconite, stevensite and swinefordite

Isomorphous substitutions may occur between $Si^{4+}$, $Al^{3+}$ and $Fe^{3+}$ in tetrahedral positions and $Al^{3+}$, $Mg^{2+}$, $Fe^{2+}$ and $Fe^{3+}$ in octahedral sites, resulting in a negative charge between 0.2 and 0.6 per half unit cell, i.e. $O_{10}(OH)_2$. For instance, montmorillonite $((Al_{3.15}Mg_{0.85})(Si_{8.00})O_{20}(OH)_4X_{0.85}.nH_2O)$ and beidellite $((Al_{4.00})(Si_{7.15}Al_{0.85})_{20}(OH)_4X_{0.85}.nH_2O)$ (Newman and Brown, 1987) (X=monovalent interlayer cation) are the aluminium-rich varieties and are distinguished on the basis of the origin of the negative charge. In montmorillonite, the charge usually arises by $Mg^{2+}$ substitution in the octahedral position, whereas in beidellite it is due to $Al^{3+}$ in tetrahedral occupancy.

The negative charge is balanced by the interlayer cations, most commonly $Na^+$, $K^+$, and $Ca^{2+}$ and $Mg^{2+}$, usually hydrated and exchangeable. There is an almost linear correlation between the interlayer distance and the ionic radius of the interlayer cation (Voora et al., 2011).

Intercalation of discrete number of water layers, usually 0 - 3, can be distinguished by XRD with shifting of d(00l) to lower 2θ angles (enlarged unit cell along $c$-axis) corresponding to 0-, 1-, 2- and 3-water layer hydrates. Dehydration is usually reversible on exposure to atmospheric humidity. Rehydration is accompanied by a rapid increase of the distance between the layers to accommodate the sorbed water molecules. Some of the main factors affecting interlayer hydration of smectites are hydration energy of the interlayer cation, polarisation of water molecules by interlayer cation, and variation of electrostatic surface potentials because of different layer charge locations. The swelling occurs in a step-wise manner in a series of phase transitions, whereby intermediate, interstratified and mixed-layer hydrates may co-exist. Based on modelling simulation of the interlayer molecular structure of swelling clay minerals, (Skipper et al., 1995) proposed that dehydrated and one-layer hydrated structures with divalent cations are more compact and rigid compared with those having monovalent cations. It is further suggested that in dehydrated structures the interlayer cation can occur both close to the tetrahedral basal oxygen atoms and symmetrically above and below the tetrahedral hole,

depending on the ionic radius. The H-bonding between water molecules and basal oxygen atoms is stronger for tetrahedral than for octahedral sheet substitutions (Sposito, 1984).
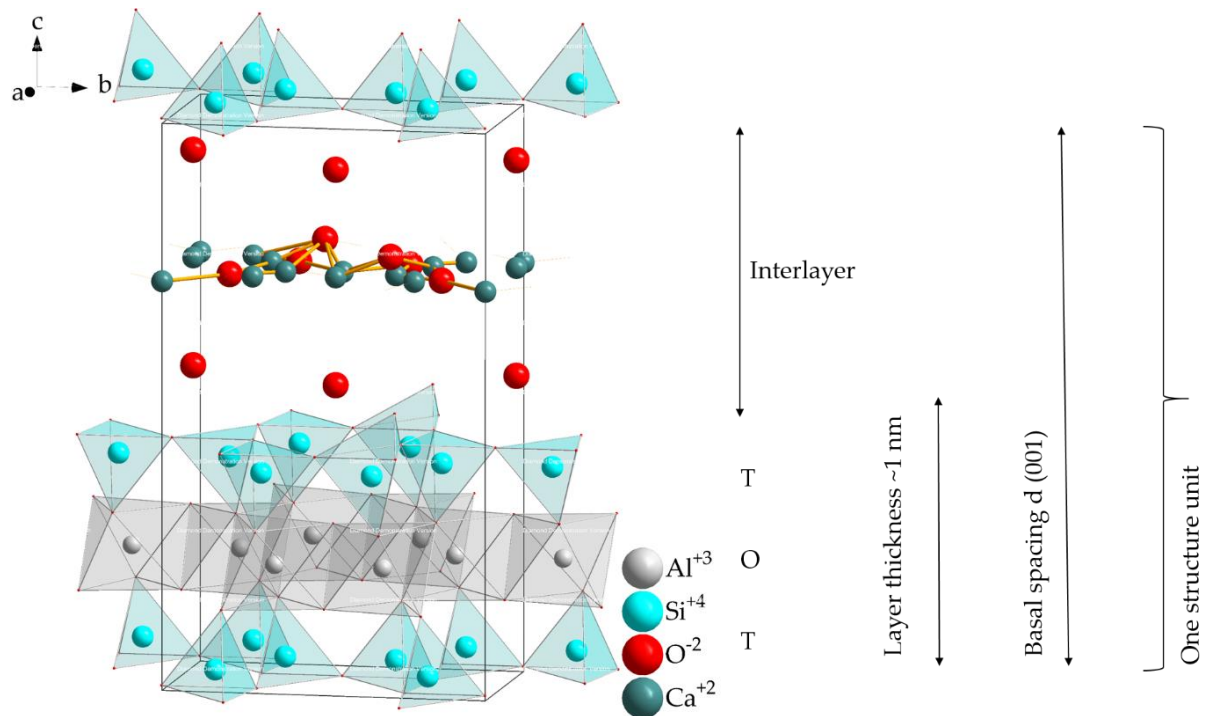


Figure 2-3. Graphical representation of the structure of montmorillonite_Ca, ICSD_51636 (Gualtieri et al., 2001) (view down crystallographic *a*-axis) with layer distances annotated on the right

Smectite clay minerals and specifically montmorillonite and saponite are those most commonly used in the preparation of polymer nanocomposites. They are easily available and possess the most compatible properties such as colloidal size, high specific surface area, moderate layer charge, large cation exchange capacity, variable interlayer separation depending on the ambient humidity, well-studied intercalation/exfoliation chemistry and the ability to swell in water, quite extensively for $Li^+$- and $Na^+$- exchanged forms. Under optimised conditions, interlayer swelling in water may eventually cause complete delamination and exfoliation of the clay particles. Interlayer reactions of smectites are the most sought-after property for technological processes and applications.

## 2.3   Mica group

Mica minerals are 2:1 phyllosilicates with non-hydrated alkaline or alkaline earth cations in the interlayer space and a net layer charge per formula unit in the broad range of 0.6–2.0. They are classified into two subgroups, namely *true* (flexible) micas and *brittle* micas, with the most common minerals speciation that by (Martin et al., 1991), with addition of a third subgroup by (Rieder et al., 1998)), among others not mentioned here:

- **True mica** species contain ≥ 50 % monovalent interlayer cations with net layer charge per formula unit of 0.6–1.0:

- Dioctahedral – celadonite, glauconite, illite, muscovite, paragonite

- Trioctahedral – biotite, lepidolite and phlogopite.

- **Brittle mica** species have ≥ 50 % divalent cations in the interlayer with net charge per formula unit of 1.8 – 2.0:

- Dioctahedral – margarite

- Trioctahedral – anandite, bityite, clintonite, kinoshitalite

- **Interlayer-deficient micas** are those with cation deficiency in the interlayer space. The name replaced the *hydromica* subgroup name, although previous species of it have been discarded:

- Dioctahedral – illite, glauconite, brammalite

- Trioctahedral – wonesite

The nomenclature of micas updated by the Mica Subcomittee of the CNMMN of the IMA (Rieder et al., 1998) is based on the chemical composition and crystal structure of mica species.
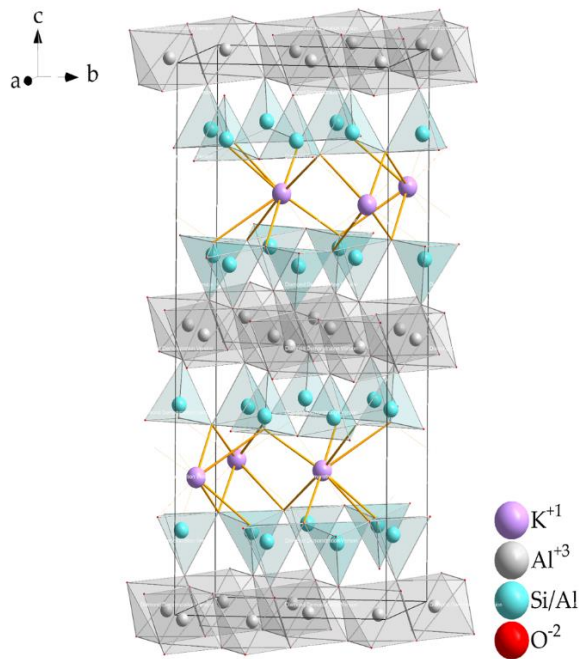
Figure 2-4. The structure of muscovite $KAl_2(Si_3Al)O_{10}(OH)_2$, ICSD_28553 (Gatineau, 1963) (view down *a*-axis)
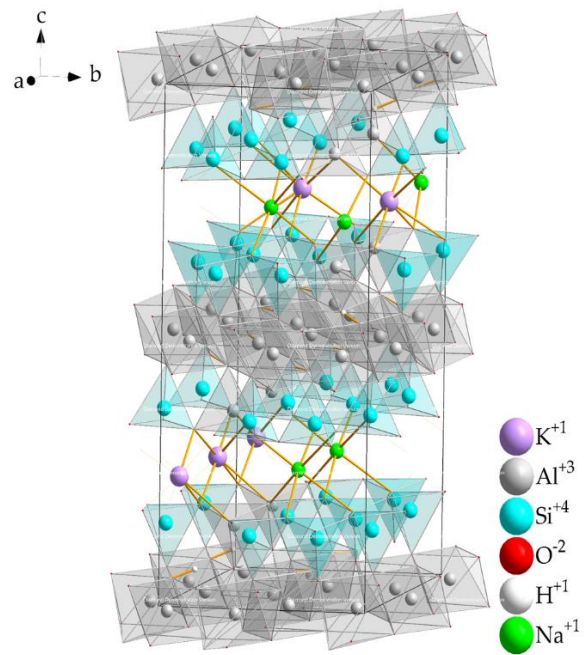
Figure 2-5. The structure of muscovite $KAl_2(Si_3Al)O_{10}(OH)_2$-paragonite $NaAl_2(Si_3Al)O_{10}(OH)_2$ series, ICSD 187574 (Hernandez-Haro et al., 2013)

Tetrahedral sheets have composition $T_2O_5$ and link to the octahedral sheet in-between by the apical oxygen atoms of each tetrahedron (Figure 2-4). The structure consists of negatively charged 2:1 layers, "keyed" together by large interlayer cations (Bailey, 1984). In the true micas the interlayer cation is predominantly monovalent, whereas in the brittle micas it is divalent. The layer-charge may arise from: (i) substitution of $R^{3+}$ (usually Al, Fe, or Cr) for $Si^{4+}$ in tetrahedral positions; (ii) substitution of $R^{1+}$ or $R^{2+}$ for $R^{2+}$ or $R^{3+}$ in octahedral positions (primarily $Al^{3+}$, $Mg^{2+}$, $Fe^{2+}$ and $Fe^{3+}$); or (iii) vacancies in octahedral positions. The resulting layer charge can be of either tetrahedral or octahedral origin, or partly from both sheets. When the tetrahedral charge exceeds unity, it is usually an indication of excess positive charge in the dioctahedral sheets, due to vacant positions. The interlayer cation is commonly monovalent $K^+$ and occasionally $Na^+$ (paragonite) in the true micas and divalent $Ca^{2+}$ in brittle micas. Species with appreciable substitutions of Li, Cr, Ni, Mn, Ti, Zn, Co, Cu and V in octahedral positions are known. Rarely, small amounts of Sr, Ba, Rb and Cs can be present in interlayer sites.

The polytypism phenomena in micas was first demonstrated by (Hendricks and Jefferson, 1939) based on an X-ray diffraction study. There are six theoretically possible mica polytypes derived experimentally by (Smith and Yoder, 1956) from natural specimens. In the stacking of 2:1 layers in the c-direction, the tetrahedral sheets have to align so that the hexagonal rings superimpose to accommodate the interlayer cation and still maintain octahedral coordination in the structure unit. This is achieved by layer shifts in positive or negative direction of any of the three pseudo-hexagonal axes X1, X2 or X3. Two polytypes form as a result of shifts along only one axis, namely 1M and 2Or, i.e. having all the layers in the same orientation. Polytypes 2M1 and 2M2 involve shifts along two axes and, respectively, shifts along all three axes produce polytypes 3T and 6H.

In the mica structure, the 2:1 layers superimpose in such a way that the hexagonal rings of basal tetrahedral planes line up to enclose the interlayer cations. In this adjustment tetrahedral rotations reduce the size of the gallery, resulting in only six nearest oxygens instead of the twelve expected for hexagonal geometry. In dioctahedral micas the most common interlayer cation $K^+$ appears to be too large for this six-coordinated hole, resulting in less tetrahedral rotation and filling the gap by pushing apart the basal oxygen planes and stretching laterally the octahedral sheet (Radoslovich and Norrish, 1962). Thus the basal spacing of 10 Å is slightly larger than the actual thickness of the layer (~9.3-9.6 Å). The average distance between centres of basal oxygens in adjacent layers (also called interlayer separation/interlayer space distance) is ~3.42 Å for muscovite 2M1 (Gatineau, 1963), ~3.46 Å for muscovite 3T (Guven and Burnham, 1967), ~3.31 Å for muscovite-(Na) and ~3.08 Å for paragonite-(K) (Burnham and Radoslovich, 1964), and for margarite 2M1 between 2.83 Å (Takeuchi, 1965) and 2.87 Å (Guggenheim and Bailey, 1975). This indicates that adjacent basal oxygen planes around the interlayer $K^+$ (diameter ~2.76 Å) in muscovite and $Na^+$ (diameter ~2.04 Å) in paragonite are very close but not in contact, whereas in margarite they are almost in contact around $Ca^{2+}$ (~2.00 Å diameter) (Bailey, 1984). In both cases the interlayer cation fills entirely the gap, i.e. it is fixed in the

gap with no space for water molecules to hydrate. As a result the 2:1 layers are held strongly together and therefore no swelling or exfoliation of the layers is possible.

In the 2:1 layer structure of mica the attractive force between the TOT layers and the interlayer cation exceeds its dehydration energy because of the high layer charge (Moore and Raynolds, 1997).

## 2.4    Rectorite

Rectorite was first reported by Brackett and Williams in 1891. It was found in the Blue Mountain mining district, Garland County, Arkansas, USA, and named after E.W. Rector, an attorney in Hot Springs, Arkansas.

**Historic record of the first description of rectorite**: Statement of ceramic manufacturer Homer Langhlin, Esq. of East Liverpool, Ohio, USA upon firing rectorite specimen from Blue Mountain mining district, Arkansas (Bracket and Williams, 1891):

*"The sample of what you call kaolinite, sent to me, was duly received and carefully examined and tested under fire. The mineral is neither kaolin nor kaolinite, but just what it should be called I am unable to say, never in all my experience having seen any mineral of its kind. Unlike kaolin it will not dissolve in water. It burns a white colour and becomes very vitreous and strong. It cannot be finished with a smooth face or skin, but roughs up like a blotting pad. It is certainly a very interesting and curious mineral, but I can think of no use for it in ceramic manufacture unless it could, after careful experiments, be made into novel ornaments".*

Later, Caillere et al. (1950) described a mineral with "remarkable skin-like" appearance. They named it allevardite after the locality Allevard in France where it was found. Based on X-ray examination, Bradley (1950) suggested that the structure of rectorite from Arkansas consists of alternate stacking of pyrophyllite and vermiculite layers separated by layers of water. Brindley (1956) described it as a swelling double-layer mica mineral.

Others (Ivkin et al., 1959 and Korolev, 1961) reported a similar swelling mineral from Dagestan, Russia. Brown and Weir (1963) re-examined the two minerals for the similarity in their structure and composition. In general agreement with previous workers, they established that rectorite and allevardite are identical minerals and proposed that the name rectorite be used. The structure is built-up of pairs of dioctahedral 2:1 layers linked by Ca, Na or K cations. The alternating layers are mica-like and montmorillonite-like. Depending on the dominant cation, Ca-, Na- or K-rectorite varieties have been described. The swelling behaviour of rectorite is similar to that observed in montmorillonites. It is caused by the hydration of the exchangeable cations of the montmorillonite-like layers. Kodama (1966) used thermal analysis and infrared spectroscopy in addition to XRD and chemical analysis to study rectorite from Baluchistan, Pakistan. He described a regularly alternating sequence of Na-mica (paragonite) layers and expandable layers of montmorillonite-beidellite composition. In 1982 the Nomenclature Committee of the International Association for the Study of Clays (AIPEA) accepted the name rectorite for a 1:1 regular interstratification of dioctahedral mica and dioctahedral smectite (Bailey, 1982).

In South Africa, rectorite occurrence was first reported in 1991 at the Loraine and Beatrix Gold Mines located near Welkom (von Rahden et al., 1991). Beatrix mine is situated in the Free State Province of South Africa in the Magisterial District of Matjhabeng, at latitude 28° 15′ S and longitude 26° 47′ E near the towns of Welkom and Virginia, some 240 km southwest of Johannesburg (Figure 2-6).

Geologically, Beatrix Gold Mine is part of the Free State goldfields situated at the southern edge of the Witwatersrand Basin. The gold deposit is a shallow to intermediate depth type auriferous palaeoplacers (reefs), i.e. the Beatrix Reef and the underlying Kalkoenkrans Reef, both of the Kimberley Conglomerate Formation. Karoo Supergroup sediments cover the mining area underlain by the volcanic rocks of the Klipriviersberg Group (Ventersdorp Lava, Figure 2-7). The Central Rand Group that hosts the gold-

bearing conglomerates exploited by Beatrix Gold Mine follows in stratigraphy (GoldFields, 2011).
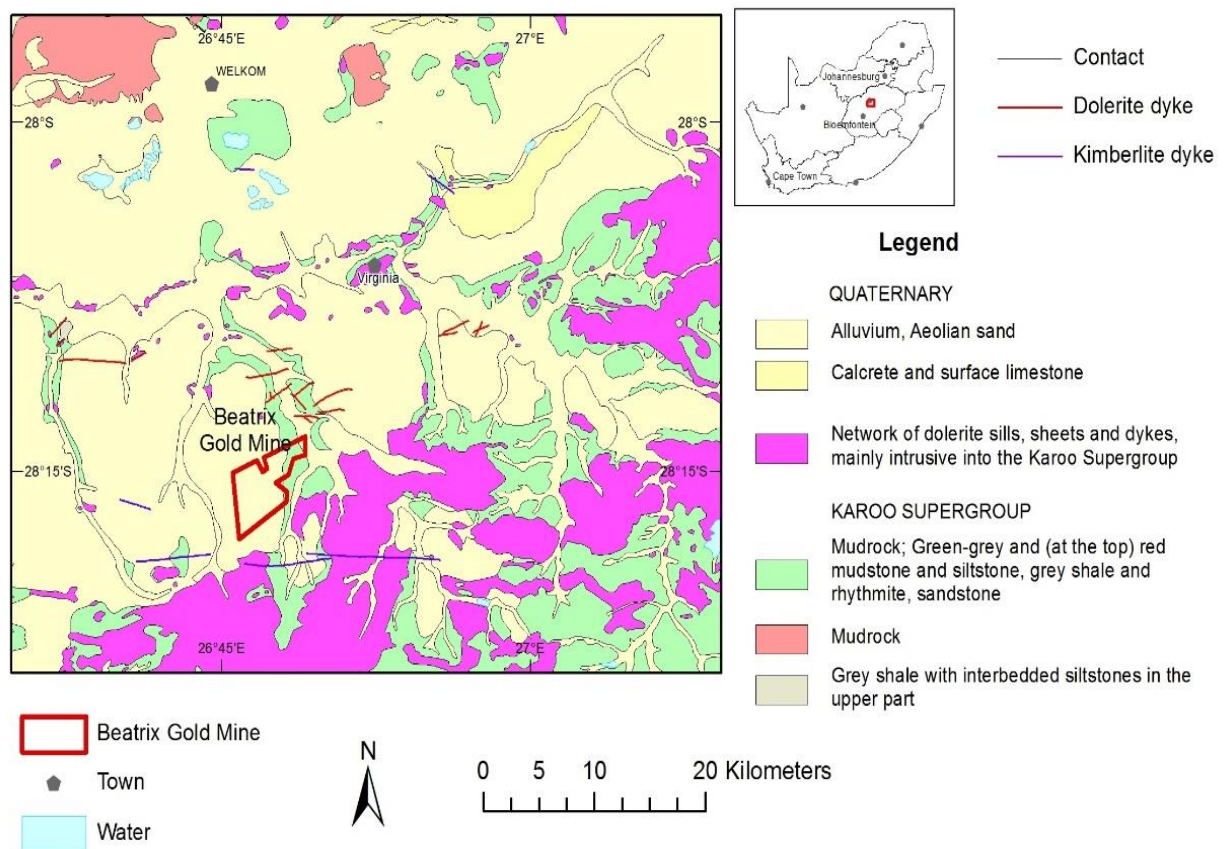


Figure 2-6. Geological map of the area around Beatrix Gold Mine

Rectorite is found in modified shale bands, up to 0.5 m thick, both in the hanging wall and footwall of the Beatrix reef (BXR in Figure 2-7) close to a major underground fault. The bands consist of low-grade metamorphic rock with mineral composition of quartz, muscovite, paragonite, chlorite, pyrophyllite, rectorite, smectite and chloritoid. The rectorite formation is associated with the alteration of other phyllosilicates, pre-existing pyrophyllite in particular, under metamorphic conditions of at least 350 °C and 250 MPa (von Rahden et al., 1991). The shale has been associated with gold losses at the mine in the process of physical and chemical extraction of the gold (Van Vuuren et al., 2000).

Jakobsen & Nielsen (1995) and (Lausen et al., 1999) described the rectorite from Beatrix mine as being Na-Ca-rich. Based on NMR spectroscopy in combination with X-ray

28

diffraction and chemical analysis, they determined the composition of Beatrix rectorite as a three-component structure (Figure 2-8), made up of smectite- (Figure 2-3), paragonite- (Figure 2-10) and margarite-type layers (Figure 2-9).
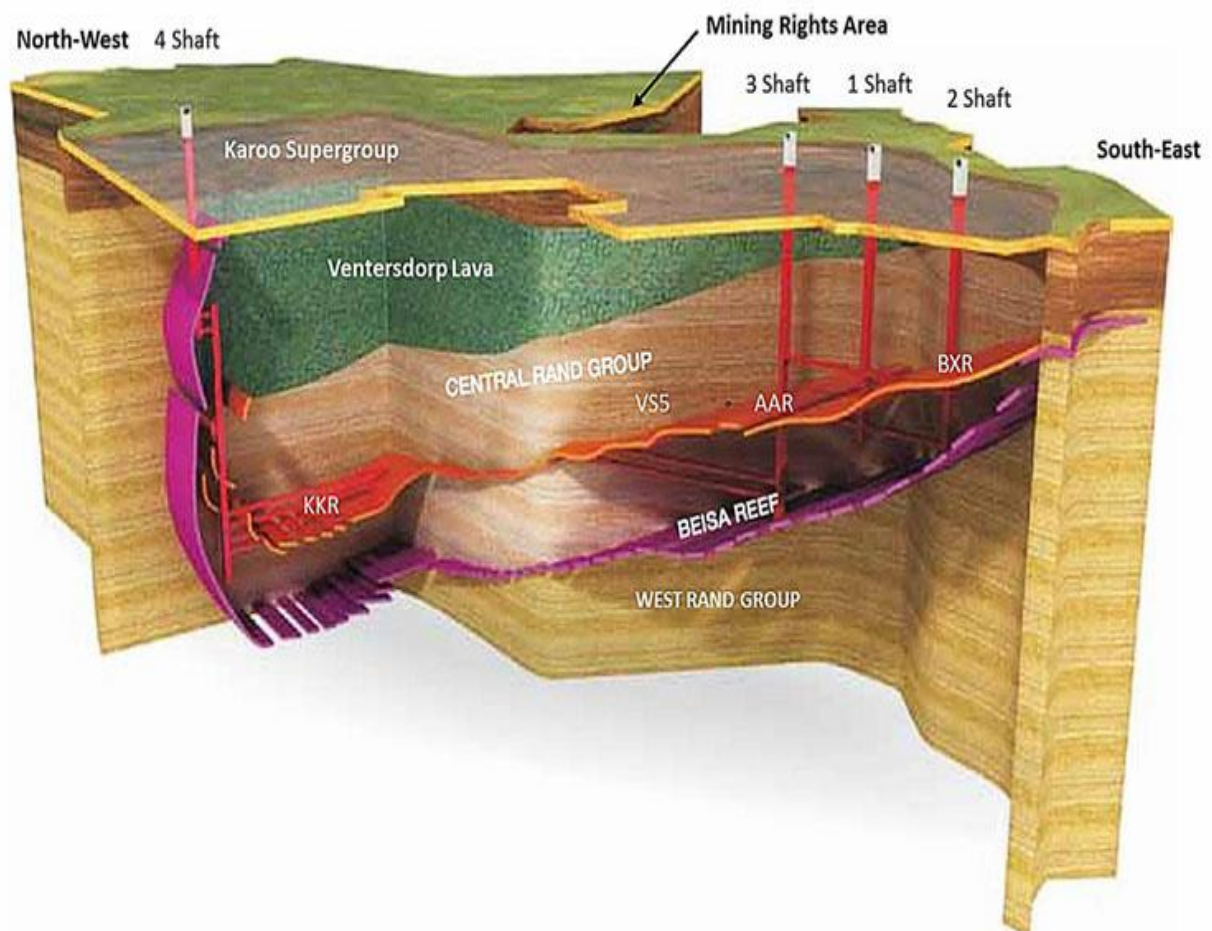


Figure 2-7. Schematic 3D section through Beatrix ore body: rectorite occurs within the modified shale bands of the Beatrix Reef indicated by BXR (Adapted from (GoldFields, 2011))

Rectorite occurrence of economic value exists in China (Hanlie et al., 2008). This large-scale deposit is hosted by Permian pelite rocks at Zhongxiang, Hubey Central China, and the rectorite is of the K-Na type.
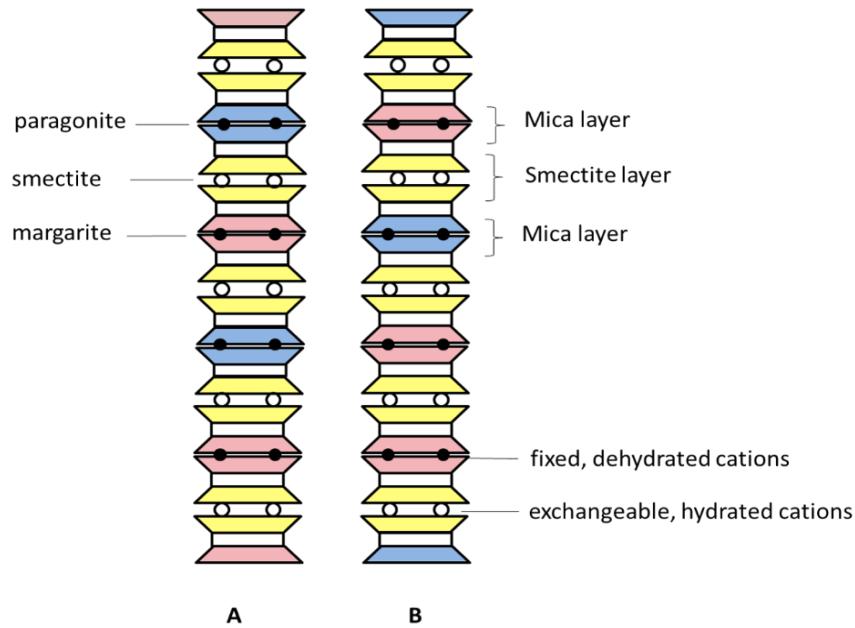
Figure 2-8. Schematic representation of the structure of rectorite adapted after (Jakobsen et al., 1995). Two configurations are shown to illustrate that the margarite and paragonite are not necessarily regularly alternating in the structure
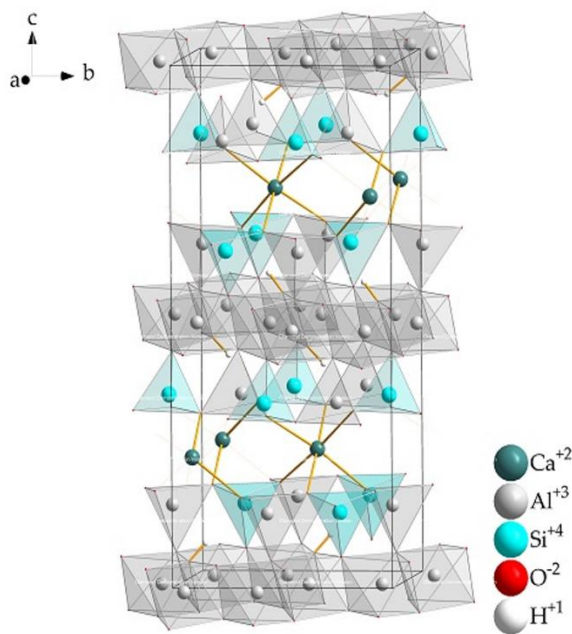


Figure 2-9. The structure of margarite CaAl$_2$Si$_2$A$_{12}$O$_{10}$(OH)$_2$, ICSD 34855 (Guggenheim and Bailey, 1975) (view down cristallographic *a*-axis)
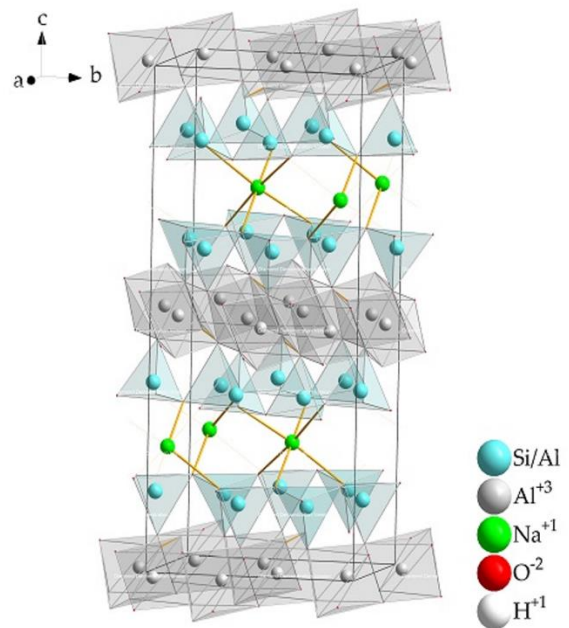


Figure 2-10. The structure of paragonite - NaAl$_2$(Si$_3$Al)O$_{10}$(OH)$_2$, ICSD_30663 (Lin and Bailey, 1984). Paragonite may contain K< 0.15 % (Rieder et al., 1998) (view down cristallographic *a*-axis)

## 2.5    Chitosan

Chitosan is the primary derivative of chitin, the most abundant biopolymer after cellulose. Chitin is a natural polysaccharide, a long-chain poly ($\beta$-(1→4)-N-acetyl-D-glucosamine), synthesised by wide range of living organisms as ordered crystalline nano-to-microfibrils and whiskers similar to isostructural cellulose. It is a major component in the exoskeleton of arthropods and the cell walls of fungi where it provides reinforcement and strength for structural components to function (Rinaudo, 2006) . The main commercial sources of chitin are crustaceans such as crab and shrimp shells. It is extracted by initial acid treatment to dissolve calcium carbonate, followed by alkaline extraction to solubilise proteins. Chitosan, a linear polysaccharide, is obtained under alkaline conditions when the degree of deacetylation of chitin reaches around 50 % (depending on the source) and it becomes soluble in aqueous acidic conditions (Figure 2-11). The solubility is enabled by protonation of the $-NH_2$ function on the C-2 position of the D-glucosamine repeat unit and the polysaccharide is converted to a polyelectrolyte in acidic solution (Rinaudo, 2006). Chitosan is characterised by its degree of deacetylation and molecular weight as these parameters have a strong effect on its solubility and solution viscosity.

There are two antiparallel chains and no water molecules in the orthorhombic unit cell of chitosan (Rinaudo, 2006). The acetyl groups are irregularly distributed along the chains due to the semi-crystalline nature of the initial polymer. In acidic solutions chitosan transforms from the random coiled structure typical of polysaccharides into extended chains due to protonation of the amine groups (Pan et al., 1999). Biopolymer intercalation in the clay interlayer space is influenced by the planar orientation of the chains and the position of the associated H-bonding network. During film formation chitosan forms arrays of parallel sheets of extended chains similar to chitin (Minke and Blackwell, 1978).

The existence of chemically active hydroxyl and amino groups facilitates modifications of chitosan to improve its properties or instil some new properties and functionality, e.g. chitosan can act as a natural electrolyte due to its ability to protonate in acidic media and become a water-soluble polycation. Chitosan is the only pseudo-natural cationic polymer and, being soluble in aqueous solutions, has proven suitable as a flocculent in protein recovery, and for the formation of gels, films and fibres in many applications. Due to its prominent biological characteristics, such as biocompatibility, biodegradability, antibacterial activity, film-forming ability and non-toxicity, chitosan has found utilisation in sectors such as biomedicals and pharmaceuticals, cosmetics, food, agriculture, and water and waste treatment (Dutta, 2004; Pillai et al., 2009; Rinaudo, 2006; Wang et al., 2016). However, properties such as weak mechanical strength, and gas and water vapour permeability limit its application spectrum. For these reasons chitosan is often combined in blends with other natural polymers such as starch, alginates, collagen and gelatin, proteins from milk or soy and clays (Elsabee and Abdou, 2013).
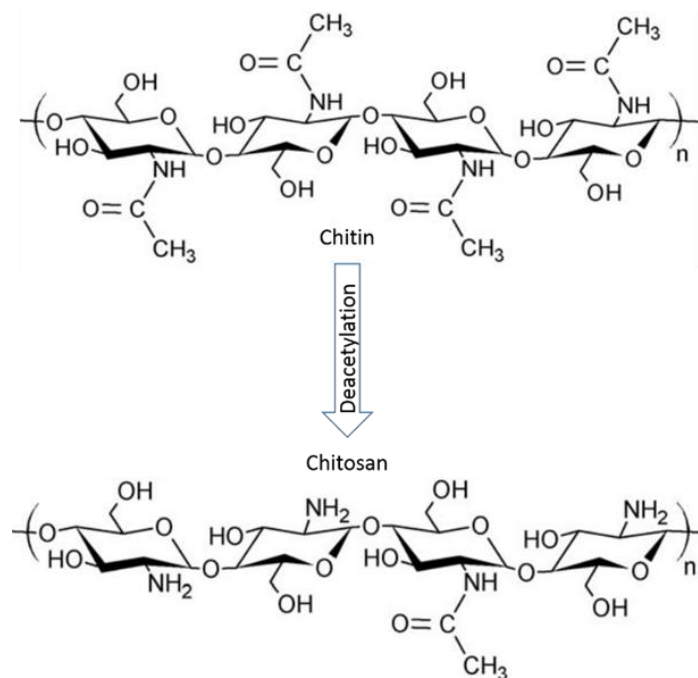


Figure 2-11. Formation of chitosan by partial deacetylation of chitin. (Adapted from (Chivrac et al., 2009))

## 2.6 Rectorite, nanoclays, biopolymers, bionanocomposites: state of research – fundamental and applied

### 2.6.1 Rectorite research

The research on rectorite during the 1950s and 1960s focused mainly on the occurrences and structural characterisation, using traditional investigative techniques such as XRD, XRF, IR spectroscopy, SEM, DTA and TGA (Brindley, 1956; Brown and Weir, 1963; Kodama, 1966; Reynolds & Hower, 1970; Korolev, 1961, 1971; Farmer and Russell, 1967). Besides the importance of interstratified clay minerals in the geological context, i.e. in the study of petroleum migration, rock permeability, and the use of smectite-to-illite transition as paleotemperature indicator in sedimentary and hydrothermally altered rocks (Hower, 1981), in recent years their properties have been increasingly investigated in search of novel materials and applications.

In the 1970s and 1980s the subject of clay-organic complexes made rapid advances in materials science, with applications in agriculture, food packaging and a variety of industries. The structures, reactions, experimental methods and applications of naturally swelling minerals have been extensively investigated by a large number of researchers and the findings have been most comprehensively summarised by (Theng, 1974, 2012).

The development of the solid-state NMR in the 1980s and 1990s added a new, highly valuable method for the structural analysis of 2:1 phyllosilicates. These studies brought more detailed insight into the nature and distribution of charged sheets in layered structures by determination of the Si/Al ratios and the ordering in tetrahedral and octahedral sites (Altaner et al., 1988; Barron et al., 1985a, b; Jakobsen et al., 1995; Lausen et al., 1999). The advancements in clay mineralogy and geochemistry allowed the development of a broad range of applications in both theoretical and practical aspects. The remarkable ability of swelling minerals to take up water and other molecules while preserving crystallographic integrity is highly advantageous for improved performance

in materials engineering. There is a growing preference for synthetic analogues where disadvantages such as stacking faults, impurities, disorders and charge heterogeneity can be controlled and tuned to attain the perfect filler with an ultra-high aspect ratio and high transparency for advanced gas-barrier applications, high water-vapour barriers, enhanced mechanical and thermal performance, and the overall increased functionality of nanocomposites (Kalo et al., 2012; Stöter et al., 2014; Stöter et al., 2013; Stöter et al., 2015; Tsurko et al., 2017).

Montmorillonite is the most widely researched and utilised clay mineral in the modification and reinforcement of polymer matrices. For the last two decades research on polymer-layered rectorite and other mixed-layer nanocomposites has been advancing notably, indicating promising prospects for organically modified rectorite (Chen et al., 2009; Huang et al., 2009; Huang et al., 2007; Yuan et al., 2007), natural rubber-rectorite nanocomposites (Wang et al., 2005) and the preparation of pillared clays (Bagshaw and Cooney, 1995; Kooli et al., 1997; Xiao et al., 2007; Zhang et al., 2010). A diverse group of investigators have evaluated the feasibility of using mixed-layer illite-smectite and clay minerals in general as caprock in $CO_2$ geological storage (Credoz et al., 2011; Gillman, 2011; Waldo, 2011) and for radioactive-waste disposal facilities (Phillips et al., 2011). Synthetic rectorite has also been obtained by a simple and fast method that can, in fact, be applied to any regularly interstratified composition (Möller et al., 2010). Clay-based nanostructured eco-materials in applications from energy storage to biomedical and other biodegradable materials is a fast-evolving field that could offer a relatively simple solution to a range of environmental problems of our time.

### 2.6.2 Clay films

The need for biodegradable alternatives to current high-performance engineering materials has focused research on sustainable resources and processes with a reduced impact on the environment. Natural phyllosilicate minerals are among the available options used for polymer property enhancement in a growing array of applications

(Lopes et al., 2014). The smectite group clay minerals, montmorillonite in particular, are commonly utilised as reinforcement agent in polymer nanocomposites. Clays are easily modified to suit specific functionalities because of their unique ion exchange capacity, reactive surface properties, lamellar morphology and favourable particle size and aspect ratio (Tjong, 2006; Zhang and Evans, 2012). Clay minerals are structurally similar to some crystalline organic systems with lamellar arrangement, e.g. polyethylene (Ballard et al., 1980). Both crystalline lamellae have comparable dimensions and large aspect ratios, with natural tendency to form oriented structures in thin films, coatings and membranes (Ballard and Rideal, 1983). Hybrid inorganic materials and clay-containing films are trending topics in materials science, especially in clay minerals research (Fernandes et al., 2014; Schoonheydt, 2014; Zhou et al., 2011).

Thanks to their platy morphology, the behaviour of clay minerals in aqueous dispersions facilitates film formation on evaporation. When clay platelets settle, they orient themselves to form brick-like microstructures analogous to that of nacre (Bennadji-Gridi et al., 2006; Sellinger et al., 1998). This natural tendency of clay platelets to assume face-to-face parallel orientation when dried from suspensions is the core principle of film formation by self-assembly (Liu et al., 2008; Walley et al., 2012).

Hauser and Le Beau (Hauser and Le Beau, 1938; Hauser and Le Beau, 1939) first demonstrated the preparation of clay films from bentonite gels. The so-called "Alsifilm" (aluminium silicate film) was developed as a replacement for mica in electrical applications, including insulation (Anon, 1939). Walley et al. (Walley et al., 2012) extended the work of Hauser and Le Beau and confirmed that the simplest way to obtain nanocomposites similar to the microstructural arrangements seen in nacre was to allow dilute clay suspensions to evaporate by slow drying. Biomimetic nanocomposites have shown that layered microstructure is critical for attaining the remarkable properties of nacre (Fernandes et al., 2014; Kawasaki et al., 2010; Liu et al., 2008; Walley et al., 2012; Walther et al., 2010).

Binder-supported composite films with high clay loading exceeding 80 wt.% (Ebina and Mizukami, 2007) displayed high temperature stability and excellent gas-barrier and flame-blocking properties (Wang et al., 2013). Binderless clay films were produced by hydrothermally pre-treating the clay to increase the particle size (Nam et al., 2009b). Due to the presence of impurities, natural clay is usually regarded as unsuitable and hence synthetic smectite clays are preferred to achieve the desired transparency of the films (Ebina and Mizukami, 2007) (Nam et al., 2009b). The effect of interlayer cations in montmorillonite on film formation and properties was also investigated (Nam et al., 2009a). Films prepared from monovalent cation-exchanged montmorillonite appeared well-ordered with thin wavy layers, while those made with polyvalent cations featured poorly ordered layers of larger particles. Bennadji-Gridi et al., (2006) reported a 120 MPa bending strength for montmorillonite films prepared with 10 wt.% sodium hexametaphosphate $(NaPO_3)_6$ as a binder. However, it seems that to date no significant mechanical properties for binder-free, clay-only films have been reported.

## 2.6.3 Bionanocomposites: polysaccharides, rectorite-chitosan nanocomposite films

Bionanocomposites are hybrid materials made from structurally combined biopolymers such as polysaccharides, proteins, lipids and nucleic acids with inorganic solids such as clays or other layered materials, phosphates or carbonates at nanometre scale (Darder et al., 2007; Ruiz-Hitzky et al., 2005). In recent years they have become the ultimate alternative to reduce human impact on the environment by the development of efficient ecological solutions for new environmentally friendly hybrid materials. As defined by ASTM Standard D 5488-94d, biopolymers are biodegradable materials capable of undergoing decomposition through microorganisms and enzyme-induced degradation (ASTM, 1994). The synergy of a biodegradable, biocompatible and non-toxic component with the mechanical and thermal properties of the inorganic counterpart produces an environmentally friendly composite material with superior performance. Most

bionanocomposites are synthesised by biomimetic or nature-inspired design and, as such, encompass the advantages of green technologies and enhanced performance. Thus these hybrid materials defeat an old common presumption that materials are either high performance or eco-friendly, but nor both simultaneously.

Biobased nanoparticles are efficient building blocks for innovative materials with a diverse scope of application. The biocompatibilty requirement is limited merely to specialised advanced biomedical use for tissue engineering, drug delivery and regenerative medicine (Anitha et al., 2014; Armentano et al., 2013). The non-toxic and biodegradable characteristics combined with mechanical, thermal and barrier properties in the new hybrid multifunctional materials attract user and manufacturer interest in a constantly expanding application range. This range includes food packaging and gas-diffusion barriers (Rhim et al., 2013), electrochemical devices (Darder et al., 2003, 2005; Darder et al., 2006), bioplastics and membranes, water purification and treatments, metal toxicity, controlled drug release and pesticides delivery, and energy applications (Brambilla et al., 2014; Liu et al., 2017; Reddy et al., 2013; Zafar et al., 2016; Zhao et al., 2014). Bio-sourced plastics (bioplastics) such as polylactide and plasticised starch are already in use and commercially available. However, their properties, e.g. mechanical strength and barrier property, need to be enhanced to make them really compatible with petroleum-based plastics. Natural phyllosilicate minerals are among the most suitable inorganic property enhancers for polymer applications (Lopes et al., 2014). An addition of clay (up to 5 vol.%) to the polymer matrix may dramatically improve the properties of nanocomposites. In similar manner, the dispersion of nano-sized clay in a biopolymer matrix produces a bionanocomposite with enhanced performance. Hybrid materials with functional properties based on polysaccharides (starch, chitin, chitosan, cellulose acetate, pectin) and nanoclays (smectites – montmorillonite, hectorite, saponite; fibrous clays – sepiolite, palygorskite, halloysite) are being intensively explored at present for novel multicomponent and multifunctional materials (Chivrac et al., 2009; Ruiz-Hitzky et al., 2013). Layered silicates enhance the physicochemical characteristics and mechanical

properties of biocomposite products, among others those of chitosan and its derivatives (Wang et al., 2009b; Wang et al., 2008).

A large volume of research on biomimetic or nature-inspired designs of new nanocomposite materials has been conducted and published in science literature (Fernandes et al., 2014; Kawasaki et al., 2010; Liu et al., 2008; Luz and Mano, 2009; Luz and Mano, 2010; Walley et al., 2012; Zhao et al., 2014). Research on natural and artificial nacre has pinpointed that, in fact, it is the layered microstructure that defines its remarkable properties with functionalities different from or superior to those of the primary constituents. The platelet shape and attractive interactions between clay surfaces are crucial for the formation of textured layers in the preparation of artificial nacre (Bennadji-Gridi et al., 2006). Exfoliation of montmorillonite is critical for the successful formation of clay-based nanocomposites (Kolman et al., 2012). The ability of exfoliated layered clay structures to intercalate compatible biopolymer molecules allows the formation of hybrids with functional properties. However, manufacturing large volumes of these biomimetic aligned structures with unique characteristics and remarkable performance by an effective production process has not been yet achieved.

Clay-containing films and hybridisation of inorganic materials is a hot topic in clay research, materials science and industrial research in general (Fernandes et al., 2014; Schoonheydt, 2014; Zhou et al., 2011). The physico-chemical properties of clay minerals, and especially expandable species from the smectite group, define their specific behaviour in aqueous dispersion crucial for film formation. Upon evaporation from suspensions, the dispersed clay platelets are highly susceptible to the formation of brick-like microstructures similar to that of nacre (Bennadji-Gridi et al., 2006; Sellinger et al., 1998). The natural tendency of clay platelets to assume face-to-face parallel orientation when dried from suspension is the core principle of film formation by self-assembly (Liu et al., 2008; Walley et al., 2012).

Composites and bionanocomposites with mixed-layered clay minerals and specifically ordered structures such as rectorite are not as popular as those with montmorillonite for instance, most probably because rectorite is not as easily available commercially as smectite clays. A substantial part of the research involves organically modified rectorite with the aid of thermal pre-treatments and plasticisers to improve the properties of the clay and resulting composites. Addition of up to 20 wt.% modified rectorite to thermoplastics and natural rubber has improved the glass transition temperatures and stress-strain behaviour of the nanocomposites (Ma et al., 2005; Ma et al., 2004; Wang et al., 2005) and just 2 wt.% organic rectorite positively affected the mechanical strength and thermal and ultraviolet aging in polyester resin composites (Yuan et al., 2007). Organically modified rectorite combined with various biopolymers has been found to impart desirable mechanical properties, e.g. improving the ductility of poly(lactic acid) (Li et al., 2009), enhancing ultraviolet ray resistance, and imparting mechanical and thermal stability properties in rectorite-sodium alginate bionanocomposites (Yang et al., 2009), as well as composites with plasticised starch (Chang et al., 2012) and soy protein (Yu et al., 2007).

Research on rectorite-chitosan (Rec/CS) composites has explored a variety of preparation techniques, clay pre-treatments for property enhancement and fields of applications (Deng et al., 2012; Wang et al., 2007; Wang et al., 2009b; Wang et al., 2005). Among other properties, the excellent catalytic efficiency of Rec/CS-metals has been recorded (Ling et al., 2015; Zhang et al., 2017), as well as organic Rec/CS composites in magnetic separation technology for the remediation of polluted water (Zeng et al., 2015b) and the adsorption of other metals (Zeng et al., 2015a). Rec/CS hybrid materials are highly sought-after in food packaging and preservation due to their good antibacterial activity (Deng et al., 2012; Huang et al., 2012; Wang et al., 2009b; Wang et al., 2006) for biomedical and agricultural applications in drug encapsulation for delivery and controlled release (Wang et al., 2007; Xu et al., 2012) and as a potential non-viral gene carrier (Wang et al., 2008).

## 2.7    Analytical and characterisation techniques

### 2.7.1  Brunauer–Emmett–Teller (BET)

The BET technique is used to measure the specific surface area and porosity of macro-, meso- and micro-porous materials. Because of their generally small particle size (< 2 µm), clay minerals have a large and variable surface area which has a significant effect on their properties (Table 2-2). The external surface area, which is a function of mean crystallite size and morphology, can be determined by the BET method.

The BET theory was developed in 1938 by a team consisting of Hungarian chemist Stephen Brunauer, American chemical engineer Paul Emmett and Edward Teller, a Hungarian physicist, while working on ammonia catalysts. It was named by combining the first letters of each surname of the three researchers. The theory is principally an extension of the Langmuir theory based on the physical adsorption of gas molecules on a solid surface developed by Irving Langmuir in 1916 (Langmuir, 1918). While the Langmuir theory relates to a monolayer adsorption, the BET theory assumes a multi-layer adsorption model for gas molecules on a solid surface (Brunauer et al., 1938).

Adsorption is defined as the adhesion of gas atoms or molecules to a solid surface. The BET method usually uses nitrogen gas as adsorbate because it is easily available in high purity and is known for its relatively strong interaction with solids. Helium gas is used as a blank before and after each measurement to calibrate the dead volume in the sample cell. Prior to measurements, the sample is degassed in a glass cell for 16 h in vacuum at a high temperature, chosen such that it will not destroy the structure. The solid surface is pre-cooled with liquid $N_2$ to enhance interaction. Known amounts of nitrogen gas are then released stepwise into the sample cell under partial vacuum to maintain relative pressures below the atmospheric pressure. Saturation pressure is achieved when adsorption has subsided, regardless of any further increase in pressure. Thereafter the sample is removed from the nitrogen atmosphere and heated to release the adsorbed gas,

which is then measured and quantified. The amount of adsorption depends on the exposed surface area as well as the temperature, gas pressure and strength of gas–solid interaction. The data is displayed in the form of a BET isotherm, which plots the amount of gas adsorbed as a function of the relative pressure.

### 2.7.2   Infrared and Fourier transform infrared spectroscopy (FTIR)

Infrared (IR) absorption spectroscopy is a rapid, non-destructive method applied across a broad range of applications in materials science (McKelvy et al., 1996). It is the main complementary method to X-ray diffraction for structural analysis in clay mineralogy and soil sciences (Farmer, 1968, 1974; Farmer and Russel, 1967; Madejova and Komadel, 2001; Russell, 1987). It provides information on the chemical bonds and their environment with the advantage of differentiating poorly crystalline (amorphous) materials. The technique is based on the absorption of multi-wavelength IR radiation and measures the degree of absorption of the IR spectra. Absorption is related to the molecular stretching and bending vibration modes. In inorganics it is controlled by the constraints of the total unit cell symmetry and local site symmetry of each atom, degree of crystalline order, atomic mass and interatomic bonds in the structure. The absorption of IR radiation is strongly affected by the size and shape of the mineral particles and particle orientation relative to the IR beam (Farmer and Russel, 1966). The number of potentially active internal vibrations is given by $3n$-6 where $n$ is the number of atoms in the unit cell (Russell, 1987). Active infrared vibrations are those where a change in dipole moment occurs during the absorption. The absorption bands in the IR spectra are used to identify minerals, variations in structures and their causes, which are often not easy to identify by other methods.

The rapid development of IR spectroscopy in the 1980s to 1990s led to the replacement of the IR dispersive instruments by the more sensitive and quicker Fourier transform spectrometers (Rintoul et al., 1998). The IR dispersive instruments used transmittance mode and utilised attenuated total reflectance (ATR) as a sampling technique. They were

mostly used, and still are, in the characterisation and analysis of organic compounds. At present IR techniques such as diffuse reflectance, specular reflectance, attenuated total reflectance, photoacoustic spectrometry, infrared microscopy, long-path spectrometry, and remote fibre optic spectrometry are routinely used. They have expanded the utilisation of FTIR methods into more diverse and complex materials such as minerals, polymers, thin films, living cells and biological tissues. ATR combined with the more sensitive FTIR is routinely used in the study of clay minerals, specifically in the adsorption of organic substances. Its main advantage is that it allows IR measurements of dispersions, gels and pastes (Li et al., 2008; Shewring et al., 1995).

In a routine FTIR spectrometer, the detector monitors the full pre-set wavenumber range of radiation emitted by the IR source. The output interferogram is transformed into an absorption spectrum by a computer interface. The FTIR spectrometers are either single beam or double beam. A typical set-up includes the reflectance method (ATR) and classic transmission methods such as KBr-pellet. The ATR experiments are widely preferred as they require less sample preparation, but the method needs corrections for constant optical path to obtain spectra, and processing of the spectral data is more complex. For transmission experiments clay samples are pelletised in KBr; however, due to its hydrophilic nature this method is not suitable for studying water-absorption properties and also poses a risk of spontaneous exchange of $K^+$.

Clay minerals are generally distinguished by their characteristic O-H, Si-O, Si-O-Al and Si-O-Si bands in the mid-IR region 4000–400 cm$^{-1}$.

### 2.7.3 Characterisation of functional properties

### 2.7.3.1 Mechanical properties

Mechanical properties are an important measure of product quality characteristics. Testing for film mechanical properties include tensile strength (at yield or at break, MPa), strain at yield (%), elongation at break (%), Young's modulus or elastic modulus (GPa).

For a tensile test a load is applied along the longitudinal axis of a test specimen and the applied load with resulting elongation are measured. Load-deformation data obtained from tensile test do not give a direct indication of the material behaviour, because they depend on the specimen geometry. Using the relationships in equations (Eq.) (2-1) and (2-2) the obtained measurement data can be converted to stress ($\sigma$) and strain ($\varepsilon$) values respectively:

$$\sigma = P/A$$

(2-1)

$$\varepsilon = \delta/L$$

(2-2)

where $\sigma$ is normal stress on a plane perpendicular to the longitudinal specimen axis; $P$ is the applied load; $A$ is the original cross sectional area; $\varepsilon$ is the normal strain in the longitudinal direction; $\delta$ is the change in the specimen's gage length, and $L$ is the gauge length.

The resulting stress-strain curve or diagram gives a direct indication of the material properties. For most materials used in engineering the initial section of the stress-strain diagram is a straight line. For this initial portion of the diagram, the stress $\sigma$ is directly proportional to the strain $\varepsilon$, i.e. the case of uniaxial loading. Thus, for a specimen subjected to a uniaxial load, this relationship can be expressed by Hooke's Law in Eq. (2-3), first recorded in 1678 by Robert Hooke, an English mathematician (Ugural and Fenster, 2003).

$$\sigma = E\varepsilon$$

(2-3)

The slope of the straight-line portion of the stress-strain diagram is called the Modulus of Elasticity or Young's Modulus E (McNaught and Wilkinson, 1997) and is calculated by:

for normal stress-strain:
$$E = \sigma/\varepsilon \qquad (2\text{-}4)$$

for shear stress-strain:
$$G = \tau/\gamma \qquad (2\text{-}5)$$

where $E$ is the Young's modulus or modulus of elasticity, and $G$ is the Shear modulus or modulus of rigidity.

### 2.7.3.2 Optical property

Ultraviolet-visible (UV-Vis) spectrophotometry uses the principle of absorbance of light by a substance at a given wavelength to determine its concentration. The method uses the light in the ultraviolet and visible range of the electromagnetic spectrum. The electromagnetic spectrum ranges from very short wavelengths $10^{-4}$ nm to 1 nm (including gamma and X-rays) to very long wavelengths $10^5$–$10^{10}$ nm (including microwaves and broadcast radio waves). The visible spectrum constitutes only a small part of the total radiation spectrum. Most of the radiation that surrounds us cannot be seen, but can be detected by dedicated sensing instruments.

When a beam of light passes through a substance or liquid, a portion of it gets absorbed and the other part is transmitted through. The ratio between the intensity of the light entering the sample ($I_0$) and that exiting ($I$) at a particular wavelength is defined as transmittance ($T$). The absorbance ($A$) is the negative logarithm of $T$, i.e.:

$$A = -\log T \qquad (2\text{-}6)$$

The Beer-Lambert Law relates to the attenuation of light to the properties of the material that the light is passing through within well-defined prerequisites of the law. A simplified definition states that the absorbance of a beam of collimated monochromatic radiation in a homogeneous isotropic medium at a given wavelength is proportional to

the absorptivity of the material $a$ (constant at each wavelength) or also $\varepsilon$ (molar absorption coefficient), the concentration of the substance $c$ and the path length $l$ (the distance light travels to exit the sample, i.e. thickness) (McNaught and Wilkinson, 1997). So the Beer-Lambert Law for absorbance of light is:

$$A = \varepsilon cl \tag{2-7}$$

A basic UV-Vis instrumental set-up includes: a source of radiation, usually a tungsten lamp for the visible region and either a hydrogen or deuterium lamp for the UV spectral range; a monochromator and optical geometry to ensure that a single-wavelength monochromatic light beam enters the sample compartment; a sample handler; a detector and a measurement system for light intensity; and a software interface for data processing.

### 2.7.4 Microscopy

#### 2.7.4.1 Scanning electron microscopy (SEM)

SEM is used for high-magnification imaging and to obtain elemental spectra to determine mineral chemistry, provided an analytical system is available. In a principal set-up, an electron gun emits a beam of high-energy electrons under high-vacuum conditions. This beam travels through a series of magnetic lenses designed to focus the electrons on a very fine spot. Near the sample, a set of scanning coils moves the focused beam back and forth across the specimen (Goldstein et al., 1992; Wilson, 1987).

SEM images are produced by scanning the electron beam over a specimen surface and displaying the signal from an electron detector on a computer monitor by means of an amplifier.

Depending on whether secondary or backscattered electrons are used, the images provide either topographic or compositional information on the specimen. Secondary electrons (SE) are low-energy electrons ejected from the sample as a result of inelastic

collisions with beam electrons. They are produced near the surface of the sample, from a small area/volume around the beam tip (analytical volume). The resolution of the image is therefore very good and provides topographic information on the sample. Backscattered electrons (BSE) are high-energy primary electrons emitted as a result of elastic collisions with specimen electrons. BSE emission intensity is a function of the specimen's atomic number or average atomic mass, i.e. the higher the atomic number or average atomic mass, the brighter the signal, i.e. the image. BSE imaging is used to obtain qualitative compositional information from the sample.

Theoretically, SEM requires a highly polished surface for optimum imaging and X-ray microanalysis. For the imaging of clay minerals, the specimens are prepared as grain mounts, preferably freeze-dried to preserve fresh surfaces and structures. Specimens are commonly coated with gold or carbon for conductivity.

An Energy Dispersive System (EDS) linked to a SEM enables X-ray microanalysis. The process for X-ray microanalysis is as follows: when the electron beam interacts with matter, energy is released in the form of radiation over a variety of wavelengths. This energy results from beam electrons ionising the inner electron shells of an atom. When the excited atom relaxes, i.e. an outer electron fills the inner shell, radiation is released which is characteristic of the atom's electron shells' energy level. The portion of radiation in the X-ray part of the spectrum is referred to as characteristic X-rays. The generated X-rays are collected and plotted as an elemental spectrum. Each peak on the spectrum represents a transition with a characteristic energy – every element has its own "fingerprint" of peaks.

Maps of relative concentration for multiple elements can be generated using the SEM. This is achieved when an electron beam is scanned across the sample, stopping at regular intervals to count the number of X-rays arriving at the detector. The number of counts at each stop (pixel) can then be displayed as a map. By maximising the number of points at which X-rays are counted and by scanning the beam multiple times over the sample,

high-resolution maps can be produced. Element distribution maps could show concentration differences not detectable using backscattered electron imaging.

## 2.7.4.2 Transmission electron microscopy (TEM)

TEM and SEM are the two basic types of electron beam instruments. Usage of TEM for examination of clay minerals is not very popular due to the delicate nature of clay specimens and the risks of damaging structures of interest during sample preparation or by the electron beam during analysis. However, the high-resolution information that can be obtained at a unit cell level by imaging layered structures, with the ability to measure layer distances, can be invaluable for clay mineral studies.

In TEM the electron beam is transmitted through an ultra-thin section of the specimen under examination. The image is produced as a result of differential scattering and absorption as a function of the variation in electron density of the specimen. Areas of higher density scatter and absorb more and thus appear darker than areas of lower electron density (Flegler et al., 1993). Routinely, image resolutions of tenths of nanometres can be achieved. Proper sample preparation is crucial to provide the required electron-optically transparent specimens.

## 2.7.5   Nuclear magnetic resonance (NMR) spectroscopy

Solid-state NMR spectroscopy is a theoretically complex and powerful analytical technique fast becoming the preferred method for structural characterisation of powdered molecular crystals. NMR spectroscopy is the dominant method of analysis for organic compounds, but it is also increasingly gaining interest in inorganic chemistry and biochemistry for valuable structural information (Lambert and Mazzola, 2004). Nuclear magnetic resonance is a property of the nucleus of the atom known as nuclear spin ($I$). Although isotopes can have various spin values $I$ including 0, the most useful for spectroscopy are those nuclei with $I$= ½. A nucleus with a spin is associated with magnetic moment resembling thin atomic bar magnets. NMR spectroscopy is based on

the fact that when a population of magnetic nuclei is placed in an external magnetic field, the individual nuclei align in a finite number of orientations. The energy levels are determined by thermodynamics as described by the Boltzmann distribution, i.e. the lower energy level (nucleus aligned with the field) will contain slightly more nuclei than the higher level (aligned against the field). An NMR experiment involves electromagnetic radiation to induce the nucleus to jump to the higher energy state by absorbing energy, or by release of energy the nucleus may "relax" back to the lower energy state. Radio waves are at the very low energy end of the electromagnetic spectrum and are sufficient to induce the desired energy transition. An NMR instrument uses the Fourier transform method to apply a broad pulse of radio waves to excite all nuclei and the results are recorded and analysed by computer. In a real molecule, the effective magnetic field experienced by a nucleus ($B_{eff}$) includes not only the applied field ($B_0$), but also the magnetic effect of the surrounding nuclei and electrons. This causes interference in the absorption frequency, and is corrected for by using a standard, usually tetramethylsilane (TMS), defined as zero point. The output from the absorption experiment is plotted as a series of peaks in an NMR spectrum. The difference in ppm (parts per million) from the zero point is referred to as the chemical shift ($\delta$). A typical range for $\delta$ is around 12 ppm for $^1$H and 220 ppm for $^{13}$C. It is customary to have the zero point at the right-hand side of the spectrum, with numbers growing to the left ("downfield"). Typical isotopes useful for clay mineral crystallography by means of NMR spectroscopy are $^1$H, $^{27}$Al, $^{23}$Na and $^{29}$Si analysed by solid-state magic angle spinning NMR (MAS NMR).

### 2.7.6 Particle size determination and $\zeta$-potential

Particle size is a fundamental characteristic of clays and other particulate materials. Particle size distribution (PSD) may critically affect materials' behaviour and the properties of solids, suspensions, emulsions and aerosols. Therefore its accurate determination is of the upmost importance for research and industrial quality and performance. There are many different methods to measure particle size, e.g.

sedimentation, laser diffraction, dynamic light scattering, electron microscopy and image analysis. Each technique detects size according to its own physical principle and the particle shape factor is the major cause of disagreement between analysers. It is crucial to select the most suitable technology depending on the physical and chemical attributes of the material, property scope and application. It is always beneficial, if possible, to combine at least one imaging and one direct measurement technique. Microscopy or automated image analysis are the only techniques that, besides particle size, can describe multiple parameters such as shape and morphology which are important for particles with a larger aspect ratio, such as phyllosilicates.

## 2.7.6.1 Particle size distribution (PSD) in submicron to millimetre size range

Laser diffraction (LD) is a well-established and widely used technique for the determination of particle sizes ranging from < 0.02 µm to ~ 2 mm particles, depending on material and instrument sensors. The core principle of the LD method is measuring the angular variation in intensity of light scattered from a laser beam passing through a dispersed particulate sample. The angle of light scattering is inversely proportional to particle size, i.e. small particles scatter light at large angles relative to the laser beam. The measured scattering intensity data is processed and analysed by the system to calculate the size of the particles using the Mie theory of light scattering (Bowen, 2002; Lips et al., 1992). Reporting of results should define "average particle size" and always be accompanied by reference to the method of measurement or distribution base. There are different ways to define particle size. Many techniques use the assumption of spherical particles and report results as an equivalent spherical diameter. Most common is the equivalent volume spherical diameter, $d_v$, defined as the diameter of a sphere having the same volume as the particle. Thus, an irregular-shaped particle can be described in terms of the diameter of imaginary spherical particles that occupy the same volume as the measured irregular particle. The size distribution derived by laser diffraction technique is volume-based. For instance, if results indicate that 10 % of particles are in the size

category 20–22 μm, this means that the total volume of all particles with diameters in this range represent 10 % of the total volume of all particles in the distribution. Once the output data is analysed, the information can be displayed in different ways depending on application. A frequency curve shows the "modes" or peaks in the graph: several peaks indicate that there are distinct sizes of particles in the sample. Cumulative undersize or oversize indicates results "under" or "over" in the form of the percentage of the sample below or above a certain size of particle. The statistics of the PSD are calculated from the data using the derived diameters d(m,n), which is an internationally agreed standard method for the mean and other moments of particle size BS 2955: 1993 (BSI, 1993).

### 2.7.6.2 Particle size distribution (PSD) in nanometre to submicron size range

Dynamic light scattering (DLS), also called photon correlation spectroscopy (PCS) or quasi-elastic light scattering (QELS), is the technique commonly used to measure the size of particles in the submicron and nanoparticle region while dispersed in liquid. It is often complemented by the atomic force microscopy (AFM) technique for its capability for 3D visualisation of morphology, surface texture and particle roughness. Some of the modern ultra-sensitive analysers can measure the size of macromolecules in solution, e.g. proteins. The theoretical principles were laid out in the earliest work on light scattering by the atmosphere by Lord Rayleigh (real name John Strutt) for particles much smaller than the wavelength of incident radiation (Rayleigh, 1881, 1899; Strutt, 1871). Later experimental research combined Rayleigh and Mie scattering theories for complete solution for spherical particles of any size and refractive index (Cox et al., 2002; Drake and Gordon, 1985; Weiner et al., 2001). DLS measures Brownian motion and relates this to particle size.

The primary results from DLS are the mean value from intensity distribution called Z-ave (Z average) and polydispersity index (PDI), which describes the distribution width. Usually it is possible to convert results to a volume or number distribution for easy

comparison with other techniques. The cumulant analysis by the DLS method calculates the autocorrelation function as defined by ISO 13321 and ISO 22412 standards for particle size analysis by DLS. In order to produce comparable results, all systems should comply with the standard (ISO, 1996, 2017). The polydispersity index (PDI) is dimensionless and derived from the autocorrelation function with the assumption of a monomodal sample. It describes the width of Gaussian distribution. PDI values less than 0.05 indicate a highly monodisperse mode rarely seen in real dispersions. Values greater than 0.7 suggest an extremely broad size distribution and a sample that is not suitable for the DLS technique. Approximate guide values for dispersity parameters by DLS regard a PDI between 0.00 – 0.1 as monodisperse uniform and narrow distribution respectively, whereas a PDI in the range 0.1–0.4 and > 0.4 indicates a moderate polydisperse and a broad distribution respectively.

The Z-average is a hydrodynamic parameter and therefore only applicable for particles in dispersion or molecules in solution. Particle size derived as Z-ave (d.nm) will only be comparable with other techniques if the sample is monomodal, with a very narrow width of distribution, i.e. monodisperse, and particles are spherical or near-spherical in shape. In the case of a polydisperse system, particle size can be reported as $d$ (intensity), $d$ (volume) or $d$ (number).

### 2.7.6.3 Zeta potential

Zeta potential ($\zeta$-potential) is a physical property of any particle in suspension, macromolecule or material surface. It is a measure of the charge on a particle surface in a specific liquid. Determination of $\zeta$-potential is useful in predicting suspension stability and understanding inter-particle interactions in suspension. The stability of colloidal systems is explained by the DLVO theory (named after Derjaquin, Landau, Verwey and Overbeek – scientists who developed the theory in 1940) (Van Olphen, 1987). It deals with the balance between two opposing forces, i.e. electrostatic repulsion and van der Waal's attraction. The ionic environment around a charged colloid particle is best

described by the electric double-layer model: the Stern layer of counter-ions directly adjacent to the charged particle surface, followed by the diffuse layer further away but still attached to the particle such that it moves together with the particle. The thickness of the double layer depends on the type and concentration of ions in solution. The boundary between the double layer and the ions in equilibrium in the solution is called the slipping plane. The potential in mV measured at the slipping plane distance from the particle surface is defined as $\zeta$-potential and is related to the mobility of the particle (Figure 2-12).
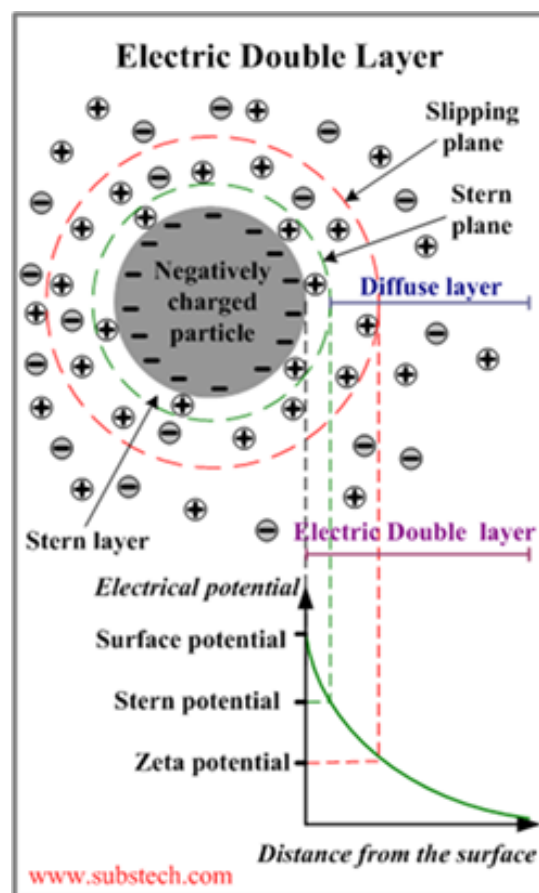


Figure 2-12. Schematic illustration of electric double layer and $\zeta$-potential

To measure $\zeta$-potential, a small volume of dispersed sample is injected into a cell containing two electrodes for the induced electric field. In a voltage field the particles move towards either the cathode or the anode depending on their surface charge. The direction of the motion indicates positive or negative charge respectively.

The instrumentation for $\zeta$-potential is usually combined with that for DLS. Optical configuration for $\zeta$-potential measurements includes a laser as a light source for incident and reference beams. The incident beam is aimed at the centre of the sample cell and the scattered light is detected. In an electric field applied to the cell, any particle moving through the measurement volume will cause fluctuation in light intensity with a frequency proportional to the particle speed. The speed of the particle motion is captured by a detector and transmitted to a digital signal processor to calculate the magnitude of the charge. The data is processed by the appropriate software to produce a frequency spectrum, from which the electrophoretic mobility and $\zeta$-potential, respectively, are calculated.

### 2.7.7 Thermal analysis

Thermoanalytical methods are used complementary to the principal mineralogical tool, XRD, in the qualitative and quantitative analysis of mineral mixtures. While the XRD uses structural information to characterise and identify phases, thermal techniques study the response and change in physical properties of materials upon heating under controlled conditions. Thermal analysis is most beneficial in the study of reaction processes and their products under dynamic temperature-pressure regimes such as dehydration/hydration, interaction of clays with organic and inorganic substances, or oxidation and reduction processes (Wilson, 1987). The most useful for clay studies are differential thermal analysis (DTA) and thermogravimetric analysis (TGA). DTA analysis detects changes in thermal properties by measuring the difference $\Delta T$ in temperature between the sample and a thermally inert reference standard under a controlled temperature range up to 1 400 °C. The DTA curves show endothermic or exothermic reactions indicating the energy changes in a sample. For instance in clays, endothermic reactions result from the desorption of surface $H_2O$ and dehydration (loss of interlayer $H_2O$) at temperatures < 1 000 °C or dihydroxylation and eventually melting at more elevated temperatures. Recrystallisation at high temperatures is exothermic and it may

occur concurrently with dihydroxylation and melting in this temperature range (Guggenheim and Van Gross, 2001). Alternatively, differential scanning calorimetry (DSC) can be used to monitor endothermic and exothermic reactions by measuring the energy input required to keep a sample and the standard at the same temperature over a controlled heating period. DSC is especially used for determination of enthalpy values.

The TGA curves indicate weight changes during heating. In clay minerals these changes are basically a function of water content and provide a very good indication of the mode of water present in the clay structure, i.e. surface absorbed water, interlayer bound water, hydroxyl or crystalline water. The TGA analysis produces an integral weight loss data curve that can be better interpreted using the first derivative of the weight loss curve, i.e. the derivative thermogravimetric analysis (DTG). Quantitative DTG is used mostly for poorly crystalline substances that cannot be adequately quantified by XRD due to the limitations of the technique with such materials.

### 2.7.8   X-ray diffraction (XRD)

X-ray diffraction (XRD) is by far the most commonly used laboratory tool for mineral/phase identification and structure characterisation. The discovery of X-rays in 1895 enabled scientists to determine crystal structure at atomic level. Because the wavelength of X-rays is comparable to the size of atoms, they are ideally suited for studying the structural arrangement of atoms and molecules in a wide range of materials. The technique provides information about the types and nature of crystalline phases, their structural make-up and degree of crystallinity, microstrain and size, and orientation of crystallites. X-rays are electromagnetic radiation with typical photon energies in the range of 100 eV–100 keV. For diffraction applications, only short-wavelength X-rays in the range of a few Angstroms to 0.1 Angstrom are used, which is about the same size as an atom. In the electromagnetic spectrum they occur between gamma rays and the ultraviolet rays.

Diffraction occurs as waves interact with a regular structure whose repeat distance is about the same as the wavelength (Moore and Raynolds, 1997). Bragg's Law (Eq. 2-8) empirically defines the conditions for diffraction in terms of the wavelength of the incident X-rays ($\lambda$), the interatomic distance between atoms planes ($d$), and the incidence angle of the X-ray beam to the atom planes ($\theta$) (Figure 2-13), i.e.

$$n\lambda = 2d\sin\theta \qquad\qquad (2\text{-}8)$$

If the atoms are arranged in a periodic fashion, as in crystals, the diffracted waves will consist of sharp interference maxima (peaks) with the same symmetry as in the distribution of atoms.

$$n\lambda = 2d \sin \theta$$
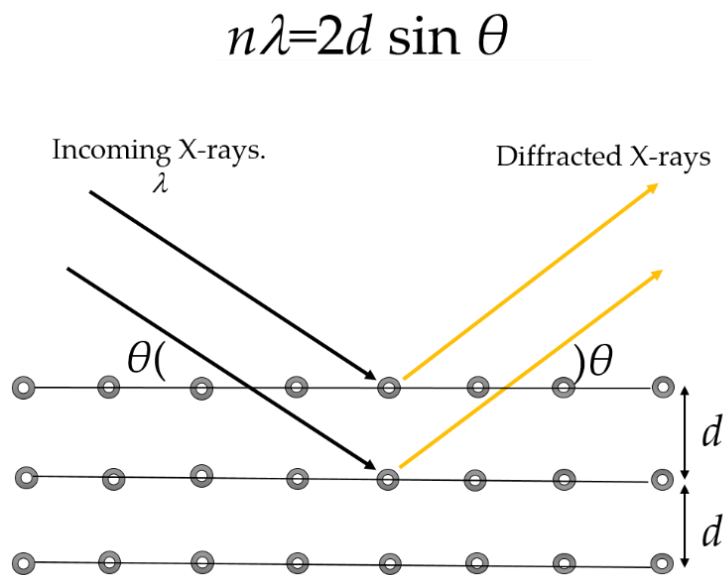


Figure 2-13. Schematic representation of Bragg's Law for X-ray diffraction

Measuring the diffraction pattern therefore allows the deduction of the distribution of atoms in a material (Figure 2-13). The peaks in XRD diffraction patterns are directly related to the atomic distances and thus allow determination of crystal structure. Each crystalline solid has its unique characteristic X-ray pattern that may be used as a "fingerprint" for its identification.
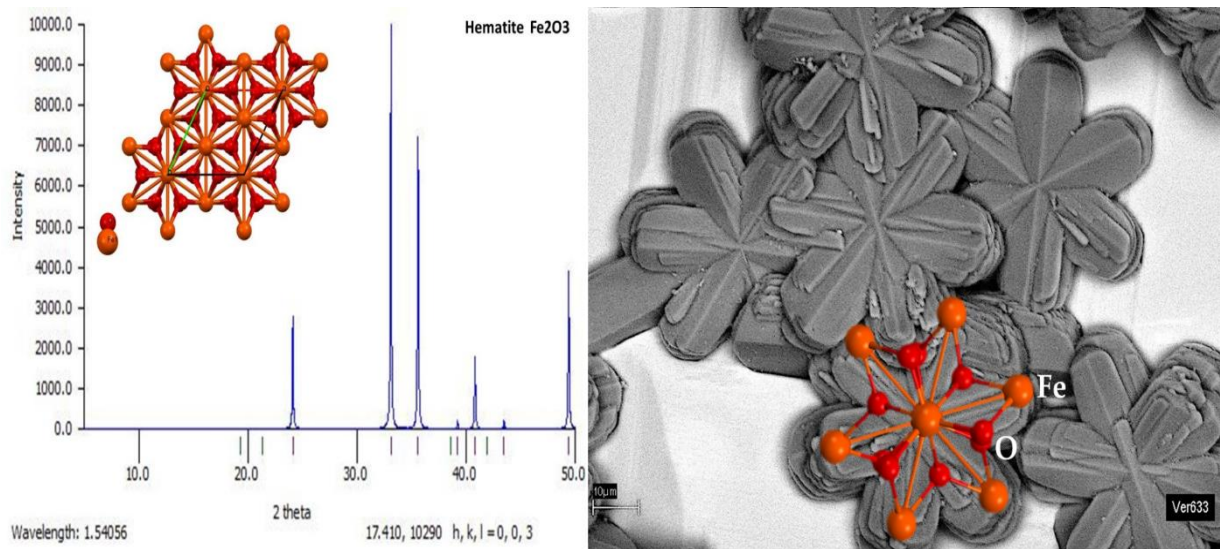
Figure 2-14. X-ray diffractogram (left) showing the peaks of hematite and insert of its structure model; (right) SEM image of a hematite crystal group with a fragment of the structure model superimposed to fit crystal morphology; FOV 137 µm

## 2.7.9   X-ray fluorescence (XRF) spectroscopy

The method most commonly employed for bulk chemical elemental analysis of clay materials is X-ray fluorescence spectroscopy (XRF). The technique is based on the ability of atoms constituting the matter to act as a secondary source of fluorescent X-rays when material is irradiated with primary X-rays or an electron beam source. The energy of the emitted X-rays is a function of the atomic number and concentration of each element constituent, which is the basis of quantitative elemental XRF analysis. The technique is applicable to all but the elements with a very low atomic number with sensitivities of parts per millions (ppm) (Jenkins, 1999). Fluorescent X-rays can be detected based on energy using energy-dispersive spectrometers (EDS) or their wavelength by means of wavelength-dispersive spectrometers (WDS). Modern technology offers combined EDS-WDS systems to accommodate a versatile range of materials and applications. An X-ray photon beam with enough energy to affect the electrons in the inner shells of the atoms in a sample is emitted by an X-ray tube (or an electron beam source) and focused on the sample. Upon interaction, electrons from the inner orbital shells of the atom are displaced

56

("kicked out"), creating vacancies and energy unbalance in the atom. Those vacancies can be filled by electrons from higher orbits that move down to a lower orbit. An electron loses energy when it drops from a higher binding electron shell to a shell closer to the nucleus (Figure 2-15). The amount of energy lost is equivalent to the difference in energy between the two electron shells, which is unique to each element. These energies can be used to identify the element from which it emanates and determine the quantity of each element present by either the instrument or by other software. Characteristic X-rays are labelled K, L, M or N, in analogy to the transitional shells from which they originate. Accordingly, the suffixes alpha ($\alpha$), beta ($\beta$) or gamma ($\gamma$) indicate different subshell levels (Jenkins, 1999).
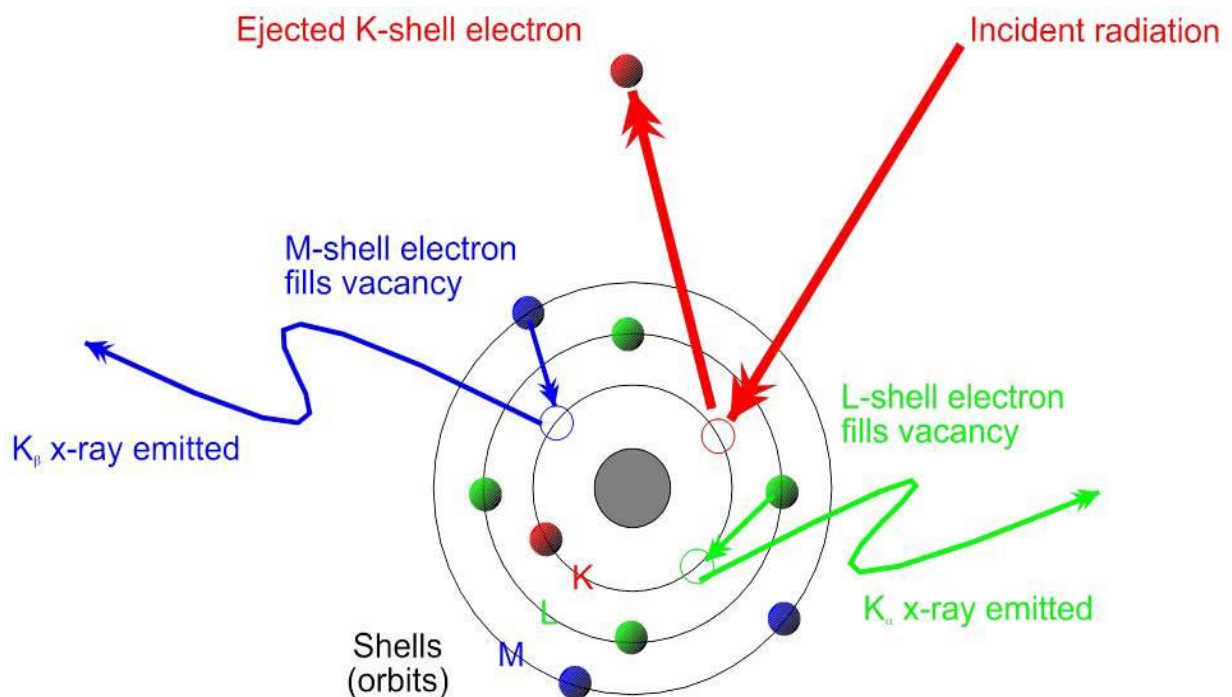


Figure 2-15. Production of a characteristic X-ray

# CHAPTER 3 EXPERIMENTAL: MATERIALS, METHODOLOGY, CHARACTERISATION TECHNIQUES AND INSTRUMENTATION

## 3.1 Materials

Three samples of mine host-rock material containing rectorite (Figure 3-1) were obtained from Beatrix Gold Mine and marked RT1, RT2 and RT3. Sample RT1 was collected in 1995, sample RT2 in 2010 and sample RT3 in 2012. The samples differ in their visual appearance with RT1 containing large light blue-grey platy aggregates with a silky lustre, whereas RT2 and RT3 represented disintegrated host rock mine material (Figure 3-2 (A, B and C)). Note that throughout this text RT followed by a number 1, 2 or 3 denotes the sample name/number, whereas in the composites the abbreviation Rec is used for rectorite mineral proportion in the composites.



Figure 3-1. In situ rectorite-rich material in the shale footwall at Beatrix mine

All samples were purified to concentrate high-purity rectorite clay for characterisation tests and experimental work. Unless otherwise indicated, the characterisation presented here is based on purified material with a rectorite content above 90 wt.% (as determined by XRD analysis). Structurally and chemically, the purified materials from the three samples are very similar and are categorised as rectorite, except where applicable specifics are highlighted. For rectorite characterisation mostly material from sample RT1 was used, whereas for cation-exchanged modifications and nanocomposite films purified rectorite from sample RT3 was used because of its abandance.
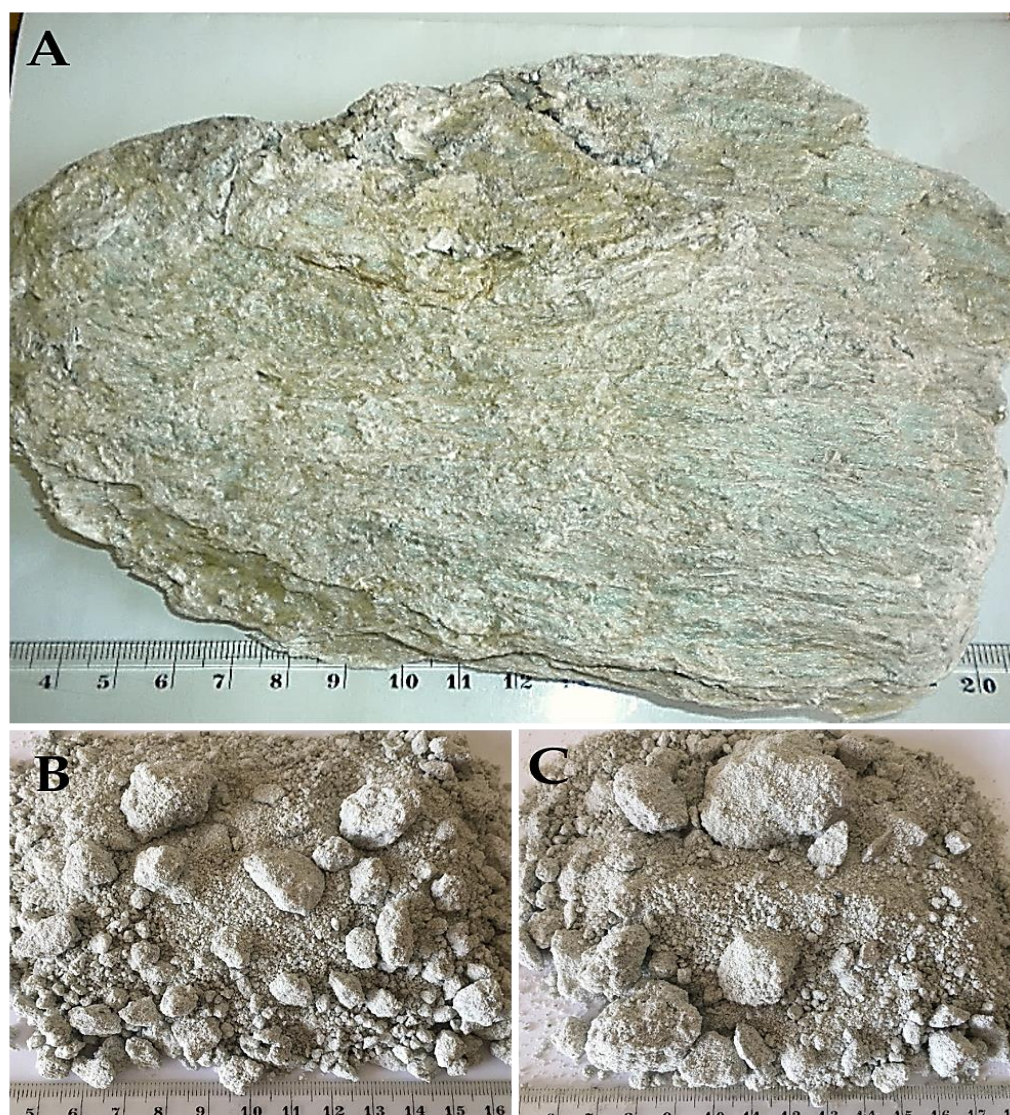


Figure 3-2. Macroscopic view of Beatrix rectorite from: (A) sample RT1 with rectorite content ~72 %; (B) disintegrated mine material from sample RT2 with rectorite content ~60 %; and (C) sample RT3 containing ~46 % rectorite

Organic surfactants, i.e. long-chain dodecyl-dimethyl ammonium chloride (DCC10), dialkylmethylammonium chloride (DCC18) and hexadecyltrimethyl-ammonium chloride (SCC16), as well as the metal chlorides of Li, Na, $NH_4$, K, Cs, Mg, Ca, Sr and Ba for cation exchange, were sourced from Merck Chemicals, SA. Chitosan (CS) of average molecular weight, i.e. viscosity of 150 mPas (1.0 wt.% solution in 1 % acetic acid at 25 °C) and degree of deacetylation 86.7 %, was obtained from G.T.C. Bio Corporation, China.

Other chemicals used in the laboratory experimental work such as acetic acid ($CH_3COOH$), silver nitrate ($AgNO_3$), calcium nitrate tetrahydrate ($Ca(NO_3)_2 \cdot 4H_2O$) and other supplementary laboratory consumables were supplied by either Merck Chemicals, SA or Sigma Aldrich, SA (since 2014 Sigma Aldrich has been a subsidiary of Merck KGaA). High-purity corundum ($Al_2O_3$) and zincite (ZnO) used for calibration and/or as internal XRD standards for structure modelling were purchased from Sigma–Aldrich, SA.

## 3.2 Primary processing of rectorite clay material

Primary processing of raw clay material and sample preparation were done as carefully as possible to prevent any physical distortion of the clay structure that may affect its behaviour, properties and the respective experimental results. The general guidelines on sample preparation for clay minerals outlined by Brindley and Brown (1984) and Moore and Raynolds (1997) were followed, with slight adaptations to accommodate specifics encountered in the preparation process. All pre-treatments were kept to a minimum and as mild as possible, both physically and chemically.

The method and degree of primary sample processing were determined by the physical appearance and aggregate size of the raw material of the three samples. Where applicable, the material containing raw rectorite was first disaggregated with a laboratory jaw crusher (sample RT1) to break down large platy aggregates to around 1 – 2 mm, followed by further size reduction in a swing mill, coffee-grinder, kitchen blender,

or McCrone micronising mill (McCrone Research Associates Ltd., London). Samples RT2 and RT3 were first sieved and the < 75 µm fraction used for further purification. As needed, vibrating mill (Retsch GmbH, MM30401, 80W) was utilised to prevent lump formation and aggregation of milled material.

## 3.3    Purification of rectorite

Structural identification and characterisation of clay minerals is usually performed on a concentrated clay fraction extracted from the bulk. In most cases the extraction of a small portion of < 2 µm clay fraction by gravity separation is sufficient for analytical purposes. However, for the characterisation of the engineering properties of rectorite products in this study a more efficient purification process was required to obtain larger quantities of concentrated pure material. The design and extent of the purification procedure was based on bulk mineral composition and mineral associations determined by a preliminary XRD and SEM investigation of the starting material. These observations suggested that impurities could be liberated through ultrasonic dispersion and separated by gravity sedimentation which served as the basis for the design of the purification procedure. In this way it was possible to remove the larger-than-clay fraction components such as quartz and other lump-sized clay minerals from the bulk.

Different methods including sieving, a Wilfley table for gravity separation by shaking, chemical treatment and gravity sedimentation were experimentally tested and evaluated to optimise the final process. It was established that the most efficient and successful method/procedure for best rectorite recovery involved primary disaggregation as needed, dispersion by ultrasound, gravity separation through sedimentation and recovery by centrifugation.

### 3.3.1  Removal of calcium carbonate

Calcite impurity in sample RT1 was removed using 0.3 M acetic acid following a standard method (Ostrom, 1961). The separation was performed at room temperature and the

process was closely monitored by measuring the pH after each cycle. The samples were repeatedly washed after effervescence had subsided. X-ray diffractograms were compared before and after exposure to acid to ensure that calcite had been removed and no damage to the rectorite structure had occurred. In the process some quartz and clinochlore were also washed out.

### 3.3.2 Removal of quartz, clinochlore, mica and pyrophyllite

This procedure was applied to samples RT2 and RT3 using the < 75 μm fraction of the bulk disintegrated mine material. The method was carefully designed and experimentally refined according to the mode of occurrence of rectorite in the Beatrix material with optimal utilisation of the available laboratory equipment. The aim was to find the most efficient, fast and economical process for maximum recovery of high-purity rectorite clay.

For the development and optimisation of the rectorite purification method, a Malvern Mastersizer 2000 instrument was utilised. The analyser bath was used to mimic the process of particle disaggregation and dispersion. Values for solid/liquid ratio, ultrasound settings, obscuration and dispersion time were monitored, measured, evaluated and adjusted for optimal performance. The concentration of particles in suspension during a measurement in a particle size analyser was monitored by the obscuration of the laser beam caused by the sample. It is a measure of the fraction of light "lost "when the incident laser beam passes through the sample in suspension due to scattering or absorption.

The intensity and duration of ultrasound dispersion was derived from the outcomes of two experiments: (i) three runs were performed at different ultrasound (US) settings, namely 70 %, 30 % and 0 % US over a duration of 2 h, measuring obscuration every 5 min; (ii) the particle sizer was run overnight at 30 % US, measuring obscuration every 5 min. The plots in Figure 3-3 show that the obscuration increased quickly in the first 30

min, then slowed down and became almost a straight line before increasing again after 60 min, best evident in the 30 % experiment. This ultrasound setting also provided obscuration within 10–20 % for up to 60 min, which is the optimal range recommended by the particle analyser.

The experiment run overnight for 15 h at 30 % US in the particle sizer showed a similar trend for a slow but steady increase in particle concentration over time. However, particle distribution curves indicated that after the second hour an additional population of intermediate particle size starting to form, most possibly due to the re-aggregation and formation of lumps or measurement artefacts caused by particle orientation with respect to the laser beam during prolonged measurement. Based on these two experiments, dispersion for 30 min at 30 % ultrasound intensity proved to achieve fast production and is at the point before the obscuration curve begins to flatten out. This conclusion was also supported by measurements of derived diameters d(m,n), suggesting that after 30 min of dispersion the mean particle size almost reaches a plateau (Figure 3-4).
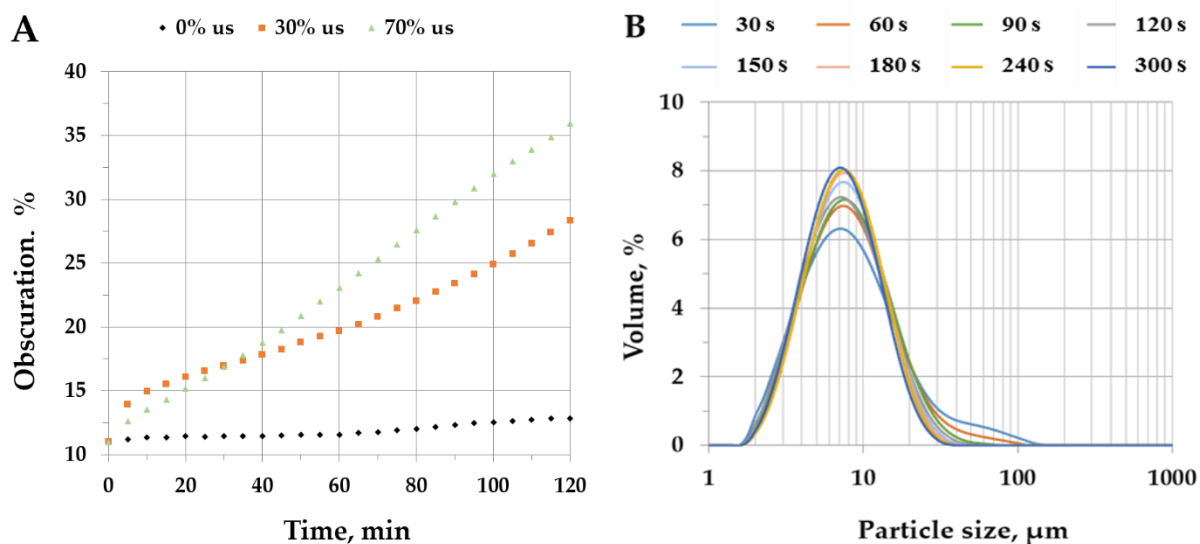


Figure 3-3. Obscuration vs. time: (A) 0.6 g dispersed over 2 h at different ultrasound settings; (B) particle distribution for 0.6 g sample over 5 min at 30 % ultrasound

The experiments in the method development stage conducted in the particle analyser bath were performed with a 0.6 g of sample. This amount was calibrated as optimal for

the rectorite material to maintain obscuration in the ideal recommended range of 10–20 % and prevent blockage of and damage to the equipment. To optimise the process for large volums production, this mass was extrapolated by experimentally monitoring the particle size distribution at the already established obscuration-ultrasound-time settings (Figure 3-3). Careful account was taken of process artefacts such as heat generation and lump formation during sonication step and size measurements. The capacity of the available stand-alone ultrasound bath (LABOTEC SCIENTECH 702, 50Hz, 5.7 l) and glassware was also considered to achieve the highest production rate with the least loss of material and efficiency. Thus it was decided that 50 g of starting material would be mixed with 250 ml of ultrapure water and subjected to ultrasound treatment for 30 min. Five 400 ml glass beakers were placed in the ultrasound bath at a time at optimised settings for frequency, power and temperature, i.e. high frequency equivalent to 30 % ultrasound as discussed above, power set to 4, temperature set to ambient and timer set to 30 min.
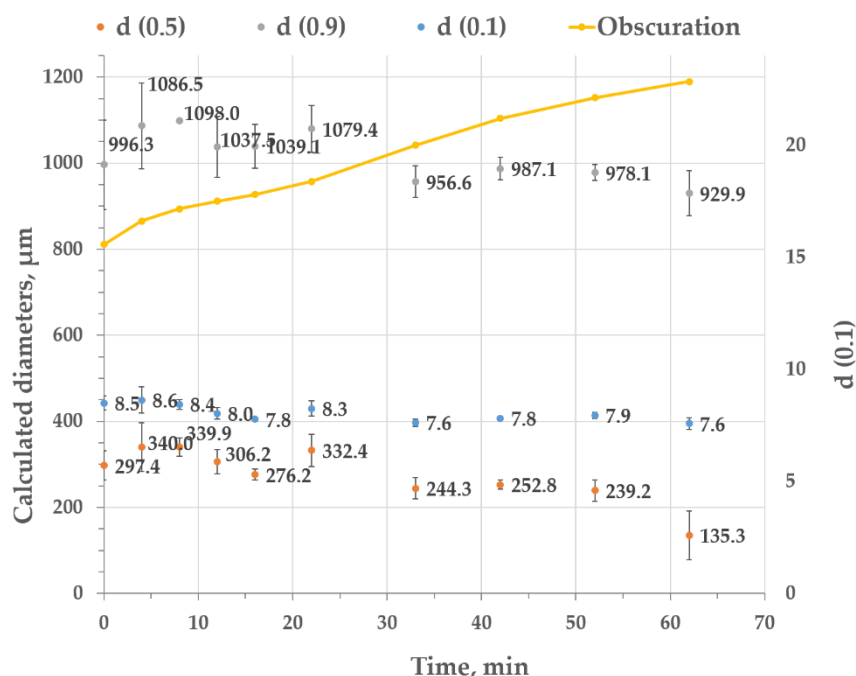


Figure 3-4. Obscuration and derived diameters vs. time: 0.6 g dispersed over 60 min at 30 % ultrasound

To determine the optimum settling time, two experiments were undertaken: (i) five beakers containing 50 g of rectorite material were treated for 30 min in the ultrasound bath. Each beaker was decanted every 30 s in sequence and the particle size measured. The particle size distribution curves are shown in Figure 3-5(A); (ii) the same experiment was carried out in time steps 120 s, 300 s, 900 s, 1200s and 1800 s and the results are plotted in Figure 3-5(B). These results and the XRD quantification on the purified material showed that settling for 5 min gave good particle distribution, good recovery (> 5 g) and high purity of rectorite clay (90–95 %). The results of the second run (2) showed the narrowest particle size distribution after settling for 15–20 min with good purity (> 90 % rectorite), but a lower recovery rate (< 3 g per 50 g), suggesting that due to the longer settling time some of the rectorite clay particles also settled down with the impurities. The 5 min settling time was chosen and applied throughout all the recycling steps of the final process as it is the optimum with least loss and gave the best recovery rate during the first run. As would be expected, recovery progressively decreased with every recycle run.
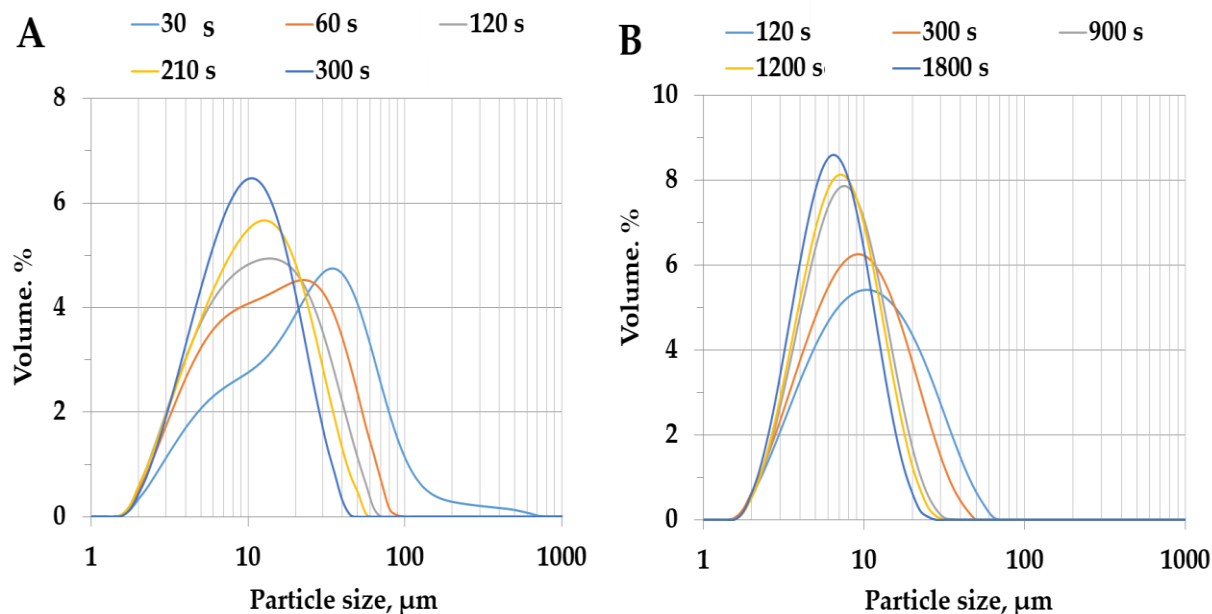


Figure 3-5. Particle size distribution of 50 g sample after settling time of (A) 5 min and (B) 30 min

During the method development stage, process optimisation and mass purification particle size (Malvern Mastersizer) and mineral composition (XRD D8 Advance) were interactively monitored at each step. The final purified product was collected by centrifugation (Hettich ROTIXA 50S), followed by oven drying at 40 °C. The sequence of steps and processes in the optimised final method is schematically presented in Figure 3-6. Approximately 50 g of < 75 μm sieved rectorite-containing material was dispersed ultrasonically in ultrapure water (~250 ml) for 30 min to allow disaggregation and the formation of suspension. A settling time of 5 min was established for optimal recovery of the clay fraction. The supernatant (Top 1) containing the clay fraction was carefully decanted from the bottom (Bottom 1) where the denser impurity particles had settled. The suspension (Top 1) was subjected to centrifugation at 2000 rpm for 30 min to separate the solid clay particles from the water. The coarse remainder (Bottom 1) was recycled up to four times by adding ultrapure water (~250 ml) and repeating the above procedure. After each cycle quantitative XRD analysis was conducted on the top and bottom solid fractions until optimal extraction of rectorite clay was achieved.
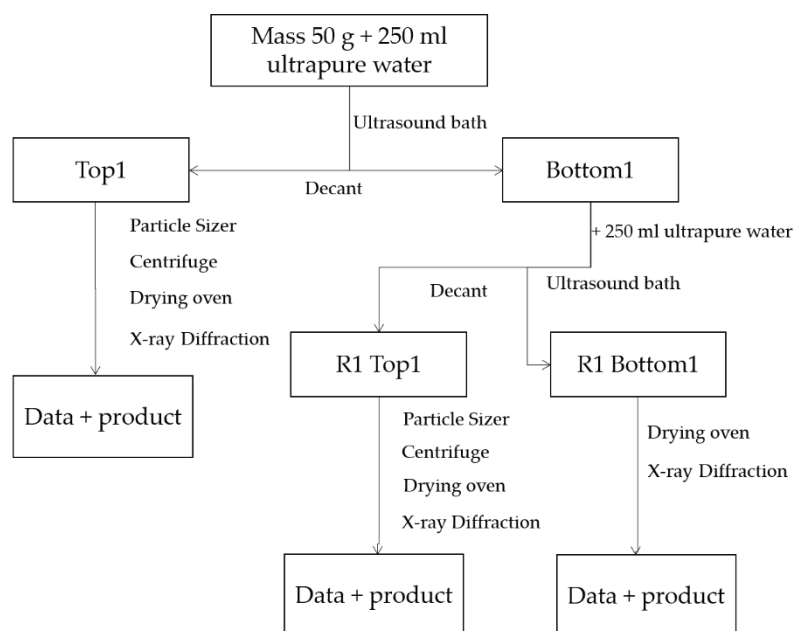


Figure 3-6. Flow chart of the rectorite purification process designed and used in this study. R1 denotes the first recycle and usually up to four recycles were performed per starting mass of 50 g.

The final solid product containing mainly rectorite clay particles was then dried and gently ground to produce powdered high-purity rectorite clay for use in further experiments. The particle size distribution of rectorite-rich material from samples RT1, RT2 and RT3 at various stages of disaggregating pre-treatments is shown in Figure 4-2 (A, B and C) and their respective XRD diffractograms are displayed in Figure 4-1.

## 3.4 Modifications of purified rectorite

### 3.4.1 Inorganic cation exchange

Inorganic cation exchange of purified rectorite was achieved by saturation with a metal chloride. Ion-exchanged $Li^+$, $Na^+$, $NH_4^+$, $K^+$, $Cs^+$, $Mg^{2+}$, $Ca^{2+}$, $Sr^{2+}$ and $Ba^{2+}$ rectorite modifications were used for rectorite structural characterisation and in the preparation of clay films and nanocomposite films. The saturation process involved treating about 20 g of sample with a 1 M solution of the respective chlorides. The exchange procedure was carried out using a shaker (LABOTEC Shaker 202) for three days at room temperature. The frequency of the shaker was adjusted to 225 rpm. The saturation was repeated three times per day, replacing the liquid each time with fresh solution containing an excess of the exchanging cation. The last round was completed by multiple washing with ultrapure water through three shaking sessions to remove excess chloride. To ensure that all chloride ions had been removed a test was performed by reaction of an aliquot of supernatant solution with 0.1 M $AgNO_3$. The washed clay was separated by centrifugation in acetone for 30 min at a speed of 2000 rpm.

### 3.4.2 Organic modification

Modification of rectorite with organic surfactants followed a procedure similar to that above. Intercalation was achieved via the ion exchange mechanism by which inorganic interlayer cations are replaced by organic molecules. Three different organic surfactants in liquid form, i.e. dodecyldimethyl ammonium chloride (DCC10), dialkylmethyl ammonium chloride (DCC18) and hexadecyltrimethyl ammonium chloride (SCC16),

were used. Mixtures were prepared from 30 g clay with a sufficient amount of surfactant solution so that there would be a 50 % excess of ions based on a CEC of 45 mEq/100 g. Ultrapure water was added to make solutions of 250 ml. The intercalation reaction took place over 20 days under constant shaking at room temperature. The frequency of the shaker was adjusted to 200 rpm. After the elapse of time, the organically modified rectorite was repeatedly washed with ultrapure water until all excess surfactant had been quantitatively removed. The test was performed by reaction of supernatant solution with 0.1 M $AgNO_3$ until the mixtures were free of chloride ions. The moist solid material was recovered by centrifugation for 30 min and dried under ambient temperature. Sufficient material was produced to carry out the necessary characterisation tests, including SEM, XRD, TGA, FTIR and chemical composition by XRF.

## 3.5 Preparation of rectorite clay films (RecF)

Rectorite clay films (RecF) were prepared by a solution casting process. The aqueous clay dispersions were poured into shallow pans and allowed to evaporate and dry slowly at ambient conditions. Aqueous suspensions of neat purified rectorite clay and its ion-exchanged $Li^+$, $Na^+$, $NH_4^+$, $K^+$, $Cs^+$, $Mg^{2+}$, $Ca^{2+}$, $Sr^{2+}$ and $Ba^{2+}$ modifications were prepared in the concentration range between 1 and 5.8 wt.%. Parameters such as concentration, sonication time, stirring time and type of casting pan were varied to tune the method for optimum mechanical performance of the films.

Prior to film casting, all suspensions were ultrasonically dispersed in ultrapure water for either 5 or 30 min using a LABSONIC 2000U/ B. Braun sonicator fitted with a generator, transducer anda 2000U titanium probe of 19 mm tip. The operating output frequency was 20 kHz. The instrument settings were optimised experimentally by the interactive measurements of the degree of dispersion, i.e. obscuration in a particle sizer. In order to prevent overheating, low power-output settings were selected, i.e. the instrument amplitude dial was set close to the minimum and a duty cycle of 1 was chosen. After sonication the suspensions were cast immediately or subjected to further agitation by

stirring for either 4 or 24 h before casting. The particle size (proxy for the degree of exfoliation) and the intrinsic stability of each suspension were monitored by $\zeta$-potential measurements. Suspensions were cast into shallow pans (glass or teflon) and dried at room temperature. The casts were left undisturbed to evaporate at a slow rate over 3–4 days until completely dry films could be peeled off the surface.

## 3.6 Preparation of NH$_4^+$-rectorite-chitosan nanocomposite films (Rec/CSNCF)

Rec/CS NCF films were produced by self-assembly of intercalated ammonia-exchanged rectorite-chitosan composites during slow evaporation from aqueous dispersions. Parameters such as clay-chitosan concentration, degree of dispersion, exfoliation and mixing methodology, and pH were experimentally determined, closely controlled and tuned to achieve the best mechanical strength of the final film product.

Rectorite clay of > 90 % purity from sample RT3 was cation-exchanged to obtain NH$_4^+$-rectorite used in the preparation of the composite films. Mixtures of ion-exchanged ammonium rectorite (NH$_4$-Rec) and chitosan (CS) were prepared in NH$_4$-Rec/CS proportions in the range 100–0 wt.% clay-chitosan (wt.% based on chitosan mass) in increments of 5 wt.%. In the following text, the nanocomposites are denoted by the initial clay/chitosan ratio, given as NH$_4$-Rec/CS, used for their preparation, e.g. 100/0 means neat NH$_4$-Rec film, 80/20 stands for 80 % NH$_4$-Rec and 20 % CS and so forth.

Each weighted clay portion was dispersed in ultrapure water by ultrasonication for 30 min, followed by stirring for 4 h. Simultaneously, a powdered CS portion (0–100 wt.%) was dissolved in 2 % (v/v) aqueous acetic acid while continuously stirring. The latter solution was added very slowly to the stirring NH$_4$-Rec clay solution and the resulting mixtures were stirred for another 24 h. Thereafter, the NH$_4$-Rec/CS suspensions were cast on glass Petri dishes (145 mm internal diameter) and dried at room temperature over 3–

4 days until completely dry films could be peeled off the flat surface. The stability of each suspension was monitored by $\zeta$-potential measurements.

## 3.7 Sample preparation and treatments for XRD analysis

For rectorite characterisation X-ray diffraction measurements were performed on random powder preparations (pXRD), thin flakes of raw rectorite (sample RT1) and oriented slides.

Random powder diffraction tests on micronised material (by McCrone micronizing mill) were carried out for bulk qualitative and quantitative analysis. For Rietveld quantitative analysis, modelling of the rectorite structure was required because there were no structure files for rectorite in the commercially available databases or other open access online sources at the time. Modelling by the Rietveld method was performed (as detailed further below) and the resulting structure file was then used for quantification to determine the proportion of impurities and the respective concentrations of rectorite in the mixtures.

Diffraction data from oriented slides in air-dry state and after various treatments was used for identification of the clay species and characterisation of the rectorite structure and its swelling properties. There are considerable limitations to a phyllosilicate analysis based only on the data of basal reflections from oriented air-dry samples because of overlapping reflections of clay minerals as they frequently occur together. It is therefore beneficial to examine air-dry oriented clay specimens after various treatments that alter the diffraction patterns of the components due to their structural properties. To enable this, four air-dry orientated preparations per sample were produced and X-rayed before and after treatment. Generally, treatment with ethylene glycol (EG) and/or glycerol (G) is performed to aid the identification of smectite species, vermiculites and interstratifications (Brindley and Brown (1984), Moore and Raynolds (1997)). Heat treatment at 500 °C collapses swelling minerals by dehydrating the interlayer content

and destroys or transforms minerals such as kaolinites and chlorites respectively. X-ray diffraction on clay films and bionanocomposite films was done to study the orientation of the particles and the microstructure of the films.

### 3.7.1 Sample preparation for powder XRD analysis (pXRD)

A McCrone micronising mill with corundum grinding elements was utilised to reduce the mean particle size of the milled sample (by laboratory swing mill) and ensure homogeneous size distribution for X-ray diffraction. About 4 g of milled sample was ground with 10 ml ethanol for 8 min and each sample was prepared in duplicate. Calibration mixtures, prepared by adding ZnO (or corundum) as an internal standard, were ground and homogenised following the same procedure. Slurries were air-dried and homogenised in a vibrating mill (VM) with steel balls prior to XRD measurements. Powder was pressed in a shallow sample holder against filter paper to ensure random particle orientation.

### 3.7.2 Oriented clay preparations and treatments

Purified clay was dispersed in ultrapure water by means of ultrasound probe. Small volume of the supernatant containing < 2 µm clay particles was deposited onto glass slides by a pipette and air-dried (AD) for XRD analysis. Glycerol (G) and ethylene glycol (EG) saturation was achieved by the vapour method. The AD oriented mounts were placed in a desiccator with G or EG for 16–18 h at a temperature of 80 °C and analysed again on the X-ray diffractometer. The nature of the expandable component in the mixed-layer structure of rectorite was determined by the Greene-Kelly test. It entails X-ray diffraction of Li-saturated oriented specimens after heating at 300 °C, followed by G saturation (Greene-Kelly, 1952). The test was duplicated with high repeatability of the results. Relative humidity in the laboratory was maintained at between 50 % RH and 60 % RH.

### 3.7.3 Heat treatment

Heating experiments were carried out in a high-temperature muffle furnace (LABOTEC LABCON RM4, 50 Hz, Max Temp. 1200 °C) with a pre-calibrated and thermocouple-monitored temperature regime. Heating from 25 °C–1 200 °C was done on oriented specimens in increments of 50 °C for 1 h. Heated specimens were transferred to a desiccator and as rapidly as possible scanned in the diffractometer through an angular range of 2 – 36 °2θ where the major basal clay reflections occur. XRD measurements on heated rectorite specimens were performed under controlled relative humidity to prevent possible rehydration of the clay specimens.

## 3.8 Rectorite structure refinement, modelling and quantitative phase analysis

The Rietveld method (Rietveld, 1969) is widely accepted and utilised as the most accurate method for quantitative phase analysis (QPA) from diffraction data of powdered mixtures. The Rietveld quantification method generally requires that all phases in a mixture are crystalline and their structures are well described. The method performs full pattern fitting and needs input of crystal structure data for each constituent.

Disordered layer structures such as clay minerals present a real challenge when their phase concentrations and associated impurities in a mixture need to be determined. The compositional and structural variations due to turbostratic disorders, hydration state, easily exchangeable cations, degree of ordering and anisotropic peak broadening may cause deviations of the observed diffraction patterns from published structure information. Discrepancies in relative intensities are also common as basal reflections could be preferentially enhanced due to platelet orientation during sample preparation.

Mixed-layer clay minerals are very common in nature, and the most common of these contain expandable layers, i.e. mica-smectite (I/S) interstratifications. The sequence of expandable and non-expandable layers can be irregular (random) or regular as in the

case of rectorite structure. Very often no structure information or only partial information (space group and cell parameters, but no atomic positions) is available and in these cases the traditional Rietveld method cannot be used for quantification. The application of the Rietveld method for quantification of phases in a mixture requires structure models for each phase. Refinement of the structure parameters of clay minerals, including mixed-layer minerals, is further complicated due to the cis-vacant and trans-vacant configurations of the dioctahedral 2:1 layers, random rotations and translations of the layers relative to each other, and the frequent occurrence of stacking faults in these structures. Upon X-ray diffraction these structural specifics and defects modify the intensity distribution (Drits and Tchoubar, 1990), rendering structure refinement by Rietveld code meaningless. Various software packages and modelling approaches exist for elucidating the nature of the stacking order in clay minerals (Drits and Sakharov, 1976);(Ufer et al., 2008; Ufer et al., 2012a, b). However, their use for routine QPA is often restricted by specialised software codes, proprietary regulations and limited structure models for clay mineral structures. Furthermore, for mixed-layer structures, including rectorite, there are no published structure files. A method for the quantification of phases with Partial or Not Known Crystal Structures (PONKCS) (Scarlett and Madsen, 2006) offers an alternative approach that overcomes some of these obstacles. It uses a calibrated method to derive empirical "structure factors" by measuring peak intensities from the diffraction pattern of a pure material of the "unknown".

In the present study the rectorite structure was empirically modelled based on a monoclinic unit cell with primitive lattice using the Rietveld method and DIFFRAC.TOPAS V4.2 software from BRUKER AXS (BrukerAXS, 2009). Diffraction data collected from purified material (rectorite content above 91 %) was used for modelling and calibration.

### 3.8.1 Derivation of unit cell parameters and instrument function

Combined indexing information, i.e. unit cell parameters from published partial structural information for rectorite (Brindley, 1977; Korolev, 1971) (Bayliss, 1989), served to generate an *hkl* phase file by the Le Bail method (Le Bail et al., 1988). This approach uses the space group and cell parameters to constrain the peak positions while permitting the intensities to vary until the best fit to the observed diffraction data is achieved. After the refinement, a peaks file was generated with calculated *hkl* values, multiplicity information, peak positions and intensities. This input file can then be used as a rectorite structure file in the refinement of raw data and for quantitative Rietveld analysis.

The instrument function was modelled using the fundamental parameters approach (FPA) (Cheary and Coelho, 1992a) for peak profile modelling adopted by TOPAS software. The instrument parameters were defined by refinement of the $LaB_6$ diffraction data obtained with the same diffractometer set-up as the experimental data. Background function was modelled by a Chebychev polynomial of order 1–6 and 1/X Bkg correction was applied to account for possible air scattering at low angles.

The *a*, *b* and *c* lattice parameters of the modelled rt_*hkl* (i.e. rectorite_*hkl*) phase were refined within reasonably set limits to accommodate the variation in cell parameters from an expanded to a dehydrated state of rectorite. From the angular parameters only beta ($\beta$) was set to refine. Crystallite size and microstrain were always refined with the limits set to achieve the best fit, i.e. the minimum level for crystallite size was set to 12 nm and microstrain was set within limits of 0–1.

### 3.8.2 Generation of a calibration model

Calibration mixtures were prepared using zincite (ZnO) as internal standard following the procedure described in Scarlett and Madsen (2006). The Rietveld-based method uses an algorithm (Eq.3-1) to calculate the weight fraction of phase *a* in a mixture of *n* phases by the relationship (Hill and Howard, 1987):

74

$$W_a = \frac{S_a(ZMV)_a}{\sum_{k=1}^{n} S_k(ZMV)_k} \tag{3-1}$$

where $W_a$ is the weight fraction of phase $a$; $Z$ is the number of formula units in the unit cell; $M$ is the molecular mass of the formula unit; $V$ is the unit cell volume; and S is the Rietveld scale factor. In TOPAS code the phase constant ZMV is defined as mass M, which represents $Z \times M$ and the volume $V$.

Calibration mixtures of 50 % purified rectorite sample and 50 % zincite (ZnO) were prepared and homogenised. Some impurities of quartz, calcite, muscovite and chlinochlore in the rectorite samples were quantified from the same standard mixture before the calibration of ZMV for rectorite. The total of impurities was then used to calculate by difference the exact amount of rectorite in the mixture. The refinement of the calibration mixture by TOPAS provided the scale factor and the volume of the rectorite unit cell needed to calculate the "phase constant ZMV" in the equation:

$$(ZM)_{RT} = \left(\frac{W_{RT}}{W_{ZnO}}\right)\left(\frac{S_{ZnO}}{S_{RT}}\right)\left(\frac{ZMV_{ZnO}}{V_{RT}}\right) \tag{3-2}$$

where $ZM$, $W$, $S$ and V are the mass, weight, scale factor and volume for phase $RT$-rectorite and the zincite standard respectively.

### 3.8.3 Quantitative phase analysis (QPA) of rectorite mixtures

The PONKCS method for quantitative analysis of phases described above (Scarlett and Madsen, 2006) allows the accurate quantification of compounds where the traditional Rietveld method or other classic quantification methods fail. Disordered phases or phases with unknown or partial crystal structures (e.g. mixed-layer structures, new polymorphs) can be quantified with the same or even higher accuracy as for well-defined crystalline phases.

Quantification of mixtures by the Rietveld method requires knowledge of the crystal structure of each component in the mixture. The structure information comprises the

lattice parameters, crystal system and starting parameters of site occupancies; for well-known structures this is usually found in the literature. The calibrated rectorite model *rt_hkl* generated by the procedure explained above contains measured intensities from a pure rectorite flake reference sample and is used here in place of crystal structure information for rectorite. The structural data on the additional minerals, namely quartz (Gualtieri, 2000.), calcite (Effenberger et al., 1981), muscovite (Gatineau, 1963), chlinochlore (Guggenheim and Zhan, 1999), pyrophyllite (Gruner, 1934), gypsum (Wooster, 1977) and zincite (Albertsson et al., 1989) was taken from the ICSD structure database (Table 3-1). The peak list file rt_*hkl* (Appendix I) resulting from this calibration was then applied to the raw samples containing rectorite.

Table 3-1. Sources of crystal structure data used in the quantification of rectorite mixtures by the Rietveld method

| Mineral | Structural formula | Source of crystal structure data |
|---|---|---|
| Rectorite | $(Na_{0.76}Ca_{0.44}K_{0.13})[Al_{4.03}Ti_{0.03}(Fe.Mg)_{0.006}](Si_6Al_2)O_{20}(OH)_4.nH_2O$ | *rt_hkl* model this study |
| Quartz | $SiO_2$ | Gualtiery (2000) |
| Muscovite | $KAl_2(AlSi_3O_{10})(OH)_2$ | Gatineau (1963) |
| Chlorite | $Mg_3(Mg_2Al)((Si_3Al)O_{10})(OH)_2O_3$ | Guggenheim and Zhan (1999) |
| Pyrophyllite | $Al_2(Si_4O_{10})(OH)_2$ | Gruner (1934) |
| Calcite | $Ca(CO_3)$ | Effenberger et al. (1981) |
| Gypsum | $Ca(SO_4)(H_2O)_2$ | Wooster (1977) |
| Zincite | $ZnO$ | Albertsson et al. (1989) |

The precision of the method was tested by in-laboratory replicate sample preparation and analysis. The consistency between phase analysis by the Rietveld method and bulk chemical analysis for the purified rectorite samples was evaluated and verified to estimate the degree of confidence in the model and method applied. The modal abundance of minerals in a mixture can be expressed as chemical oxide compositions for direct comparison with XRF-derived compositions (Monecke et al., 2001; Ward and Gómez-Fernández, 2003). For the rectorite samples, chemical compositions implied by the Rietveld analysis were calculated assuming ideal stoichiometric compositions from the literature for all minor impurity minerals. Due to the variability of published rectorite compositions caused by the exchangeable interlayer cations and layer substitutions, an

individual chemistry for Beatrix rectorite of this study was considered. Rectorite material of highest purity was analysed by XRF, and the results were recalculated adjusting for mineral impurities and used as a basis to calculate the mean structural formula (Atanasova et al., 2016) (Table 4-7). For reasons of comparison, published compositions for rectorite samples with similar interlayer content were also used (Gaines et al., 1997; Nishiyama and Shimoda, 1981).

Another source of uncertainty in the comparison of calculated and observed chemical compositions is the estimate of volatile components, i.e. LOI. These include non-structural water or pore water, structural $OH^-$ in hydroxyls and hydroxides or $CO_3^{2-}$ in carbonates. To overcome complications with differentiation between structural and non-structural components, and correct for their influence on the accuracy of the method, the LOI component was ignored in the calculations. Thus, the normative compositions were only calculated from the oxide forms for all minerals.

## 3.9    Characterisation techniques

### 3.9.1  Microscopy

**Optical microscopy** was used for preliminary visual description and colour imaging with a Leica Wild10 binocular microscope and a Leica DVM6 digital microscope. The latter is equipped with a tilting stand, a combined motorised precision XY-stage with manual coarse positioning, and a motorised focus for automatic 3D image-stacking. With a PlanAPO FOV 12.55 objective and a 10 MP camera with a focus resolution of 0.5 $\mu$m and a 16:1 zoom range, sharp multi-focus images, 3D-analysis and high-resolution scans on larger areas are allowed.

**SEM** was used for morphological and structural observations and imaging, and X-ray microanalysis by EDS. **SEM/EDS analysis** was carried out on a Leica Stereoscan 440 SEM linked to an OXFORD INCA EDS at an acceleration voltage of 5 kV. The system is equipped with an Oxford X-Max SDD detector with 20 mm² active area and a resolution

of ca. 128 eV for Mn K$\alpha$ (5895 eV). Examination was performed on polished specimens and grain mounts, coated with carbon for conductivity. SEM imaging was obtained by ultrahigh-resolution field emission SEM (FESEM) Zeiss Ultra Plus 55 with an In Lens detector at acceleration voltages of 0.6 kV to ensure maximum resolution of surface detail.

For **TEM** imaging a JEOL-JEM 2100F field emission transmission microscopy (FETEM) was utilised operated at 100 kV. Rectorite platelets were dispersed in ethanol using ultrasound, deposited on a Cu grid and left to air-dry.

### 3.9.2 Nuclear magnetic resonance (NMR) spectroscopy

Purified rectorite clay was characterised by $^1$H, $^{27}$Al, $^{23}$Na and $^{29}$Si solid-state MAS NMR. All NMR measurements were performed on a 11.7 T Bruker Avance 500 spectrometer operating at the resonance frequencies of 500.13 MHz for $^1$H, 130.34 MHz for $^{27}$Al, 132.31 MHz for $^{23}$Na and 99.36 MHz for $^{29}$Si using a Bruker BL4 HXY 4 mm MAS and a BL 2.5 mm MAS probe-head. All spectra were fitted using Dmfit (Massiot et al., 2002).

$^{27}$Al MAS NMR spectra were acquired at a spinning frequency of 14 kHz. A single pulse of 2 µs pulse duration (< $\pi$/3 for 30 kHz rf-amplitude) was applied to ensure a quantitative excitation of the central transition. High-power two-pulse phase modulation (TPPM) $^1$H decoupling of 80 kHz rf field strength was applied. A recycle delay of 1 s and 256 repetitions were used. $^{27}$Al chemical shifts were referenced externally to 1M AlCl$_3$ aqueous solution at 0 ppm.

The $^{29}$Si solid-state NMR spectra were acquired at a spinning frequency of 5 kHz with direct $^{29}$Si polarisation with $^1$H decoupling (cw field strength 50 kHz), a single 90° pulse of 3 µs duration, recycle delays of 60 s (for higher signal-to-noise ratio) and 600 s (for a quantitative excitation) and 1 024 repetitions. The $^{29}$Si chemical shifts were referenced relative to TMS using Q8M8 as an external standard, which gives an Si(–CH$_3$)$_3$ signal at 12.6 ppm.

^{1}H MAS NMR spectra were measured at a recycle delay of 5 s employing a single 90° rf-pulse of 3 μs duration. The ^{1}H NMR spectra were referenced to TMS at 0 ppm using an $NH_4$ signal of ammonium dihydrogen phosphate at 6.7 ppm as an external reference.

For ^{23}Na MAS NMR measurements, a single $\pi/2$ pulse of 2.5 μs was applied, ensuring a quantitative excitation of the central transition. High-power two-pulse phase modulation (TPPM) ^{1}H decoupling of 80 kHz was applied. A recycle delay of 5 s and 2 048 repetitions were used. [23]Na chemical shifts were referenced externally to 1M NaCl aqueous solution at 0 ppm.

### 3.9.3   X-ray diffraction analysis (XRD)

X-ray data was recorded on a Bruker D8 Advance diffractometer with 2.2 kW Cu K$\alpha$ radiation ($\lambda$=1.54060 nm), a LynxEye detector with an active area of 3.7 ° and Ni filter. The beam path included 0.2 mm (0.1 °) Fixed Divergence Slit (FDS), 0.1 mm Receiving Slit (RS) and Soller slits of 2.5 ° on the primary and secondary sides. Scans from 2 – 70 °2θ for random powder preparations (pXRD) and 2 – 36 °2θ for oriented specimens and films were recorded in step scan mode at a speed of 0.02 °2θ steps, size/5 s and generator settings of 40 kV and 40 mA. A sample spinner was on for all powder measurements for representative particle statistics. Qualitative phase analysis was performed by the conventional search/match procedure using the BRUKER DIFFRAC. EVA software program and the ICDD PDF database. Rietveld refinements and quantification were done with DIFFRAC.TOPAS V4.2 software using the fundamental parameters approach (FPA) (Cheary and Coelho, 1992).

The NEWMOD (Reynolds, 1985) computer program for modelling one-dimensional X-ray diffraction patterns of mixed-layer structures was used to compare the experimental XRD data with calculated patterns.

### 3.9.4 Chemical analysis by X-ray fluorescence (XRF) spectroscopy

For major element analysis a milled sample (< 75 μm) of the neat, purified or exchanged material was roasted at 1 000 °C for at least 3 h to oxidise $Fe^{2+}$ and S and to determine the loss of ignition (LOI). Glass discs were prepared by fusing 1 g of roasted sample and 8 g 12–22 flux consisting of 35 wt.% $LiBO_2$ and 64.71 wt.% $Li_2B_4O_7$ at 1 050 °C. For trace element analysis 12 g of milled sample and 3 g of Lico wax were mixed and pressed into a powder briquette by a hydraulic press with the applied pressure at 344 MPa. The glass discs and wax pellets were analysed by a PANalytical wavelength dispersive Axios X-ray fluorescence spectrometer equipped with a 4 kW Rh tube.

### 3.9.5 Carbon and sulphur (C&S) analysis

Quantitative carbon and sulphur analyses were performed on an Eltra CS 800 double dual range carbon-sulphur analyser. An amount of 0.2 g of milled or sieved to < 75 μm sample material was weighed and homogenised by slow rotation into a ceramic crucible with iron and tungsten chips. Method detection limits for carbon and sulphur of 0.017 and 0.009 g/100 g respectively were achieved by repeat analyses of blank samples. The instrument was calibrated using the Euronorm-CRM 484-1 Whiteheart malleable iron, Euronorm-CRM 058-2 sulphur steel and Euronorm-CRM 086-1 carbon steel standards, while instrument stability was monitored using in-house reference standards.

### 3.9.6 Carbon-hydrogen-nitrogen (CHN) elemental analysis

CHN analyses were performed using LECO CHN628 instrumentation. Samples of 0.1 - 0.2 g in the fraction below 212 μm were weighed and homogenised. The material was combusted in oxygen at 950 °C, converting elemental carbon, hydrogen, and nitrogen into $CO_2$, $H_2O$, $N_2$ and NOx. These gases pass through infrared cells that determine the carbon and hydrogen content, and a thermal conductivity cell that determines $N_2$. Method detection limits were achieved by repeat analyses of blank samples. The instrument was calibrated using the LECO EDTA CRM 2015, while instrument stability

was monitored by the Central Control Standard (CCS) analysed in duplicate for each batch of samples. CCS data is recorded in a quality control chart and monitored within the upper and lower warning ($\pm 2\sigma$) and control limits ($\pm 3\sigma$) of the charts.

### 3.9.7 Fourier transform infrared spectroscopy (FTIR)

Infrared spectra were recorded using a diamond ATR cell, which fitted in the macro sample compartment of a Bruker Optics Vertex 70v spectrometer. Small amount of powdered sample (enough to cover the crystal area) was placed onto the ATR crystal and the spectrum was collected under pressure of up to 70 psi. The spectra were acquired in the range $400 - 4000$ cm$^{-1}$ wavelength in 32 acquisitions at a resolution of 4.0 cm$^{-1}$. The sample compartment was evacuated during acquisitions and the contact area between the sample and the diamond ATR crystal was 2 mm in diameter.

FT-IR spectra by the KBr method were recorded using a Perkin Elmer Spectrum RX FT-IR with a scan resolution of 2.0 cm$^{-1}$. Applying single-beam radiation, a total of 32 interferograms were collected for each sample. KBr compressed pellets were prepared using a mortar and pestle to disperse fine powdered sample with 100 mg of dehydrated KBr.

### 3.9.8 Thermogravimetric analysis (TGA)

TGA was performed using the dynamic method on a Mettler Toledo A851 TGA/SDTA instrument. About 15 mg of sample powder was placed in an open 70 µl alumina pan. The temperature was scanned from 25 - 1200 °C at a rate of 10 °C/min$^{-1}$ with an air flowing rate of 50 ml/min$^{-1}$.

DSC scans were recorded on a Mettler Toledo DSC instrument. Samples of about 5 mg were placed in aluminium pans with a small hole in the lid. The samples were heated (and cooled) from $- 40$ °C to 220 °C at a scan rate of 10 °C/min$^{-1}$. The heating and cooling runs were carried out under nitrogen flowing at 50 ml/min$^{-1}$.

### 3.9.9  Brunauer–Emmett–Teller (BET) analysis

Specific surface area determinations by BET analysis were performed on powdered rectorite clay and rectorite clay films. The instrumentation used was a Micromeritics Flowsorb II 2300 and a Nova 1000e BET instrument in $N_2$ at 77 K.

### 3.9.10 Particle size distribution and $\zeta$-potential measurements

Particle size distribution was determined by laser diffraction technique using a Malvern Mastersizer 2000 equipped with a Hydro 2000G dispersion unit (Malvern Instruments Ltd, Malvern, UK). Scattered light data was recorded from 2 000 - 5 000 snapshots of 10 µs. A polydispersity mode of analysis and a refractive index of 1.533 with an adsorption of 0.1 were chosen. Size data collection was performed at a constant obscuration in the range 10–20 %, and the built-in ultrasonic bath was set at 30 % before and during measurements to achieve adequate disintegration of aggregates and proper dispersion of primary particles. The method is volume-based and assumes that all particles are spherical. In the case of phyllosilicates such as clays and other platy materials, the results are usually overestimated due to their aspect ratio and represent equivalent spherical diameter (Bowen, 2002).. The results therefore describe the volume concentration of irregular-shaped particles contained in the sample in terms of the diameter of imaginary spherical particles that occupy the same volume. For these reasons the results do not represent absolute particle sizes, although they provide very useful information for comparative purposes between various treatments.

Electrophoretic mobility measurements of colloidal rectorite particles present in aqueous suspensions were carried out in an electric field using the Malvern Zetasizer Nano ZS system (Malvern Instruments Ltd, Malvern, UK). The $\zeta$-potential was then calculated from the electrophoretic mobility ($u_c$) of the rectorite particles using the Smoluchowski equation. All measurements were performed at 25.0 ± 0.1 °C, with an attenuance in the range 5–6. Each reported value of $\zeta$-potential is an average of three measurements. The

pH of the suspensions was also recorded. The size of the dispersed particles in the sub-micron region below 0.02 μm was determined by the Dynamic Light Scattering (DLS) technique using the same instrument; the reported values represent mean size distribution by number (polydispersity index (PDI) was > 0.1, i.e. the system has moderate to broad polydispersity, in which case size distribution by volume is meaningless).

## 3.10 Characterisation of functional properties

Rectorite clay films and bionanocomposite films were tested for their mechanical properties and UV-Vis characteristics.

### 3.10.1 Characterisation of mechanical properties

**Tensile measurements** were performed on an Ametek Lloyd Instrument LRX Plus single-column tensile tester fitted with a 50 N load cell. Film thickness was measured using a Mitutoyo Digimatic micrometer with a measurement accuracy of ± 0.2 μm and the average of multiple measurements along the strip was used. Film strips with dimensions 100 mm long and 10 mm wide were cut and conditioned in a desiccator at room temperature for at least 48 h prior to measurements (ASTM, 2012, 2013a, b). Controlled humidity in the desiccator was maintained around 55 % using a saturated calcium nitrate tetrahydrate ($Ca(NO_3)_2 \cdot 4H_2O$) solution at room temperature. The ends of the strips were sandwiched with masking tape before being fastened in the clamps of the tester, with the gauge length (grip separation) set at 75 mm. The tensile tests were conducted at a draw speed of 20 mm/min$^{-1}$. At least three measurements per film were made and the maximum value is reported together with the overall standard deviation. This approach was followed as the objective was to determine the ultimate strength of the clay films. In the case of bionanocomposites, films of each composition were replicated at least three times.

### 3.10.2 Visible and ultraviolet spectroscopy (UV-Vis)

UV-Vis transmission spectra of rectorite and composite films were recorded on a PerkinElmer Lambda 750S spectrophotometer.

### 3.11  Statistical analysis

**Statistical analysis** of the available experimental data was carried out in two steps. First, a global fit of the tensile strength (or the Young's modulus) of the films was modelled and analysed using extreme value analysis (EVA) by means of the generalised extreme value (GEV) distribution (Beirlant et al., 2005; Reiss and Thomas, 2007). Parameter estimation was carried out using the generalised maximum likelihood (gMLE) (Gilleland and Katz, 2016). The location and scale parameters of the GEV distribution were considered to be linear combinations of possible additional variables. Based on the outcomes, the data was split into three groups. Permutational multivariate analysis of variance (MANOVA), using distance matrices (Anderson, 2001; McArdle and Anderson, 2001), was performed to check whether the data split into these three sets according to the interlayer charge variables can be justified from a statistical point of view. The resultant $p$-value from this test was 0.007, which signifies an overall effect. This was followed by the Kruskal-Wallis rank sum test (Hollander and Wolfe, 1973) for testing the individual effects, the results of which indicated that this was indeed the case for both tensile strength ($p$-value = 0.0019) and Young's modulus ($p$-value = 0.0004) as dependent variables, and with the interlayer charge as independent variable. Secondly, a peak-over-threshold (POT) model was fitted to each of the six possible permutations for determining the maximum potentially attainable values for tensile strength and Young's' modulus. Maximum likelihood estimation (MLE) was used to fit the exponential distribution to all the cases. The parametric bootstrap (Efron and Tibshirani, 1993) was then used in each case in deriving 95 % upper confidence limits.

# CHAPTER 4        RESULTS

## 4.1        Characterisation of neat and cation-exchanged rectorite

### 4.1.1   Primary materials processing, disintegration and particle size statistics

Due to the platy morphology and sensitivity to relative humidity, the rectorite material was fairly resistant to crushing and milling using routine laboratory techniques. The pXRD data plotted in Figure 4-1 demonstrate the effect of various size-reduction treatments on the relative intensities, preferred orientation and peak profile resolution, shape and broadening.

The particle size distribution of the rectorite-rich material from samples RT1, RT2 and RT3 at various stages of disaggregation is shown in Figures 4-2, 4-3 and 4-4 respectively. The frequency curves display an apparent bimodal distribution for the crushed and blender-treated material with maxima around 1.2 mm. With the use of a coffee grinder, ball mill and McCrone micronising mill, followed by a short vibrating mill spin, a much finer and more homogeneous product was achieved. The crushing and the blender reduced the size of the raw material below 1 mm with 35 % and 18 % of the particles being smaller than 100 μm. At this stage only 10 % and 5 % of the sample were smaller than 20 μm after crushing and using the blender respectively. The vibrating mill reduced the particle size of lumpy crushed material further, with the samples now containing 90 % of sub-100 μm particles and *ca*. 40 % of sub-20 μm particles. The milling process produced a more homogeneous distribution with 90 % of sub-20 μm particles. Surprisingly, the population represented by the shoulder at around 500 μm (ranging from 280 μm to 700 μm) was not affected by the use of the vibrating mill as would have been expected if it represents larger lumps and aggregates.
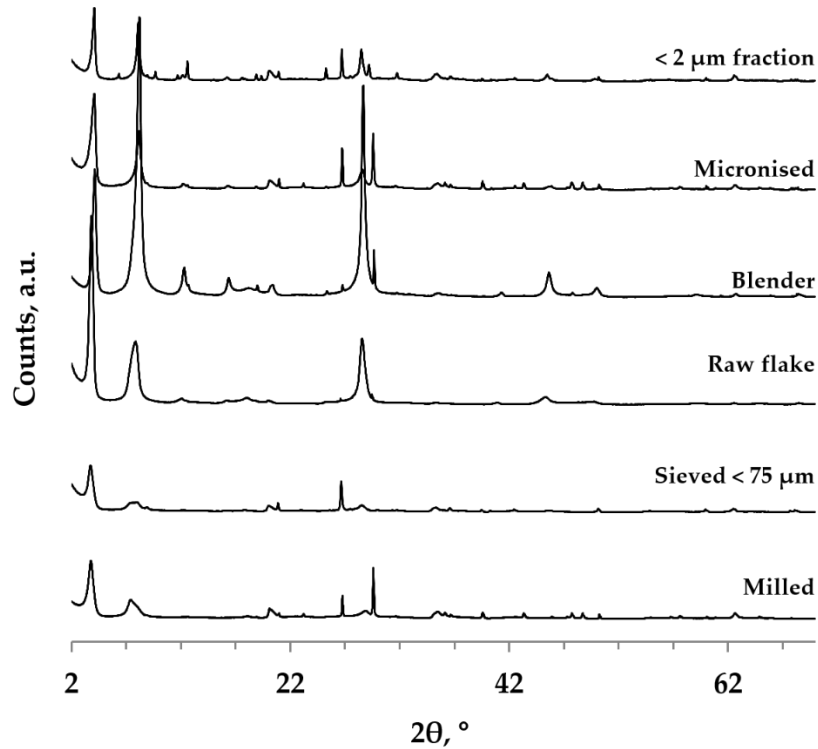
Figure 4-1. Powder diffraction patterns of rectorite-rich material (RT1) after various processing treatments

Wet grinding in the McCrone micronising mill produced the most narrow grain-size distribution; it decreased the particle size of milled samples further (95 % ≤ 20 μm) and eliminated the shoulder formed by the population of larger particles. Only about 50 % of the particles were below 5–7 μm in size, i.e. the ideal particle size for random powder diffraction.

The observed bimodal distribution is indicative of two characteristic aspects of clay particles: firstly, differences in the dispersion properties of complex particles; and secondly, the high aspect ratio of the clay particles which tend to orient preferentially as they traverse the measuring cell of the instrument and refract the incident light during measurement. It is generally expected that mixed-layer assemblages will show relatively good dispersability, particularly when one of the component layers is non-expandable. The mixing would cause weakening of the bonds between particles which would enhance the ease of splitting into thinner units and consequently lead to dispersion.
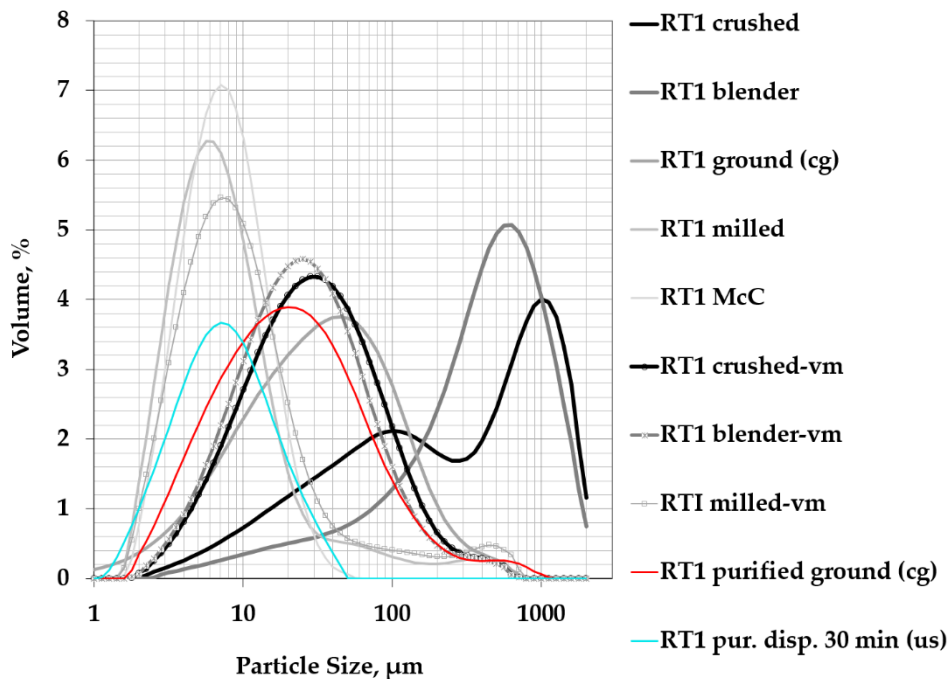
Figure 4-2. Particle size distribution of Beatrix rectorite from sample RT1, after various disintegrating pre-treatments: purified (pur.); coffee grinder (cg); dispersion (disp.); vibrating mill (vm); micronising mill (McC); and ultrasound(us)

However, the effect of particles' aspect ratio at this size range seems to remain vital, irrespective of the degree of dispersion. As a consequence, the sample preparation induced preferred orientation is almost unavoidable when performing pXRD on clay minerals, despite the various preparation techniques used to prevent it.

Theoretically, the method of fractionation by sedimentation is based on Stokes's Law, which generally applies to spherical particles. In the case of platy clay particles, it is assumed that Stokes's Law would approximately apply below a particle size of about 20 μm (Moore and Raynolds, 1997). Particle size analysis of sample RT1 after various disaggregating pre-treatments showed that the sequential use of jaw crushing and blender processing, followed by use of the vibrating mill produced the largest (~ 50 %) size fraction below 25 μm.
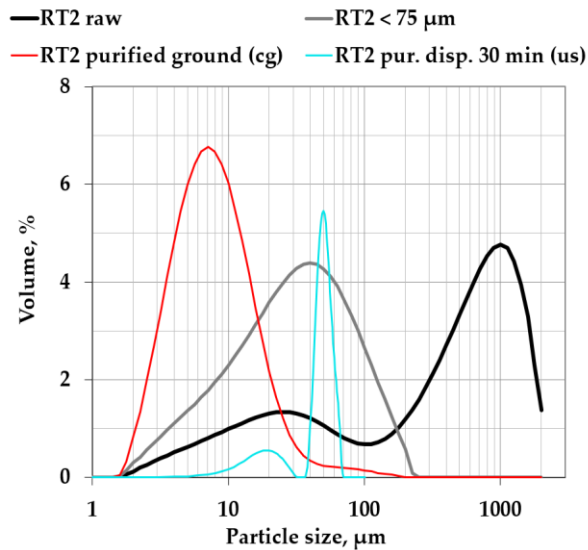
Figure 4-3. PSD frequency curves of Beatrix rectorite sample RT2 after various disintegrating procedures: purified (pur.); coffee grinder (cg); dispersion (disp.); and ultrasound (us)
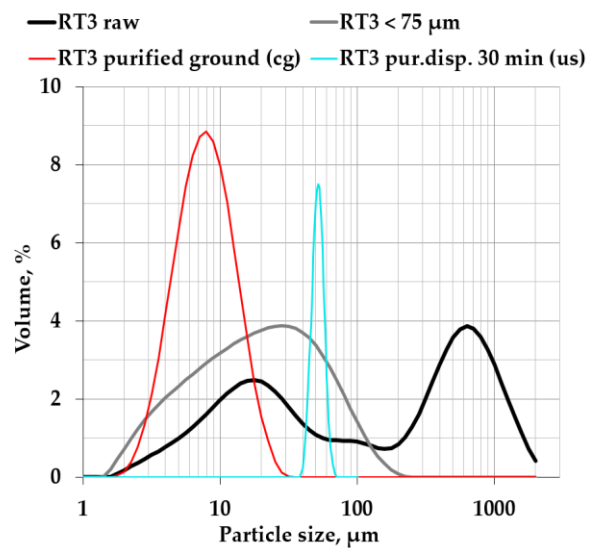
Figure 4-4. PSD frequency curves of Beatrix rectorite sample RT3 after various disintegrating treatments: coffee grinder (cg); dispersion (disp.); and ultrasound (us)

A portion of this material was dispersed ultrasonically under high frequency in ultrapure water (~250 ml) to allow disaggregation and the formation of a suspension. The material of samples RT2 and RT3 was sieved and the < 75 µm fraction was dispersed ultrasonically under the same settings. Based on interactive particle distribution measurements, a settling time of 5 min was established as optimal for best clay fraction recovery. By that time the settling of the remaining clay aggregates and impurities larger than 2 µm is theoretically complete and the cloudy supernatant should contain only the clay fraction with individual particles < 2 µm.

### 4.1.2 Purification and recovery

Preliminary XRD analysis of the bulk material from Beatrix mine showed that the material was very heterogeneous. After purification the rectorite content increased by almost 30 % for sample RT1, around 40 % for sample RT2 and doubled in the case of sample RT3. The mineral quantities in the bulk and purified material are presented in

Table 4-1 with standard deviations (e.s.d), in terms of the least-significant figure to the left (Hill and Howard, 1987).

Table 4-1. XRD-derived proportions of rectorite and associated impurities in bulk and purified samples (wt.%)

| Sample | RT1 | | RT2 | | RT3 | |
|---|---|---|---|---|---|---|
| Phase | Raw | Purified | Raw | Purified | Raw | Purified |
| Rectorite | 72.37 (74) | 91.27 (33) | 60.66 (66) | 86.32 (65) | 45.69 (33) | 91.45 (71) |
| Quartz | 7.78 (19) | 3.21 (10) | 28.83 (45) | 5.64 (17) | 48.81 (20) | 5.95 (48) |
| Calcite | 13.42 (35) | 0.66 (15) | n.d. | n.d. | n.d. | n.d. |
| Muscovite | n.d. | n.d. | 1.63 (27) | 2.93 (35) | 3.74 (55) | 1.66 (20) |
| Chlorite | 6.45 (64) | 4.86 (30) | 3.94 (35) | 2.44 (47) | 1.77 (29) | 1.52 (27) |
| Pyrophyllite | n.d. | n.d. | 3.40 (37) | 2.66 (37) | n.d. | n.d. |
| Gypsum | n.d. | n.d. | 1.55 (14) | n.d. | n.d. | n.d. |

* Figures in parenthesis represent the e.s.d, in terms of the least-significant figure to the left (Hill, R.J. and Howard, C.J., 1987).

The three samples collected at Beatrix mine differ in macroscopic and microscopic appearance and in the mode of occurrence of rectorite, as well as mineral associations (Figure 3-2). Larger platy rectorite fragments in sample RT1 appear to have calcite and quartz particles trapped between sheets, as seen on the SEM micrographs in Figure 4-5.

In samples RT2 and RT3 a visibly disintegrated mix of fine and coarse material (Figure 3-2) is seen by SEM to contain complex particles of mainly quartz grains coated by rectorite or fine rectorite clay binding quartz and other impurities to form larger aggregates and lumps (Figures 4-5 and 4-6). These observations informed the purification procedure described above (Figure 3-6), in which, once liberated, the various mineral grains could be separated by gravity, removing the larger-than-clay fraction components such as quartz and other lump-sized clay minerals of the bulk, and concentrating the rectorite as the main component of the clay fraction.

The method for purification and mass production was developed step by step with careful evaluation of every parameter to achieve the most efficient and productive process for highest purity rectorite clay.
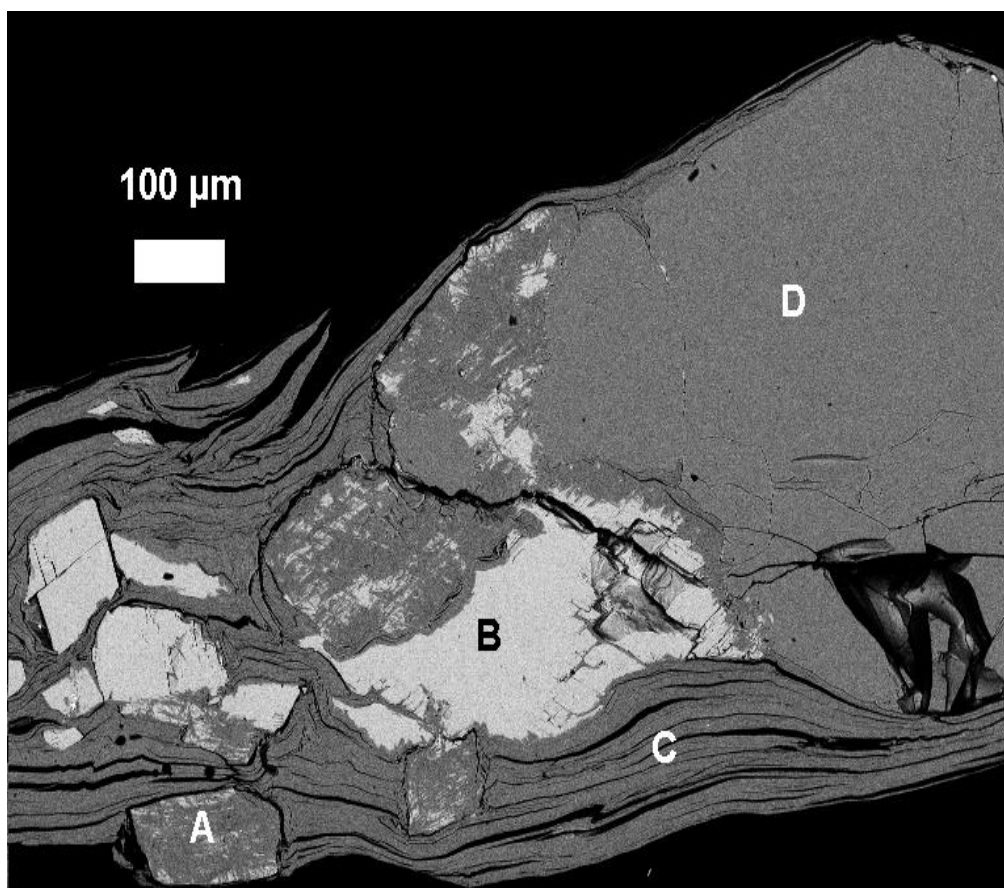
Figure 4-5. SEM image of raw material from sample RT1 showing the distribution of (A) clinochlore (light-grey solid and finely mixed); (B) calcite; (C) rectorite (grey layered); and (D) quartz (grey solid)

Although optimised, it is a tedious process as only 250 g could be processed at a time, from which about 40 g of pure material was recovered. With the available centrifuge, it took two centrifuge runs to process a batch, which also hampered the process with respect to time. If a scale-up process for a more efficient production rate is sought, it is recommended to increase the batch volume starting material by using a larger ultrasound bath and centrifuge. This should, however, also ensure that the negative effects of upscaling on expected losses in recovery and purity of the final product are kept to a minimum.
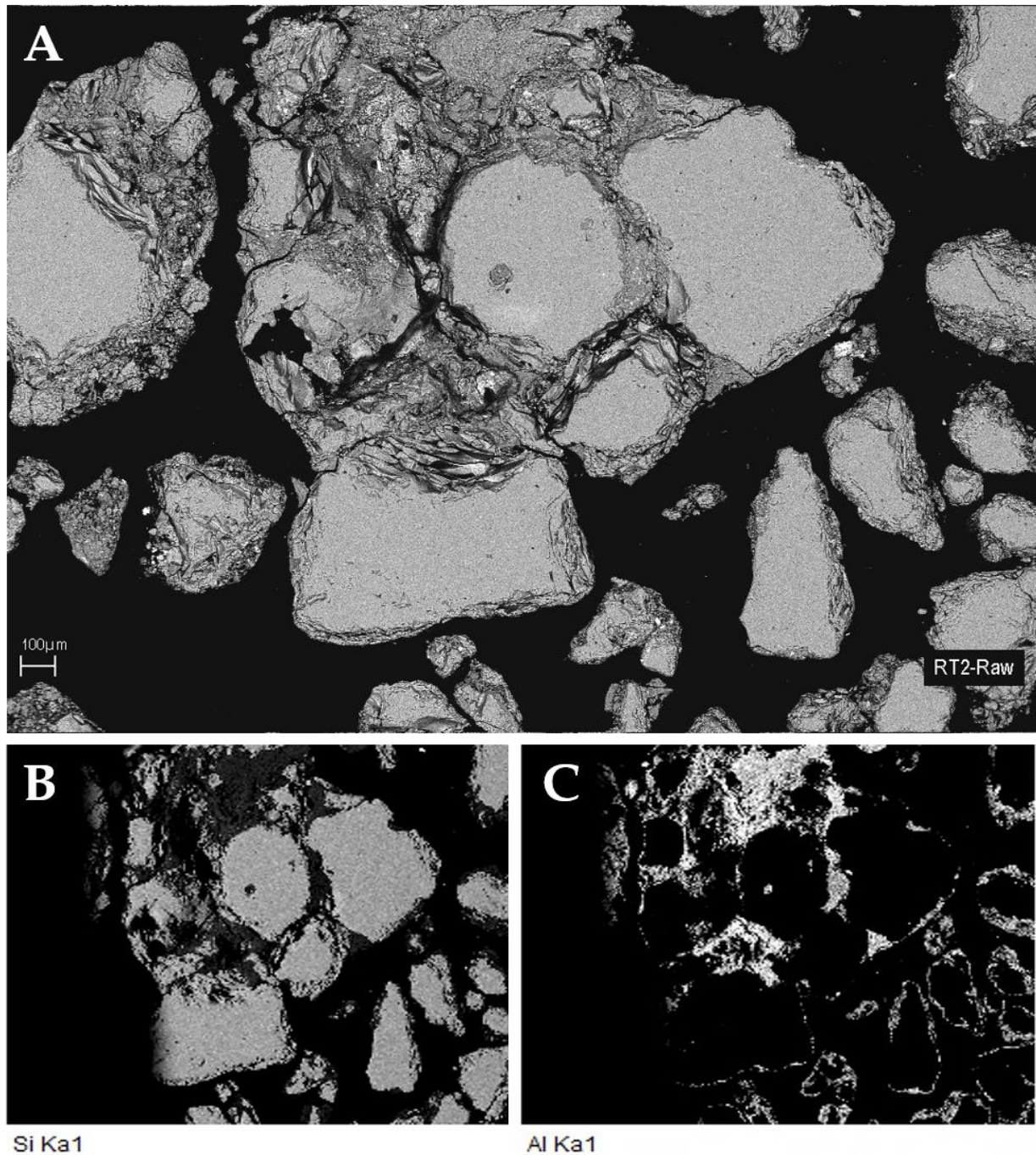
Figure 4-6. (A) Low-magnification backscatter electron (BE) SEM images and element distribution maps for (B) Si and (C) Al from raw material (sample RT2), showing the natural occurrence and spatial relationship between rectorite, quartz and other minor impurities

### 4.1.3 Microscopy

Natural "pure" rectorite from Beatrix mine features a platy-leafy morphology with a pale blue-grey colour and brown pigmentation along cracks and folds, probably caused by iron contamination. Aggregates of stacked ultrafine flakes have a pearly lustre with an earthy appearance and a soft soapy feel to the touch. Individual flakes are translucent to transparent (Figure 3-2 and Figure 4-8) with thin, sharp edges. SEM showed typical layered morphology. Platy and folded aggregates of compact parallel layers are either stacked continuously or thinly curled at the edges, as seen in Figure 4-7. High-resolution FETEM imaging performed on raw rectorite platelets shows continuous silicate layers in parallel to sub-parallel orientation. Ultra-thin edges display unambiguously regular periodicity of well-distinguished light and dark layers of about 2.0 nm and domains of higher thickness. Within the domains, alternating contrast layers of spacing 1.00, 1.30 and 2.20 nm are visible at high magnification (Figure 4-9), identical with the basal spacing of mica and smectite or complete rectorite crystallite.
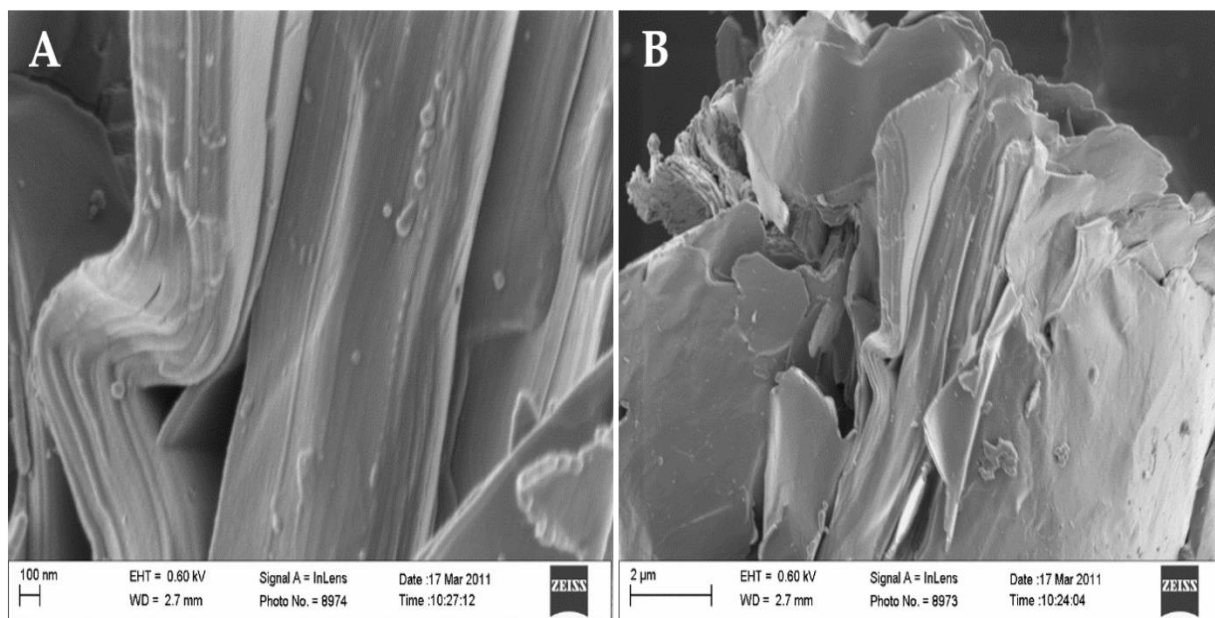


Figure 4-7. SEM images of rectorite (RT1) displaying typical layered textures
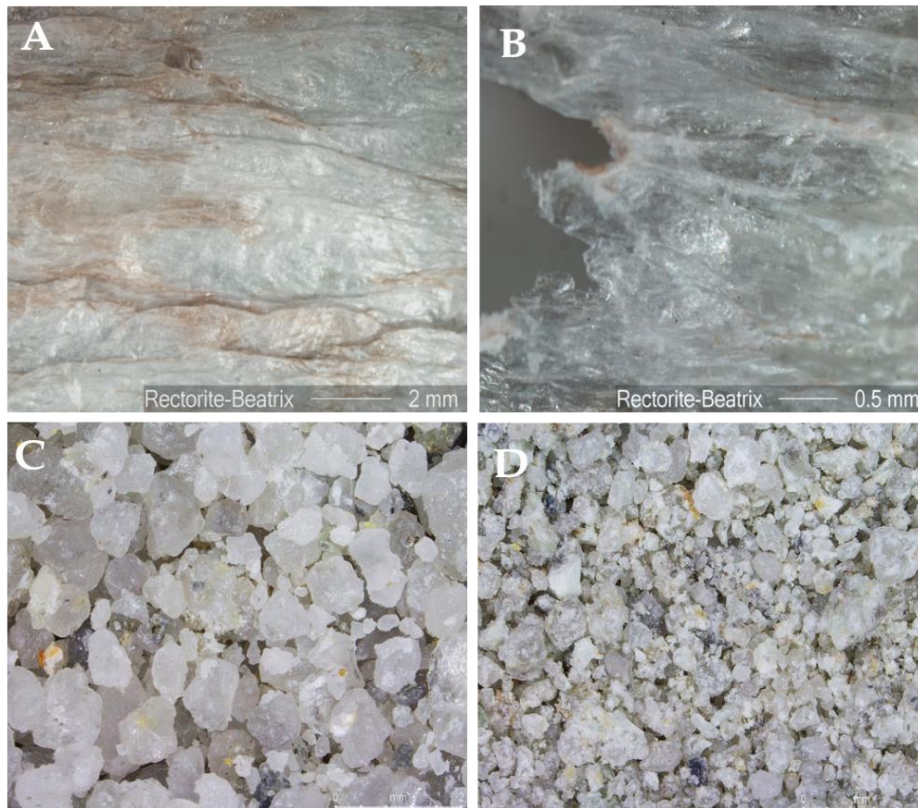
Figure 4-8. Microscope photographs of rectorite sample RT1: (A) compact aggregate; (B) thin flake fragment with translucent to transparent at sharp edges. Disintegrated mine material containing rectorite: (C) sample RT2 and (D) sample RT3
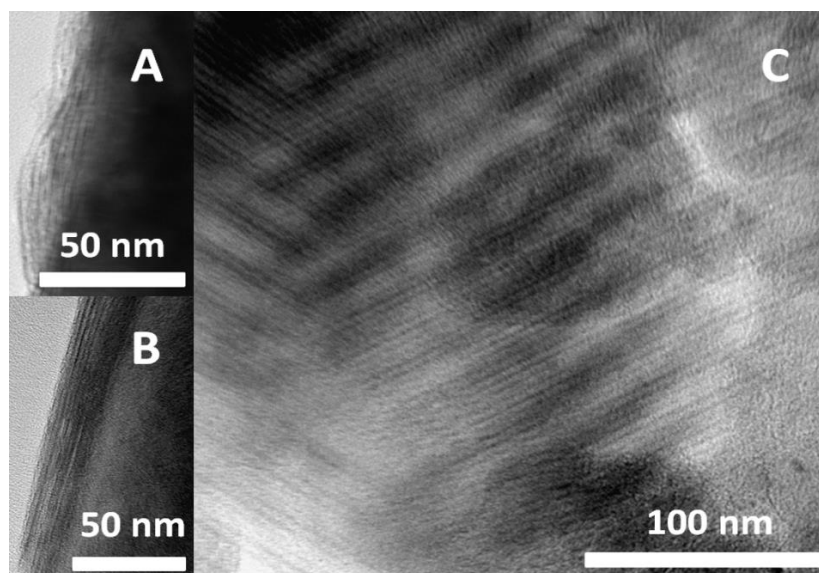


Figure 4-9. FETEM images of sample RT1 showing the typical layer arrangement of rectorite. The thickness of the light and dark domains is ~2.2 nm. The distances between the alternating contrast fringes within the domains are ~1 and ~1.3 nm, corresponding to the basal spacing of mica and smectite respectively.

### 4.1.4 X-ray diffraction and thermal analysis: neat and cation-exchanged rectorite

Typical pXRD diffractograms for a raw and a highly purified sample are presented in Figure 4-10. Quantitative pXRD analysis of bulk material from the three samples showed heterogeneous mineral assemblage with a rectorite content between 45 wt.% and 72 wt.% associated with quartz (7–49 wt.%) and chlorite (1–6 wt.%) in all three samples, calcite (12–14wt.%) in sample RT1, muscovite (1–4 wt.%) in samples RT2 and RT3, pyrophyllite (2–4 wt.%) and gypsum (ca. 2 wt.%) detected only in sample RT2 (Table 4-1).

The diffraction data of powdered raw rectorite obtained at room temperature and humidity showed variations in basal spacing with average $d_{001}$ values ranging from 22.00 Å to 23.73 Å within the three samples. Exposure to controlled 55 % relative humidity (RH) in a desiccator showed that absorption of moisture is a function of time, with full expansion achieved after 90 h. The rectorite lattice expanded to 23.64 Å, 23.48 Å and 23.66 Å for RT1, RT2 and RT3 respectively.
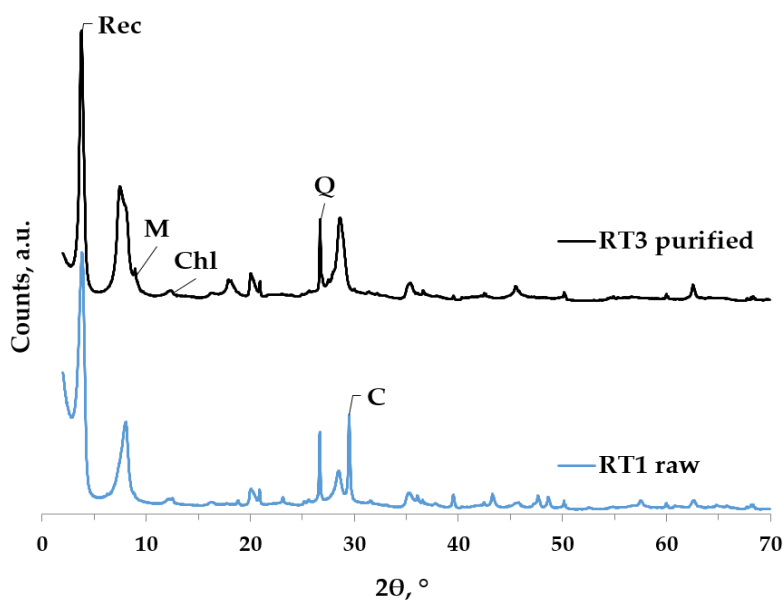


Figure 4-10. Representative powder diffraction patterns of a raw and a purified rectorite sample: rectorite (Rec), muscovite (M), chlorite (Chl), calcite (C), quartz (Q)

Besides being directly related to the layer charge, interlayer cation radius, degree of saturation and hydration state, the basal spacing of expandable materials is also a function of ambient humidity (Moore and Hower, 1986). Therefore, the peak positions from air-dried specimens in Figure 4-11 may vary slightly and should serve only as a baseline to observe diagnostic structural changes upon various organic and cation saturations.
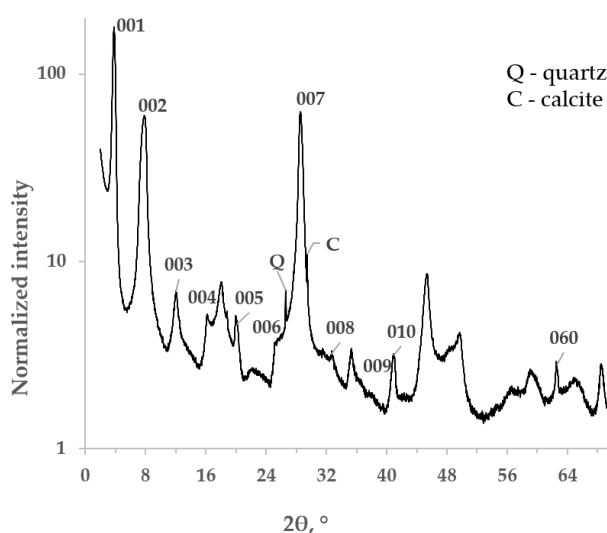


Figure 4-11. XRD diffractogram of purified rectorite in oriented slide at air-dried state (sample RT1)

Diffraction data from oriented air-dry and glycolated specimens show a good integral sequence of basal reflections with an average coefficient of variation (CV) of 0.12 (Bailey, 1982). The 060 reflection at 1.48 Å (2θ 62.40 °) indicates the dioctahedral character of the 2:1 structure. The average $d_{001}$ spacing is between 22.07 Å and 22.20 Å, and the periodicity of smaller order $d_{001}$ is consistent with a well-ordered 1:1 layered structure.

Upon saturation for 24 h, the mixed-layer structure expanded to $d_{001}$ 26.75 Å when exposed to ethylene glycol (EG) and to 27.32 Å after exposure to glycerol (G) (Figure 4-12(A)). $Mg^{2+}$-exchanged specimens showed cell dimensions of 24.60 Å and $d_{001}$ at 27.49 Å after glycerol exposure. Rectorite exchanged with $Li^+$ has $d_{001}$ at 22.48 Å and exchanged with $Na^+$ at 22.16 Å in air-dry state(Figure 4-12(B)). The latter expanded to 27.24 Å–27.67 Å and 26.80 Å–28.69 Å after exposure to EG and G respectively for 24 h.
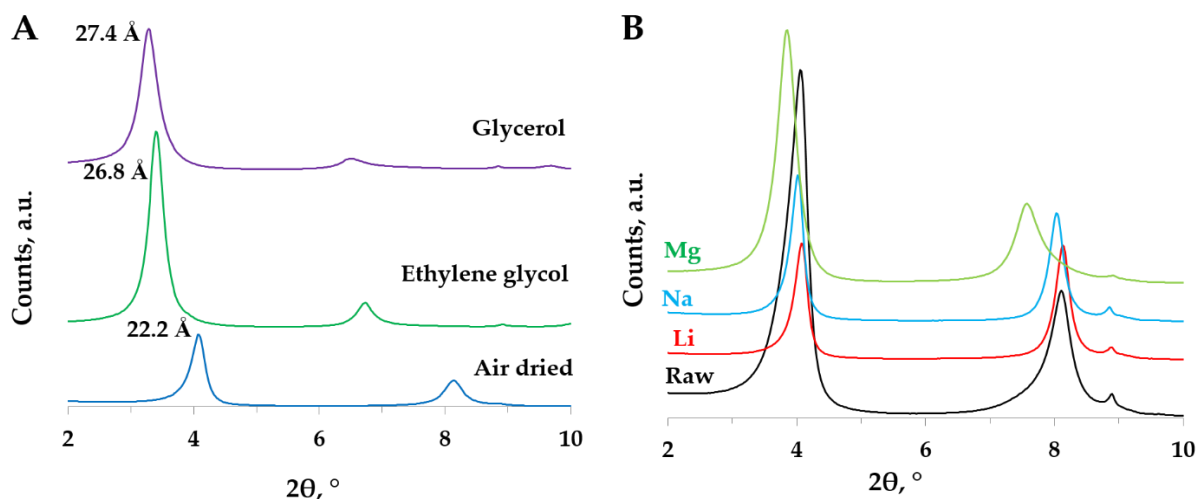
Figure 4-12. Diffraction data: (A) neat rectorite oriented specimens in air-dry state and after saturation with ethylene glycol (EG) and glycerol (G); (B) overlay of Li-, Na- and Mg-exchanged rectorite compared to neat rectorite in air-dry state

The almost identical values observed for the raw and Na-exchanged specimens suggest that Na$^+$ is a major exchangeable cation or is the cation most susceptible to exchange in the smectite interlayer component of rectorite. These values are consistent with the 1:1 stacking sequence of the smectite-mica interstratification of an expanding single water layer: Na-smectite at 1.24 nm alternating with a non-expanding layer of Na-mica (paragonite) at around 0.96 nm, producing a "superstructure" with a basal spacing above 2.2 nm. A similar spatial relationship is observed with glycolated specimens at 1.72 nm or 1.77 nm: glycerol-expanded smectite layers alternated in regular manner with a 0.96 nm mica layer not affected by the organic intercalation. Pattern simulation for glycolated specimens using NEWMOD indicate compositions of 50 % dioctahedral mica and 50 % dioctahedral smectite with R1 ordering.

The Greene-Kelly test (Greene-Kelly, 1951) suggested that the expandable smectite layer is of montmorillonite-beidellite composition. Partial collapse of the rectorite structure was observed, which produced reflections around 1.96 nm and 0.96 nm indicative of montmorillonite. The remaining strong reflection at around 2.76 nm, identical with that of Li-saturated glycerol expanded rectorite, serves as evidence for the beidellite component of the smectite layer. The basal 00l reflections move upon organic saturation

or cation replacement in a manner much similar to montmorillonite. Consequently, the type of exchangeable interlayer cation and its hydration energy will ultimately determine the swelling behaviour of rectorite.

The results of TGA/DSC thermal analysis (Figure 4-13) supplemented by XRD examination of heated specimens demonstrate the response of rectorite to heating. Overlays of XRD diffractograms recorded from rectorite specimens heated to 1 200 °C in steps of 50 °C are presented in Figure 4-14.
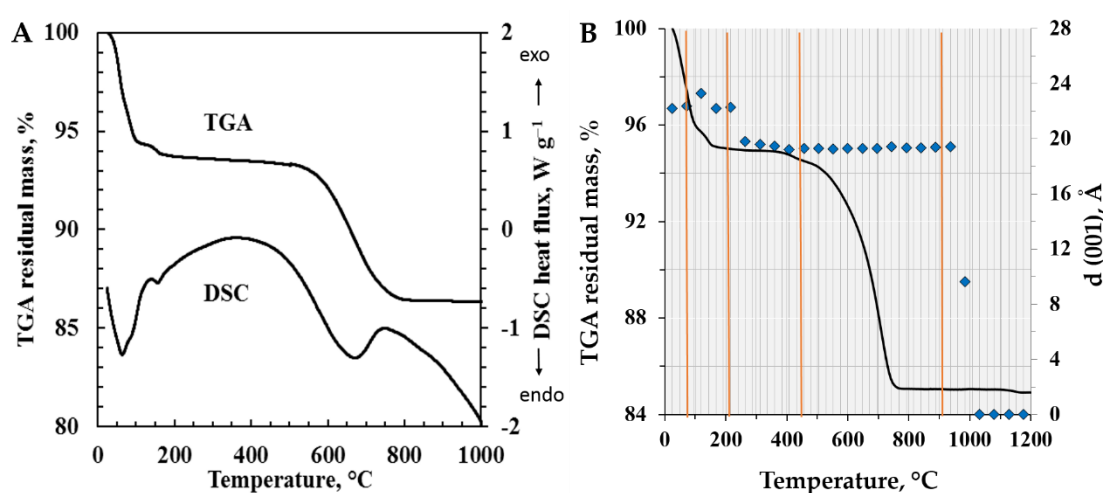


Figure 4-13. (A) TGA/DSC curves for rectorite from the Beatrix mine recorded at a scan rate of 10 °C min$^{-1}$ with air flowing at 30 mL min$^{-1}$. The sample was equilibrated at 55 % RH in a desiccator for more than 90 h; (B) $d_{001}$ values (Å) for heated rectorite versus residual mass (%) as a function of increasing temperature.

The two methods generally agreed that full decomposition of rectorite occurred in three major steps with a total weight loss of 15.2 %. A fast, steep drop below 150 °C is followed by slow and continuous mass loss between 200 and 470 °C and a significant decrease in mass between 470 and 800 °C (Figure 4-13(A)). Initially, the structure expands slightly between 50 °C and 100 °C, possibly due to the formation of steam in the interlayer region on heating. At the start, 50 °C to 100 °C basal reflections fluctuate with $d_{001}$ from 22.20 Å through 22.37 Å to 23.29 Å and then revert to the initial 22.29 Å at 150 °C–200 °C (Figure 4-13(B)).

The DSC patterns feature three endothermic peaks at 53 °C, 73 °C and 140 °C associated with progressive TGA mass loss of 5.9 wt.% completed at 150 °C. This mass loss is consistent with the desorption of surface water and loss of the interlayer water (Kodama, 1966). The two endothermic peaks at low temperatures indicate dehydration from the smectite layer with a divalent cation, i.e. beidellite where $Ca^{2+}$ is the interlayer cation. The IR spectra support this observation by the disappearance of OH stretching bands at 3420 $cm^{-1}$ and 1640 $cm^{-1}$ (Figure 4-15). A downshift and a significant drop in intensity of $d_{001}$ to 19.79 Å, accompanied by increased $d_{002}$ now at 9.89 Å, marks the loss of regularity and the collapse of the clay structure at 250 °C.
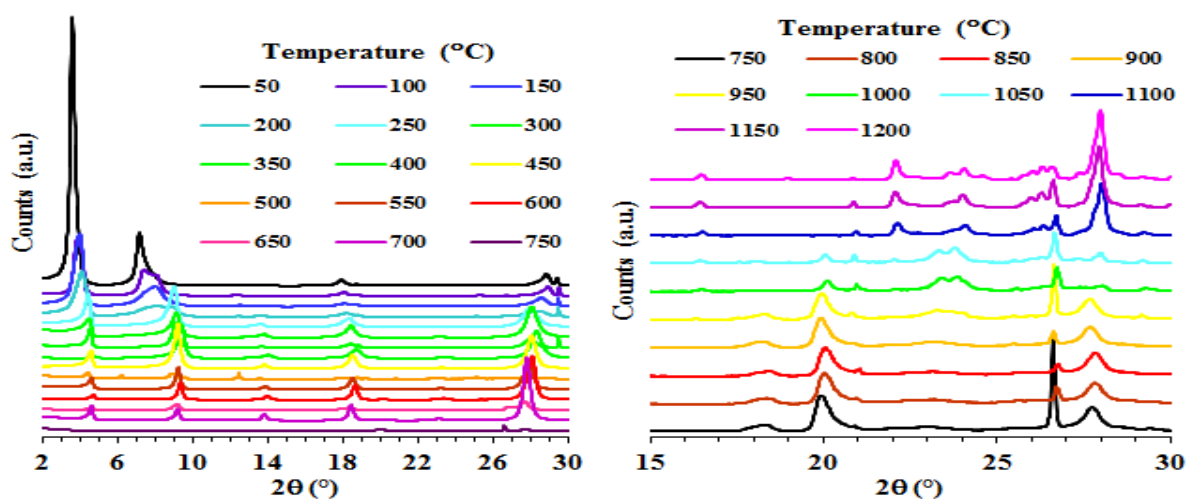


Figure 4-14. Overlay of the X-ray diffraction patterns of rectorite heated at 50 °C intervals: temperature range is 50 °C to 1 200 °C

A further increase in temperature results in a change of profile intensity ratios, i.e. a very weak 001, enhancement of intensity around the mica region and adjusting positions to those consistent with paragonite $d_{002}$ at 0.965 nm, $d_{004}$ at 0.48 nm and $d_{006}$ at 0.32 nm around 450 - 500 °C. From this point up to around 750 °C the 001 reflection is very weak and gradually disappears. The loss of intensity at the first basal reflection indicates the end of dehydroxylation with the complete breakdown of the interlayer, i.e. the periodicity along the *c*-direction has ceased to exist. On the TG/DSC plots a weak, broad peak at around 470 °C and a more intense one at 715 °C are attributed to dehydroxylation (Kodama, 1966). At 950 °C the formation of mullite commences, followed by cristobalite

at 1 050 °C and albite at 1 100 °C. By 1 000 °C the clay structure is completely destroyed. The TGA curve indicated a mass loss of 7.7 wt.% between 500 °C and 820 °C related to dehydroxylation of structural hydroxyl groups.

### 4.1.5 FTIR

An IR vibration spectrum of untreated rectorite is in general agreement with published data for rectorite, montmorillonite and beidellite (Farmer and Russel, 1967; Kloprogge et al., 1999; Kodama, 1966b; Madejova and Komadel, 2001; Shimoda and Brydon, 1971).
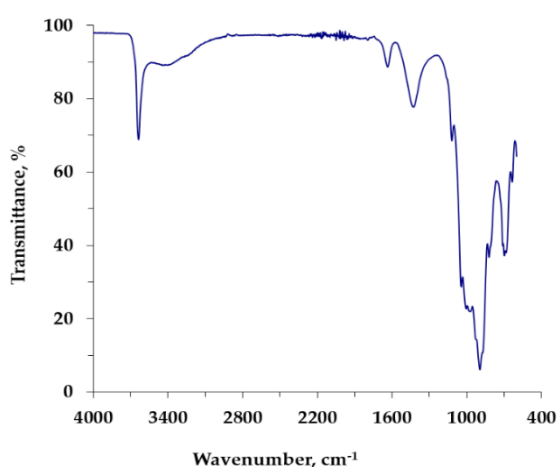


Figure 4-15. FTIR spectrum for purified rectorite (sample RT1)

Although the spectrum of raw rectorite generally resembles a mixture of muscovite-paragonite and montmorillonite-beidellite spectra, it also contains unique bands and exhibits spectral sharpness not seen in either of the individual components or other interstratified clay mineral. Such bands at 1120 cm$^{-1}$, 993 cm$^{-1}$ and 710 cm$^{-1}$ could be ascribed to Si-O stretching, while the vibration observed at 925 cm$^{-1}$ can be associated with the Al-Al-OH deformation. A group of well-resolved sharp bands in the low-frequency range from 450 cm$^{-1}$ to 1200 cm$^{-1}$, typically characteristic of a phyllosilicate structure, are present in both the raw and modified rectorite spectra.

Apart from the relatively minor shifts in peak positions, the modified forms feature considerable broadening of the absorption bands compared to those of the neat sample.

This is due to structural imperfections and reduced order arising from organic substitution. Two sharp bands at 1045 cm$^{-1}$ and 1006 cm$^{-1}$ assigned to the Si-O-Si group are in close proximity to Si-O stretching in the tetrahedral sheet of beidellite at 1041 cm$^{-1}$ and montmorillonite at 1010 cm$^{-1}$ (Farmer and Russel, 1967). Two bands at 820 cm$^{-1}$ and 698 cm$^{-1}$ closely resemble Al-O out-of-plane vibrations in beidellite at 819 cm$^{-1}$ and Si-O-Al bending at 693 cm$^{-1}$. These originate from Al for Si substitutions in the tetrahedral sheet of beidellite and are analogous to similar vibrations in muscovite (Farmer, 1974). The absorption peak at 892 cm$^{-1}$ represents the OH deformation band in either the Al-OH-Al or Al ($Fe^{3+}$)-OH groups described for Wyoming-type montmorillonite with high iron content (Russell et al., 1970) and results from the substitution of $Fe^{3+}$ for $Al^{3+}$ in the octahedral sheet. However, this vibration has also been reported for montmorillonites with very low iron content (Farmer and Russell, 1967) and could therefore also be ascribed to the Al-OH band of rectorite.

The OH absorption spectra in the high-frequency region above 3500 cm$^{-1}$ are generally similar for raw and modified rectorite, with slight broadening and intensity progressively decreasing from double- to single-chain surfactant intercalation. The sharp intense absorption band at 3638 cm$^{-1}$ corresponds to the structural H bonding vibrations in the Si-O-Si linkage of rectorite (Kloprogge et al., 1999). Two less pronounced broad peaks at 3420 cm$^{-1}$ and 1638 cm$^{-1}$ are assigned to OH stretching and bending respectively in the H-O-H group of molecular water. Kodama (1966b) attributed the latter two to absorbed and interlayer water molecules as both peaks disappeared upon heating at 200 °C. The band at 3638 cm$^{-1}$ disappears at 900 °C following complete dehydroxylation of the structure. Where a very weak and broad band appears in the spectra of raw samples at around 1375 cm$^{-1}$, it is due to trace amounts of absorbed $NH_4^+$.

Table 4-2. Band positions (cm⁻¹) and assignments for the IR absorption maxima of neat purified rectorite from Beatrix mine with the literature data for comparison as indicated

| Band Assignment | Rectorite | Rectorite | Modified rectorite | Modified rectorite | Modified rectorite | Rectorite | Rectorite | Synthetic mica-montmorillonite | Synthetic beidellite | Paragonite | Swy-2, Wyoming montmorillonite | Rectorite |
|---|---|---|---|---|---|---|---|---|---|---|---|---|
| | This study: Untreated | This study: Untreated | This study: Hexadecyltrimethyl Ammonium Chloride-(SCC16) | This study: Didecyldimethyl Ammonium Chloride-(DCC10) | This study: Dialkyldimethyl Ammonium Chloride-(DCC18) | Li et al., 2008. | Kloprogge et al, 1999. | Kloprogge et al, 1999. | Kloprogge et al, 1999. | Kloprogge et al, 1999. | Madejova and Komadel, 2001 | Kodama, 1966. |
| | KBr | ATR | KBr | KBr | KBr | ATR | KBr | KBr | KBr | KBr | KBr | KBr |
| Si-O bending | | 481 | | | | 479 | 478 | 471 | 473 | 481 | | |
| Si-O-Al bending | | 523 | | | | 523 | 545 | 536 | 535 | 542 | 524 | |
| Si-O-Al deformation | 638 | 636 | | | | 635 | 615 | 620 | 625 | 625 | 620 | |
| Si-O-Al bending | 699 | 694 | | | | 699 | 693 | 699 | 694 | 694 | | |
| Si-O-Al bending | 710 | 710 | | | | | | | | | | |
| Al-O-Si in-plane | 732 | 732 | | | | | 726 | 732 | | | | 730 |
| Al-O-Si in-plane | 760 | 760 | | | | | 758 | 756 | 753 | | 778 | |
| Al-O-H libration | 815 | 815 | | | | | 804 | 819 | 812 | 805 | | 810 |
| Al-O-out-of-plane | 820 | 821 | | | | 823 | 822 | | | 832 | 842 | 823 |
| Al-O-H libration | 875 | 877 | | | | | 875 | 888 | 884 | 883 | 885 | 875 |
| Al-O-H libration | 897 | 896 | | | | 895 | | | | | | |
| Al-O-H libration | 925 | 928 | | | | | 914 | 936 | 928 | 935 | 917 | 920 |
| Si-O-Si stretching | 993 | | | | | | | | | | | 995 |
| Si-O-Si stretching | 1006 | 1006 | | | | 1004 | | | | | | |
| In-plane Si-O-Si stretching | | 1034 | | | | | 1021 | 1030 | 1028 | 1009 | | 1023 |
| In-plane Si-O-Si stretching | 1046 | 1046 | | | | 1048 | 1058 | 1053 | | | 1041 | 1050 |
| Si-O stretching | | 1088 | | | | | 1082 | | | | | 1080 |
| Si-O stretching | 1121 | 1120 | | | | 1120 | 1123 | 1126 | 1124 | 1125 | | 1125 |
| NH4 | 1375 | | | | | | | 1401 | | | | 1388 |
| C-H bending vibration | | | 1448 | 1434 | 1442max | | | 1441 | | | | |
| C-H bending vibration | | | 1470max | 1468max | 1466 | 1469 | | | | | | |
| H2O bending (OH deformation of H2O) | 1640 | 1645 | 1648 | 1655 | 1644 | 1634 | 1639 | 1637 | 1634 | | 1634 | 1640 |
| C-H symmetric stretching vibrations | | | 2851 | 2856 | 2855 | 2850 | | | | | | |
| CH2 asymmetric stretching | | | 2924 | 2927 | 2929 | | | | | | | |
| C-H asymmetric stretching vibrations | | | 2954 | 2959 | 2962 | 2919 | | | | | | |
| Chemically bonded interlayer H2O | 3240 | 3240 | | 3282 | 3246 | | 3240 | 3266 | 3230 | | | |
| H2O stretching or H-bonding vibrations in Si-O-Al linkage | 3420 | 3420 | 3410 | 3421 | 3442 | 3390 | 3433 | 3478 | 3453 | 3420 | 3422 | 3420 |
| H bonding vibrations in Si-O-Si linkage | 3640 | 3640 | 3644 | 3644 | 3640 | 3639 | 3638 | 3651 | 3659 | 3620 | 3632 (3627) | 3645 |

### 4.1.6  Rectorite structure refinement, modelling and quantitative analysis

### 4.1.6.1 Structure refinement and modelling

Similarly to other mixed-layer structures, only partial indexing information for rectorite is available in the two PDF files in the ICDD database. This data contains 00l reflections only and describes a 2-dimensional crystal structure characteristic of clay minerals where layers are stacked along the third dimension. The observed diffraction data from the Beatrix mine rectorite fits a structure intermediate between those of PDF 025-0781 (Korolev, 1971) and PDF 029-1495 (Brindley, 1977). Based on the empirically modelled rt_*hkl* phase (Figure 4-16), the cell parameters of purified raw Beatrix rectorite refined to $a$ = 5.177(13) Å; $b$ = 8.980(33) Å; $c$ = 22.489(20) Å and $\beta$ = 97.335(44)°. The calculated volume weighted mean crystallite size was around 14 nm and the cell volume was 1045.41(16) Å$^3$.
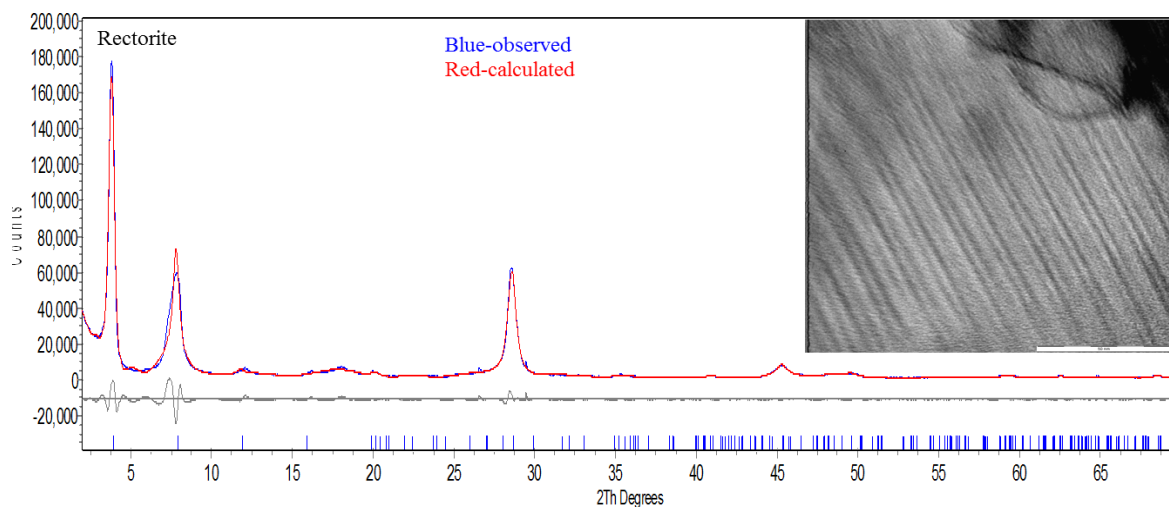


Figure 4-16. Observed (blue), calculated (red) and difference curve (grey) patterns after refinement using the modelled rectorite phase in place of a structure file. The TEM image (FOV 150 nm) displays layer periodicity; the approximate thickness of a set of light/dark fringes is below 15 nm, i.e. in the range of calculated crystallite size.

The refinement data from Na-exchanged rectorite was $a$ = 5.090(11) Å; $b$ = 9.026(30) Å; $c$ = 22.200(66) Å and $\beta$ = 98.836(23) ° with V of 1008.06(50) Å$^3$ and the Mg-exchanged

structure showing unit cell parameters $a$ = 5.138(17) Å; $b$ = 9.001(47) Å; $c$ = 24.349(26) Å, $\beta$ = 97.52(44) ° and cell volume 1094.60(41) Å$^3$.

The quality of the Rietveld refinement was assessed by inspection of the difference curve between the measured and calculated XRD patterns and the numerical quality criteria Rwp (weighted residual). Figure 4-10 shows a typical refinement plot to demonstrate the goodness of fit for rectorite refinement using the modelled *rt_hkl* structure file. The weighted residual errors Rwp ranged from 5.3 % to 15 %, indicating a very good agreement between observed and simulated XRD patterns.

### 4.1.6.2 Quantitative phase analysis (QPA): accuracy and validation

The closeness of the qualitative and quantitative determinations of the replicate samples was comparatively small within laboratory errors. The QPA percentage, inferred by the Rietveld method, of major oxides for rectorite in each sample was compared to the respective oxide proportions determined by XRF and the results are plotted against each other in Figure 4-17. RecBea indicates the unique chemistry for Beatrix rectorite determined in this study (Table 4-7). This chemistry is used as a basis to calculate the mean structural formula, and here for the calculation of normative compositions. Calculations were also done based on chemical compositions for rectorite from the literature data (Gaines et al., 1997; Nishiyama and Shimoda, 1981). These calculations were used to assess the accuracy of rectorite modelling, QPA and mineral chemistry determined in this study. Linear regression lines are shown for each oxide plot, together with the respective equation ($y = ax+b$) and the relevant correlation coefficient $R^2$. The diagonal line on each plot is drawn to visualise statistical fit: in the case of exact agreement, the points would fall on the diagonal line. Points below this line would indicate underestimation and points above it, an overestimation by the Rietveld phase quantification. For $SiO_2$ and $Al_2O_3$ all samples show good agreement between the values from the XRD and XRF results (Figure 4-17(A, B and D)). The slight deviations shown on plots (B) and (C) by empty circles all belong to recalculation data

103

based on rectorite compositions from published sources. This is confirmed in plots (D) and (E) by the improved correlation coefficient $R^2$ after removal of the literature-based recalculated data, i.e. where only RecBea compositions are used. The comparison of CaO, $Na_2O$ and $K_2O$ shows greater dispersion, more pronounced in the lower values range. These elements comprise the interlayer content of rectorite with $Ca^{2+}$ and $Na^+$ present in the exchangeable and fixed interlayer, and minor $K^+$ in the fixed interlayer only and also in the free-standing muscovite. In sample RT1 some $Ca^{2+}$ is also related to the calcite occurrence that carries a substantial LOI component and may explain the underestimation of CaO by Rietveld at a higher concentration range (Figure 4-17(C and E)). The wide spread in the $K_2O$ population is most probably due to the low concentrations and greater degree of variation of its occurrence, confirmed by the drastic improvement of correlation $R^2$ when local RecBea composition was used for normative calculation. The latter also applies to the CaO and $Na_2O$ correlation trends (Figure 4-17 (C and E)).

Despite some individual outliers, comparison of the major oxide percentages of the theoretical and measured compositions shows a generally high level of agreement. All data points, including those based on published rectorite compositions, plot close to the equality line with slight deviations indicating under- or overestimation of the Rietveld QPA (Figure 4-17(A)). The best agreement is achieved when the mineral chemistry of RecBea is used for calculation. This is a good indication that the proposed quantification method for rectorite-containing samples provides a quantitative estimation of mineral percentages that are consistent with independent chemical determinations, in this case by XRF. This further confirms the accuracy of the *rt_hkl* model proposed here, the calibrated QPA method generated with the modelled rectorite structure file, and the chemical determinations by XRF.
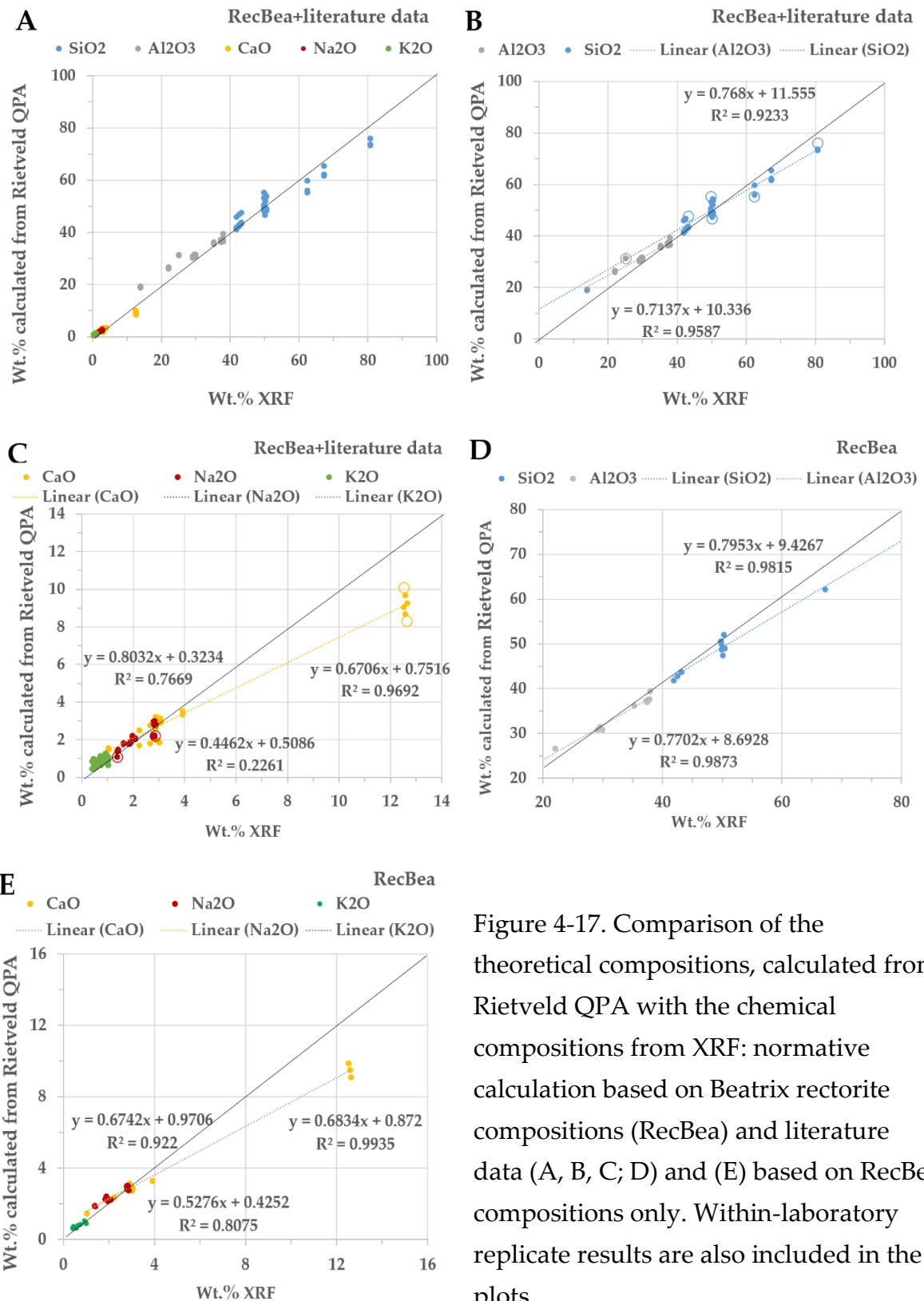
Figure 4-17. Comparison of the theoretical compositions, calculated from Rietveld QPA with the chemical compositions from XRF: normative calculation based on Beatrix rectorite compositions (RecBea) and literature data (A, B, C; D) and (E) based on RecBea compositions only. Within-laboratory replicate results are also included in the plots.

### 4.1.7   NMR

NMR probes the local environment of the nucleus under study and thus it focuses on the short-range order. It is therefore ideally suited for disordered materials or materials exhibiting short-range order only. The NMR spectra provide quantitative information complementary to the scattering experiments on the relative content of various species. NMR inherently gives an ensemble average. For this reason the solid-state NMR spectra of all NMR-active nuclei in the sample were recorded.

### 4.1.7.1 $^{27}$Al MAS NMR

The $^{27}$Al MAS (14 kHz) NMR spectra of all samples showed two signals with spinning side-bands (ssb) (Figure 4-18 (a) and (b)). The central transitions of the lines featured characteristic second-order quadrupolar broadened line shapes. The dominating line at *ca.* 5 ppm is attributed to six-coordinated (or octahedral or $AlO_6$ or Al-VI) Al sites, while the second peak at ca. 70 ppm is known to arise from Al sites in the tetrahedral coordination (four-coordinated $AlO_4$ or Al-IV) (Vyalikh et al., 2009). The relative ratio of $AlO_4$ (Al-IV) to $AlO_6$ (Al-VI) is 1:2 and remained constant across all samples. Deviation from the characteristic second-order quadrupolar line shape due to inhomogeneous broadening indicates a distribution of Al environments. The fit parameters changed only slightly within the uncertainty limits, pointing to the fact that the local structure around Al was not affected by purification and ion substitutions. Similar spectral parameters and the invariance of the 27Al NMR spectra on modification of the local environment in interlayers were previously reported for synthetic beidellite (Kloprogge et al., 1992). Slight deviations of the fit parameters for RT2 and its remarkable line broadening reflect a more disordered and less symmetric environment as compared to other samples (Table 4-3).
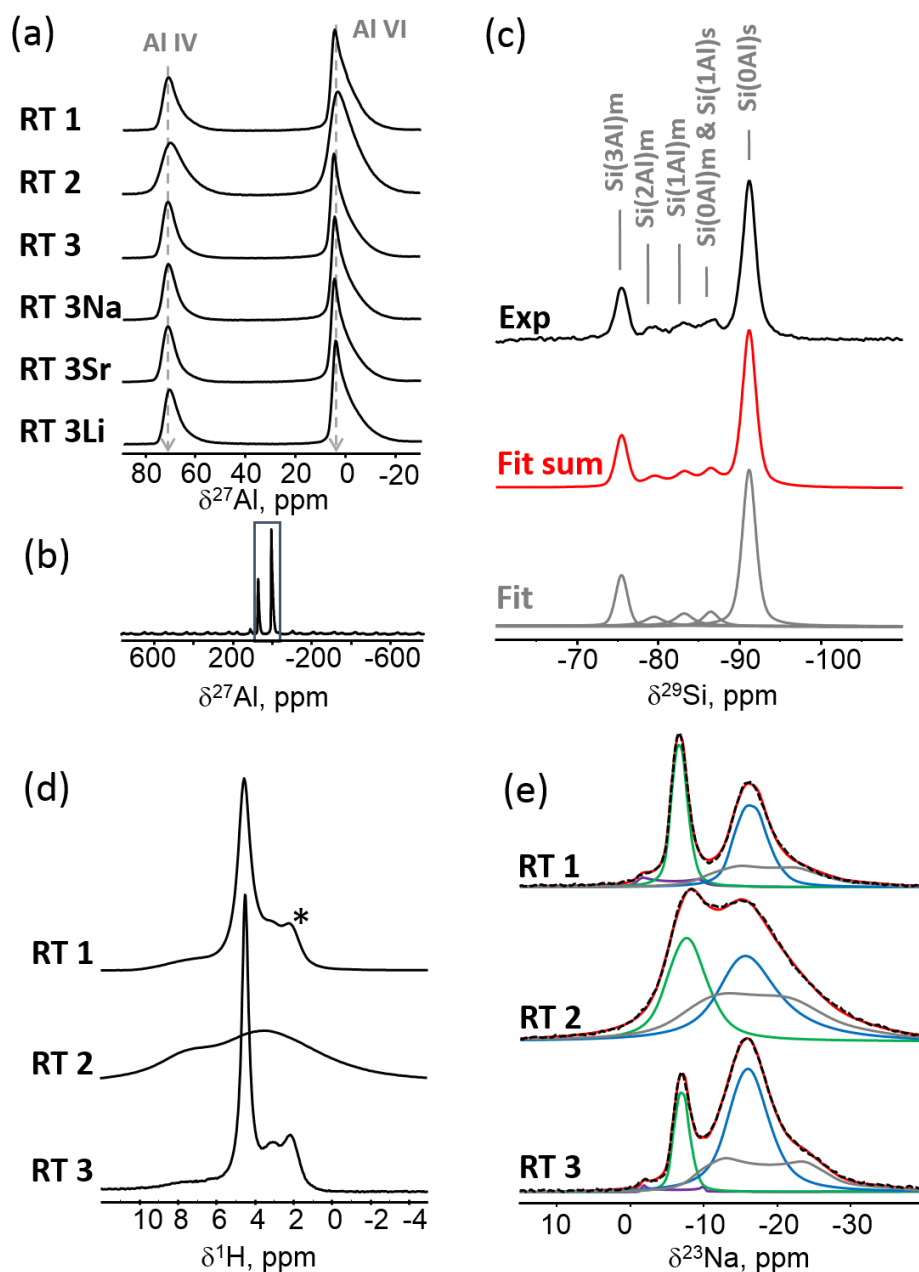
Figure 4-18. (a) $^{27}$Al MAS NMR spectra of rectorite samples; (b) broad width $^{27}$Al MAS NMR spectrum of RT1 with spinning sidebands. The frame shows the spectral region expanded in (a). (c) $^{29}$Si MAS NMR spectrum of RT1 (Exp) with spectral deconvolution (Fit) and a sum of fit components (Fit sum). (d) $^{1}$H MAS NMR spectra at 20 kHz spinning speed of the three rectorite samples. The spectra are normalised at the high-field peak shown by the asterisk. (e) $^{23}$Na MAS NMR spectra of the three rectorite materials (black dotted lines) with their deconvolution, including the sum of fit components (red line). Site I is green, Site II is grey, Site III is blue and Site IV is lilac.

Table 4-3. Fit data for $^{27}$Al NMR spectra, where $^{27}\delta$ is the isotropic chemical shift (± 0.2 ppm) and $C_Q$ is the quadrupolar coupling constant (± 0.2 MHz). The relative intensities (± 1 %) for the two components are calculated from central transitions and spinning sidebands.

| Sample | $^{27}\delta$, ppm | | $C_Q$, MHz | | Relative intensities, % | |
|---|---|---|---|---|---|---|
| | Al-IV | Al-VI | Al-IV | Al-VI | Al-IV | Al-VI |
| RT1 | 74.3 | 6.6 | 3.4 | 3.6 | 33 | 67 |
| RT2 | 74.5 | 6.8 | 4.0 | 4.2 | 32 | 68 |
| RT3 | 74.0 | 6.5 | 3.1 | 3.5 | 33 | 67 |
| RT3 Na | 74.2 | 6.6 | 3.2 | 3.5 | 33 | 67 |
| RT3 Sr | 74.2 | 6.6 | 3.2 | 3.5 | 33 | 67 |
| RT3 Li | 74.1 | 6.5 | 3.3 | 3.6 | 33 | 67 |

## 4.1.7.2 $^{29}$Si MAS (5 kHz) NMR

Since $T_1$ relaxation times can be different for various $^{29}$Si sites, the repetition time had to be adjusted according to the longest $T_1$ in the sample in order to obtain quantitative spectra. Due to the very long $^{29}$Si $T_1$ relaxation times in these materials, $^{29}$Si MAS NMR spectra were measured at two repetition time values in order (*i*) to obtain a sufficient signal-to-noise ratio for signal assignment, and (*ii*) to obtain quantitative information from fully relaxed spectra. Five lines are found in all $^{29}$Si spectra, which are attributed to silicon tetrahedra surrounded by aluminium atoms located in either the mica (m) or the smectite (s) layers (Figure 4-17(c)). The nomenclature Si (*n*Al) designates a Si atom bonded via oxygen bridges to *n* Al atoms in tetrahedral sheets (*n* = 0-3). Due to their similar positions, Si(0Al)$_m$ and Si(1Al)$_s$ cannot be distinguished in the present experiment. The Si (*n*Al) intensity distribution presented in Table 4-4 shows a deviation from the expected binomial intensity distribution in mica, pointing to a high degree of Al substitution (high fraction of the Si(3Al)$_m$ component).

Table 4-4. Fit data for $^{29}$Si NMR spectra, where $^{29}\delta$ is isotropic chemical shift (± 0.1 ppm). Relative intensities (± 5 %) are calculated from the fully relaxed spectra (at a repetition time of 600 s).

| Sample | $^{29}$Si chemical shifts | | | | | Relative intensities |
|---|---|---|---|---|---|---|
| RT1 | -75.5 | -79.5 | -83.2 | -86.3 | -91.1 | 20 : 6 : 7 : 7 : 60 |
| RT3 | -75.5 | -79.5 | -82.7 | -86.7 | -91.0 | 13 : 10 : 10 : 15 : 52 |
| RT3 Na | -75.5 | -79.3 | -82.8 | -85.7 | -91.0 | 11 : 8 : 16 : 17 : 48 |
| RT3 Sr | -75.5 | -79.3 | -83.6 | -86.3 | -91.1 | 12 : 12 : 14 : 12 : 50 |
| RT3 Li | -75.5 | -79.3 | -83.2 | -86.1 | -91.0 | 11 : 13: 12 : 15 : 49 |
| Assignment | Si(3Al)m | Si(2Al)m | Si(1Al)m | Si(0Al)m / Si(1Al)s | Si(0Al)s | |

### 4.1.7.3 $^{1}$H MAS (20 kHz) NMR

High-resolution MAS NMR spectra (Figure 4-17(d)) show sharp signals at 2.1 ppm, 3.1 ppm, and 4.6 ppm and a broad background signal at ca. 8 ppm for the samples RT1 and RT3, while only two broad peaks are seen for RT2 (Table 4-5). The broadening can arise from structural disorder and/or the presence of minor paramagnetic impurities (e.g. the presence of iron oxide or iron substitution in the octahedral sheets of the rectorite itself) and is consistent with the $^{27}$Al and $^{23}$Na data for RT2. The peaks at 2.1 ppm and 3.1 ppm are assigned to the hydroxide groups of hydrated $Al_2O_3$ and $SiO_2$ in the mineral structure, while the peak at 4.6 ppm is attributed to water physically adsorbed on the mineral surface. Similar peaks have been noted in a study on aluminium layered hydroxides (Wang et al., 2009a). In contrast with the latter study, the narrower line width and Lorentzian line shape in the present study point to weak residual dipolar interactions and thus higher mobility of water, because the proton dipolar coupling is the major source of broadening. The broad peak at ca. 8 ppm can arise from interlayer water surrounding the $Na^+$ in the interlayer space of the smectite layers. In general, the presence of water and hydroxide signals is in a good agreement with the FTIR data reported above.

Table 4-5. Fit data for ^{1}H NMR (14 kHz MAS) spectra, where [1]$\delta$ is isotropic chemical shift ($\pm$ 0.1 ppm)

| | Exp. No: | [1]H chemical shifts | | | | Relative intensities, % |
|---|---|---|---|---|---|---|
| **RTI** | 30 | - | - | 2.55 | - | |
| **RT3** | 31 | 4.5 | 4.2 | 3.1 | 2.1 | 25:33:19:23 |
| **RT3 Na** | 32 | - | - | 3.2 | 2.0 | 68:32 |
| **RT3 Sr** | 33 | 4.5 | 4.2 | 3.2 | 2.0 | 30:31:15:24 |
| **RT3 Li** | 34 | - | 4.2 | 3.0 | 2.0 | 55:20:25 |

## 4.1.7.4 ^{23}Na MAS (20 kHz) NMR

The ^{23}Na NMR spectra of RT1 and RT3 exhibit at least three major components, while in the spectrum of RT2, only two components are resolved due to the very strong line broadening (Figure 4-17(e) and Table 4-6. The well-resolved signal at the low-field side (positive ppm values) characterised by a $\delta$([23]Na) value of ca. $-5$ ppm, a $C_Q$ value of 1 MHz, $\eta$ of 0.5 and narrow line broadening is attributed to Na^{+} fixed in-between the margarite tetrahedral sheets according to the literature data (Site I, green line in Figure 4-17(e)) (Jakobsen et al., 1995). The deviations in both $\delta$([23]Na) and $C_Q$ for RT2 point to changes in the local electron environment around the sodium atom in RT2 the margarite sheets, while the increase of its line width (EM) indicates greater disorder in comparison to the other samples.

The high-field broad line represents a superposition of the components with more pronounced quadrupolar characteristics, in which the strength and distribution of quadrupolar interactions point to symmetry and ordering in the local sodium environment. Site II at ca. $\delta$([23]Na) = $-7$ ppm possesses a large $C_Q$ of ca. 2.8 MHz (grey line in Figure 4-17(e)), indicating even larger deviations from the spherical symmetry around a sodium atom in RT2 and RT3. The higher EM value informs about structural inhomogeneity and disorder, which has been significantly improved in Sample RT3. Site III (blue line in Figure 4-17(e)) is characterised, in general, by a $\delta$([23]Na) value of ca.

−13 ppm and a $C_Q$ value of 1.2 - 1.5 MHz. According to the data reported for Beatrix rectorite (Jakobsen et al., 1995), the high-field broad line giving rise to Sites II and III may result from overlap between $Na^+$ fixed between the paragonite tetrahedral sheets and exchangeable $Na^+$. In addition, a very weak signal (lilac line in Figure 4-16(e)) at ca. 1 ppm and a $C_Q$ of 2.2 MHz (up to 5 % of total intensity) is visible in RT1 and RT3.

Table 4-6. Major components in the ^{23}Na MAS NMR spectra with their relative integral intensities (± 2 %) and assignment

| Sample | Spectral intensity, % | | | | Ratio Site I: Site II |
|---|---|---|---|---|---|
| | Site I | Site II | Site III | Site IV | |
| | $^{23}\delta$ =-5.1 ppm | $^{23}\delta$ =-7.9 ppm | $^{23}\delta$ =-13.1 ppm | $^{23}\delta$ =1.2 ppm | |
| RT1 | 31 | 26 | 37 | 5 | 1:0.8 |
| RT2 | 27 | 37 | 36 | - | 1:1.4 |
| RT3 | 15 | 32 | 51 | 2 | 1:2.2 |
| Assignment | Mica interlayer $Na^+$ fixed between margarite sheets | $Na^+$ fixed between paragonite sheets | Smectite interlayer $Na^+$ exchangeable in smecte interlayer | n.a. | |

In the literature, the narrow [23]Na peak at ca. 0 ppm is attributed to trapped $Na^+$ ions in symmetric cavities created by a mica-type stacking or to the non-exchangeable part of the sodium interlayer cations (Möller et al., 2010). In contrast to that work, the quadrupolar interactions for this peak are not averaged out, and they can tentatively be assigned to a variety of Na-containing mica in the samples under study. Although for accurate assignment additional experiments are required, the assumption is that Site III with smaller quadrupole parameters results from more mobile exchangeable $Na^+$ in the smectite interlayer. This allows estimation of the ratios of $Na^+$ fixed between the margarite and paragonite tetrahedral sheets, which are found to be 1:0.8, 1:1.4 and 1:2.2 for RT1, RT2 and RT3, respectively. Exact quantification for RT2 is impossible at this stage due to strong signal overlapping. The effect of interlayer composition on the distribution of $Na^+$ for various exchanged forms of rectorite is beyond the scope of the present study.

In summary, the NMR results indicate that two Al sites are present in all rectorites (Al-VI and Al-IV). The local structure around Al does not vary upon modification and a high degree of Al substitution is indicated. Structural inhomogeneity and disorder are indicated for RT2 rectorite. The relative concentrations of $Na^+$ fixed between the margarite and paragonite layers differ in the three rectorite samples.

## 4.1.8 XRF

The average chemical composition of purified rectorite (RT3) determined by XRF analysis is listed in Table 4-7. The components in the samples with the highest rectorite content were recalculated, adjusting for mineral impurities, and used as a basis to calculate the mean structural formula. Trace concentrations of $P_2O_5$, $Cr_2O_3$, ZnO and BaO were considered to be due to matrix contamination and omitted from further calculations. The CEC, estimated from the XRF-determined compositions of the purified and the various RT3 cation-exchanged samples, was $45 \pm 7$ mEq/100 g. Such a value is expected if alternate interlayers are of the montmorillonite type. The compositions of the fixed and exchangeable interlayers were determined from the $Na^+$ and $K^+$ cation-exchanged rectorite forms under the assumption that all exchangeable cations reside in the swelling interlayer region. The exchangeable interlayer composition is ($Na_{0.10}Ca_{0.13}$) with a layer charge of $-0.36$ per $O_{20}(OH)_4$, and the fixed interlayer contains ($Na_{0.66}Ca_{0.31}K_{0.13}$) with a total charge of $-1.41$.

The summarised formula derived from the ignited composition (dry basis) based on $O_{20}(OH)_4$ is:

$$(Na_{0.76}Ca_{0.44}K_{0.13})[Al_{4.03}Ti_{0.03}(Fe, Mg)_{0.006}](Si_6Al_2)O_{20}(OH)_4.nH_2O \qquad (4\text{-}1)$$
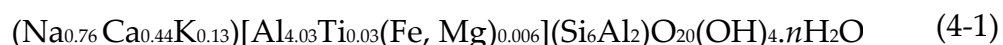
The structural formula indicates that monovalent $Na^+$, $K^+$ and divalent $Ca^{2+}$ cations are available in the interlayer of natural rectorite. The fixed interlayer space (mica interlayer space) contains proportionally dominant $Na^+$ and $Ca^{2+}$ and minor $K^+$. The exchangeable smectite interlayer contains almost equal $Na^+$ and $Ca^{2+}$ ions. This

elemental distribution implies that the mica layer is represented by paragonite (Na-mica)-margarite (Ca-mica with minor Na) series, rather than muscovite (K-mica). Potassium is most probably contributed by paragonite which may contain up to 0.15 % K (Rieder et al., 1998). Furthermore, this composition suggests a 1:2.5 margarite-to-paragonite distribution. This agrees well with the margarite-to-paragonite distribution of 1:2.2 in RT3 estimated from the ^{23}Na NMR data.

Table 4-7. Major element concentrations of rectorite determined by X-ray fluorescence spectroscopy, recalculated for concentrations of impurities compared to published data (von Rahden, 1994). The reported chemical compositions represent the mean values for five purified rectorite samples (RT3).

| | Composition, wt.% | | |
|---|---|---|---|
| Oxide | Average | Recalculated[a] | Literature[b] |
| $SiO_2$ | 50.09 ± 0.38 | 49.56 | 51.02 |
| $TiO_2$ | 0.27 ± 0.01 | 0.310 | |
| $Al_2O_3$ | 37.57 ± 0.36 | 42.27 | 40.69 |
| $Fe_2O_3(t)$ | 0.04 ± 0.02 | 0.049 | 0.40 |
| MgO | 0.01 ± 0.00 | 0.012 | 0.57 |
| CaO | 2.94 ± 0.07 | 3.388 | 5.33 |
| $Na_2O$ | 2.81 ± 0.03 | 3.25 | 1.68 |
| $K_2O$ | 0.95 ± 0.07 | 0.87 | 0.31 |
| $P_2O_5$ | 0.02 ± 0.00 | 0.023 | |
| $Cr_2O_3$ | 0.05 ± 0.05 | 0.058 | |
| $V_2O_5$ | 0.02 ± 0.00 | 0.021 | |
| BaO | 0.05 ± 0.01 | 0.059 | |
| ZnO | 0.02 ± 0.01 | 0.024 | |
| $ZrO_2$ | 0.01 ± 0.00 | 0.010 | |
| SrO | 0.08 ± 0.01 | 0.096 | |
| LOI | 5.40 ± 0.04 | | |
| Dry basis | 94.95 ± 0.61 | | |
| Total | 100.14 ± 0.62 | | 100.00 |

[a] Recalculated (ignited basis) adjusting for impurities based on XRD mineral composition: rectorite 91.45 wt.%; quartz 5.95 wt.%, mica 1.66 wt.% and chlorite 1.52 wt.%.
[b] Ignited-weight basis, (von Rahden, 1994).

The expandable layer charge of −0.36 is predominantly due to tetrahedral substitution; this is characteristic of beidellite rather than montmorillonite in which the net layer charge arises from octahedral substitutions. In the dioctahedral 2:1 structure, the four octahedral sites are dominantly occupied by $Al^{3+}$ with minor $Ti^{4+}$, $Fe^{3+}$ and $Mg^{2+}$. Based on chemical data, the distribution of tetrahedral and octahedral Al is proportionally 1:2. These conclusions support the XRD identification of beidellite by the Greene-Kelly test (Greene-Kelly, 1952) and the identification of paragonite by the thickness of the mica layer of 9.65 Å as opposed to the muscovite layer thickness of 10.00 Å. Hence, Beatrix rectorite identifies with Na-Ca-rectorite, which conforms well with previously reported XRF data for rectorite (Jakobsen et al., 1995; Lausen et al., 1999; von Rahden, 1994).

Smectites and other 2:1 layered structures commonly exhibit heterogeneous charge distribution among the different layers (Lagaly and Beneke, 1991). In mixed-layer structures heterogeneity is further emphasised by the existence of two types of 2:1 layer. Therefore the structural formulae derived from the major element concentrations as given above represent average compositions of the layers.

## 4.2    Characterisation of organically modified rectorite

Modified complexes of rectorite with long-chain dodecyldimethyl-ammonium chloride (DCC10), dialkyldimethylammonium chloride (DCC18) and hexadecyltrimethylammonium chloride (SCC16) were characterised by XRD, FTIR spectroscopy and TGA. The surfactant loading of 50 % excess was based on a CEC of 45 mEq/100 g. The XRD patterns (Figure 4-19) show well-defined peaks as the surfactant was homogeneously intercalated between the rectorite layers. The expansion of the interlayer with the double-chain surfactants was 3.60 nm and 3.70 nm for DCC10 and DCC18 respectively, while the d-spacing corresponding to single-chain intercalation with SCC16 was 3.20 nm. The shift of the basal spacing is due to the exchange and adsorption of larger organic molecules into the smectite layer in the

rectorite structure. Homogeneous intercalation implies an increase in the organophilic properties of rectorite at the expense of its hydrophilic nature, and suggests that adsorption is feasible and can be used as a precursor step to the subsequent adsorption of non-polar organic compounds.

The FTIR spectra of raw rectorite and rectorite modified by SCC16, DCC10 and DCC18 in the middle IR region 400–4000 cm$^{-1}$ are plotted in Figure 4-20. Table 4-2 lists the band positions and assignments together with some relevant published data for comparison. Expected similarities in the spectra are well displayed in the regions typical of neat rectorite. The well-resolved bands in the low-frequency range from 450 cm$^{-1}$ to 1 200 cm$^{-1}$, typically characteristic of a phyllosilicate structure, are present in both the raw and modified rectorite spectra.
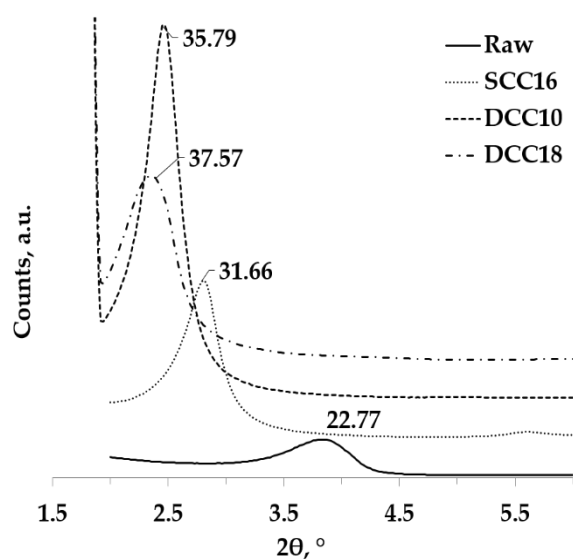


Figure 4-19. Basal spacing $d_{001}$, Å of the rectorite-organic complexes with reference to raw rectorite
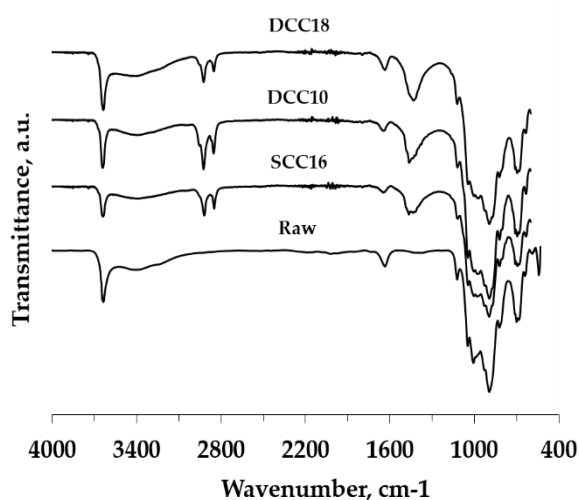
Figure 4-20. FTIR spectra of raw rectorite and the DCC10, DCC18 and SCC16 intercalated forms

The FTIR spectra of the organically modified rectorite contain additional absorbance peaks characteristic of the infrared active vibrations of the main functional groups of the surfactant. A pair of sharp bands between 2820 cm$^{-1}$ and 2970 cm$^{-1}$ is ascribed to the symmetric and asymmetric stretching vibrations of CH$_2$ groups of the alkyl chains,

of which the bending vibrations are visible around 1460 cm$^{-1}$ (Table 4-2). The former two were stronger with the DCC10 chain and proportionally weakened for DCC18, being the weakest for the single-chain SCC16 intercalated rectorite. The maxima of CH$_2$ bending vibrations in the range 1440–1480 cm$^{-1}$ gradually shifted towards higher frequencies from 1442 cm$^{-1}$ for DCC18 through DCC10 (1468 cm$^{-1}$) to 1470 cm$^{-1}$ for SCC16 intercalated rectorite. There is also slight movement of the O-H stretching band in the region between 3800 and 3200 cm$^{-1}$ in the SCC16 and DCC10 spectra to 3644 cm$^{-1}$ compared to 3640 cm$^{-1}$ of the raw and DCC18 modified rectorite. Higher frequency usually reflects a higher energy state of the OH groups and an increase of 1 cm$^{-1}$ corresponds to an energy increase of 2.859 cal/mol (Kodama, 1966).

Generally, the thermal behaviour of alkyl ammonium-modified rectorite resembles the decomposition pattern of neat material (Figure 4-21). The deviations are strongly affected by the surfactant chain length and initial loading. Peak shifts and variations in relative intensity proportions reflect the effect of modification on the structure and consequently its influence on the water-loss reactions.

With 50 % excess loading of DCC10 and DCC18 ions, the TG/DTG results of the double alkyl chain organorectorite show a small peak at 53 °C identical to that in the neat rectorite and assigned to the removal of loose water. The first mass loss calculated at 150 °C was 1.30 % for DCC10 and 1.44 % for DCC18. This is lower compared to the raw material and reflects the change of surface properties from hydrophilic to hydrophobic as a result of the exchange. These values are slightly lower than observations reported in the literature (Li and Jiang, 2009) for a higher surfactant loading of 1.56 CEC and a mass loss of 2.1 %. The TG curve of DCC10-intercalated rectorite shows three additional peaks at 253 °C, 293 °C and 427 °C. For DCC18-modified material, corresponding peaks occurred at 250 °C and 421 °C.

The second mass loss in the range of 258–431 °C for DCC10 and 295–454 °C for DCC18 is attributed to the combustion of the adsorbed surfactants. At more elevated

temperatures the last weight change is a result of the loss of structural OH groups leading to full dehydroxylation. The DTG patterns of both double alkyl chain organorectorites confirmed this change with a peak at 730 °C. Proportionally, this peak is less intense here than in the single-chain form and the neat rectorite.

The derivative curve of rectorite intercalated with a single alkyl chain (SCC16) shows two small peaks at 46 °C and 122 °C, accounting for a mass loss of 2.19 % due to the removal of adsorbed water. This value is intermediate compared to 3.0 % at 1.25 CEC and 1.8 % at 1.75 CEC for single-chain modifications reported previously (Li and Jiang, 2009). The mass loss due to decomposition of the surfactant was recorded between 331 and 531°C, which is confirmed in the DTG plot by the peak at 425 °C. The dehydration peak at 717 °C is as strong as in the neat sample, marking the release of the structural OH groups and the associated mass loss.

The two-step decomposition of alkylammonium intercalated in the rectorite interlayer at 50 % excess loading, irrespective of surfactant configuration, indicates the existence of two types of bonding mechanism of intercalation (Li and Jiang, 2009). The larger mass loss in the temperature range 200 °C–350 °C and the smaller loss in the range 350 °C–500 °C suggest that the intercalation occurred mainly by hydrophobic interactions and to lesser extent by cation exchange. The FTIR results support these observations with the location and shifts of the CH2 stretching bands at around 2850 cm$^{-1}$ and 2930 cm$^{-1}$. This conforms to previous findings (Lee and Kim, 2002) for the expansion of smectite by hexadecyltrimethylammonium with loading above CEC of the smectite, where adsorption via hydrophobic bonding dominates the cation exchange.
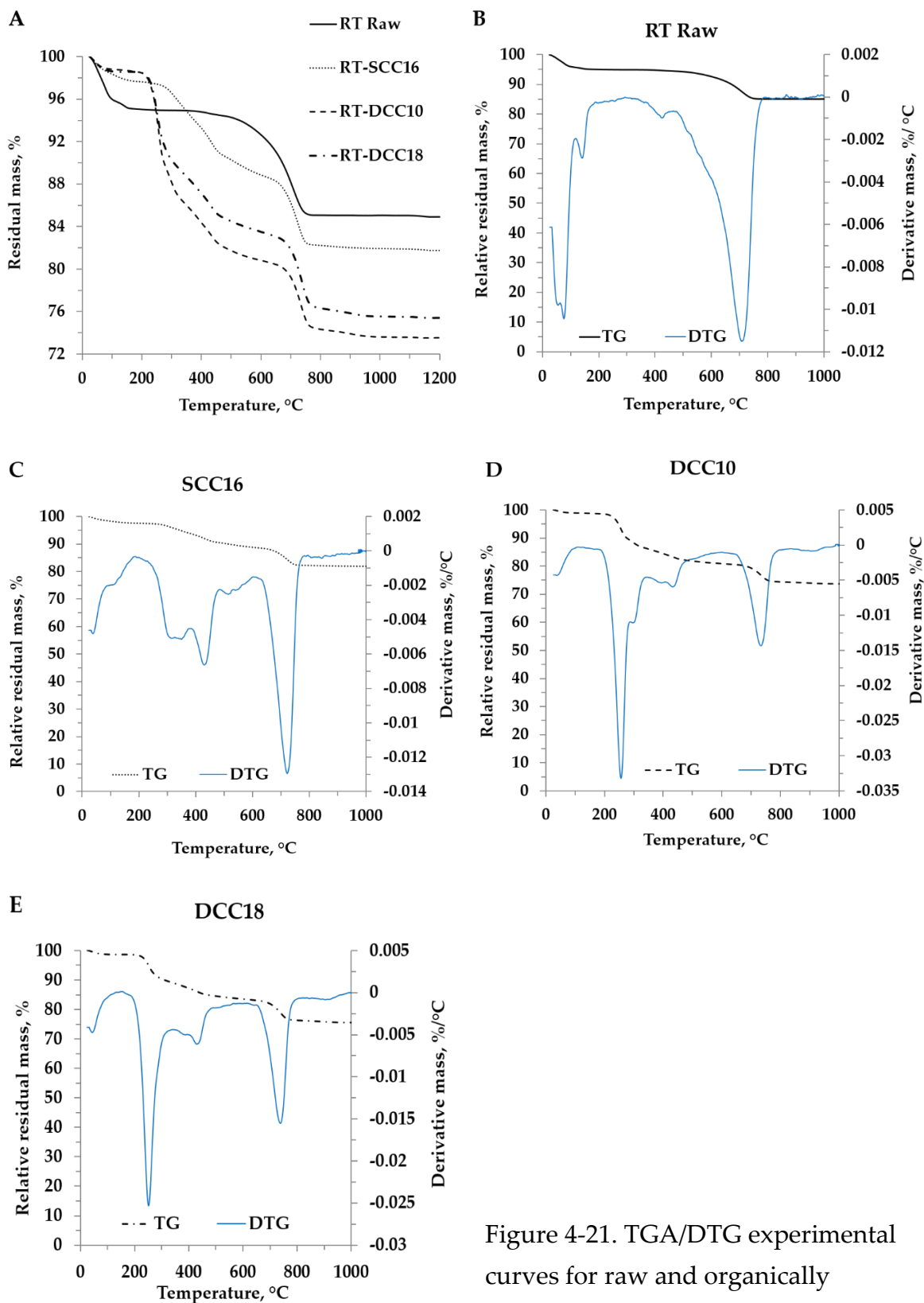
Figure 4-21. TGA/DTG experimental curves for raw and organically modified rectorite

## 4.3    Rectorite clay films (RecF)

The primary aim of this study was to find the best rectorite clay derivative (via ion exchange) and to optimise the preparation method (slurry-solids content, ultrasonication conditions, etc.) for maximum strength or stiffness of the cast inorganic films. In this process a large number of experiments (246) were conducted. The experimental conditions, and the properties of the resultant films, are provided as Appendix III (Tables: Rectorite-only films dataset). This dataset lists the physical properties of the particle suspensions employed, the processing conditions and the tensile properties of the cast films that were obtained.

### 4.3.1  Processing conditions and properties of the clay suspensions

For each ion-exchanged clay sample, the film that featured the best mechanical properties, and the procedures that were used to prepare it, were identified. Additional measurements were performed on the parent slurry as well as the resultant films. Table 4-8 shows the processing conditions and the physical properties of the corresponding clay suspensions, together with the pH, $\zeta$-potential and number mean particle size. An attempt is made to link the film with the best mechanical properties to the process conditions that made them possible.

Upon casting, the divalent suspensions settled relatively quickly and at similar rates. However, those from the purified neat material and the monovalent-exchanged samples formed more-or-less viscous gels at the higher solids loadings. The particle size distributions of all the suspensions featured moderate to broad polydispersity indices (PDI > 0.1) for which the number mean particle diameter ($d$) is reported in Table 4-8.

The neat and monovalent rectorite suspensions produced stable colloidal systems with $\zeta$-potential values below –30 mV. Lithium- and sodium-containing dispersions with $\zeta$-potential values of –52 mV and –48 mV respectively did not settle before full

evaporation. These films also took a longer time to dry. The divalent suspensions showed electric potential shifts towards less negative values, i.e. above –30 mV where agglomeration typically commences. This is supported by the larger mean particle sizes listed in Table 4-8, and the experimental observation that they had a higher tendency to flocculate. The size of the exchangeable interlayer cation also had an effect on the suspensions' flocculation rate. Cations larger than $Na^+$ exhibited a progressively more unstable suspension which readily re-aggregated after dispersion. The neat rectorite suspensions with mixed Na-Ca-ion interlayers showed stability similar to that of the monovalent rectorite modifications. The RT1 suspension featured a lower ζ-potential, probably due to the higher pH of 8.85 caused by the presence of calcite as impurity.

Table 4-8. Processing conditions and physical properties of slurries that yielded rectorite films with the highest mechanical performance. In all cases the solids content was 1.0 g clay/100 ml and sonication time was 30 min (except for RT1 where it was 5 min).

| Cation | Stirring time | pH | ζ-potential | d (Number mean) |
|--------|---------------|-----|-------------|-----------------|
|        | h             |     | mV          | mm              |
| Li     | 0             | 9.62 | -52.3 ± 0.9 | 0.31 ± 0.16 |
| Na     | 4             | 8.58 | -48.5 ± 0.3 | 0.23 ± 0.01 |
| NH4    | 4             | 7.10 | -38.7 ± 1.8 | 0.62 ± 0.17 |
| K      | 4             | 8.8  | -43.7 ± 0.3 | 0.66 ± 0.02 |
| Cs     | 0             | 5.50 | -31.4 ± 1.6 | 0.70 ± 0.04 |
| RT1    | 24            | 8.85 | -34.8 ± 0.4 | 0.57 ± 0.23 |
| RT2    | 24            | 6.80 | -46.5 ± 1.7 | 0.19 ± 0.01 |
| RT3    | 4             | 6.85 | -47.6 ± 0.2 | 0.21 ± 0.05 |
| Mg     | 24            | 8.22 | -20.6 ± 2.5 | 1.12 ± 0.60 |
| Ca     | 4             | 6.30 | -25.9 ± 0.9 | 1.09 ± 0.07 |
| Sr     | 0             | 6.20 | -27.2 ± 0.3 | 0.89 ± 0.13 |
| Ba     | 0             | 6.80 | -30.8 ± 0.8 | 1.17 ± 0.09 |

There is a distinct positive correlation for the monovalent rectorite modifications, i.e. the ζ-potential increased with increases in pH. However, the Mg-rectorite, with pH 8.2, dropped towards lower negative values. These results indicate a strong

120

dependence of the electrostatic behaviour of rectorite colloidal systems on the ionic composition and is in agreement with previous reports for Na- and Ca-forms of smectite (Chorom and Rengasamy, 1995; Kaya and Yukselen, 2005). It is interesting to note how the largest ions of both groups, i.e. monovalent $Cs^+$ and divalent $Ca^{2+}$, $Sr^{2+}$ and $Ba^{2+}$, had $\zeta$-potentials approaching the critical system stability boundary value, bordering the lowest values for the former and the highest values for the latter at the same clay concentrations and pH below 7.0. These results suggest that the net negative charge is affected by the pH of the suspensions and that it plays a role in the behaviour and stability of rectorite dispersions.

### 4.3.2 Characterisation and properties of the clay films

The tensile properties of the clay films from neat rectorite and ion-exchanged rectorite modifications are presented in Figures 4-22 and 4-23, and Table 4-9. Figure 4-22 shows examples of the stress-strain curves for the stronger monovalent, divalent and mixed valence rectorite films. In all cases the strain at break was very small, seldom exceeding 2 %. Noteworthy (from visual observations) is the fact that many samples failed by developing tears that started either at an edge defect or right at the end where the sample was gripped. This means that the intrinsic mechanical properties were not achieved. Rather, the measured values were notably influenced by the numerous defects present in the cast films, by handling during testing, and perhaps even by small alignment errors when they were clamped into the tester. Nevertheless, the measured values for tensile strength and Young's modulus compare quite favourably with the values featured by polymer films.

Among the large set of films with thickness ranging up to 150 μm, those with a tensile strength exceeding 5 MPa were less than 65 μm thick. The films that featured the highest strengths invariably had a thickness less than 30 μm. For neat rectorite films the maximum measured tensile strength varied from 12 - 34 MPa and the modulus values from 19 - 50 GPa. Those from the ion-exchanged modifications ranged from 8

- 44 MPa with modulus 18–56 GPa. The films obtained from monovalent cation forms performed notably better, ranging from 13 - 44 MPa and 43 - 56 GPa, than those made with rectorite modified with divalent ions (tensile strength 8 - 23 MPa and modulus 18–25 GPa) (Table 4-9). The films made from the $NH_4$-Rec also showed excellent tensile properties, with strength and modulus values reaching 44 MPa and 47 GPa respectively.
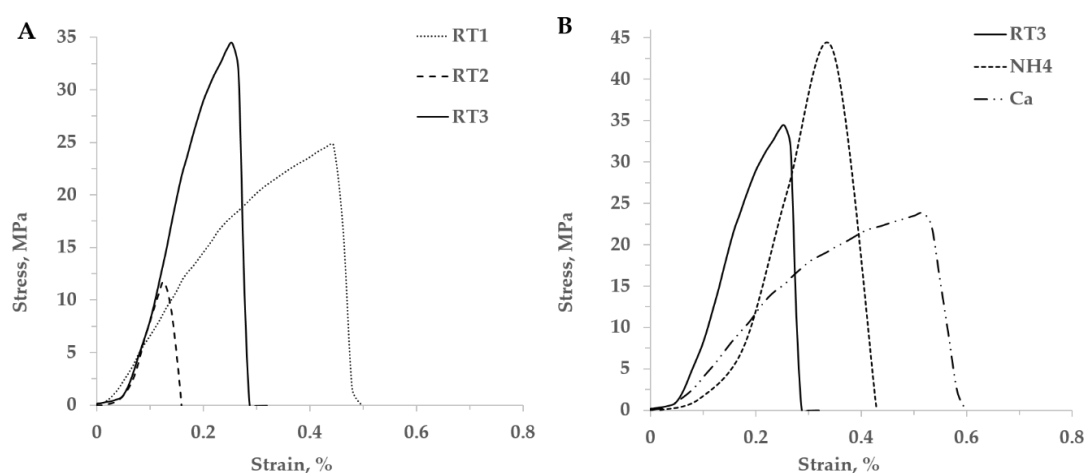


Figure 4-22. Representative stress-strain curves for rectorite films prepared from (A) the three purified rectorite samples, and (B) a comparison of the films with the highest performance from neat, monovalent and divalent exchanged rectorite

The films with the best tensile properties did not necessarily originate from suspensions prepared under the same dispersion conditions. However, the dispersion regime of sonicating for 30 min with subsequent stirring for 4 h proved most effective for producing strong films from each of the three groups – monovalent, divalent and neat rectorite. The exceptions are RT1 where 5 min sonication followed by 24 h stirring, and RT2 and $Mg^{2+}$-films where 30 min sonication followed by 24 h stirring, yielded the best results. Dispersions of $Li^+$- and $Cs^+$-based films and divalent $Sr^{2+}$ and $Ba^{2+}$ proved more suited to casting after 30 min sonication without stirring.

The data in Figures 4-23 and 4-24 and Table 4-9 show considerable scatter in both the strength and the modulus characteristics of the rectorite films. There is variation not only between films from different rectorite modifications, but also within ion-

exchanged samples, despite all the attempts made to exercise strict control over the processing parameters used in the preparation.
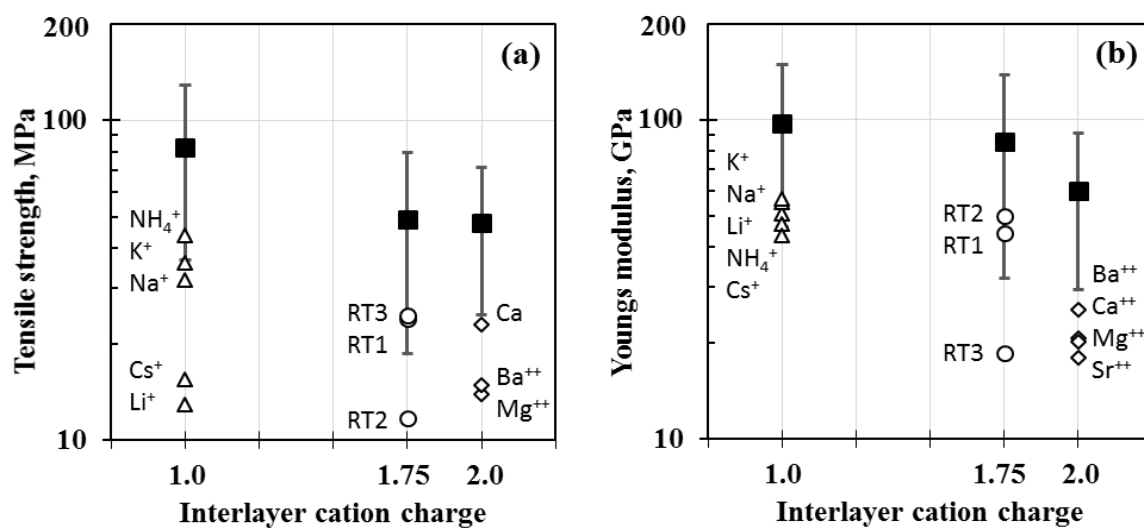


Figure 4-23. Tensile strength and Young's modulus of films from neat and cation-exchanged rectorite. The black square symbols indicate the projected maximum values possible, with the error bars show the 95 % confidence intervals. The open symbols indicate actual maximum values measured.
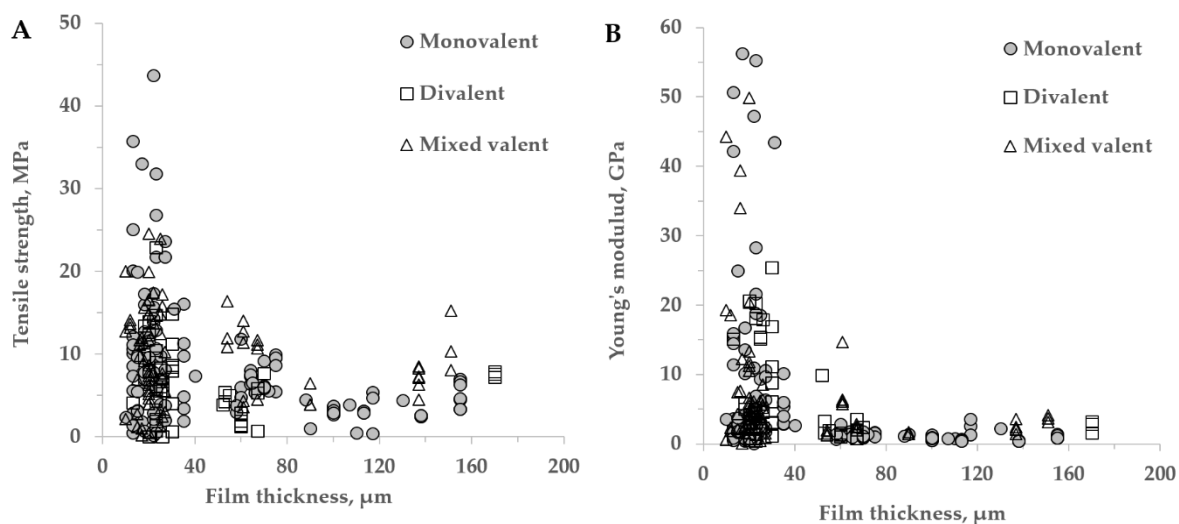


Figure 4-24. Film thickness and the mechanical performance of rectorite films (based on 246 measurments)

Table 4-9. Mechanical and physical properties of the best rectorite-derived clay films. The maximum tensile properties (instead of average values), together with the standard deviation based on all samples measured, are indicated.

| Cation | Film thickness | d-spacing | Crystallite size | BET | Tensile strength | Young's modulus |
|--------|----------------|-----------|------------------|-----|------------------|-----------------|
| | $\mu m$ | nm | nm | $m^2g^{-1}$ | MPa | GPa |
| Li | 23 | 2.23 | 6.8 | 259 | $12.9 \pm 4.9$ | $50.7 \pm 11.7$ |
| Na | 23 | 2.19 | 10.8 | 163 | $31.8 \pm 7.1$ | $55.3 \pm 10.1$ |
| $NH_4$ | 22 | 2.15 | 13.7 | 354 | $43.7 \pm 8.3$ | $47.3 \pm 18.0$ |
| K | 17 | 2.1 | 6.5 | 251 | $35.7 \pm 10.9$ | $56.3 \pm 16.3$ |
| Cs | 25 | 2.16 | 12.6 | 139 | $15.5 \pm 5.3$ | $43.4 \pm 15.3$ |
| RT1 | 18 | 2.16 | 8.1 | 259 | $23.9 \pm 5.7$ | $44.3 \pm 10.0$ |
| RT2 | 20 | 2.34 | 6.9 | 115 | $11.7 \pm 3.4$ | $49.8 \pm 17.3$ |
| RT3 | 23 | 2.28 | 5.7 | 208 | $34.4 \pm 7.9$ | $18.6 \pm 4.0$ |
| Mg | 20 | 2.37 | 9 | 184 | $13.9 \pm 4.6$ | $20.6 \pm 6.0$ |
| Ca | 22 | 2.38 | 8.6 | 128 | $22.9 \pm 6.8$ | $20.2 \pm 7.9$ |
| Sr | 30 | 2.32 | 9.2 | 169 | $8.0 \pm 2.9$ | $18.0 \pm 8.3$ |
| Ba | 30 | 2.16 | 11.2 | 176 | $14.9 \pm 2.5$ | $25.4 \pm 4.5$ |

Figure 4-25A illustrates the translucence of the clay films obtained from neat rectorite. The UV-Vis spectra of a 28 $\mu m$ ammonium-exchanged rectorite film is compared to that of an 8 $\mu m$ raw rectorite film in Figure 4-26. All films had an off-white colour with a subtle blue-grey tint and pearly lustre on the smooth underside. The films also displayed a noteworthy flexibility, allowing folding and bending. It was even possible to crease the thinner films that were made from raw and monovalent-exchanged rectorite (Figure 4-25(B)).
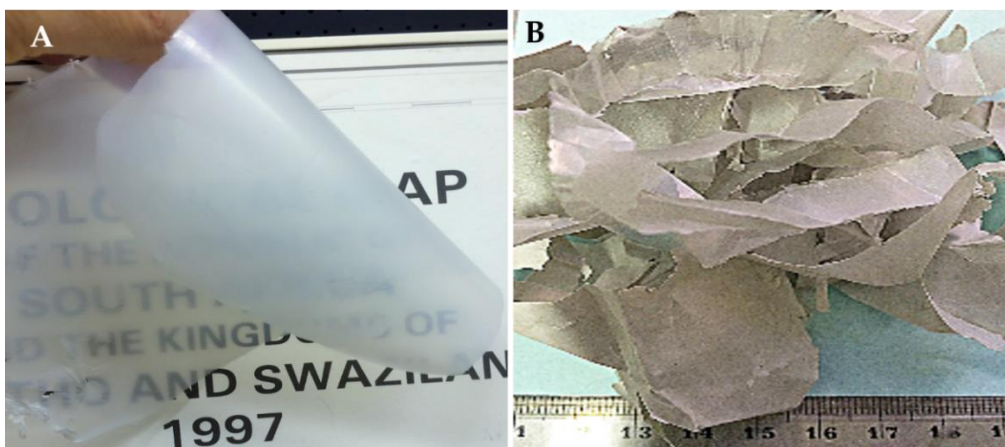
Figure 4-25. (A) Illustrates the transparency of translucent flexible films made from purified rectorite clay without the use of additives or binders, and (B) shows the flexing, bending and creasing of ribbon offcuts. The film thickness was 8.0 μm in both cases.
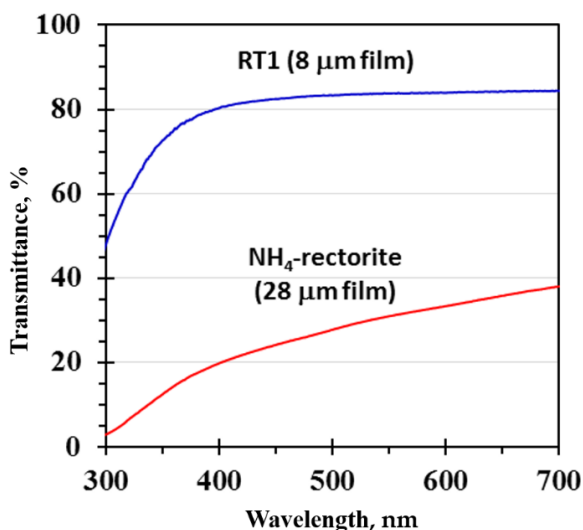


Figure 4-26. UV-Vis spectrum of an ammonium ion-exchanged film with a thickness of 28 μm and a raw (purified) rectorite film with a thickness of 8 μm

SEM micrographs of multilayer textured rectorite films are shown in Figures 4-27 and 4-28. The microstructure of the films is defined by more-or-less planar orientations of the flakes. Clay platelets are arranged in continuous layers with faces aligned sub-parallel to parallel to each other (face-to-face orientation) and to the casting surface. Figure 4-27 (A) and (B) shows polygonal clay platelets, with frayed edges that smoothly interconnect laterally in continuous layers.The platelets bend randomly and join neighbouring layers through edge-to-face contacts resulting in structured coherent sheets, flexible enough to withstand ripple formation (Figure 4-27 (C) and

(D). This geometrical model produces a random but somewhat complex network of cavities of variable shape and size. Nanoscale porosity is clearly observed in the high-resolution SEM micrographs of Figure 4-27 and 4-28. The high surface areas of the films, reported in Table 4-9, are also consistent with the presence of nanoporosity.
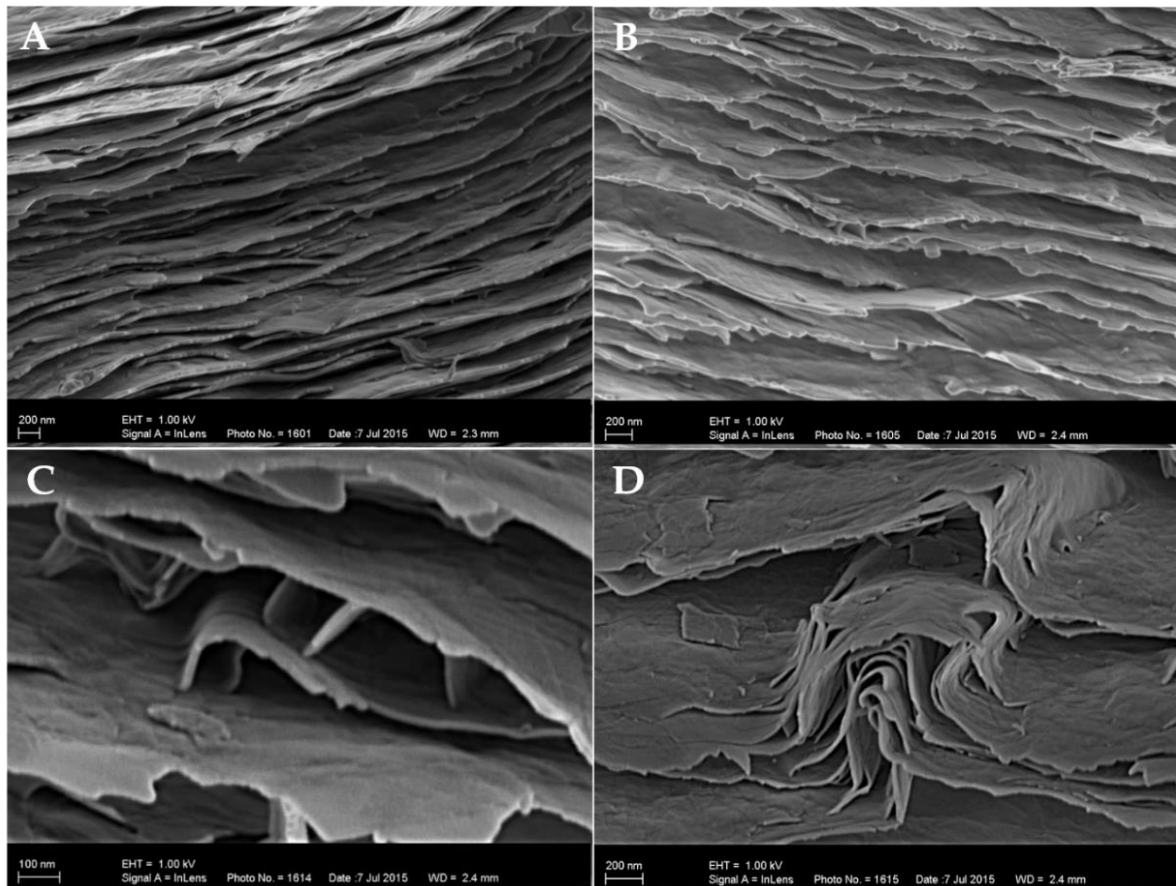


Figure 4-27. SEM micrographs of cross-sectional views of rectorite films from raw purified clay, showing the microstructures of (A&B) parallel layering and layer overlap; (A&B) face-to-face and (C) edge-to-face relationships, and (D) ripple formation

All films exhibit unevenly frayed fracture surfaces with a rather curved profile pattern. The upper sections of the films are usually made of lightly waved, finely layered parallel clay sheets which appear to be much more tightly stacked compared to the more ruggedly textured middle and base sections. This is an apparent artefact of size segregation that occurs during the gravity-driven settling of clay particles on drying.
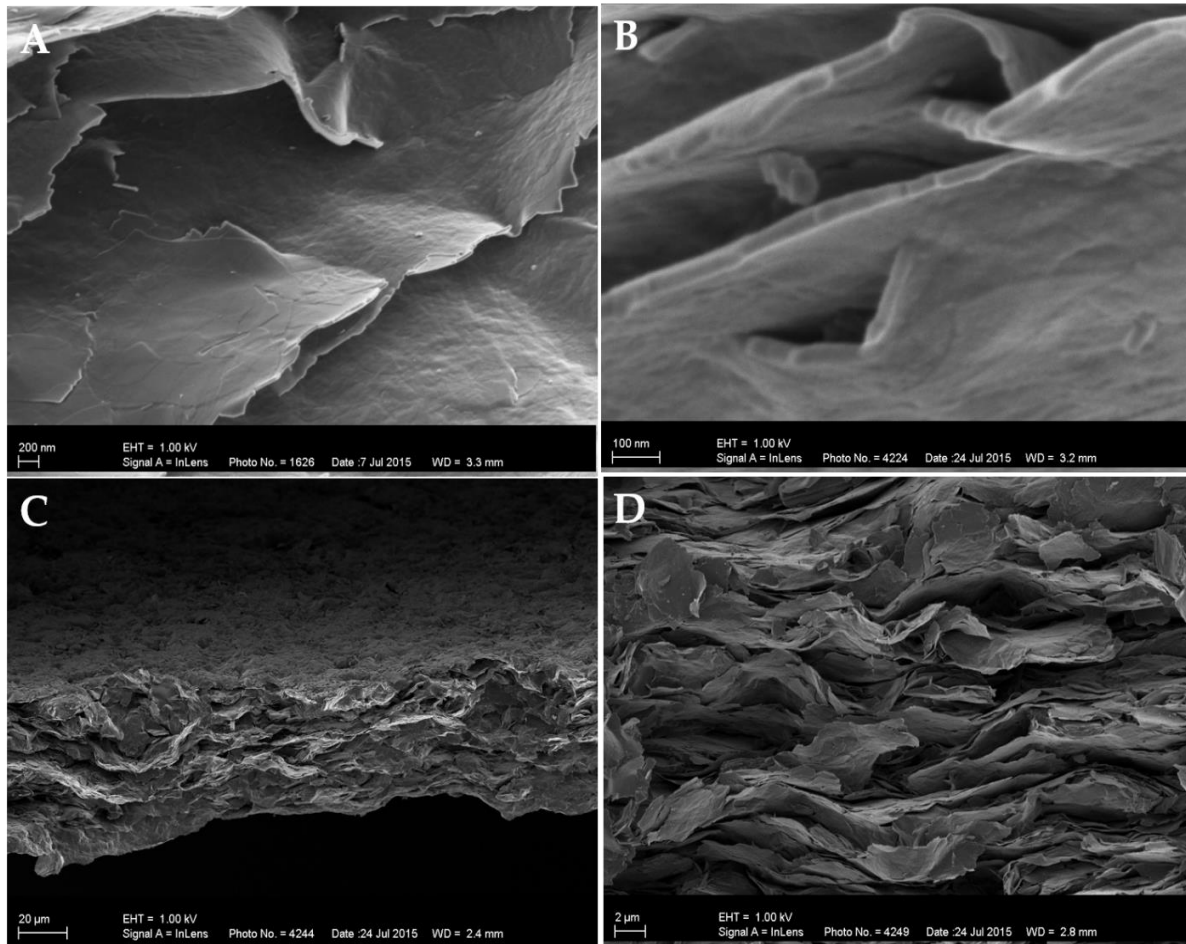
Figure 4-28. SEM micrographs showing a cross-section view of rectorite films from exchanged rectorite clay: (A) $Li^+$; (B) $Na^+$; (C) $Mg^{2+}$ and (D) $Ba^{2+}$

The top section is layered by nano-sized particles which are the last to assemble during evaporation. These flakes have the most favourable aspect ratio to align into compact sheets with the highest surface-to-volume ratio. This anisotropic texture is less pronounced in the raw and monovalent clay films, whereas the films from divalent rectorite feature large undulations throughout the profile with visibly more loosely assembled sheets (Figure 4-28 (C) and (D)). Similar effects of the interlayer content on the microstructure of clay films has been observed previously (Nam et al., 2009a) and is attributed to differences in the tendency of the ion modifications to delaminate and aggregate in aqueous suspensions. The texture of an anisotropic film has a direct effect on the performance characteristics, especially the damage tolerance. For instance, rectorite films with a thickness exceeding 20 µm drastically lose flexibility on bending

(Figure 4-24). Folding distorts the orientation of the sheets; this is typically initiated at the weakly textured base of the films made up of larger, loosely connected particles. Eventually this results in facile crack propagation and ultimately in mechanical failure (Figure 4-29).
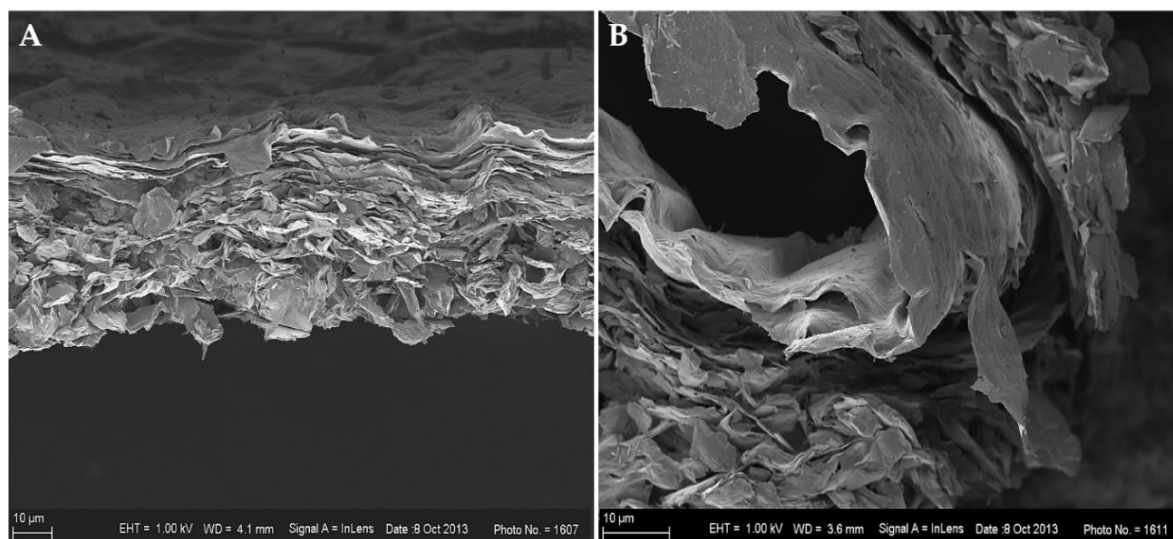


Figure 4-29. SEM micrographs of ammonia-modified rectorite film: (A) cross-section view of a film about 40 μm thick showing a finely layered top of about 10 μm and a random sheet arrangement through the rest of the profile; (B) continuous top layer of parallel clay platelets withstanding the banding of the film as opposed to the bottom layer, which is seen to be in the process of fracturing

The XRD plots of the films presented in Figure 4-30 provide further information on the microstructural organisation of the clay films. The strong first-order basal reflections indicate well-ordered laminated structures that complement well the SEM observations of oriented multi-layer films (Figure 4-27). Furthermore, evidence of preferred orientation is provided not only by the enhanced intensity, but also the second- and third-order peaks are prominent in the diffractograms of the films which is usually not possible for clay powders. Beatrix rectorite is a Na-Ca smectite-mica interstratified structure with a d-spacing between 2.18 and 2.22 nm, a mean crystallite size in the range 14–21 nm and 6–10 2:1 layers per tactoid (Atanasova et al., 2016). Basal spacing d(001) of 2.22 nm for neat Na-Ca-rectorite corresponds to one water-layer structure with an $Na^+$-$Ca^{2+}$ expandable interlayer content in the ratio of 3:4. A

128

reverse trend in the d(001)/d(002) intensity ratio is clearly observed in the diffractograms of the films, with transition from monovalent to divalent rectorite forms (Figure 4-30).
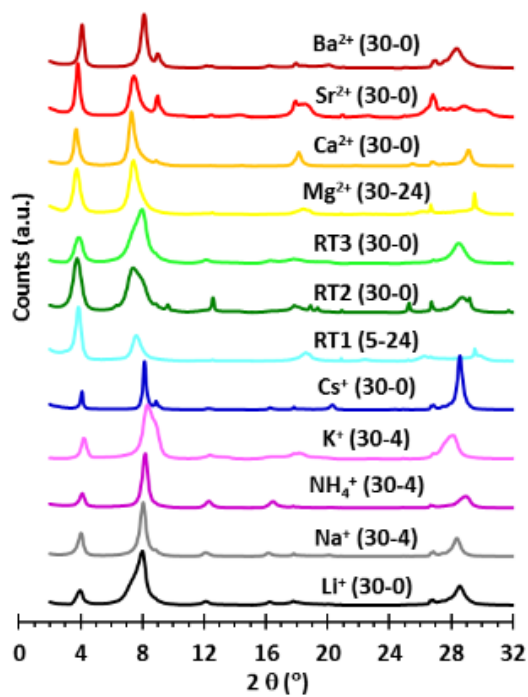


Figure 4-30. XRD profiles of films from purified neat Na-Ca-rectorite and exchanged rectorite modifications. Numbers in brackets behind the cation indicate the dispersion regime.

This is due to differences in the scattering efficiency of the monovalent and divalent atoms which is dependent on their electron configurations (Moore and Raynolds, 1997). The phenomenon has been used to determine the Na:Ca ratio in bi-ionic interlayer structures or other substitutions common in clay minerals using XRD data (Kodama, 1966b). One 2:1 layer of rectorite is about 2.20 nm thick, consisting of 0.96 nm and 1.30 nm mica- and smectite-type layers respectively stacked along the c-direction. The primary tactoids in the natural rectorite consist of up to ten 2:1 silicate layers and have a thickness of about 200 nm (Atanasova et al., 2016). The tactoid thickness in the films from neat rectorite and its exchanged modifications was estimated to range from two to six layers, suggesting the successful exfoliation and increased aspect ratio of the rectorite platelets. This is also supported by the very high

BET surface areas measured for the films (Table 4-9). A large surface area provides for enhanced inter-lamellar interaction, largely attributable to the nature of the interlayer cation.

### 4.3.3 Estimating the ultimate mechanical property values for rectorite films

The presently reported mechanical property measurements do not represent the intrinsic values that can potentially be attained. This is because of the many flaws and defects in the films caused by limitations in the preparation methods. The measurement process itself was flawed, including the way the samples were clamped. It was of interest to estimate limits for the ultimate material properties. This was attempted via a statistical analysis of the available experimental data as described in some detail in the Experimental Chapter (Chapter 3). First, a global fit of the tensile strength (or the Young's modulus) of the films was modelled and analysed using extreme value analysis (EVA) by means of the generalised extreme value (GEV) distribution (Beirlant et al., 2005; Reiss and Thomas, 2007). Parameter estimation was carried out using generalised maximum likelihood (gMLE) (Gilleland and Katz, 2016). The location and scale parameters of the GEV distribution were considered to be linear combinations of possible additional variables. In both cases, it was found that a significant improvement was observed when the interlayer cation was included as a variable in the model. The $p$-values corresponding to the significant categories for interlayer cation of the location and scale parameters of the fitted distributions were location = (0.0025371, 0.0025370) and scale = (0.0166080, 0.0448101), for tensile strength, and with location = 0.0235088 and scale = 0.0065562 for Young's modulus. The nature of the interlayer cation determines the interlayer charge. The data was therefore split into groups that contained monovalent cations (122 samples; dummy variable assigned = 0), divalent cations (48 samples; dummy variable assigned unity), and the mixed cation situation for the RT samples (77 samples; dummy variable = 0.75).

Table 4-10. Best values for tensile strength and Young's modulus obtained experimentally compared to projected values based on a statistical analysis of the data

| Cation type | Experimental[#] | Estimate[†] | 95 % lower CI | 95 % upper CI |
|---|---|---|---|---|
| **Tensile strength (MPa)** | | | | |
| Monovalent | 44 | 83 | 37 | 129 |
| Divalent | 23 | 48 | 25 | 71 |
| Mixed valent | 25 | 49 | 19 | 79 |
| **Young's modulus (GPa)** | | | | |
| Monovalent | 56 | 97 | 46 | 149 |
| Divalent | 25 | 60 | 29 | 91 |
| Mixed valent | 50 | 85 | 32 | 139 |

[#]Highest value actually measured. [†]Statistical projection for maximum attainable value.

Permutational multivariate analysis of variance (MANOVA), using distance matrices (Anderson, 2001; McArdle and Anderson, 2001), was performed to check whether the data split into these three sets according to the Interlayer Charge variables can be justified from a statistical point of view. The resultant $p$-value from this test was 0.007, which signifies an overall effect. This was followed up by the Kruskal-Wallis rank sum test (Hollander and Wolfe, 1973), for testing the individual effects, for which the results indicated that this was indeed the case for both tensile strength (p-value = 0.0019) and Young's modulus (p-value = 0.0004) as dependent variables, and with interlayer charge as independent variable. Secondly, a peak-over-threshold (POT) model was fitted to each of the six possible permutations in determining the maximum potentially attainable values for tensile strength and Young's modulus. Maximum likelihood estimation (MLE) was used to fit the exponential distribution to all the cases. The parametric bootstrap (Efron and Tibshirani, 1993) was then used in each case in deriving the 95 % upper confidence limits, which are listed in Table 4-10. The highest value actually measured in each case is also listed.

## 4.4    NH₄-rectorite-chitosan bionanocomposite films (NH₄-Rec/CS NCF)

The NH₄-Rec/CS suspensions produced stable colloidal mixtures with $\zeta$-potential values above 44 mV in the pH range 2.6–4.0. X-ray diffraction of oriented slurries showed that the clay structure was successfully exfoliated and intercalated by the polymer using the applied preparation methodology (Figure 4-31).

The X-ray diffraction data of the neat starting components NH₄-Rec and CS and selected composites is displayed in Figures 4-31 and 4-32. The neat NH₄-rectorite has a strong and sharp d(001) reflection at $2\theta$=4.12 ° (d=2.15 nm) and d(002) at $2\theta$=8.25 ° (d=1.07 nm). The XRD patterns of powdered chitosan featured two broad peaks around $2\theta$=10.65 ° (d=0.840 nm) and $2\theta$=20.06 ° (d=0.444 nm). Interestingly, the diffraction data obtained from the chitosan films showed more crystalline regions around $2\theta$=8.47 ° (d=1.042 nm), $2\theta$=11.55 ° (d=0.765 nm), $2\theta$=16.26 ° (d=0.544 nm), $2\theta$=18.30 ° (d=0.484 nm) and $2\theta$=23.04 ° (d=0.386 nm), suggesting sheet-like orientation in the films, attributed to parallel sheets of chains similar to chitin (Darder et al., 2003; Minke and Blackwell, 1978).
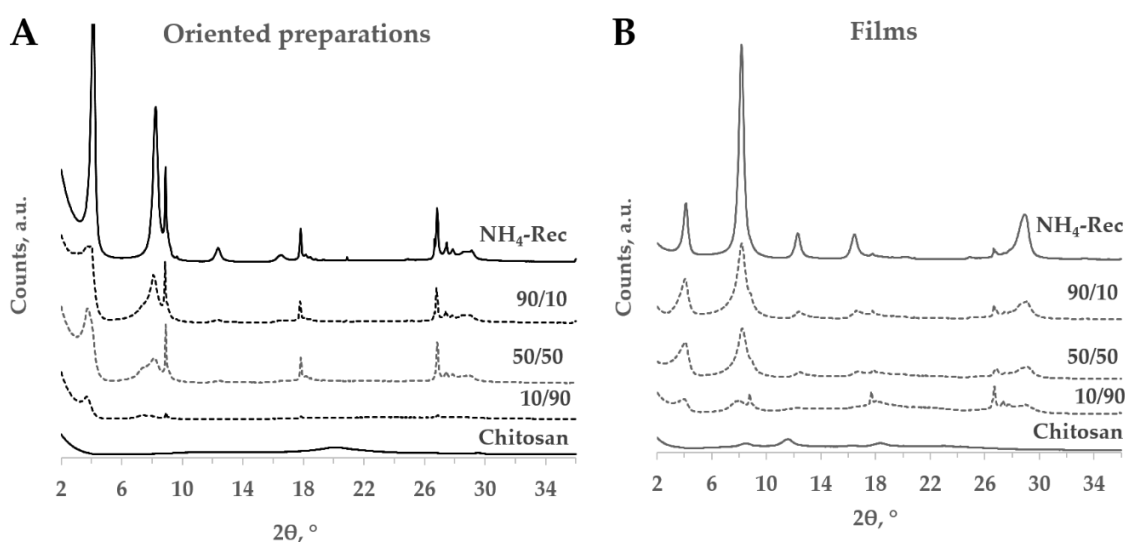


Figure 4-31. X-ray diffraction data for neat NH₄-Rec and chitosan (CS) and their derivative composites 90/10, 50/50 and 10/90 (Rec/CS); (A) glass slides; (B) films

With the addition of chitosan, the spacing of the $NH_4$-Rec/CS composites moved to lower angles, indicating continuous enlargement of the rectorite unit cell. The d-values between 2.15 and 2.19 nm for the $NH_4$-Rec/CS nanocomposites are consistent with the intercalation of a monolayer of chitosan in the interlayer space (Darder et al., 2003). Diffraction peaks from the expanding composite structure became broader and asymmetric (Figure 4-32), suggesting loss of regularity and layer orientation in the initial rectorite structure. However, even in compositions 10/90 $NH_4$-Rec/CS some of the original reflections of rectorite, although very broad, were still visible around the respective basal spacings (Figure 4-31B). The original structure of chitosan disappeared completely in the composite diffraction patterns from oriented slides of the dispersions and the films (Figure 4-31). These changes indicate that the rectorite sheets have been exfoliated and chitosan has intercalated into the interlayer space of rectorite with the increase of chitosan content and the corresponding decrease of clay. It also indicates that the presence of the rectorite interferes with the crystallisation of the bulk chitosan.
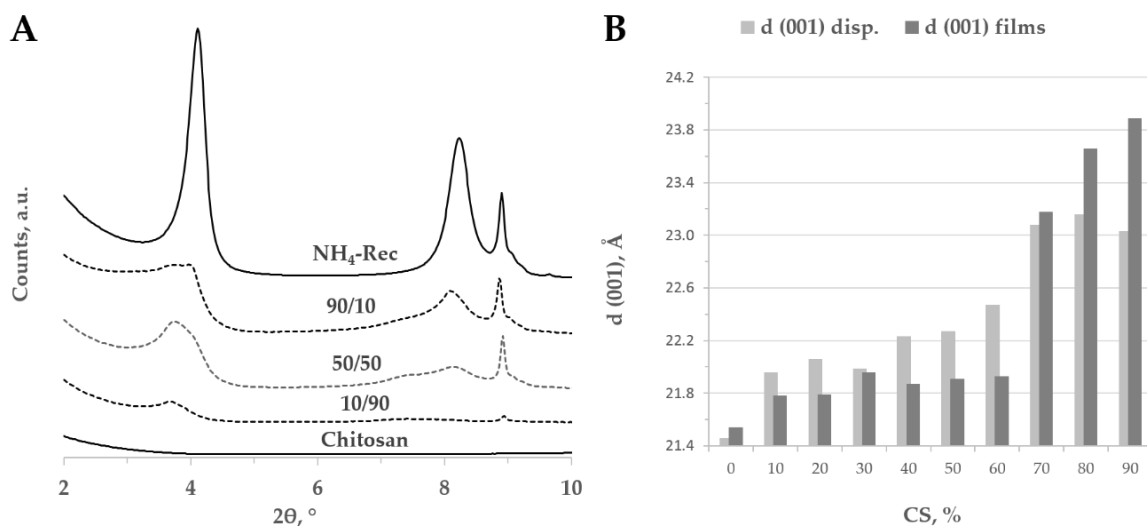


Figure 4-32. (A) X-ray diffraction data of neat $NH_4$-Rec and chitosan and their composite derivatives 90/10, 50/50 and 10/90 (Rec/CS); (B) migration of d(001) with increasing proportion of chitosan for dispersions and their respective films

The swelling of rectorite occurs at the smectite-type layer in its structure (Atanasova et al., 2016) and therefore defines similar exchange properties. The interlayer $NH_4^+$ ions in the smectite layer of rectorite are easily exchanged with the protonated $-NH_3^+$ cations from chitosan, resulting in partial to almost complete chitosan intercalation into the rectorite layers.

The FTIR spectra of neat $NH_4$-rectorite, chitosan and their derivative composites (range 90 % to 10 % in increments of 10 %) are presented in Figure 4-33. The FTIR spectra of purified rectorite and organically modified rectorite have been discussed in a previous communication on rectorite from this deposit (Atanasova et al., 2016). The composites' spectra resemble a combination of peaks featured in the spectra of the clay and chitosan. Characteristic peak maxima for both end-components appear to be drastically decreased at intermediate composition. As the proportion of rectorite/chitosan decreases, the composite spectra feature progressive broadening of the absorption bands, with relatively minor shifts in the peak positions attributed to reduced structural ordering and imperfections arising from organic interaction.

Apart from the vibrational bands of Si-O-Si and Si-O-Al in the low-frequency range from 500 $cm^{-1}$ to 1200 $cm^{-1}$, which are characteristic of phyllosilicates, unique bands for rectorite at 1120 $cm^{-1}$, 976 $cm^{-1}$ and 707 $cm^{-1}$ were ascribed to Si-O stretching, while the vibration at 926 $cm^{-1}$ can be associated with the Al-OH deformation. In this frequency range chitosan spectra also have overlapping resonance bands. Bands between 1039 $cm^{-1}$ and 1155 $cm^{-1}$ are characteristic for primary and secondary hydroxyl in chitosan (Wang et al., 2010). The band at 1080 $cm^{-1}$ is ascribed to C-O-C vibrations (Darder et al., 2003). The two sharp bands in the spectra of neat $NH_4$-Rec at 1440 $cm^{-1}$ and 1640 $cm^{-1}$ result from the $NH_4^+$ deformation band in the interlayer space of rectorite and from OH stretching and bending in the H-O-H group of molecular water respectively (Kloprogge et al., 1999; Russel and White, 1968).
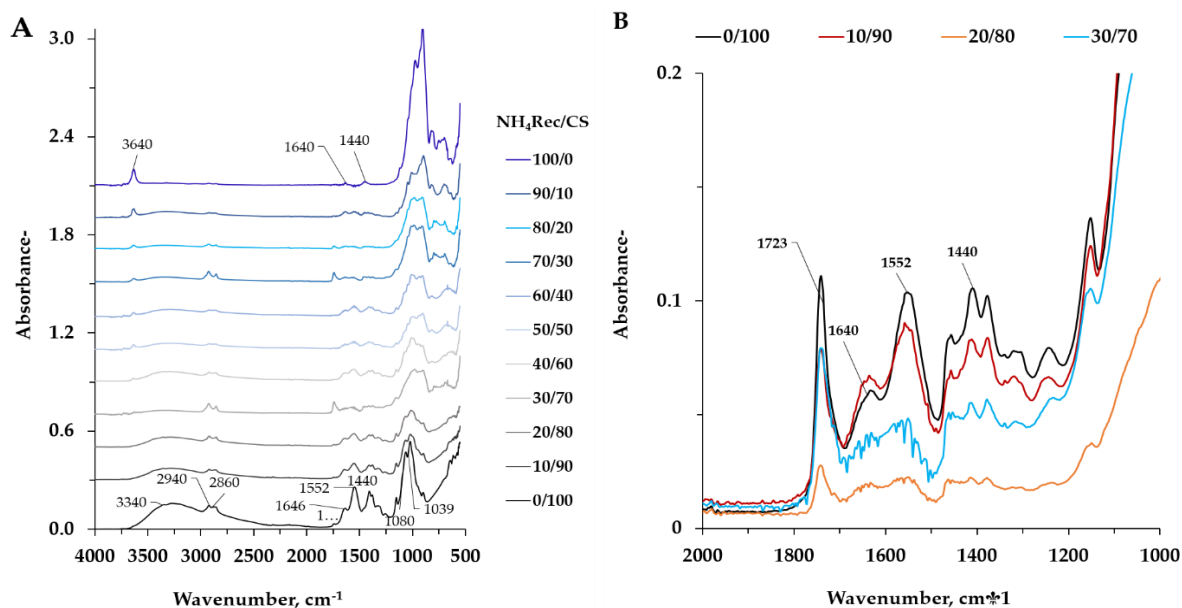
Figure 4-33. (A) FTIR spectra of neat NH₄-Rec and chitosan films and their derivative composite films; (B) enlarged segment of the IR spectra for the three highest CS composites where 1723 cm⁻¹ and 1553 cm⁻¹ bands occur

In the chitosan spectra, deformation vibration of the protonated amine group NH₃ appears at 1552 cm−1 whereas the band at around 1646 cm−1 is ascribed to the stretching of amide I (C=O). In the composite spectra the former shifts slightly towards the lower frequency with a decrease in the amount of CS, whereas the latter disappears or is assimilated into the broader band, now 1640 cm−1, of the H-O-H group in the clay spectra. The shift has been explained as being caused by the electrostatic interaction between the protonated amine groups and the negatively charged clay surfaces in montmorillonite-chitosan composites (Darder et al., 2003, 2005). An additional stretching band at 1723 cm−1 appears in the spectra of one of the two film surfaces (all films were analysed on both sides) for each of the composite films, including chitosan, but not in the neat NH₄-Rec films. The band has been previously attributed to acetate salt ions and associated with a double layer of chitosan in the intercalated composite structure (Darder et al., 2003, 2005), or to the C=N from cross-linking of chitosan by glutaraldehyde (Lu et al., 2015). As the XRD data of the Rec/CS composites reported above do not indicate a double layer spacing and no

135

cross-linking reagents were used in the preparation of the films, the observed acetate band most probably indicates the presence of acetate salts in the bulk of the chitosan phase. A pair of sharp bands at 2860 cm$^{-1}$ and 2940 cm$^{-1}$ is ascribed to the symmetric and asymmetric stretching vibrations of the –CH$_2$ and –CH$_3$ groups of the alkyl chains, the bending vibrations of which are visible in the region around 1440–1430 cm$^{-1}$ (Atanasova et al., 2016; Li et al., 2008; Wang et al., 2006). The presence of these two bands in all the composite FTIR spectra confirms the presence of chitosan in the interlayer space of NH$_4$-Rec. In the high-frequency region above 3000 cm$^{-1}$, characteristic H$_2$O and H-O-H resonance bands for silicates and chitosan broadly overlap. The hydroxyl stretching typical of silicates is seen as a sharp, intense absorption band at 3640 cm$^{-1}$ in the spectra of neat NH$_4$-Rec and indicates H-bonded Si-O-Si linkages (Kloprogge et al., 1999). In the composite spectra the peak progressively drops intensity and broadens with the decrease of rectorite proportion until it becomes completely invisible below compositions of 30/70 with the advancement of chitosan intercalation. At this frequency the vibration of N-H bonded to O-H in chitosan around 3340 cm$^{-1}$ broadened over the lower wavenumber region centred between 3300 cm$^{-1}$ and 3000 cm$^{-1}$ in all composites, indicative of hydrogen bonding between rectorite and chitosan (Wang et al., 2006). The intensity of the broad peak is higher with the increase of chitosan proportions, suggesting an increase of hydrogen bonding between the hydroxyl and amine groups during film formation (Park et al., 2002).

The microstructural characteristics of the composite films are demonstrated by the SEM micrographs in Figure 4-34 in parallel to the neat NH$_4$-Rec and CS films (Figure 4-35). The upper surfaces of both neat films appear almost identical; however, the cross-section views show distinct differences. Although at first sight layering is observed in both film types, the NH$_4$-Rec films display more-or-less planar orientation of the flakes arranged in continuous thin clay layers parallel to each other. The CS films show a semi-layered fracture surface with unclear layer boundaries and dim,

smeared sections due to the poorly crystalline nature of chitosan also demonstrated on the XRD patterns. It can be observed how the parallel layering of the neat rectorite clay films slowly becomes ruggedly open and more widely spaced-out with the increase of chitosan proportion (and corresponding decrease of clay) in the composite mixture. The rectorite flake structure opens to accommodate the chitosan phase and becomes more irregular, affecting the layer orientation within the microstructure of the films. This is illustrated on the image of composite film 20/80 (Figure 4-35(D)) where the view is almost identical to that of neat chitosan film (Figure 4-34(A-2)), although in this compositional range even at 10/90 the XRD image still shows some of the original rectorite reflections. This indicates that chitosan is intercalated into rectorite preserving the clay structure, and also acting as a binder to produce a more compact film.
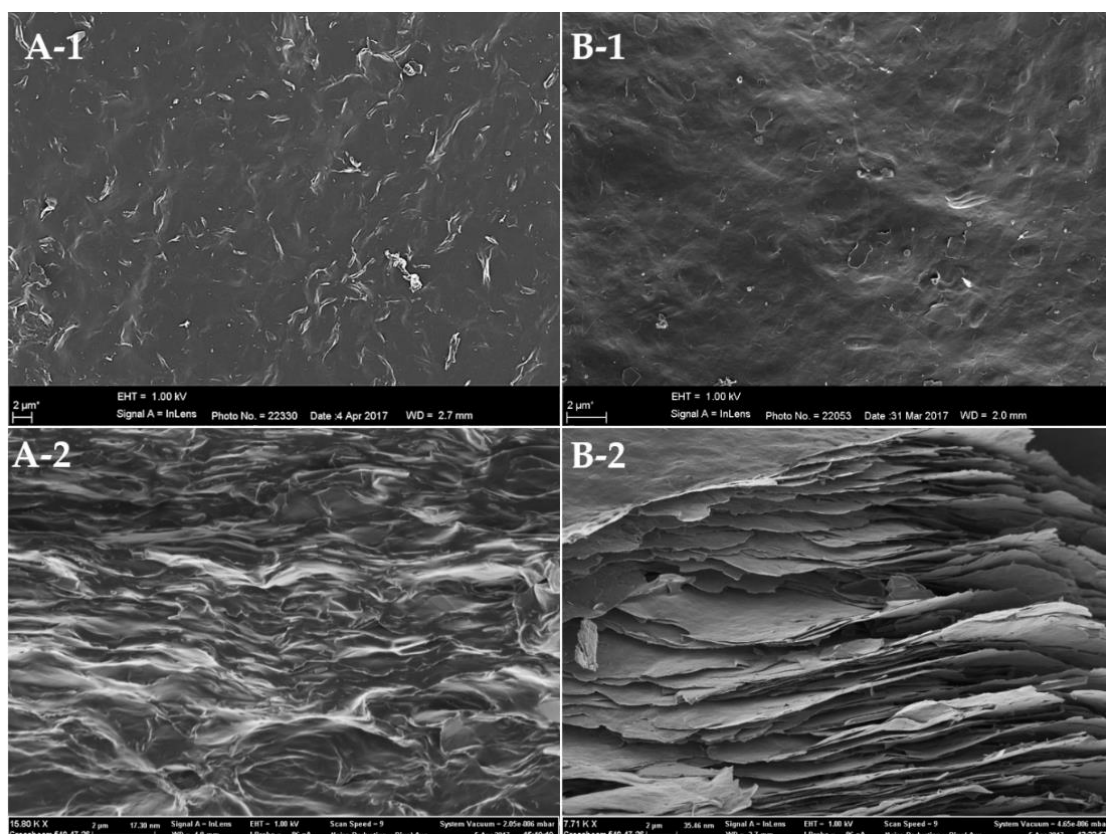


Figure 4-34. SEM micrographs of chitosan (CS) only and NH$_4$-Rec only films: (A-1) CS top surface and (A-2) CS cross-section view; (B-1) NH$_4$-Rec clay film top surface and (B-2) cross–section view
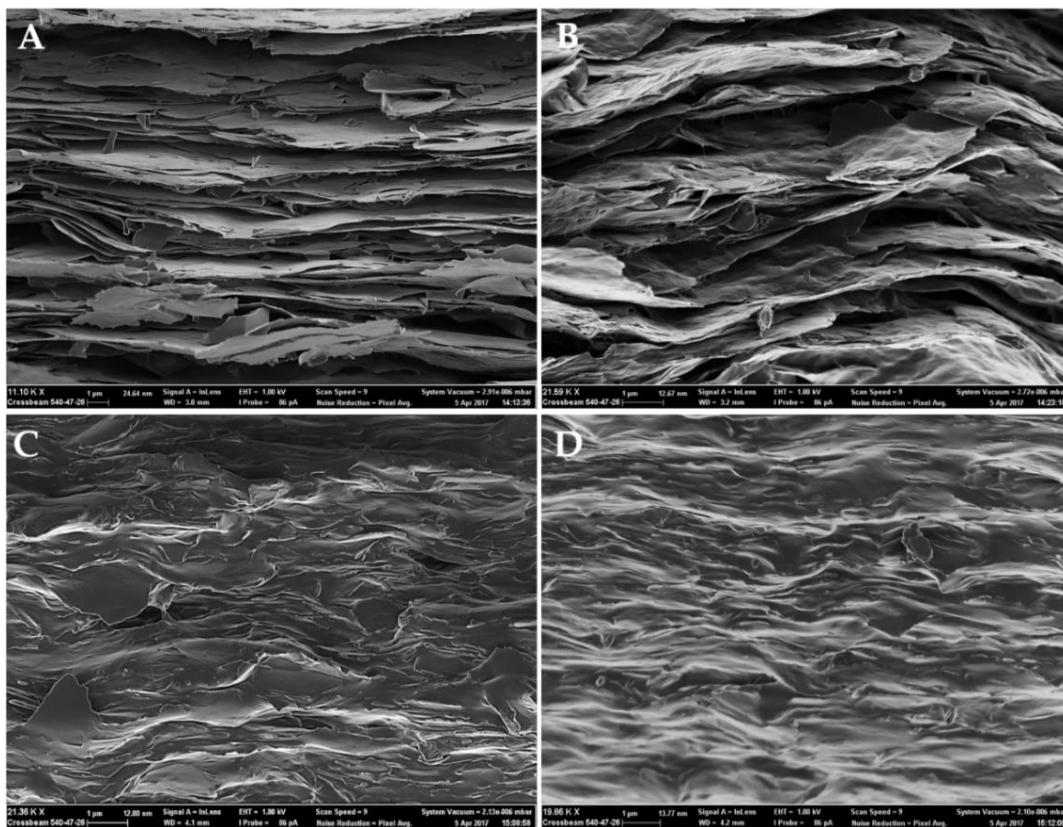
Figure 4-35. SEM images of fractured profile surface of composite films with compositions NH$_4$-Rec/CS (A) 80/20, (B) 60/40, (C) 40/60, and (D) 20/80

A compact film structure, though less ordered, might be the decisive factor for enhanced tensile strength of the composites at the expense of a decrease in the elongation at break compared to neat chitosan films (Figure 4-37).

The chemical composition of the rectorite from the Beatrix mine used to produce the bionanocomposites has been discussed in a previous communication (Atanasova et al., 2016). The CEC was estimated at $45 \pm 7$ mEq/100 g. Such a value is expected for mixed-layer structures where alternate interlayers are of the montmorillonite type. The exchangeable smectitic interlayer contains almost equal Na$^+$ and Ca$^{2+}$ ions. The fixed interlayer space (mica interlayer) contains proportionally dominant Na$^+$ and Ca$^{2+}$ and minor K$^+$. Major element concentrations determined by XRF, for the batch of purified neat and NH$_4^+$-exchanged rectorite used for preparing the bionanocomposites, are presented in Table 4-11.

Table 4-11. XRF analyses of the NH₄-Rec and purified rectorite (RT3) used for exchange. The value for N is derived by difference from LOI estimations.

| Sample | Purified Rec | NH$_4$-Rec |
|---|---|---|
| $SiO_2$ | 49.61 | 49.57 |
| $TiO_2$ | 0.28 | 0.28 |
| $Al_2O_3$ | 37.02 | 37.72 |
| $Fe_2O_{3\,(t)}$ | 0.07 | 0.04 |
| MnO | < 0.001 | 0.001 |
| MgO | < 0.01 | < 0.01 |
| CaO | 2.97 | 2.10 |
| $Na_2O$ | 2.78 | 2.51 |
| $K_2O$ | 0.86 | 0.85 |
| $P_2O_5$ | 0.022 | 0.019 |
| CoO | < 0.001 | < 0.001 |
| $Cr_2O_3$ | 0.062 | 0.046 |
| CuO | < 0.001 | < 0.001 |
| NiO | 0.002 | < 0.001 |
| PbO | < 0.001 | < 0.001 |
| $SO_3$ | < 0.001 | < 0.001 |
| $V_2O_5$ | 0.019 | 0.018 |
| BaO | 0.061 | 0.042 |
| ZnO | 0.010 | 0.012 |
| $ZrO_2$ | < 0.001 | 0.012 |
| SrO | 0.094 | 0.070 |
| N |  | 1.86 |
| LOI | 5.38 | 7.23 |
| Total | 99.24 | 100.27 |
| $H_2O$- | 5.08 | 3.19 |

The higher LOI in the ion-exchanged rectorite is consistent with the amount of ammonia ions introduced into the rectorite structure during the exchange. The amount of ammonia calculated by difference from these results is in good agreement with the carbon-hydrogen-nitrogen (CHN) determinations presented in Table 4-12.

Elemental analyses for the CHN content in the chitosan and bionanocomposite films are plotted in Figure 4-36. The carbon content of the chitosan used was 41.5 %, and therefore the expected slope of the line in Figure 4-36 is 0.415. This compares favourably with the experimental slope of 0.434. The results therefore indicate a good correlation with the theoretical clay/chitosan proportions.
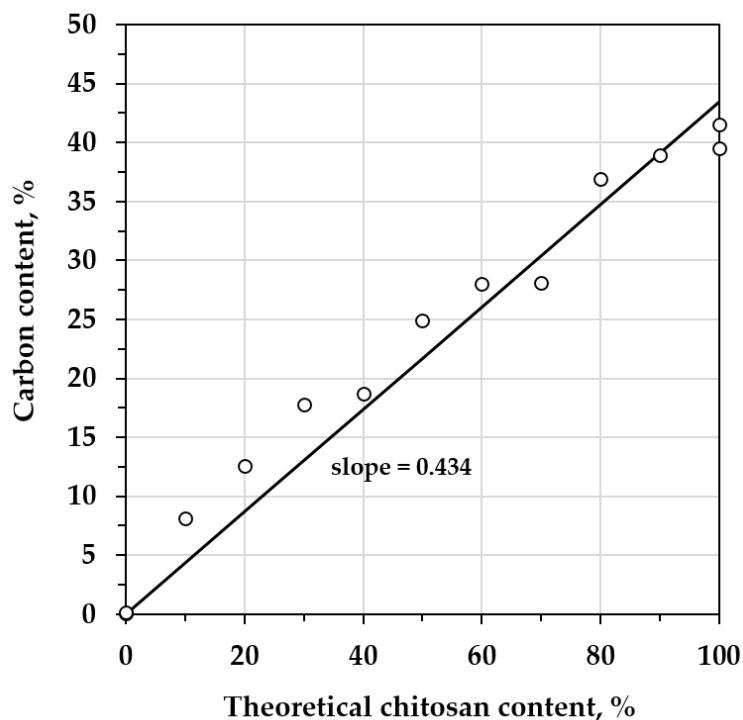
Figure 4-36. Correlation between experimental proportions of clay/chitosan and analytical estimations of CHN concentrations

Table 4-12. Elemental carbon-hydrogen-nitrogen content of neat $NH_4$-rectorite and chitosan powders, films and bionanocomposite films

| Sample | Carbon % | Hydrogen % | Nitrogen % |
|---|---|---|---|
| $NH_4$-Rec powder | 0.04 | 2.98 | 1.78 |
| 100/0F | 0.19 | 2.43 | 1.46 |
| 90/10F | 8.10 | 3.86 | 2.47 |
| 80/20F | 12.60 | 7.08 | 4.57 |
| 70/30F | 17.80 | 4.56 | 4.48 |
| 60/40F | 18.70 | 6.62 | 4.71 |
| 50/50F | 24.90 | 8.12 | 5.90 |
| 40/60F | 28.00 | 5.57 | 6.55 |
| 30/70F | 28.10 | 8.30 | 6.52 |
| 20/80F | 36.90 | 6.43 | 7.33 |
| 10/90F | 38.90 | 9.14 | 7.84 |
| 0/100F | 39.50 | 9.82 | 7.67 |
| CS powder | 41.50 | 7.45 | 7.93 |

Tensile measurements, including tensile strength (TS), Young's modulus and Elongation at break are presented in Table 4-13 and Figure 4-37. Films of each composition were replicated at least three times and a minimum of three measurements per film was performed. The summarised results Figure 4-37B and in Table 4-13 represent the maximum tensile properties (instead of average values), together with the standard deviation based on all samples measured.
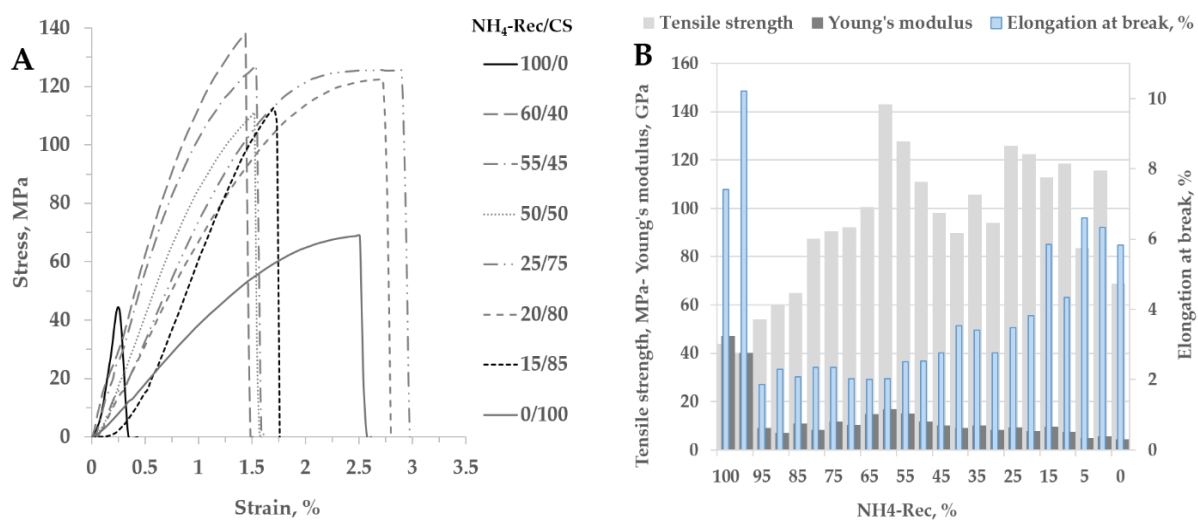


Figure 4-37. Tensile properties of the NH$_4$-Rec/CS composites: (A) stress-strain curves of end members and selected composites; (B) mechanical properties in the compositional range 100–0 %

The addition of chitosan (in increments of 5 %) to NH$_4$-Rec clay resulted in a consistent increase in the tensile strength (TS) of the composite films. The strength values at compositions 80/20 already exceeded the maximum values for neat clay films and chitosan films. Films in the mid-compositional range showed a tensile strength increase of up to 227 % and 108 % relative to the neat clay films and chitosan films respectively, with the maximum measured for the 60/40 composition. The Young's modulus followed a similar trend after the sudden drop at the two highest clay compositions. The maximum values occurred over a broad compositional range (80/20 to 30/70) and thereafter gradually decreased with a decrease of clay proportion in the mix. A similar model from Verbeek and Focke, (2002) has been attributed to composite

porosity being highly dependent on the particle aspect ratio Their model predicted significantly lower values for Young's modulus as proportions of high-aspect-ratio filler particles in a composite decrease, i.e. towards the CS-rich end. The sudden drop in Young's modulus of the neat NH$_4$-Rec films from 95/5 - 70/30 can be explained by the loss of compact layering in the clay as a result of chitosan entering the interlayer spaces, expressed in an increase in film porosity. In the range 75/25–45/55 the two components seem to be in equilibrium, producing compacted-enough films with experimentally the best modulus and strength (Figure 4-37). In composite 40/60, further addition of chitosan results in insufficient high-aspect-ratio particles to maintain a compact film microstructure.

Table 4-13. Mechanical and physical properties of the composite films (compositions are listed as proportions of NH$_4$-Rec/CS)

| Composition | Thickness | d-spacing | pH | Tensile strength | Young's modulus | Elongation at break |
|---|---|---|---|---|---|---|
| NH$_4$-Rec/CS | μm | nm | | MPa | GPa | % |
| 100/0 | 22 | 2.15 | 7.10 | 43.7 ± 10.4 | 47.3 ± 13.1 | 7.4 ± 2.1 |
| 98/2 | 20 | 2.16 | 3.98 | 40.2 ± 13.2 | 40.1 ± 14.7 | 10.2 ± 4.6 |
| 95/5 | 32 | | 3.88 | 53.9 ± 15.4 | 9.5 ± 6.3 | 1.9 ± 0.4 |
| 90/10 | 32 | 2.16 | 3.95 | 59.8 ± 3.4 | 9.2 ± 1.1 | 2.3 ± 0.3 |
| 85/25 | 33 | | 3.68 | 65.0 ± 8.8 | 10.8 ± 0.9 | 2.1 ± 0.3 |
| 80/20 | 33 | 2.14 | 3.77 | 87.5 ± 15.2 | 11.7 ± 1.2 | 2.3 ± 0.4 |
| 75/25 | 35 | | 3.78 | 90.6 ± 17.9 | 11.6 ± 1.8 | 2.3 ± 0.4 |
| 70/30 | 32 | 2.16 | 3.92 | 92.2 ± 16.2 | 10.3 ± 1.1 | 2.0 ± 0.2 |
| 65/45 | 28 | | 3.56 | 100.5 ± 22.3 | 14.8 ± 2.6 | 2.0 ± 0.3 |
| 60/40 | 30 | 2.15 | 3.85 | 143.5 ± 26.4 | 17.0 ± 3.3 | 2.0 ± 0.3 |
| 55/45 | 25 | | 3.88 | 127.5 ± 21.9 | 15.3 ± 2.8 | 2.5 ± 0.4 |
| 50/50 | 30 | 2.16 | 3.78 | 111.0 ± 18.3 | 11.8 ± 1.6 | 2.5 ±0.3 |
| 45/55 | 38 | | 3.65 | 98.3 ± 14.1 | 10.3 ± 1.5 | 2.8 ± 0.3 |
| 40/60 | 34 | 2.17 | 3.58 | 89.8 ± 9.4 | 9.0 ± 1.2 | 3.5 ± 0.6 |
| 35/75 | 33 | | 3.50 | 105.7 ± 12.8 | 10.2 ± 1.2 | 3.4 ± 0.5 |
| 30/70 | 37 | 2.19 | 3.50 | 93.9 ± 14.3 | 8.4 ± 0.7 | 2.8 ± 0.3 |
| 25/75 | 35 | | 3.75 | 125.7 ± 19.0 | 9.4 ± 1.2 | 3.5 ± 0.6 |
| 20/80 | 42 | 2.26 | 3.60 | 122.4 ± 19.5 | 7.7 ± 1.3 | 3.8 ± 0.6 |
| 15/85 | 25 | | 2.90 | 112.9 ± 16.7 | 9.7 ± 1.3 | 5.8 ± 1.2 |
| 10/90 | 37 | 2.31 | 2.98 | 118.6 ± 16.6 | 7.4 ± 0.8 | 4.4 ± 0.6 |
| 5/95 | 38 | | 2.90 | 83.6 ± 11.1 | 5.5 ± 0.8 | 6.6 ± 0.9 |
| 2/98 | 36 | 2.41 | 2.70 | 115.5 ± 21.9 | 5.8 ± 0.9 | 6.3 ± 1.3 |
| 0/100 | 45 | | 2.60 | 68.9 ± 12.7 | 4.3 ± 1.0 | 5.8 ± 1.1 |

The measured values for elongation at break (Table 4-13, Figure 4-37) were significantly affected by the surface flaws in the films. Nevertheless, overall it appeared that the increase of TS was accompanied by a decrease in the elongation at break ($\varepsilon$) and this was more pronounced in the compositional range 90/10 - 30/70. Similar inverse relation has been attributed to nanofillers/chitosan interactions enhancing the stress transfer at the interface (Luo et al., 2003; Xu et al., 2006; Chivrac et al., 2009). The property enhancements indicate that film microstructure have become more compact as a result of good interaction of the two end-components, also observed by Ruiz-Hitzky et al., 2005, Darder et al., 2005, Darder et al., 2006, Chivrac et al., 2009.

The UV-Vis absorption spectra of the $NH_4$-rectorite and chitosan films and their derivative composite films are presented in Figure 4-38. They show a gradual improvement of transparency with the decrease in clay content. The films from the two end-components differ visually in colour and surface topography (Figure 4-39).
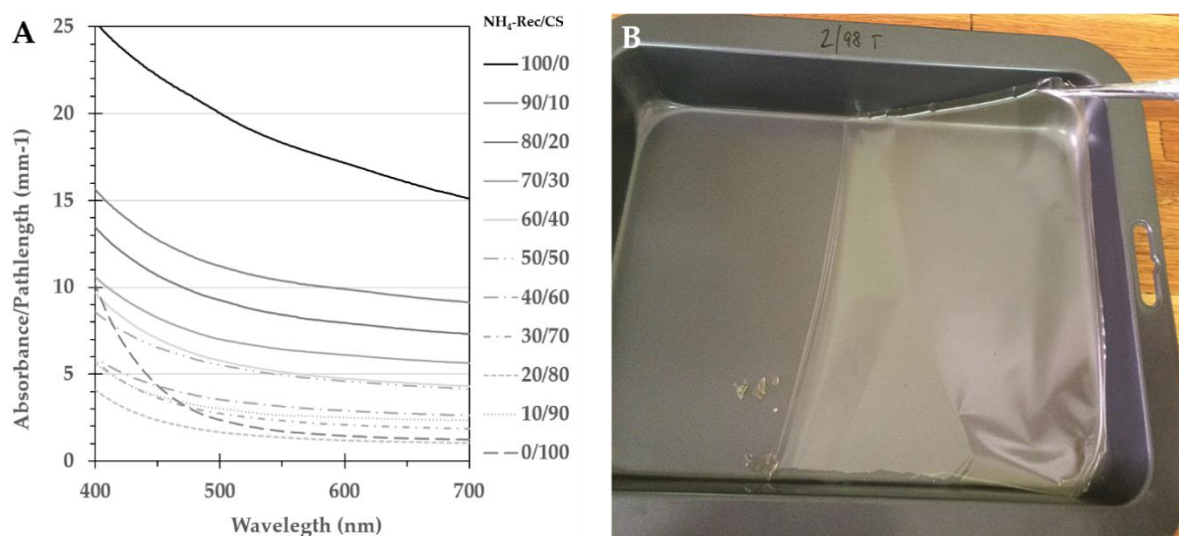


Figure 4-38. (A) UV-Vis spectra of ammonium ion-exchanged film, chitosan film and films of derivative composites; (B) peeling off of a 2/98 composite film

The rectorite films had an off-white colour with a subtle blue-grey tint and pearly lustre on the smooth underside, whereas the chitosan films showed a smoky brown-yellow appearance often with a wavy top surface after drying (Figure 4-39). The neat

clay films were translucent to transparent when the thickness was below 25 μm, whereas the chitosan films were transparent even at a thickness of 40 μm and above. The composite films appeared generally dull yellow-grey with the yellow tint becoming more intense with an increase of chitosan proportion (Figure 4-39).
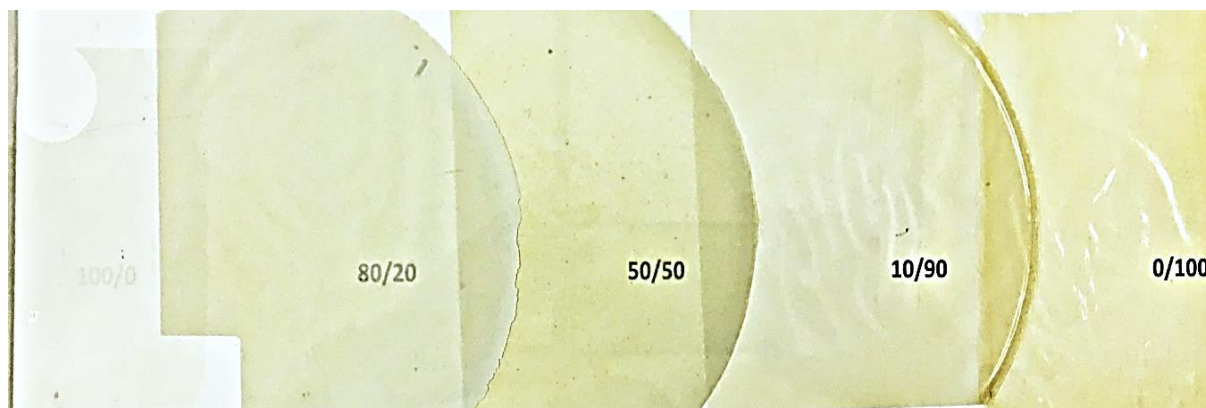


Figure 4-39. Visual comparison of transparency: at left NH$_4$-Rec film (100/0) 22 μm thick (top left corner has a round cut to visually discriminate the film from the white background of a similar shade); and composites as indicated: thickness from left to right 22 μm, 33 μm, 25 μm, 37 μm and chitosan film (0/100) of thickness 45 μm

The NH$_4$-Rec/CS nanocomposite films were highly solvent-resistant even in water, despite the fact that both starting components are water-dispersible under suitable pH conditions. Figure 4-40 shows fragments of composite films that remained fully intact even after being immersed in water for 277 days.
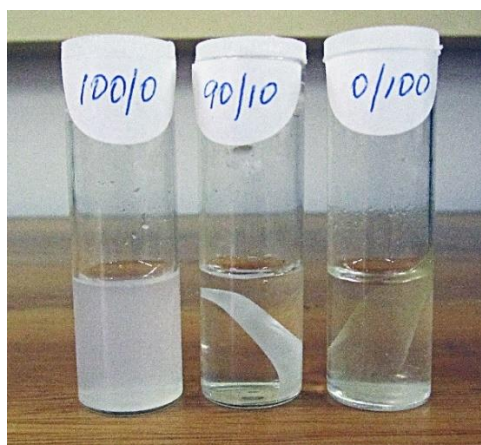


Figure 4-40. Film fragments of the two starting components and composite film 90/10 immersed in water for 277 days

# CHAPTER 5     KEY FINDINGS AND DISCUSSION

## 5.1     Characterisation of rectorite

Three rectorite-rich samples from the Beatrix Gold Mine, South Africa, were characterised. The samples differed in their visual appearance with RT1 containing large, light blue-grey platy aggregates with a silky lustre, while RT2 and RT3 represented disintegrated host rock mine material. All samples were subjected to various purification procedures aimed at producing high-purity material. The characterisation presented in this document is based on purified material with a rectorite content above 90 wt.% (XRD analysis). Structurally and chemically, the purified materials from the three samples were very similar and were categorised as rectorite, except where applicable specifics are highlighted.

SEM of the rectorite clay particles revealed a layered morphology. High-resolution TEM showed well-distinguished light and dark layers of about 2.20 nm, consistent with the 1:1 interstratified mica-smectite nature. XRD measurements confirmed the basal spacing $d_{001}$ of 2.20 nm, indicating a one-water-layer structure. Unit cell parameters, for a monoclinic unit cell with primitive lattice, refined to $a$ = 5.177 Å; $b$ = 8.980 Å; $c$ = 22.489 Å and $\beta$ = 97.335 °, with a mean crystallite size around 14 nm and a calculated cell volume of 1045 Å$^3$. The Greene-Kelly test suggested that the expandable smectite layers have montmorillonite-beidellite composition. Nuclear magnetic resonance (NMR) spectroscopy indicated a high degree of Al substitution and the presence of two different Al sites corresponding to six- and four-fold octahedral and tetrahedral aluminium respectively. The chemical composition and diffraction data suggest that the mica is Na-Ca-rich, i.e. of paragonite-margarite series. The fixed interlayer regions (mica interlayers) contain proportionally dominant Na$^+$ and Ca$^{2+}$ and minor amounts of K$^+$. The exchangeable smectitic interlayers contain almost equal amounts of Na$^+$ and Ca$^{2+}$ ions. The distribution of the interlayer Na$^+$ ions was quantified by $^{23}$Na solid-state NMR spectroscopy. These results point to a three-

component mixed-layer structure with considerable variation in the composition of the mica layer of the different samples.

Organically modified layered silicates such as clay minerals are the commonly preferred property modifier in materials processing and manufacture. Modification complexes of rectorite with long-chain dodecyldimethylammonium chloride (DCC10), dialkyldimethylammonium chloride (DCC18) and hexadecyltrimethylammonium chloride (SCC16) were characterised by XRD, FTIR spectroscopy and TGA. The XRD data showed well-defined peaks as the surfactant was homogeneously intercalated between the rectorite layers. The expansion of the interlayer with the double-chain surfactants was 3.60 nm and 3.70 nm for DCC10 and DCC18 respectively, while the d-spacing corresponding to single-chain intercalation with SCC16 was 3.20 nm. The shift of the basal spacing of the rectorite indicates the exchange and adsorption of the larger organic molecules into the smectite layer in the rectorite structure. The FTIR analysis confirmed the presence of organic surfactants in the rectorite, showing absorbance peaks at 2840 cm$^{-1}$ and 2913 cm$^{-1}$. Homogeneous intercalation implies an increase in the organophilic properties of rectorite at the expense of its hydrophilic nature, and suggests that the adsorption is feasible and can be used as a precursor step to the subsequent adsorption of non-polar organic compounds.

## 5.2    Rectorite clay films

The behaviour of a rectorite particle in aqueous suspension is defined by its mixed-layer structure and in particular by the exchangeable interlayer in the smectite component. The physico-chemical dynamics in the interlayer space of a clay structure in suspension eventually result in swelling and subsequent delamination of the clay tactoids into smaller entities. The interlayer cations diffuse into the double layers around the separated silicate layers in a state of "osmotic swelling" (Lagaly, 2006). The mixed-layer structure of rectorite comprises alternating interlayer spaces with

different cation densities, i.e. non-expandable (mica-like) and expandable (smectite-like) layers in a 1:1 ratio with an average CEC of 45 mEq/100 g (Atanasova et al., 2016). The expandable smectite layer is of montmorillonite-beidellite composition and the mica component is of the brittle mica species paragonite-margarite. Previous NMR and XRD studies of Beatrix rectorite (Atanasova et al., 2016; Jakobsen et al., 1995; Lausen et al., 1999) reported a high degree of regularity in the layered structure (coefficient of variation for $d_{001}$ of 0.12). A high degree of Al substitution in the mica tetrahedral sheet was established, resulting in the pairing of high-charge top and bottom tetrahedral sheets in a MacEwan crystallite model (MacEwan and Amil, 1958; MacEwan, 1956, 1957). The mica component layer carries a charge density solely of tetrahedral origin almost four-fold higher than that of the alternating smectite layer where the charge is of a dual nature, i.e. partially octahedral from isomorphous substitutions in montmorillonite and partially tetrahedral substitutions in beidellite. The tetrahedral charge is more localised (on three surface oxygens) than the octahedral charge, resulting in stronger H-bonding of adsorbed $H_2O$ as in micas and vermiculites (Schoonheydt and Johnston, 2006). Hence, the bonding strength between silicate layers in the stacking direction of rectorite tactoids is stronger at the mica component layers, inflicting stronger rectorite lamellae as opposed to smectite-only lamellae. Reportedly, this has significant effects on the elastic constant of micas and mica-containing products, and ultimately on their mechanical properties (Kunz et al., 2009; Moller et al., 2010). In suspension, rectorite crystallite will swell only in half of the layers, i.e. at the smectite interlayer. It is also known that monovalent ions cause more extensive swelling of the interlayer than divalent ions (Norrish, 1954) and that micas do not swell at all (Grim, 1968). Consequently, during delamination the mixed-layer rectorite tactoids will separate only at the low-charged interlayer space, i.e. that of smectite. Theoretically, this process could produce a suspension of "fundamental particles" consisting of a single or just a few mica layers (Nadeau et al., 1985; Srodon et al., 2000) with separation distances in the range of 1 nm, short enough for van der

Waals' attraction forces to preserve elementary particle integrity. Furthermore, upon drying and re-assembling, the high tetrahedral charge of the outer rectorite layers would promote strong forces bonding the phyllosilicate layers back together. The X-ray diffraction profiles of the dried films (Figure 4-30) showed peak positions and ordering identical to the rectorite source material. This provides additional confirmation that the delaminated layers re-assembled in an orderly and regular manner and not as random physical mixtures. The primary tactoids in the raw rectorite consisted of up to ten 2:1 silicate layers and had a thickness of about 220 nm, whereas after delamination and re-assembling into coherent films, the stacks contained an average of two to six 2:1 silicate layers. This confirms that delamination occurred and that an increased aspect ratio of the rectorite platelets was achieved, resulting in the generation of a large surface area in the films, as confirmed by the BET results. These results also suggest that dual ordering was attained during the film formation process: at structure level the ordering of 2:1 rectorite layers after delamination and at film microstructure level the two-dimensional organisation of the clay sheets.

**The role of heterogeneous layer charge:** The physico-chemical properties of rectorite are defined by the regular alternation of low-charge (smectite) and high-charge (mica) layers and their respective interlayer spaces. The expandable smectite layer controls the thickness and the mica layer serves to maintain the structural integrity of the rectorite platelet. Within a tactoid unit, the former layer acts as a shear-labile and the latter as a shear-stiff reinforcement of the rectorite nanoplatelets (Moller et al., 2010). This functional distribution at a structure level resembles other natural mineralised structures such as bone and nacre where ordered arrangements of "soft" and "stiff" phases act synergistically to promote superior mechanical performance tantamount to advanced engineering materials. The hierarchical arrangement of such layered nanostructures has a dramatic effect on the stress and strain propagation in materials and their derivatives (Dimas and Buehler, 2012). The Coulomb attractions between

silicate layers and interlayers along the stacking direction are stronger for micas compared to smectites (Kunz et al., 2009) and have a strong impact on the mechanical properties of materials containing mica. Hence, when rectorite platelets self-assemble from aqueous suspension, the bonding strength along the lamellar stacking and corresponding layer stacking in the film organisation is stronger than would be expected in smectite suspensions and films.

## 5.3    $NH_4$-rectorite-chitosan bionanocomposite films ($NH_4$-Rec/CS NCF)

$NH_4$-Rec/CS NCF were produced over the full compositional range (100 - 0 % clay, i.e. 0 - 100 % chitosan respectively). Precursor dispersions were prepared by combining partially exfoliated ammonia-exchanged rectorite with a solution of protonated chitosan. The films formed at slow evaporation of the aqueous phase. In this process composites were obtained via re-assembly of chitosan-intercalated rectorite. The intercalation occurred through electrostatic interaction as cation exchange between the $NH_4$ cations in the interlayers of rectorite and the protonated amino groups of chitosan. At high chitosan content the tactoids were uniformly dispersed in the bulk matrix. Parameters such as clay-chitosan proportions, degree of dispersion, exfoliation and mixing methodology and pH were experimentally determined, closely controlled and tuned to achieve optimal mechanical strength of the final film product. Consistent increase of tensile strength of the composite films was observed with the addition of chitosan to $NH_4$-Rec clay. At 80/20 compositions, values already exceeded the maximum values for neat clay films and chitosan films. Films in the mid-compositional range showed a tensile strength increase of up to 227 % and 108 % relative to the neat clay films and chitosan films respectively, with the maximum measured for composition 60/40. The Young's modulus followed a similar trend after the sudden drop at the higest clay composition, with the maximum values occurring over a broader compositional range (80/20 - 30/70) and gradually decreasing with the decrease of clay proportion in the mix. It overall appeared that the increase of tensile

strength was corelated to a decrease in the elongation at break ($\varepsilon$), more pronounced in the compositional range 90/10 - 30/70. Such inverse relation has been attributed to nanofillers/chitosan interactions resulting in enhancment of stress transfer at the interface (Luo et al., 2003; Xu et al., 2006; Chivrac et al., 2009). The enhancement of the properties indicates an effective interaction between the clay and the biopolymer also observed by Ruiz-Hitzky et al., 2005, Darder et al., 2005, Darder et al., 2006 and Chivrac et al., 2009.

The composite films showed a gradual improvement in transparency with the decrease of clay content. The rectorite films have an off-white colour with a subtle blue-grey tint and pearly lustre on the smooth underside, whereas the chitosan films have a smoky yellow-gray appearance often with a wavy top surface.

The $NH_4$-Rec/CS nanocomposite films prooved to be extremely solvent-resistant even in water, despite the fact that both starting components are water-dispersible under suitable pH conditions. Film fragments remained fully intact after being immersed in water for 277 days.

# CHAPTER 6    CONCLUSIONS

Both starting materials, i.e. clay and biopolymer, can be obtained as waste materials. The rectorite occurs as a host rock alteration and could be recovered from mine tailings. Similarly, chitosan is derived from chitin produced from shellfish waste from the seafood industry.

## 6.1    Characterisation of rectorite

Based on major element concentrations from XRF, X-ray diffraction (XRD) and nuclear magnetic resonance (NMR) evidence, rectorite from Beatrix mine identifies with Na-Ca-rectorite, a dioctahedral regular interstratification of mica-smectite type. The dioctahedral character of the interstratified structure was confirmed by $d_{060}$ at 1.48 Å.

The structure of rectorite was empirically modelled by refinement of high-resolution XRD data collected from a single "pure" rectorite flake. Unit cell parameters, for a monoclinic unit cell with primitive lattice, refined to $a$ = 5.177 Å; $b$ = 8.980 Å; $c$ = 22.489 Å and $\beta$ = 97.335 ° with a mean crystallite size around 14 nm and a calculated cell volume of 1045 Å$^3$. The Greene-Kelly test suggested that the expandable smectite layers have montmorillonite-beidellite composition.

Scanning electron microscopy (SEM) of rectorite clay particles revealed a layered morphology. High-resolution transmission microscopy (TEM) showed well-distinguished light and dark layers of about 2.20 nm, consistent with the 1:1 interstratified mica-smectite nature.

There are Na$^+$, Ca$^{2+}$ and K$^+$ cations in the fixed interlayer region (mica interlayer) in a ratio of approximately 15:7:3, and the cationic presence of the exchangeable smectite interlayer comprises Na$^+$ and Ca$^{2+}$ ions in a ratio of about a 3:4. The distribution of the interlayer Na+ ions was quantified by $^{23}$Na solid-state NMR spectroscopy. It points to a three-component mixed-layer structure with considerable variation in the composition of the mica layer in the different samples. These compositions indicate that the mica layer is represented by paragonite (Na-mica) -margarite (Ca-mica) series, rather than muscovite (K-mica). The structural formula also indicates relatively high tetrahedral substitution, resulting in an expandable layer charge of −0.36 which is characteristic of beidellite rather than montmorillonite in which the net layer charge arises from octahedral substitutions. Furthermore, the chemical data and derived structural formula of Beatrix rectorite suggest an Al-IV:Al-VI ratio of 1:2. The four octahedral sites are dominantly occupied by Al$^{3+}$ with minor Ti$^{4+}$, Fe$^{3+}$ and Mg$^{2+}$. Variable interlayer composition of the mica component among the samples is also indicated by NMR and chemically by the XRF data. NMR spectroscopy confirmed a high degree of Al substitution and the presence of two different Al sites corresponding to six- and four-fold octahedral and tetrahedral aluminium respectively. These

findings conform to previous reports on paragonite-margarite-type mica layers alternating with an Na-montmorillonite-beidellite swelling component in rectorite from this locality (Jakobsen et al., 1995). In addition, the ^{1}H MAS (20 kHz) NMR data reported in the present work contributed to the understanding of the nature and position of the metal hydroxide groups in the mineral structure and the physically adsorbed water and metal-bound OH-groups in the rectorite studied here. A previous study on aluminium layered hydroxides (Wang et al., 2009a) reported similar peak positions, but the peak characteristics observed in the present work point to weak residual dipolar interactions and thus higher mobility of water.

Although the bulk "in situ" occurrence of rectorite in the three samples from Beatrix mine shows rather heterogeneous mineral associations and physical appearance, mineralogically, structurally and chemically all purified rectorite samples were identified as Na-Ca-rectorite. Thus the Beatrix rectorite appears to be compositionally different from the (K, Na, Ca)-rectorite from the Zhongxiang deposit in Hubei, China (Hanlie et al., 2008), the Na-rich rectorite from Arkansas, USA (Jakobsen et al., 1995) and the (Na, K, Mg, Ca, Sr)-rectorite specimens from Baluchistan, Pakistan (Kodama, 1966).

## 6.2    Rectorite clay films

The capability of rectorite to form strong, flexible self-standing clay films without binders and property enhancers was investigated and the limits of their ultimate material properties evaluated. Clay-only films were prepared by casting aqueous dispersions of exfoliated neat and ion-exchanged rectorite clay through self-assembly during slow evaporation.

The clay films consisted of continuous layers of well-aligned clay platelets parallel to the casting surface. Layers overlapped face to face in the lateral direction and joined vertically in an irregular manner by face-to-face and edge-to-face bridging to form

coherent multi-layer nanostructured films with a platelet-void microstructure. All films showed good mechanical properties with some comparing favourably to values featured by polymer films. Rectorite clay films with monovalent interlayer content exhibit higher strength and stiffness compared to films with divalent modifications and neat Na-Ca-rectorite films. Of all the modifications, only $NH_4$-Rec films showed enhancement of both tensile properties compared to films from the neat material used for the exchange. Statistical projection for the maximum attainable values for mechanical properties indicates that defect-free films could offer significantly better performance.

The results presented highlighted the lamellar crystal morphology along with the hybrid layer charge of the mixed-layer structure as the most relevant and unique characteristics of rectorite with regard to its potential to produce strong cohesive films. The large surface area of the clay particles is critical for efficient particle interactions during self-assembly. The increase in the particle aspect ratio was achieved through exfoliation and delamination of the clay tactoids in aqueous suspensions. This is largely dependent on the physico-chemical dynamics in the interlayer space and the nature of the exchangeable interlayer cation in the smectite component of the rectorite structure. XRD of the films confirmed that the delaminated layers re-assembled in a regular and orderly manner and not as random physical mixtures, i.e. maintaining the original configuration of pairing the high tetrahedral charge of the outer rectorite layers originating from the mica component of the mixed-layer structure. Average tactoid thickness in the films was two to six layers as opposed to ca. ten 2:1 silicate layers in the primary tactoids. During self-assembly, the thinner tactoids were able to compact better into textured layered structures due to the stronger forces bonding the phyllosilicate layers back together.

Hypothetically, the alternating hybrid layer functionality and charge density distribution in rectorite domains at the structural level could synergistically translate

at the level of re-assembly of the rectorite clay layers into sheets to form nanostructured hierarchical films, imparting property reinforcement to the nanoplatelets and ultimately rendering films with strong mechanical performance.

## 6.3 NH₄-rectorite-chitosan bionanocomposite films (NH₄-Rec/CS NCF)

Bionanocomposite films with enhanced mechanical strength and optical transparency were successfully prepared from rectorite clay and chitosan without organic pre-modifications, binders, plasticisers, thermal pre-treatments or other property enhancers. NH₄-rectorite-chitosan nanocomposites were prepared over the complete compositional range (100 - 0 % clay, i.e. 0 - 100 % chitosan respectively). Partially exfoliated and intercalated ammonia-exchanged rectorite-chitosan composites were directly mixed in aqueous acetic dispersions and cast for self-assembly during slow evaporation.

The enhancement of the mechanical and optical properties of the NH₄-rectorite-chitosan nanocomposite films indicates good compatibility of the two end-components and feasibility of the ion-exchange method for the preparation of strong clay-chitosan nanocomposite films with high clay loading. The partially exfoliated and intercalated rectorite structure was confirmed by XRD and FTIR analysis, and SEM imaging. Chemical analysis suggested that all chitosan in solution has been incorporated into the clay and film structure. Composite films became compact as a result of structural interaction between the clay and the biopolymer, also acting as a binder during film formation.

# References

Albertsson, J., Abrahams, S.C., Kvick, A., 1989. Atomic Displacement, Anharmonie Thermal Vibration, Expansivity and Pyroeleetrie of zibcite. . Acta Crystallographica B 45, 34-40.

Altaner, P., Weiss, C.A., Kirkpatrick, R.J., 1988. Evidence from 29Si NMR for the structure of mixed-layer illite-smectite clay minerals. Nature 331, 699-701.

Anderson, M.J., 2001. A new method for non-parametric multivariate analysis of variance. Austral Ecology 26, 32-46.

Anitha, A., Sowmya, S., Kumar, P.T.S., Deepthi, S., Chennazhi, K.P., Ehrlich, H., Tsurkan, M., Jayakumar, R., 2014. Chitin and chitosan in selected biomedical applications. Progress in Polymer Science 39, 1644-1667.

Anon, 1939. Science: Alsifilm Onward, Time Magazine.

Armentano, I., Bitinis, N., Fortunati, E., Mattioli, S., Rescignano, N., Verdejo, R., Lopez-Manchado, M.A., Kenny, J.M., 2013. Multifunctional nanostructured PLA materials for packaging and tissue engineering. Progress in Polymer Science 38, 1720-1747.

ASTM, 1994. ASTM Standard D5488-94D Standard Terminology of Environmental Labeling of Packaging Material and Packages (Discontinued 2002). ASTM International.

ASTM, 2012. ASTM Standard E104, 2002 (2012a). Standard Practice for Maintaining Constant Relative Humidity by Means of Aqueous Solutions. ASTM International.

ASTM, 2013a. ASTM Standard D618, 2013a. Practice for Conditioning Plastics for Testing. ASTM International.

ASTM, 2013b. ASTM Standard D1708 2013a. Standard Test Method for Tensile Properties of Plastics by Use of Microtensile Specimens. ASTM International.

Atanasova, M.T., Vyalikh, A., Scheler, U., Focke, W.W., 2016. Characterization of rectorite from the Beatrix Gold Mine in South Africa. Applied Clay Science 126, 7-16.

Bagshaw, S., Cooney, R.P., 1995. Preparation and Characterization of a Highly Stable Pillared Clay-GaAl12-Pillared Rectorite. Chemistry of Materials 7, 1384-1389.

Bailey, S.W., 1982. Nomenclature for regular interstratifications. American Mineralogist 67, 394-398.

Bailey, S.W., 1984. Structures of Layer Silicates, in: Brindley, G.W., Brown, G. (Eds.), Crystal structures of Clay Minerals and Their X-ray Identification. Mineralogical Society London, UK, pp. 1-125.

Bailey, S.W., Brindley, G.W., Kodama, H., Martin, R.T., 1982. Report of the Clay Mineral Society Nomenclature Committee for1980-1981: Nomenclature for Regular Interstratifications. Clays and Clay Minerals 30, 76-78.

Ballard, D.G.H., Burgess, A.N., Nevin, A., Cheshire, P., Longman, G.W., 1980. Small Angle Neutron Scattering Studies on Polypropylene. Macromolecules 13, 677-681.

Ballard, D.G.H., Rideal, G.R., 1983. Flexible inorganic films and coatings. Journal of Materials Science 18, 545-561.

Barron, P.F., Slade, P., Frost, R.L., 1985a. Ordering of Aluminum in Tetrahedral Sites in Mixed-Layer 2-1 Phyllosillicates by Solid State High-Resolution NMR. Journal of Physical Chemisty 89, 3880-3885.

Barron, P.F., Slade, P., Frost, R.L., 1985b. Solid State Silicon-29 Spin-Lattice Relaxation in several 2-1 Phyllosilicate Minerals. Journal of Physical Chemisty 89, 3305-3310.

Barshad, I., 1950. The effect of the interlayer cations on the expansion of mica type crystal lattice. American Mineralogist 35, 225.

Bayliss, P., 1989. Unit-cell Dimensions of Two-Dimensional Clay Minerals. Powder Diffraction 4, 19-20.

Beirlant, J., Goegebeur, Y., Teugels, J., Segers, J., De Waal, D., Ferro, C., 2005. Statistics of extremes: Theory and applications.

Bennadji-Gridi, F., Smith, A., Bonnet, J., 2006. Montmorillonite based artificial nacre prepared via a drying process. Material Science and Engineering B 130, 132-136.

Bergaya, F., Lagaly, G., 2013. General Introduction: Clays, Clay Minerals and Clay Science, in: Bergaya, F., Lagaly, G. (Eds.), Handbook of Clay Science. Elsevier, Amsterdam, The Netherlands, Printed and bound in the UK, pp. 1-19.

Bergaya, F., Theng, B.K.G., Lagaly, G., 2006. Handbook of Clay Science, First Edition 2006 ed. Elsevier, UK.

Bowen, P., 2002. Particle Size Distribution Measurement from Millimeters to Nanometers and from Rods to Platelets. Journal of Dispersion Science and Technology 23, 631-662.

Bracket, R.N., Williams, J.F., 1891. Vewtonite and Rectorite-two new minerals of the Kaolinite Group. American Journal of Science 42, 11-21.

Brambilla, D., Luciani, P., Leroux, J.C., 2014. Breakthrough discoveries in drug delivery technologies: the next 30 years. Journal of controlled release : official journal of the Controlled Release Society 190, 9-14.

Brindley, G.W., 1966. Discussions and recommendations concerning the nomenclature of clay minerals and related phyllosilicates. Clays and Clay Minerals 14, 27-34.

Brindley, G.W., 1977. Rectorite PDF 00-029-1495, ICDD Grant-in-Aid, pp. ICDD Grant-in-Aid.

Brindley, G.W., Bailey, S.W., Faust, G.T., Forman, S.A., Rich, C.I., 1968. Report of the Nomenclature Committe 1966-1967 of the Clay Mineral Society. Clays and Clay Minerals 16, 322-324.

Brindley, G.W., Brown, G., 1984. Crystal structures of Clay Minerals and Their X-ray Identification, Second ed. Mineralogical Society, London, UK.

Brindley, G.W., Robinson, K., 1946. The structure of kaolinite. Mineralogical Magazine 27, 242-253.

Brown, G., Weir, A.H., 1963. The identity of rectorite and allevardite., Proccedings of International Clay Conference, 1963., Stockholm,.

BrukerAXS, 2009. Topas: General Profile and Structure Analysis Software for Powder Diffraction Data Bruker AXS, Karlsruhe, Germany.

Brunauer, S., Emmett, P.H., Teller, E., 1938. Adsorption of Gases in Multimolecular Layers. Journal of the American Chemical Society 60, 309-319.

BSI, 1993. BS 2955_1993 Glossary of terms relating to particle technology. British Standard Institution, p. 36.

Burnham, C.W., Radoslovich, E.W., 1964. Crystal structures of coexisting muscovite and paragonite. Carnegie Institution of Washington Year Book 63 63, 232-236.

Chang, P.R., Wu, D., Anderson, D.P., Ma, X., 2012. Nanocomposites based on plasticized starch and rectorite clay: structure and properties. Carbohydrate polymers 89, 687-693.

Cheary, R.W., Coelho, A., 1992. A fundamental parameters approach to X-ray line-profile fitting. Journal of Applied Crystallography 25, 109-121.

Chen, F., Ma, X., Qu, X., Yan, H., 2009. Structure and Properties of an Organic Rectorite Nanocomposites. . Journal of Polymer Science 114, 2632-2638.

Chivrac, F., Pollet, E., Avérous, L., 2009. Progress in nano-biocomposites based on polysaccharides and nanoclays. Materials Science and Engineering: R: Reports 67, 1-17.

Chorom, M., Rengasamy, P., 1995. Dispersion and zeta potential of pure clays as related to net particle charge under varying pH, electrolyte concentration and cation type. European Journal of Soil Science 46.

Conway, B.E., Ayranci, E., 1999. Effective Ionic Radii and Hydration Volumes for Evaluation of Solution Properties and Ionic Adsorption. Journal of Solution Chemistry, 28.

Cox, A.J., DeWeerd, A.J., Linden, J., 2002. An experiment to measure Mie and Rayleigh total scattering cross sections. American Journal of Physics 70, 620-625.

Credoz, A., Bildstein, O., Jullien, M., Raynal, J., Trotignon, L., Pokrovsky, O., 2011. Mixed-layer illite–smectite reactivity in acidified solutions: Implications for clayey caprock stability in CO2 geological storage. Applied Clay Science 53, 402-408.

Darder, M., Aranda, P., Ruiz-Hitzky, E., 2007. Bionanocomposites: A New Concept of Ecological, Bioinspired, and Functional Hybrid Materials. Advanced Materials 19, 1309-1319.

Darder, M., Colilla, M., Ruiz-Hitzky, E., 2003. Biopolymer−Clay Nanocomposites Based on Chitosan Intercalated in Montmorillonite. . Chemistry of Materials 15, 3374-3780.

Darder, M., Colilla, M., Ruiz-Hitzky, E., 2005. Chitosan–clay nanocomposites: application as electrochemical sensors. Applied Clay Science 28, 199-208.

Darder, M., Mar, Lopez-Blanco, M., Aranda, P., Aznar, A.J., Bravo, J., Ruiz-Hitzky, E., 2006. Microfibrous Chitosan−Sepiolite Nanocomposites. Chemistry of Materials 18, 1602-1610.

Deng, H., Lin, P., Xin, S., Huang, R., Li, W., Du, Y., Zhou, X., Yang, J., 2012. Quaternized chitosan-layered silicate intercalated composites based nanofibrous mats and their antibacterial activity. Carbohydrate polymers 89, 307-313.

Dimas, L.S., Buehler, M.J., 2012. Influence of geometry on mechanical properties of bio-inspired silica-based hierarchical materials. 036024.

Drake, R.M., Gordon, J.E., 1985. Mie scattering. American Journal of Physics 53, 955-962.

Drits, V.A., 2003. Structural and chemical heterogeneity of layer silicates and clay minerals. Clay Minerals 38, 403-432.

Drits, V.A., Sakharov, B.A., 1976. X-ray analysis of Mixed-layer Clay Minerals. Nauka, Moscow.

Drits, V.A., Tchoubar, C., 1990. X-Ray Diffraction by Disordered Lamellar Structures: Theory and Applications Springer-Verlag, Berlin, Heidelberg.

Dutta, P.K., 2004. Chitin and chitosan-Chemistry, properties and applications. Journalof Scientific and Industrial Research 63-1, 20-31.

Ebina, T., Mizukami, F., 2007. Flexible Transparent Clay Films with Heat-Resistant and High Gas-Barrier Properties. Advanced Materials 19, 2450-2453.

Effenberger, H., Mereiter, K., Zemann, J., 1981. Crystal structure refinements of Magnesite, Calcite, Rhodochrosite, Siderite, Smithonite, and Dolomite, with the discussion of some aspects of the stereochemistry of Calcite type carbonates. Zeitschrift fuer Kristallographie 156, 233-243.

Efron, B., Tibshirani, R.J., 1993. An Introduction to the Bootstrap. Chapman-Hall New York.

Elsabee, M.Z., Abdou, E.S., 2013. Chitosan based edible films and coatings: a review. Materials Science and Engineering C 33, 1819-1841.

Farmer, V.C., 1968. Infrared spectroscopy in clay mineral studies. Clay Minerals 7, 373-387.

Farmer, V.C., 1974. The Infrared Spectra of Minerals. Mineralogical Society, London.

Farmer, V.C., Russel, J.D., 1966. Eftects of particle size and structure on the vibrational frequencies of layer silicates. Spectrochimica Acta 22, 389-398.

Farmer, V.C., Russel, J.D., 1967. Infrared absorption spectroscopy in clay studies: Vibrations of the Hydroxyl Group. Clays and Clay Minerals 15, 121-141.

Fernandes, F.M., Baradari, H., Sanchez, C., 2014. Integrative strategies to hybrid lamellar compounds: an integration challenge. Applied Clay Science 100, 2-21.

Ferrage, E., Lanson, B., Malikova, N., A., P., Sakharov, B.A., Drits, V.A., 2005a. New Insights on the Distribution of Interlayer Water in Bi-Hydrated Smectites. Chemistry of Materials 17, 3499-3512.

Ferrage, E., Lanson, B., Sakharov, B.A., Drits, V.A., 2005b. Investigation of smectite hydration properties by modeling experimental X-ray diffraction patterns: Part I. Montmorillonite hydration properties. American Mineralogist 90, 1358-1374.

Ferrage, E., Lanson, B., Sakharov, B.A., Geoffroy, N., Jacquot, E., Drits, V.A., 2007. Investigation of dioctahedral smectite hydration properties by modeling of X-ray diffraction profiles: Influence of layer charge and charge location. American Mineralogist 92, 1731-1743.

Flegler, S.L., Heckman, J.W.J., Klomparens, K.L., 1993. Scanning and transmission electron microscopy: an introduction. Oxford University Press, UK.

Gaines, R.V., Skinner, H.C.W., Foord, E.E., Mason, B., Rosenzweig, A., 1997. Phyllosilicates: Regularly Interstratified Phyllosilicate Group, Danas New Mineralogy, Eighth Edition ed. John Wiley and Sons, Inc. 1819 p. 1515.

Gatineau, L., 1963. Localisation des remplacements isomorphique dans la muscovite. Comptes Rendus Hebdomadaires des Seances de l'Academie des Sciences, Paris 256, 4648-4649.

Gilleland, E., Katz, R.W., 2016. ExtRemes 2.0: An extreme value analysis package in R. Journal of Statistical Software 72, 1-39.

Gillman, G.P., 2011. Charged clays: An environmental solution. Applied Clay Science 53, 361-365.

GoldFields, 2011. Beatrix Gold Mine-Technical Short Form Report 2011, Technical Short Form Report. Gold Fields, Johannesburg, South Africa, p. 22.

Goldstein, J.I., Newbury, D.E., Echlin, P., Joy, D.C., Romig Jr.A.D., Lyman,C.E. , Fiori, C., Lifshin, E., 1992. Scanning Electron Microscopy and X-Ray Microanalysis. Second Edition, Goldstein, J.I. and Echlin, P.(Eds.), Plenum Press, New Yurk, p. 820.

Greene-Kelly, R., 1951. Irrevirsible dehydration in montmorillonite. Clay Minerals Bulletin 1, 221-227.

Greene-Kelly, R., 1952. A test for montmorillonite [19]. Nature 170, 1130-1131.

Grim, R.E., 1962. Applied Clay Mineralogy. McGraw-Hill Book Company, Inc., New York.

Grim, R.E., 1968. Clay Mineralogy, Second ed. McGraw-Hill, New York.

Gruner, J.W., 1934. The crystal structures of talc and pyrophyllite. Zeitschrift fuer Kristallographie, Kristallgeometrie, Kristallphysik, Kristallchemie 88, 412-419.

Gualtieri, A.F., 2000. Accuracy of XRPD QPA using the combinedRietveld-RIR method. . Journal of Applied Crystallography 33, 267-278.

Gualtieri, A.F., Viani, A., Banchio, G., Artioli, G., 2001. Quantitative Phase Analysis of Natural Raw Materials Containing Montmorillonite. Materials Science Forum 378-381, 702-707.

Guggenheim, S., Adams, J.M., Bain, D.C., Bergaya, F., Brigatti, M.F., Drits, V.a., Formoso, M.L.L., Galán, E., Kogure, T., Stanjek, H., 2006. Summary of recommendations of nomenclature committees relevant to clay mineralogy: report of the Association Internationale pour l'Etude des Argiles (AIPEA) Nomenclature Committee for 2006. Clays and Clay Minerals 54, 761-772.

Guggenheim, S., Bailey, S.W., 1975. Refinement of the Margarite Structure in Subgroup Symmetry. The American Mineralogist 60, 1023-1029.

Guggenheim, S., Martin, R.T., 1995. Report definition of clay and clay mineral: joint report of the AIPEA nomenclature and CMS nomenclature committees. Clays and Clay Minerals 43, 255-256.

Guggenheim, S., Van Gross, A.F.K., 2001. Baseline studies of the Clays Minerals Society Source Clays-Thermal Analysis. Clays and Clay Minerals, 49, 433-443.

Guggenheim, S., Zhan, W., 1999. Crystal structures of two partially dehydrated chlorites:-the "modified" chlorite structure. American Mineralogist 84, 1415-1421.

Guven, N., Burnham, C.W., 1967. The crystal structure of 3T muscovite. Zeitschrift fur Kristallographie,Bd. 125, 163-183.

Hanlie, H., Xiaoling, Z., Miao, W., Yijun, H., Dengwen, D., 2008. Morphological Characteristics of (K, Na)-Rectorite from Zhongxiang Rectorite Deposit, Hubei, Central China. Journal of China University of Geosciences 19, 38-46.

Harland, C.E., 1994. Ion Exchange: Theory and Practice, 2nd Revised edition ed. Royal Society of Chemistry Paperbacks.

Hauser, E.A., Le Beau, D.S., 1938. Studies on gelation and film formation of colloidal clays. I. Journal of Physical Chemistry 42, 961-966.

Hauser, E.A., Le Beau, D.S., 1939. Studies on gelation and film formation. II Studies in Clay Films. Journal of Physical Chemistry, 43, 1037-1048.

Hendricks, S.B., Jefferson, M.E., 1939. Polymorphism of the micas. American Mineralogist 24, 729-771.

Hernandez-Haro, N., Ortega-Castro, J., Del Valle, C.P., Munoz-Santiburcio, D., Sainz-Diaz, C.I., Hernandez-Laguna, A., 2013. Computational study of the elastic behavior of the 2M1 muscovite-paragonite series. American Mineralogist 98, 651-664.

Hill, R.J., Howard, C.J., 1987. Quantitative Phase Analysis from Neutron Powder Diffraction Data Using the Rietveid Method Theory. Journal of Applied Crystallography 20, 467-474.

Hollander, M., Wolfe, D.A., 1973. Nonparametric Statistical Methods. John Wiley & Sons, New York.

Hower, J., 1967. Order of mixed-layering in illite-montmorillonite. Clays and Clay Minerals 15, 63-74.

Hower, J., 1981. Shale diagenesis, in: Longstaffe, F.J.e. (Ed.), pp. 60-80.

Huang, W., Xu, H., Xue, Y., Huang, R., Deng, H., Pan, S., 2012. Layer-by-layer immobilization of lysozyme–chitosan–organic rectorite composites on electrospun nanofibrous mats for pork preservation. Food Research International 48, 784-791.

Huang, Y., Ma, X., Liang, G., Yan, H., 2009. Structure and properties of polypropylene/organic rectorite nanocomposites. Clay Minerals 44, 35-50.

Huang, Y., Ma, X.Y., Liang, G.Z., Yan, H.X., Qu, X., Chen, F., 2007. Preparation and characterization of organic rectorite composite gel polymer electrolyte. Clay Minerals 42, 59-68.

ISO, 1996. ISO 13321_1996. Particle size analysis-Photon correlation spectroscopy (PCS). ISO, International Organization for Standardiztaion

ISO, 2017. ISO 22412_2017. Particle size analysis-Dynamic light scattering (DLS).pdf>. ISO, International Organization for Standardiztaion

Jakobsen, H.J., Nielsen, N.C., Lindgreen, H., 1995. Sequences of charged sheets in rectorite. American Mineralogist 80, 247-252.

Jenkins, R., 1999. X-ray Fluorescence Spectrometry Second Edition ed. John Wiley & Sons, Inc., New York / Chichester / Weinheim / Brisbane / Singapore / Toronto.

Kalo, H., Moller, M.W., Kunz, D.A., Breu, J., 2012. How to maximize the aspect ratio of clay nanoplatelets. Nanoscale 4, 5633-5639.

Kawasaki, K., Ebina, T., Mizukami, F., Tsuda, H., Motegi, K., 2010. Development of flexible organo-saponite films and their transparency at high temperature. Applied Clay Science 48, 111-116.

Kaya, A., Yukselen, Y., 2005. Zeta potential of clay minerals and quartz contaminated by heavy metals. Canadian Geotechnical Journal 42, 1280-1289.

Kloprogge, J.T., Frost, L., Hickey, L., 1999. Infrared absorption and emission study of synthetic mica-montmorillonite compared to rectorite, beidellite and paragonite. Journal of Matterials Science Letters 18, 1921-1923.

Kloprogge, J.T., Jansen, J.B.H., Schuiling, R.D., Geus, J.W., 1992. The interlayer collapse during dehydration of synthetic Na0.7-Beidellite: A 23Na solid-state magic-angle spinning NMR study. Clays and Clay Minerals 40, 561-566.

Kodama, H., 1966. The nature of the component layers in rectorite. American Mineralogist 51, 1035-1055.

Kolman, K., Steffen, W., Bugla-Ploskonska, G., Skwara, A., Piglowski, J., Butt, H.J., Kiersnowski, A., 2012. Exfoliation of montmorillonite in protein solutions. Journal of colloid and interface science 374, 135-140.

Kooli, F., Bovey, J., Jones, W., 1997. Dependance of the properties of Ti pillared clays on the host matrix- montmorillonite, saponite and rectorite. Journal of Materials Chemistry 7, 153-158.

Korolev, Y.M., 1971. Rectorite PDF 00-025-0781. Kristallografiya (Crystallography Reports) 16, 250-250.

Kunz, D.A., Max, E., Weinkamer, R., Lunkenbein, T., Breu, J., Fery, A., 2009. Deformation measurements on thin clay tactoids. Small 5, 1816-1820.

Lagaly, G., 2006. Colloid Clay Science, in: Bergaya, F., Theng, B.K.G., Lagaly, G. (Eds.), Handbook of Clay Science, pp. 141-141.

Lagaly, G., Beneke, K., 1991. Intercalation and exchange reactions of clay minerals and non-clay layer compounds. Colloid & Polymer Science 269, 1198-1211.

Lambert, J.B., Mazzola, E.P., 2004. Nuclear magnetic resonance spectroscopy: an introduction to principles, applications, and experimental methods. Pearson education.

Langmuir, I., 1918. The Adsorption of Gases on Plane Surface of Glass, Mica and Platinum. Journal of the American Chemical Society 40, 1361-1403.

Lausen, S.K., Lindgreen, H., Jakobsen, H.J., Nielsen, N.C., 1999. Solid-state 29Si MAS NMR studies of illite and illite-smectite from shale. American Mineralogist 84, 1433-1438.

Lee, S.Y., Kim, S.J., 2002. Expansion of smectite by Hexadecyltrimetylammonium. Clays and Clay Minerals 50, 435-445.

Li, B., Dong, F-X., Wang, X-L., Yang, J., Wang, D.-Y., Wang, Y-Z., 2009. Organically modified rectorite toughened poly(lactic acid): Nanostructures, crystallization and mechanical properties. European Polymer Journal 45, 2996-3003.

Li, Z., Jiang, W-T., 2009. A thermogravimetric investigation of alkylammonium intercalation into rectorite. Thermochimica Acta 483, 58-65.

Li, Z., Jiang, W.T., Hong, H., 2008. An FTIR investigation of hexadecyltrimethylammonium intercalation into rectorite. Spectrochimica acta. Part A, Molecular and biomolecular spectroscopy 71, 1525-1534.

Lin, C., Bailey, S.W., 1984. The crystal structure of paragonite-2M1. The American Mineralogist 69, 122-127.

Ling, Y., Zeng, X., Tan, W., Luo, J., Liu, S., 2015. Quaternized chitosan/rectorite/AgNP nanocomposite catalyst for reduction of 4-nitrophenol. Journal of Alloys and Compounds 647, 463-470.

Lips, A., Hart, P.M., Evabs, I.D., 1992. 5th European Symposiun in Particle Characterisation, 443, 5th European Symposiun in Particle Characterisation, 443, Nurnberg Messe, Nurnberg.

Liu, T., Chen, B., Evans, J.R., 2008. Ordered assemblies of clay nano-platelets. Bioinspiration & biomimetics 3, 016005.

Liu, X., Huang, R., Zhou, X., Cai, T., Chen, J., Shi, X., Deng, H., Luo, W., 2017. Presence of nano-sized chitosan-layered silicate composites protects against toxicity induced by lead ions. Carbohydrate polymers 158, 1-10.

Lopes, A.C., Martins, P., Lanceros-Mendez, S., 2014. Aluminosilicate and aluminosilicate based polymer composites: Present status, applications and future trends. Progress in Surface Science 89, 239-277.

Lu, Y., Chang, P.R., Zheng, P., Ma, X., 2015. Porous 3D network rectorite/chitosan gels: Preparation and adsorption properties. Applied Clay Science 107, 21-27.

Luo, J.J., Daniel, I.M., 2003. Characterization and modeling of mechanical behavior of polymer/clay nanocomposites. Composites Science and Technology, 63, 1607-1616.

Luz, G.M., Mano, J.F., 2009. Biomimetic design of materials and biomaterials inspired by the structure of nacre. Review. Philosophical Transactions of The Royal Society A 367, 1587-1605.

Luz, G.M., Mano, J.F., 2010. Mineralized structures in nature: Examples and inspirations for the design of new composite materials and biomaterials. Composites Science and Technology 70, 1777-1788.

Ma, X.-Y., Liang, G.-Z., Liu, H.-L., Fei, J.-Y., Huang, Y., 2005. Novel intercalated nanocomposites of polypropylene/organic-rectorite/polyethylene-octene elastomer: Rheology, crystallization kinetics, and thermal properties. Journal of Applied Polymer Science 97, 1915-1921.

Ma, X., Lu, H., Liang, G., Yan, H., 2004. Rectorite/thermoplastic polyurethane nanocomposites: Preparation, characterization, and properties. Journal of Applied Polymer Science 93, 608-614.

MacEwan, D.M., Amil, A.R., 1958. Fourier Transform Methods for Studying X-ray Scattering from Lamellar Systems-PartIII-Some Effects for Clay Mineral Studies. Kolloid-Zeitschrifl 162, 93-100.

MacEwan, D.M.C., 1956. A study of an interstratified illite-montmorillonite clay from Wocestershire, England. Clays Journal 4-1, 166-172.

MacEwan, D.M.C., 1957. Fourier Transform Methods for Studying X-ray Scattering from Lamellar Systems-PartII-Interstratifications. Kolloid-Zeitsehri/t, Band 156 . Heft 1 156, 61-67.

Madejova, J., Komadel, P., 2001. Baseline studies of the Clay Minerals Society source clays: Infrared Methods. Clays and Clay Minerals 49, 410-432.

Martin, R.T., Bailey, S.W., Eberl, D.D., Fanning, D.S., Guggenheim, S.,Kodama, H., Pevear, D.R., 1991. Report of the Clay Minerals Society nomenclature committee: revised classification of clay materials. Clays and Clay Minerals 39, 333-335.

Massiot, D., Fayon, F., Capron, M., King, I., LeCalve, S., Alonso, B., Durand, J.-O., Bujoli, B., Gan, Z., Hoatson, G., 2002. Modelling one- and two-dimensional solid-state NMR spectra. Magn. Reson. Chem. 40, 70-76.

McArdle, B.H., Anderson, M.J., 2001. Fitting multivariate models to community data: A comment on distance-based redundancy analysis. Ecology 82, 290-297.

McKelvy, M.L., Britt, T.R., Davis, B.L., Gillie, J.K., Lentz, L.A., Leugers, A., Nyquist, R.A., Putzig, C.L., 1996. Infrared Spectroscopy. Analytical Chemistry 68, 93R-160R.

McNaught, A.D., Wilkinson, A., 1997. IUPAC Compendium of Chemical Terminology, 2nd ed. (the "Gold Book") Second ed. Blackwell Scientific Publications, Oxford.

Minke, R., Blackwell, J., 1978. The Structure of a-Chitin. Journal of Biological Molecules 120, 167-181.

Moller, M.W., Handge, U.A., Kunz, D.A., Lunkenbein, T., Altsta, V., Breu, J., 2010. Tailoring Shear-Stiff, Mika-like Nanoplatelets. ACS Nano 4, 717-724.

Möller, M.W., Hirsemann, D., Haarmann, F., Senker, J., Breu, J., 2010. Facile scalable synthesis of rectorites. Chemistry of Materials 22, 186-196.

Möller, M.W., Hirsemann, D., Haarmann, F., Senker, J., Breu, J., 2010. Facile Scalable Synthesis of Rectorites. Chemistry of Materials 22, 186-196.

Monecke, T., Kohler, S., Kleeberg, R., Herzig, P.M., Gemmel, J.B., 2001. Quantitative phase analysis by the Rietveld method using XRD. . Canadian Mineralogist 39, 1617-1633.

Moore, D.E., Raynolds, R.C., Jr., 1997. X-ray Diffraction and the Identification and Analysis of Clay Minerals, Second ed. Oxford University Press, New York.

Moore, D.M., Hower, J., 1986. Ordered Interstratification of dehydrated and Hydrated Na-Smectite. . Clays and Clay Minerals 34, 379-384.

Morodome, S., Kawamura, K., 2011. In Situ X-ray Diffraction Study of the Swelling of Montmorillonite as Affected by Exchangeable Cations and Temperature. Clays and Clay Minerals 59, 165-175.

Nadeau, P.H., Wilson, M.J., McHardy, W.J., Tait, J.M., 1984. Interparticle diffraction-a new concept for interstratified clays. Clay Minerals 19, 757-769.

Nadeau, P.H., Wilson, M.J., McHardy, W.J., Tait, J.M., 1985. Interstratified clays as Fundamental particles-A reply. Clays and Clay Minerals 33, 560.

Nam, H.-J., Ebina, T., Mizukami, F., 2009a. Formability and properties of self-standing clay film by montmorillonite with different interlayer cations. Colloids and Surfaces A: Physicochemical and Engineering Aspects 346, 158-163.

Nam, H.-J., Ishii, R., Ebina, T., Mizukami, F., 2009b. Flexible transparent self-standing binderless clay film prepared by hydrothermally-treated synthetic clay. Materials Letters 63, 54-57.

Newman, A.C.D., 1987. Chemistry of Clays and Clay Minerals. Mineralogical Society New York.

Newman, A.C.D., Brown, G., 1987. The Chemical Constitution of Clays, in: Newman, A.C.D. (Ed.), Chemistry of Clays and Clay Minerals. Mineralogical Society, New York, pp. 2-128.

Nishiyama, T., Shimoda, S., 1981. Ca-bearing rectorite from Tooho mine, Japan. Clays and Clay MInerals 29, 236-240.

Norrish, K., 1954. The Swelling of Montmorillonite. J.ournal of the Chemical Society, Discussions of the Faraday Society 18, 120-134.

Ostrom, M.E., 1961. Separation of clay minerals from carbonate rocks by using acid. Journal of Sedimentary Research 31, 123-129.

Pan, J.R., Huang, C., Chen, S., Chung, Y.-C., 1999. Evaluation of a modified chitosan biopolymer for coagulation. Colloids and Surfaces A 147, 359-364.

Park, S.Y., Marsh, K.S., Rhim, J.W., 2002. Characteristics of different molecular weight chitosan films affected by the type of organic solvents. Journal of food science 67, 194-197.

Phillips, D.H., Sinnathamby, G., Russell, M.I., Anderson, C., Paksy, a., 2011. Mineralogy of selected geological deposits from the United Kingdom and the Republic of Ireland as possible capping material for low-level radioactive waste disposal facilities. Applied Clay Science 53, 395-401.

Pillai, C.K.S., Paul, W., Sharma, C.P., 2009. Chitin and chitosan polymers: Chemistry, solubility and fiber formation. Progress in Polymer Science 34, 641-678.

Radoslovich, E.W., Norrish, K., 1962. The cell dimensions and symetry of layer silicates-Structure. American Mine. 47, 599-616.

Rayleigh, L., 1881. X.On the electromagnetic theory of light. Philosophical Magazine Series 5 12, 81-101.

Rayleigh, L., 1899. XXXIV.On the transmission of light through an atmosphere containing small particles in suspension, and on the origin of the blue of the sky. Philosophical Magazine Series 5 47, 375-384.

Reddy, M.M., Vivekanandhan, S., Misra, M., Bhatia, S.K., Mohanty, A.K., 2013. Biobased plastics and bionanocomposites: Current status and future opportunities. Progress in Polymer Science 38, 1653-1689.

Reiss, R.D., Thomas, M., 2007. Statistical analysis of extreme values: With applications to insurance, finance, hydrology and other fields: Third edition.

Reynolds, R.C., 1984. Interstratified Clay Minerals, in: Brindley, G.W., Brown, G. (Eds.), Crystal Structures of Clay Minerals and Their X-ray Identification, Second ed. Mineralogical Society, London, UK, pp. 249-303.

Reynolds, R.C., Hower, J., 1970. The nature of interlayering in mixed-layer illite-montmorillonite. Clays and Clay Minerals 18, 25.

Reynolds, R.C., Jr., 1985. NEWMOD, a Computer Program for the Calculation of One-Dimensional Diffraction Patterns of Mixed-Layered Clays. . 8 Brook Road, Hanover, NH, 03755, pp. Newmod2 Release 1.1 2010-Newmod2012 Release 2011.2011 2010.

Rhim, J.-W., Park, H.-M., Ha, C.-S., 2013. Bio-nanocomposites for food packaging applications. Progress in Polymer Science 38, 1629-1652.

Rieder, M., Cavazzini, G., D'Yakonov, Y.S., Frank-Kamenetskii, V.A., Gottardi, G., Guggenheim, S., Koval, P.V., Muler, G., Neiva, A.M.R., Radoslovich, E.W., Robert, J.-L., Sassi, F.P., Takeda, H., Weiss, Z., Wones, D.R., 1998. Nomenclature of the micas. Canadian Mineralogist, 36, 905-911.

Rietveld, H.M., 1969. A profile refinement method for Nuclear and magnetic Structures. Journal of Applied Crystallography 2, 65-71.

Rinaudo, M., 2006. Chitin and chitosan: Properties and applications. Progress in Polymer Science 31, 603-632.

Rintoul, L., Panayiotou, H., Kokot, S., George, G., Cash, G., Frost, R., Byi, T., Fredericks, P., 1998. FTIR spectroscopy. . Analyst 123, 571-577.

Ruiz-Hitzky, E., Darder, M., Aranda, P., 2005. Functional biopolymer nanocomposites based on layered solids. Journal of Materials Chemistry 15, 3650.

Ruiz-Hitzky, E., Darder, M., Fernandes, F.M., Wicklein, B., Alcântara, A.C.S., Aranda, P., 2013. Fibrous clays based bionanocomposites. Progress in Polymer Science 38, 1392-1414.

Russel, J.D., White, J.L., 1968. Infrared study of the thermal decomposition of ammonium rectorite . Paper No. 2618 of the Purdue University Agricultural Expermental Station, Lafayette, Indiana., pp. 181-191.

Russell, J.D., 1987. Infrared methods, in: Wilson, M.J. (Ed.), A Handbook of Determinative Methods in Clay Mineralogy. Chapman and Hall, New York, USA.

Russell, J.D., Farmer, V.C., Velde, B., 1970. Replacement of OH by OD in layer silicates and identification of the vibrations of these groups in infra-red spectra. Mineralogical Magazine 37, 869-879.

Scarlett, N.V.Y., Madsen, I.C., 2006. Quantification of phases with partial or no known crystal structures. Powder Diffraction 21, 278-284.

Schoonheydt, R., 2014. Functional hybrid clay mineral films. Applied Clay Science 96, 9-21.

Schoonheydt, R.A., Johnston, C.T., 2006. Surface and interface chemistry of clay minerals, in: Bergaya, F.T.B.K.G.a.L.G. (Ed.), Handbook of Clay Science. Elsevier Ltd, pp. 87-113.

Sellinger, A., Weiss, M.P., Nguyen, A., Lu, Y., Assink, R.A., Gong, W., Brinker, C.J., 1998. Continuous self-assembly of organic-inorganic nanocomposite coatings that mimic nacre. Nature 394, 256-260.

Shannon, R.D., 1976. Revised Effective Ionic Radii Acta Crystallographica, Section A, 32, 751-767.

Shewring, N.I.E., Jones, T.G.L., Maitland, G., Yarwood, J., 1995. Fourier Transform Infrared Spectroscopic Techniques to Investigate surface hydration processes on bentonite. Journal of colloid and interface science 76, 308-317.

Shimoda, S., Brydon, J.E., 1971. IR studies of some interstratified minerals of mica and montmorillonite. . Clays and Clay Minerals 19, 61-66.

Skipper, N.T., Sposito, G., Chang, F.-R.C., 1995. Monte Carlo Simulation of interlayer molecular structure in swelling clay minerals . 2 . Monolayer Hydrates. Clays and Clay Minerals 43, 294-303.

Smith, J.V., Yoder, H.S., 1956. Experimental and theoretical studies of the mica polymorphs. Mineralogical Magazine 31, 209-235.

Sposito, G., 1984. The surface chemistry of soils. Oxford University Press.

Srodon, J., Eberl, D.D., Drits, V.A., 2000. Evolution of fundamental particle size during illitization. Clays and Clay Minerals 48, 446-458.

Stöter, M., Biersack, B., Reimer, N., Herling, M., Stock, N., Schobert, R., Breu, J., 2014. Ordered Heterostructures of Two Strictly Alternating Types of Nanoreactors. Chemistry of Materials 26, 5412-5419.

Stöter, M., Kunz, D.A., Schmidt, M., Hirsemann, D., Kalo, H., Putz, B., Senker, J., Breu, J., 2013. Nanoplatelets of sodium hectorite showing aspect ratios of approximately 20,000 and superior purity. Langmuir 29, 1280-1285.

Stöter, M., Rosenfeldt, S., Breu, J., 2015. Tunable Exfoliation of Synthetic Clays. Annual Review of Materials Research 45, 129-151.

Strutt, J.W., 1871. Lord Rayleigh. On the Light from the sky, its polarization and colour. Philosophical Magazine, 41, 107-130.

Takeuchi, Y., 1965. Structures of brittle micas. Clays and Clay Minerals 13, 1-25.

Theng, B.K.G., 1974. The chemistry of Clay-Organic Reactions. Adam Hilger Ltd, August 1974.

Theng, B.K.G., 2012. Developments in Clay Science. Elsevier, Radarweg 29, PO Box 211, 1000 AE Amsterdam, The Netherlands The Boulevard, Langford Lane, Kidlington, Oxford OX5 1GB, UK.

Tjong, S.C., 2006. Structural and mechanical properties of polymer nanocomposites. Materials Science and Engineering: R: Reports 53, 73-197.

Tsurko, E.S., Feicht, P., Nehm, F., Ament, K., Rosenfeldt, S., Pietsch, I., Roschmann, K., Kalo, H., Breu, J., 2017. Large Scale Self-Assembly of Smectic Nanocomposite Films by Doctor Blading versus Spray Coating: Impact of Crystal Quality on Barrier Properties. Macromolecules 50, 4344-4350.

Ufer, K., Kleeberg, R., Bergmann, J., Curtius, H., Dohrmann, R., 2008. Refining real structure parameters of disordered layer structures within the rietveld method. Zeitschrift fur Kristallographie, Supplement, 151-158.

Ufer, K., Kleeberg, R., Bergmann, J., Dohrmann, R., 2012a. Rietveld refinement of disordered illite-smectite mixed-layer structures by a recursive algorithm. I: One-dimensional patterns. Clays and Clay Minerals 60, 507-534.

Ufer, K., Kleeberg, R., Bergmann, J., Dohrmann, R., 2012b. Rietveld refinement of disordered illite-smectite mixed-layer structures by a recursive algorithm. II: Powder-pattern refinement and quantitative phase analysis. Clays and Clay Minerals 60, 535-552.

Ugural, A. C.; Fenster, S. K. 2003. Advanced Strength and Applied Elasticity (4th ed.). Prentice-Hall. ISBN 978-0-13-047392-9.

Van Olphen, H., 1987. Dispersion and Flocculation, in: Newman, A.C.D. (Ed.), Chemistry of Clays and Clay Minerals, pp. 203-223.

Van Olphen, H., Fripiat, J.J., 1979. Data Handbook for Clay Materials and Other Non-metallic Minerals Pergamon, Oxford.

Van Vuuren, C.P.J., Snyman, C.P., Boshoff, A.J., 2000. Gold losses from cyanide solutions. Part I: the influence of the silicate minerals. Minerals Engineering 13, 823-830.

Velde, B., 1985. Clay Minerals-A physico-chemical explanation of their occurrence. ELSEVIER Science Publishing Company Inc., Amsterdam, The Nederlands.

Verbeek, C.J.R., Focke, W.W., 2002. Modelling the Young's modulus of platelet reinforced thermoplastic sheet composites. Composites Part A 33, 1697-1704.

Volkov, A.G., Paula, S., Deamer, D.W., 1997. Two mechanisms of permeation of small neutral molecules and hydrated. Bioelectrochemistry and Bioenergetics 42.

von Rahden, H.V.R., 1994. Rectorite: A New Phyllosilicate Species in Witwatersrand Palaeoplacers. Its Genesis and Implications for the Gold-Mining Industry,, in: Petruk, W., Rule, W.A. (Ed.) (Ed.), Process Mineralogy XII: Applications to Environment, Precious Metal, Mineral Beneficiation, Pyrometallurgy, Coal and Refactories. The Minerals, Metals & Materials Society, Warrendale, PA, p. 10.

von Rahden, H.V.R., Slatem, I.C., Corfield, A.A., 1991. Rectorite: A new phyllosilicate species in Witwatersrand palaeplacers., ICAM91 Proceedings, 2-4 Sept1991, CSIR, Pretoria, South Africa.

Voora, V.K., Al-Saidi, W.A., Jordan, K.D., 2011. Density functional theory study of pyrophyllite and M-montmorillonites (M = Li, Na, K, Mg, and Ca): role of dispersion interactions. J Phys Chem A 115, 9695-9703.

Vyalikh, A., Massiot, D., Scheler, U., 2009. Structural characterisation of aluminium layered double hydroxides by 27Al solid-state NMR. Solid State Nuclear Magnetic Resonance 36, 19-23.

Waldo, P., 2011. Clay minerals, carbon storage, and effects of observational scale on computational models. Applied Clay Science 53, 409-413.

Walley, P., Zhang, Y., Evans, J.R., 2012. Self-assembly of montmorillonite platelets during drying. Bioinspiration & biomimetics 7, 046004.

Walther, A., Bjurhager, I., Malho, J.M., Pere, J., Ruokolainen, J., Berglund, L.A., Ikkala, O., 2010. Large-area, lightweight and thick biomimetic composites with superior material properties via fast, economic, and green pathways. Nano letters 10, 2742-2748.

Wang, D.-Y., Costa, F.R., Vyalikh, A., Leuteritz, A., Scheler, U., Jehnichen, D., Wagenknecht, U., Häussler, L., Heinrich, G., 2009a. One-Step Synthesis of Organic LDH and Its Comparison with Regeneration and Anion Exchange Method. Chemistry of Materials 21, 4490-4497.

Wang, J., Wang, L., Yu, H., Zain, U.-A., Chen, Y., Chen, Q., Zhou, W., Zhang, H., Chen, X., 2016. Recent progress on synthesis, property and application of modified chitosan: An overview. International journal of biological macromolecules 88, 333-344.

Wang, X., Du, Y., Luo, J., Lin, B., Kennedy, J.F., 2007. Chitosan/organic rectorite nanocomposite films: Structure, characteristic and drug delivery behaviour. Carbohydrate polymers 69, 41-49.

Wang, X., Du, Y., Luo, J., Yang, J., Wang, W., Kennedy, J.F., 2009b. A novel biopolymer/rectorite nanocomposite with antimicrobial activity. Carbohydrate polymers 77, 449-456.

Wang, X., Du, Y., Yang, J., Wang, X., Shi, X., Hu, Y., 2006. Preparation, characterization and antimicrobial activity of chitosan/layered silicate nanocomposites. Polymer 47, 6738-6744.

Wang, X., Liu, B., Ren, J., Liu, C., Wang, X., Wu, J., Sun, R., 2010. Preparation and characterization of new quaternized carboxymethyl chitosan/rectorite nanocomposite. Composites Science and Technology 70, 1161-1167.

Wang, X., Pei, X., Du, Y., Li, Y., 2008. Quaternized chitosan/rectorite intercalative materials for a gene delivery system. Nanotechnology 19, 375102.

Wang, Y., Zhang, H., Wu, Y., Yang, J., Zhang, L., 2005. Preparation and properties of natural rubber/rectorite nanocomposites. European Polymer Journal 41, 2776-2783.

Wang, Y.C., Huang, T.K., Tung, S.H., Wu, T.M., Lin, J.J., 2013. Self-assembled clay films with a platelet-void multilayered nanostructure and flame-blocking properties. Sci Rep 3, 2621.

Ward, C.R., Gómez-Fernández, F., 2003. Quantitative mineralogical analysis of Spanish roofing slates using the Rietveld method and X-ray powder diffraction data. European Journal of Mineralogy 15, 1051-1062.

Weiner, I., Rust, M., Donnelly, T.D., 2001. Particle size determination: An undergraduate lab in Mie scattering. American Journal of Physics 69, 129-136.

Wilson, M.J., 1987. Handbook of Determinative Methods. Chapman and Hall, New York, USA.

Wooster, W.A., 1977. On the crystal structure of gypsum Ca S O4 (H2 O)2. Zeitschrift fuer Kristallographie, Kristallgeometrie, Kristallphysik, Kristallchemie 94, 375-396.

Xiao, J., Peng, T., Dai, K., Zan, L., Peng, Z., 2007. Hydrothermal synthesis, characterization and its photoactivity of CdS-rectorite nanocomposites. Journal of Solid State Chemistry 180, 3188-3195.

Xu, R., Xin, S., Zhou, X., Li, W., Cao, F., Feng, X., Deng, H., 2012. Quaternized chitosan-organic rectorite intercalated composites based nanoparticles for protein controlled release. Int J Pharm 438, 258-265.

Xu, Y., Ren, X., Hanna, A.A.,2006. Chitosan/Clay Nanocomposites Fil Preparation and Characterization. Journal of Applied Polymer Science, 99, 1684-1691

Yang, L., Liang, G., Zhang, Z., He, S., Wang, J., 2009. Sodium alginate/Na+-rectorite composite films: Preparation, characterization, and properties. Journal of Applied Polymer Science 114, 1235-1240.

Yu, J., Cui, G., Wei, M., Huang, J., 2007. Facile exfoliation of rectorite nanoplatelets in soy protein matrix and reinforced bionanocomposites thereof. Journal of Applied Polymer Science 104, 3367-3377.

Yuan, L., Ma, X.Y., Liang, G.Z., Yun, H., 2007. Organic Rectorite-modified Unsaturated Polyester Resin Composites. Journal of Composite Materials 41, 1051-1065.

Zafar, R., Zia, K.M., Tabasum, S., Jabeen, F., Noreen, A., Zuber, M., 2016. Polysaccharide based bionanocomposites, properties and applications: A review. International journal of biological macromolecules 92, 1012-1024.

Zeng, L., Chen, Y., Zhang, Q., Guo, X., Peng, Y., Xiao, H., Chen, X., Luo, J., 2015a. Adsorption of Cd(II), Cu(II) and Ni(II) ions by cross-linking chitosan/rectorite nano-hybrid composite microspheres. Carbohydrate polymers 130, 333-343.

Zeng, L., Xie, M., Zhang, Q., Kang, Y., Guo, X., Xiao, H., Peng, Y., Luo, J., 2015b. Chitosan/organic rectorite composite for the magnetic uptake of methylene blue and methyl orange. Carbohydrate polymers 123, 89-98.

Zhang, G., Gao, Y., Zhang, Y., G., Y., 2010. Fe2O3-Pillared Rectorite as an Efficient and Stable Fenton-Like Heterogeneous Catalyst for Photodegradation of Organic Contaminants. Environmental science & technology 44, 6384-6389.

Zhang, R., Zheng, P., Ma, X., 2017. Preparation and catalytic properties of magnetic rectorite-chitosan-Au composites. Journal of Alloys and Compounds 690, 381-389.

Zhang, Y., Evans, J.R.G., 2012. Approaches to the manufacture of layered nanocomposites. Applied Surface Science 258, 2098-2102.

Zhao, J., Zhao, X., Jiang, Z., Li, Z., Fan, X., Zhu, J., Wu, H., Su, Y., Yang, D., Pan, F., Shi, J., 2014. Biomimetic and bioinspired membranes: Preparation and application. Progress in Polymer Science 39, 1668-1720.

Zhou, C.-H., Shen, Z.-F., Liu, L.-H., Liu, S.-M., 2011. Preparation and functionality of clay-containing films. Journal of Materials Chemistry 21, 15132-15153.

# APPENDICES

**Appendix I: Chitosan Certificate of Analysis**

# 威東銘生物科技有限公司

# G.T.C. Bio Corporation

## 分 析 报 告 单

**CERTIFICATE OF ANALYSIS**

品名(product):壳聚糖（CHITOSAN）批号（Batch No.）:GC130430G

生产日期（Manufacturing Date）: 20130430 数量（Quantities）:1000KGS

| 项目(Items) | 标准参数(Specifications) | 测试结果(Results) |
|---|---|---|
| 脱乙酰基度（D.A.C）% Deacetylation degree | 85 | 86.7 |
| 粘度(Viscosity) cps | 200-600 | 150cps |
| 不溶物（Insolubles）% | ≤1 | 0.45 |
| 灰份(Ash) % | ≤1 | 1.07 |
| 水分（Moisture）% | ≤10 | 9.2 |
| 重金属（Heavy metals）ppm | ≤10 | Qualified |
| 砷(Arsenic) ppm | ≤1 | Qualified |
| 目数(Particle size) Mesh | 80（95 % Pass） | Qualified |
| 外观(Appearance) | White Powder | Qualified |

分析员(Analyst):WangZunhua 复核员（Verification）:ZhangXueling

# Appendix II. Refinement data for modelled *rt_hkl* phase used for QPA

Table AII. Refinement data for modelled rt_hkl phase used for QPA in this study

```
h k l m d   Th2   I
0 0 1 2 21.70973 4.06676 32.5
0 0 2 2 10.85487 8.13865 90.8
0 1 0 2 8.90950 9.91975 2.59
0 -1 1 2 8.24240 10.72487 1.06
0 1 1 2 8.24240 10.72487 1.06
0 0 3 2 7.23658 12.22086 17.1
0 1 2 2 6.88678 12.84414 2.11
0 -1 2 2 6.88678 12.84414 2.11
0 -1 3 2 5.61715 15.76400 2.57e-028
0 1 3 2 5.61715 15.76400 4.87e-014
0 0 4 2 5.42743 16.31871 15
1 0 0 2 5.06812 17.48442 0.41
1 0 -1 2 4.96423 17.85328 0.936
1 0 1 2 4.90710 18.06287 0.184
1 0 -2 2 4.63896 19.11645 0.00469
0 -1 4 2 4.63512 19.13242 1.28e-015
0 1 4 2 4.63512 19.13242 4e-017
1 0 2 2 4.54689 19.50725 3.22e-075
0 2 0 2 4.45475 19.91482 2.09e-016
1 -1 0 2 4.40525 20.14090 35.8
1 1 0 2 4.40525 20.14090 0.00039
0 -2 1 2 4.36383 20.33412 50.5
0 2 1 2 4.36383 20.33412 6.93
0 0 5 2 4.34195 20.43769 0.602
1 1 -1 2 4.33652 20.46356 3.6
1 -1 -1 2 4.33652 20.46356 0.00484
1 1 1 2 4.29827 20.64761 0.000562
1 -1 1 2 4.29827 20.64761 0.00971
1 0 -3 2 4.20324 21.11975 5.06
0 -2 2 2 4.12120 21.54515 1.31e-007
0 2 2 2 4.12120 21.54515 1.31e-007
1 -1 -2 2 4.11462 21.58000 7.04e-020
1 1 -2 2 4.11462 21.58000 1.12e-009
1 0 3 2 4.10121 21.65141 1.55e-020
```

```
1 -1 2 2 4.04997 21.92871 7.34
1 1 2 2 4.04997 21.92871 7.34
0 -1 5 2 3.90312 22.76459 0.77
0 1 5 2 3.90312 22.76459 20.8
1 -1 -3 2 3.80144 23.38200 0.774
1 1 -3 2 3.80144 23.38200 20.8
0 -2 3 2 3.79358 23.43110 0.339
0 2 3 2 3.79358 23.43110 0.0135
1 0 -4 2 3.75349 23.68497 0.00351
1 1 3 2 3.72546 23.86577 10.2
1 -1 3 2 3.72546 23.86577 7.21
1 0 4 2 3.65684 24.32042 3.33
0 0 6 2 3.61829 24.58356 18.3
1 1 -4 2 3.45905 25.73420 22.5
1 -1 -4 2 3.45905 25.73420 22.5
0 -2 4 2 3.44339 25.85328 0.108
0 2 4 2 3.44339 25.85328 1.11e-016
1 -1 4 2 3.38297 26.32325 37.3
1 1 4 2 3.38297 26.32325 1.68e-023
0 -1 6 2 3.35238 26.56782 1.37e-008
0 1 6 2 3.35238 26.56782 3.18e-026
1 2 0 2 3.34594 26.61989 2.56e-016
1 -2 0 2 3.34594 26.61989 1.37e-008
1 0 -5 2 3.34078 26.66180 7.12e-018
1 -2 -1 2 3.31552 26.86868 0.00097
1 2 -1 2 3.31552 26.86868 61
1 2 1 2 3.29834 27.01131 9.13e-020
1 -2 1 2 3.29834 27.01131 9.13e-020
1 0 5 2 3.25556 27.37308 28.9
1 -2 -2 2 3.21313 27.74171 33.7
1 2 -2 2 3.21313 27.74171 33.7
1 -2 2 2 3.18206 28.01810 1.48
1 2 2 2 3.18206 28.01810 1.48
1 1 -5 2 3.12810 28.51156 5.51
1 -1 -5 2 3.12810 28.51156 519
0 -2 5 2 3.10933 28.68731 26.6
0 2 5 2 3.10933 28.68731 0.645
0 0 7 2 3.10139 28.76238 1.66
1 -1 5 2 3.05782 29.18127 2.16e-017
1 1 5 2 3.05782 29.18127 1.43e-012
```

```
1 -2 -3 2 3.05719 29.18739 4.63e-031
1 2 -3 2 3.05719 29.18739 1.01e-017
1 -2 3 2 3.01725 29.58249 5.08e-020
1 2 3 2 3.01725 29.58249 239
1 0 -6 2 2.98191 29.94123 5.69
0 3 0 2 2.96983 30.06586 0.00304
0 -3 1 2 2.94243 30.35258 57.5
0 3 1 2 2.94243 30.35258 1.09e-012
0 1 7 2 2.92900 30.49507 0.219
0 -1 7 2 2.92900 30.49507 2.75
1 0 6 2 2.90907 30.70915 62
1 -2 -4 2 2.87041 31.13316 32
1 2 -4 2 2.87041 31.13316 0.0398
0 3 2 2 2.86456 31.19843 59.6
0 -3 2 2 2.86456 31.19843 0.0609
1 1 -6 2 2.82774 31.61521 2.18
1 -1 -6 2 2.82774 31.61521 12.1
1 2 4 2 2.82649 31.62955 50.6
1 -2 4 2 2.82649 31.62955 0.148
0 -2 6 2 2.80857 31.83663 27.9
0 2 6 2 2.80857 31.83663 48.1
1 1 6 2 2.76539 32.34727 82.4
1 -1 6 2 2.76539 32.34727 2.06
0 -3 3 2 2.74747 32.56419 19.8
0 3 3 2 2.74747 32.56419 19.8
0 0 8 2 2.71372 32.98066 102
1 0 -7 2 2.67672 33.44981 2.58
1 -2 -5 2 2.67270 33.50156 55.5
1 2 -5 2 2.67270 33.50156 44.5
1 -2 5 2 2.62846 34.08250 82.4
1 2 5 2 2.62846 34.08250 9.59
1 0 7 2 2.61512 34.26178 0.692
0 -3 4 2 2.60530 34.39491 0.0498
0 3 4 2 2.60530 34.39491 0.542
0 -1 8 2 2.59597 34.52243 45
0 1 8 2 2.59597 34.52243 45
1 -1 -7 2 2.56353 34.97332 0.03
1 1 -7 2 2.56353 34.97332 0.057
1 3 0 2 2.56232 34.99034 2.17
1 -3 0 2 2.56232 34.99034 2.17
```

```
1 3 -1 2 2.54858 35.18510 8.91e-008
1 -3 -1 2 2.54858 35.18510 2.11e-007
0 2 7 2 2.54530 35.23199 1.99e-006
0 -2 7 2 2.54530 35.23199 18.3
1 3 1 2 2.54075 35.29709 209
1 -3 1 2 2.54075 35.29709 167
2 0 0 2 2.53406 35.39338 3.25
2 0 -1 2 2.52458 35.53065 7.61
2 0 1 2 2.50943 35.75245 162
1 -1 7 2 2.50926 35.75490 4.63
1 1 7 2 2.50926 35.75490 0.067
1 3 -2 2 2.50119 35.87426 2.9e-007
1 -3 -2 2 2.50119 35.87426 3.26
1 3 2 2 2.48645 36.09422 4.83
1 -3 2 2 2.48645 36.09422 4.61e-007
2 0 -2 2 2.48211 36.15938 79.8
1 2 -6 2 2.47799 36.22158 32.8
1 -2 -6 2 2.47799 36.22158 20
2 0 2 2 2.45355 36.59520 162
0 -3 5 2 2.45128 36.63025 5.56
0 3 5 2 2.45128 36.63025 52.5
2 -1 0 2 2.43739 36.84652 6.97
2 1 0 2 2.43739 36.84652 12.4
1 -2 6 2 2.43572 36.87269 2.84
1 2 6 2 2.43572 36.87269 0.799
2 -1 -1 2 2.42895 36.97913 4.46
2 1 -1 2 2.42895 36.97913 1.03
1 -3 -3 2 2.42549 37.03389 22.4
1 3 -3 2 2.42549 37.03389 0.444
1 0 -8 2 2.41881 37.13983 11.1
2 -1 1 2 2.41545 37.19345 3.95
2 1 1 2 2.41545 37.19345 20.7
0 0 9 2 2.41219 37.24546 2.54
2 0 -3 2 2.41141 37.25803 47.5
1 3 3 2 2.40540 37.35458 107
1 -3 3 2 2.40540 37.35458 54.7
2 -1 -2 2 2.39106 37.58693 3.7
2 1 -2 2 2.39106 37.58693 2.53
2 0 3 2 2.37240 37.89384 22.4
1 0 8 2 2.36674 37.98782 134
```

```
2 1 2 2 2.36549 38.00868 39.5
2 -1 2 2 2.36549 38.00868 97.2
1 1 -8 2 2.33431 38.53622 8.24
1 -1 -8 2 2.33431 38.53622 51
1 -3 -4 2 2.32899 38.62777 37.7
1 3 -4 2 2.32899 38.62777 14.3
0 -1 9 2 2.32836 38.63860 6.68
0 1 9 2 2.32836 38.63860 53.2
2 1 -3 2 2.32766 38.65078 16.2
2 -1 -3 2 2.32766 38.65078 21.9
2 0 -4 2 2.31948 38.79252 31
0 2 8 2 2.31756 38.82592 15.6
0 -2 8 2 2.31756 38.82592 15.6
1 3 4 2 2.30534 39.03998 9.91
1 -3 4 2 2.30534 39.03998 5.23
0 -3 6 2 2.29559 39.21259 5.32
0 3 6 2 2.29559 39.21259 21.4
1 2 -7 2 2.29439 39.23402 54
1 -2 -7 2 2.29439 39.23402 29.9
2 -1 3 2 2.29251 39.26743 0.0573
2 1 3 2 2.29251 39.26743 0.0573
1 -1 8 2 2.28741 39.35863 1.97
1 1 8 2 2.28741 39.35863 157
2 0 4 2 2.27345 39.61045 24.8
1 -2 7 2 2.25524 39.94384 254
1 2 7 2 2.25524 39.94384 0.133
2 1 -4 2 2.24466 40.14016 5.82
2 -1 -4 2 2.24466 40.14016 0.253
0 4 0 2 2.22738 40.46521 2.91
1 3 -5 2 2.21960 40.61324 0.413
1 -3 -5 2 2.21960 40.61324 260
0 -4 1 2 2.21574 40.68700 0.16
0 4 1 2 2.21574 40.68700 13.1
2 0 -5 2 2.21393 40.72178 53.9
2 1 4 2 2.20286 40.93556 4.44e-005
2 -1 4 2 2.20286 40.93556 7.8
2 -2 0 2 2.20263 40.94012 1.81e-009
2 2 0 2 2.20263 40.94012 29.6
1 0 -9 2 2.20051 40.98127 0.000164
2 -2 -1 2 2.19639 41.06152 26.4
```

```
2 2 -1 2 2.19639 41.06152 11.6
1 3 5 2 2.19406 41.10713 0.00378
1 -3 5 2 2.19406 41.10713 0.234
2 -2 1 2 2.18639 41.25789 91.6
2 2 1 2 2.18639 41.25789 0.000165
0 -4 2 2 2.18191 41.34647 34.3
0 4 2 2 2.18191 41.34647 126
0 0 10 2 2.17097 41.56445 57.5
2 2 -2 2 2.16826 41.61892 109
2 -2 -2 2 2.16826 41.61892 8.15
2 0 5 2 2.16410 41.70260 0.00306
1 0 9 2 2.15631 41.86037 62.9
2 -2 2 2 2.14914 42.00662 182
2 2 2 2 2.14914 42.00662 0.0202
2 -1 -5 2 2.14859 42.01784 2.48
2 1 -5 2 2.14859 42.01784 0.578
0 -3 7 2 2.14499 42.09170 33.7
0 3 7 2 2.14499 42.09170 69.5
1 1 -9 2 2.13632 42.27080 7.08e-008
1 -1 -9 2 2.13632 42.27080 0.000515
0 4 3 2 2.12882 42.42687 44.6
0 -4 3 2 2.12882 42.42687 44.6
1 2 -8 2 2.12568 42.49261 79.1
1 -2 -8 2 2.12568 42.49261 79.4
0 -2 9 2 2.12118 42.58705 30.6
0 2 9 2 2.12118 42.58705 20
2 -2 -3 2 2.12065 42.59829 42.7
2 2 -3 2 2.12065 42.59829 93.1
0 -1 10 2 2.10926 42.83962 18.9
0 1 10 2 2.10926 42.83962 15.7
1 3 -6 2 2.10425 42.94669 17.1
1 -3 -6 2 2.10425 42.94669 14.3
2 -1 5 2 2.10295 42.97443 0.0619
2 1 5 2 2.10295 42.97443 14.3
2 0 -6 2 2.10162 43.00305 0.0605
1 -1 9 2 2.09580 43.12841 0.114
1 1 9 2 2.09580 43.12841 0.503
2 -2 3 2 2.09397 43.16806 30.8
2 2 3 2 2.09397 43.16806 25.3
1 -2 8 2 2.09008 43.25245 204
```

```
1 2 8 2 2.09008 43.25245 173
1 -3 6 2 2.07817 43.51278 19.1
1 3 6 2 2.07817 43.51278 133
0 -4 4 2 2.06060 43.90309 11.2
0 4 4 2 2.06060 43.90309 64.9
2 2 -4 2 2.05731 43.97690 131
2 -2 -4 2 2.05731 43.97690 146
2 0 6 2 2.05061 44.12824 16.2
2 1 -6 2 2.04548 44.24463 81.6
2 -1 -6 2 2.04548 44.24463 58.9
1 -4 0 2 2.03913 44.38967 2.25
1 4 0 2 2.03913 44.38967 4.79
1 -4 -1 2 2.03219 44.54948 17.3
1 4 -1 2 2.03219 44.54948 63.6
1 -4 1 2 2.02821 44.64152 29.8
1 4 1 2 2.02821 44.64152 76
2 -2 4 2 2.02499 44.71650 86.1
2 2 4 2 2.02499 44.71650 172
1 0 -10 2 2.01475 44.95614 38.6
1 -4 -2 2 2.00792 45.11751 25
1 4 -2 2 2.00792 45.11751 72.9
0 -3 8 2 2.00332 45.22662 13.4
0 3 8 2 2.00332 45.22662 62.6
1 -4 2 2 2.00027 45.29962 60.5
1 4 2 2 2.00027 45.29962 33.2
2 -1 6 2 1.99836 45.34525 68.6
2 1 6 2 1.99836 45.34525 12.5
1 3 -7 2 1.98830 45.58751 305
1 -3 -7 2 1.98830 45.58751 79.7
2 0 -7 2 1.98795 45.59605 53.6
2 -2 -5 2 1.98259 45.72631 107
2 2 -5 2 1.98259 45.72631 72.8
0 -4 5 2 1.98182 45.74503 29.1
0 4 5 2 1.98182 45.74503 38.9
1 0 10 2 1.97697 45.86357 11.8
0 0 11 2 1.97361 45.94617 45
1 2 -9 2 1.97293 45.96289 81.6
1 -2 -9 2 1.97293 45.96289 31.7
1 -4 -3 2 1.96811 46.08189 72.9
1 4 -3 2 1.96811 46.08189 25.8
```

```
1 1 -10 2 1.96513 46.15595 17.3
1 -1 -10 2 1.96513 46.15595 36.8
1 -3 7 2 1.96266 46.21738 12.8
1 3 7 2 1.96266 46.21738 26.3
1 -4 3 2 1.95734 46.35042 32.7
1 4 3 2 1.95734 46.35042 7.8
0 -2 10 2 1.95156 46.49563 181
0 2 10 2 1.95156 46.49563 123
2 -2 5 2 1.94656 46.62204 16.2
2 2 5 2 1.94656 46.62204 10.7
1 -2 9 2 1.94089 46.76649 24.3
1 2 9 2 1.94089 46.76649 24.3
2 -1 -7 2 1.94024 46.78306 9.88
2 1 -7 2 1.94024 46.78306 33.6
2 0 7 2 1.93766 46.84906 235
1 -1 10 2 1.93003 47.04535 7.3
1 1 10 2 1.93003 47.04535 7.3
2 -3 0 2 1.92769 47.10595 35.8
2 3 0 2 1.92769 47.10595 9.06
0 -1 11 2 1.92690 47.12635 3.54
0 1 11 2 1.92690 47.12635 41.7
2 -3 -1 2 1.92351 47.21456 29.8
2 3 -1 2 1.92351 47.21456 25.6
2 -3 1 2 1.91678 47.39042 1.92
2 3 1 2 1.91678 47.39042 0.57
1 -4 -4 2 1.91550 47.42395 272
1 4 -4 2 1.91550 47.42395 199
2 -3 -2 2 1.90452 47.71422 65
2 3 -2 2 1.90452 47.71422 108
1 -4 4 2 1.90228 47.77400 9.61
1 4 4 2 1.90228 47.77400 41.9
2 -2 -6 2 1.90072 47.81571 335
2 2 -6 2 1.90072 47.81571 16.2
0 -4 6 2 1.89679 47.92091 0.279
0 4 6 2 1.89679 47.92091 25.7
2 -1 7 2 1.89340 48.01218 0.0328
2 1 7 2 1.89340 48.01218 29.8
2 -3 2 2 1.89153 48.06266 43.1
2 3 2 2 1.89153 48.06266 0.0189
2 0 -8 2 1.87674 48.46542 0.987
```

```
1 3 -8 2 1.87547 48.50042 22.6
1 -3 -8 2 1.87547 48.50042 30.2
0 -3 9 2 1.87238 48.58562 11.2
0 3 9 2 1.87238 48.58562 27.8
2 -3 -3 2 1.87201 48.59577 512
2 3 -3 2 1.87201 48.59577 301
2 -2 6 2 1.86273 48.85376 7.7
2 2 6 2 1.86273 48.85376 7.06
1 0 -11 2 1.85556 49.05488 1.19
2 -3 3 2 1.85359 49.11066 129
2 3 3 2 1.85359 49.11066 0.0864
1 4 -5 2 1.85324 49.12045 0.195
1 -4 -5 2 1.85324 49.12045 3.46
1 -3 8 2 1.85089 49.18705 301
1 3 8 2 1.85089 49.18705 40.6
1 -4 5 2 1.83830 49.54642 0.226
1 4 5 2 1.83830 49.54642 2.8
2 1 -8 2 1.83644 49.59985 257
2 -1 -8 2 1.83644 49.59985 85.6
1 2 -10 2 1.83573 49.62046 31.5
1 -2 -10 2 1.83573 49.62046 91.8
2 0 8 2 1.82842 49.83236 144
2 -3 -4 2 1.82802 49.84408 52.5
2 3 -4 2 1.82802 49.84408 41.1
1 0 11 2 1.82304 49.98939 157
1 1 -11 2 1.81658 50.17941 227
1 -1 -11 2 1.81658 50.17941 151
2 -2 -7 2 1.81539 50.21470 0.131
2 2 -7 2 1.81539 50.21470 240
0 -4 7 2 1.80915 50.40007 0.28
0 4 7 2 1.80915 50.40007 12.8
0 0 12 2 1.80914 50.40013 31.2
1 -2 10 2 1.80702 50.46352 33.7
1 2 10 2 1.80702 50.46352 17.7
2 -3 4 2 1.80523 50.51717 26.2
2 3 4 2 1.80523 50.51717 9.53
0 -2 11 2 1.80445 50.54040 95.3
0 2 11 2 1.80445 50.54040 1.27
2 -1 8 2 1.79109 50.94425 354
2 1 8 2 1.79109 50.94425 240
```

```
1 -1 11 2 1.78604 51.09879 80.6
1 1 11 2 1.78604 51.09879 109
1 4 -6 2 1.78450 51.14600 57.6
1 -4 -6 2 1.78450 51.14600 46.4
0 5 0 2 1.78190 51.22599 20
2 -2 7 2 1.77685 51.38218 0.248
2 2 7 2 1.77685 51.38218 0.269
0 -5 1 2 1.77593 51.41079 7.71
0 5 1 2 1.77593 51.41079 7.71
2 -3 -5 2 1.77499 51.43980 21.6
2 3 -5 2 1.77499 51.43980 21.6
0 -1 12 2 1.77296 51.50311 4.84
0 1 12 2 1.77296 51.50311 9.48
2 0 -9 2 1.77044 51.58189 376
1 -4 6 2 1.76851 51.64217 87.9
1 4 6 2 1.76851 51.64217 20.2
1 3 -9 2 1.76806 51.65654 88.1
1 -3 -9 2 1.76806 51.65654 88.1
0 -5 2 2 1.75837 51.96239 42
0 5 2 2 1.75837 51.96239 171
0 -3 10 2 1.75262 52.14539 214
0 3 10 2 1.75262 52.14539 106
2 -3 5 2 1.74900 52.26154 29.7
2 3 5 2 1.74900 52.26154 257
1 -3 9 2 1.74488 52.39434 17
1 3 9 2 1.74488 52.39434 76.6
2 -1 -9 2 1.73649 52.66708 19.2
2 1 -9 2 1.73649 52.66708 560
0 -5 3 2 1.73022 52.87261 14.6
0 5 3 2 1.73022 52.87261 110
2 -2 -8 2 1.72953 52.89541 44.1
2 2 -8 2 1.72953 52.89541 130
2 0 9 2 1.72480 53.05170 64.3
0 -4 8 2 1.72170 53.15484 25.6
0 4 8 2 1.72170 53.15484 23.1
1 0 -12 2 1.71812 53.27406 207
2 -3 -6 2 1.71552 53.36126 85.5
2 3 -6 2 1.71552 53.36126 17.8
1 2 -11 2 1.71291 53.44916 352
1 -2 -11 2 1.71291 53.44916 151
```

```
1 4 -7 2 1.71213 53.47531 31.7
1 -4 -7 2 1.71213 53.47531 208
1 -4 7 2 1.69568 54.03618 349
1 4 7 2 1.69568 54.03618 26.3
2 -1 9 2 1.69336 54.11615 283
2 1 9 2 1.69336 54.11615 109
0 -5 4 2 1.69299 54.12889 7.61
0 5 4 2 1.69299 54.12889 100
2 -2 8 2 1.69149 54.18102 21.1
2 2 8 2 1.69149 54.18102 10.5
1 0 12 2 1.68991 54.23559 26.1
3 0 0 2 1.68937 54.25434 7.32
3 0 -1 2 1.68770 54.31264 1.86
2 -3 6 2 1.68744 54.32172 2.85
2 3 6 2 1.68744 54.32172 1.74
1 -2 11 2 1.68723 54.32904 15
1 2 11 2 1.68723 54.32904 15.5
1 1 -12 2 1.68704 54.33549 13.1
1 -1 -12 2 1.68704 54.33549 120
1 -5 0 2 1.68103 54.54601 46.6
1 5 0 2 1.68103 54.54601 37.3
3 0 1 2 1.68088 54.55097 59.1
1 -5 -1 2 1.67713 54.68333 65.4
1 5 -1 2 1.67713 54.68333 15.6
0 -2 12 2 1.67619 54.71652 40.3
0 2 12 2 1.67619 54.71652 13.7
3 0 -2 2 1.67595 54.72509 154
1 -5 1 2 1.67489 54.76249 36.9
1 5 1 2 1.67489 54.76249 89.6
2 -4 0 2 1.67297 54.83066 110
2 4 0 2 1.67297 54.83066 173
2 0 -10 2 1.67039 54.92255 13.2
2 -4 -1 2 1.67023 54.92804 144
2 4 -1 2 1.67023 54.92804 128
0 0 13 2 1.66998 54.93715 35.4
1 3 -10 2 1.66728 55.03346 28
1 -3 -10 2 1.66728 55.03346 21
2 -4 1 2 1.66582 55.08580 22
2 4 1 2 1.66582 55.08580 38.3
1 -5 -2 2 1.66341 55.17267 43.2
```

```
1 5 -2 2 1.66341 55.17267 24.5
3 0 2 2 1.66269 55.19864 61.5
1 -1 12 2 1.66031 55.28437 41.5
1 1 12 2 1.66031 55.28437 32
3 -1 0 2 1.65980 55.30288 62.5
3 1 0 2 1.65980 55.30288 32.4
1 -5 2 2 1.65905 55.32996 53.8
1 5 2 2 1.65905 55.32996 43.3
3 -1 -1 2 1.65821 55.36043 33
3 1 -1 2 1.65821 55.36043 39.5
2 -4 -2 2 1.65776 55.37666 17.8
2 4 -2 2 1.65776 55.37666 15.8
3 0 -3 2 1.65474 55.48636 15.4
2 -3 -7 2 1.65200 55.58641 78.8
2 3 -7 2 1.65200 55.58641 106
3 -1 1 2 1.65175 55.59573 35.6
3 1 1 2 1.65175 55.59573 25.3
2 -4 2 2 1.64917 55.69018 37.6
2 4 2 2 1.64917 55.69018 31.2
0 -5 5 2 1.64848 55.71549 30.7
0 5 5 2 1.64848 55.71549 50.5
3 -1 -2 2 1.64706 55.76766 34.8
3 1 -2 2 1.64706 55.76766 87.3
1 -3 10 2 1.64569 55.81829 54.8
1 3 10 2 1.64569 55.81829 158
2 2 -9 2 1.64527 55.83379 63
2 -2 -9 2 1.64527 55.83379 15.8
0 -3 11 2 1.64375 55.88996 8.66
0 3 11 2 1.64375 55.88996 9.86
2 1 -10 2 1.64178 55.96265 7.47
2 -1 -10 2 1.64178 55.96265 14.1
0 -1 13 2 1.64139 55.97707 55
0 1 13 2 1.64139 55.97707 31.3
1 -5 -3 2 1.64057 56.00783 128
1 5 -3 2 1.64057 56.00783 55.3
1 4 -8 2 1.63850 56.08485 5.2
1 -4 -8 2 1.63850 56.08485 38.4
0 -4 9 2 1.63643 56.16175 11.1
0 4 9 2 1.63643 56.16175 9.1
2 -4 -3 2 1.63619 56.17092 145
```

```
2 4 -3 2 1.63619 56.17092 27.1
3 0 3 2 1.63570 56.18924 10.4
3 -1 2 2 1.63447 56.23534 57.3
3 1 2 2 1.63447 56.23534 4.13
1 -5 3 2 1.63431 56.24133 123
1 5 3 2 1.63431 56.24133 57.9
2 0 10 2 1.62778 56.48701 98.8
3 -1 -3 2 1.62692 56.51955 39.9
3 1 -3 2 1.62692 56.51955 40.4
3 0 -4 2 1.62514 56.58709 89.7
2 -4 3 2 1.62384 56.63640 279
2 4 3 2 1.62384 56.63640 89.6
2 -3 7 2 1.62280 56.67601 46.9
2 3 7 2 1.62280 56.67601 81.5
1 -4 8 2 1.62202 56.70555 339
1 4 8 2 1.62202 56.70555 64.6
1 -5 -4 2 1.60972 57.17886 104
1 5 -4 2 1.60972 57.17886 162
3 -1 3 2 1.60881 57.21407 155
3 1 3 2 1.60881 57.21407 111
2 -2 9 2 1.60845 57.22822 248
2 2 9 2 1.60845 57.22822 26.3
2 -4 -4 2 1.60657 57.30139 21.1
2 4 -4 2 1.60657 57.30139 44.7
1 2 -12 2 1.60303 57.43962 12.3
1 -2 -12 2 1.60303 57.43962 94.3
1 -5 4 2 1.60185 57.48592 34.2
1 5 4 2 1.60185 57.48592 34.5
2 -1 10 2 1.60127 57.50839 19.9
2 1 10 2 1.60127 57.50839 7.01
3 0 4 2 1.60120 57.51121 33.8
3 -1 -4 2 1.59876 57.60732 122
3 1 -4 2 1.59876 57.60732 166
0 -5 6 2 1.59857 57.61499 50.1
0 5 6 2 1.59857 57.61499 96.2
1 0 -13 2 1.59856 57.61509 55.5
2 4 4 2 1.59103 57.91363 219
2 -4 4 2 1.59103 57.91363 145
3 0 -5 2 1.58850 58.01484 89.9
2 -3 -8 2 1.58651 58.09436 187
```

```
2 3 -8 2 1.58651 58.09436 112
1 -2 12 2 1.58004 58.35506 226
1 2 12 2 1.58004 58.35506 98.9
3 -2 0 2 1.57960 58.37293 17.7
3 2 0 2 1.57960 58.37293 69.5
3 -2 -1 2 1.57823 58.42850 24.1
3 2 -1 2 1.57823 58.42850 220
2 0 -11 2 1.57719 58.47066 25.1
3 -1 4 2 1.57595 58.52109 36.6
3 1 4 2 1.57595 58.52109 8.67
1 0 13 2 1.57391 58.60452 4.36
1 3 -11 2 1.57365 58.61502 4.46
1 -3 -11 2 1.57365 58.61502 175
1 1 -13 2 1.57344 58.62384 17.1
1 -1 -13 2 1.57344 58.62384 9.61
3 -2 1 2 1.57266 58.65577 36
3 2 1 2 1.57266 58.65577 18.1
1 5 -5 2 1.57223 58.67304 63.3
1 -5 -5 2 1.57223 58.67304 36.3
2 -4 -5 2 1.57022 58.75581 46.3
2 4 -5 2 1.57022 58.75581 40.6
3 -2 -2 2 1.56861 58.82189 56.9
3 2 -2 2 1.56861 58.82189 19.2
1 4 -9 2 1.56541 58.95413 34.6
1 -4 -9 2 1.56541 58.95413 30.5
2 2 -10 2 1.56405 59.01035 87
2 -2 -10 2 1.56405 59.01035 92.1
3 -1 -5 2 1.56383 59.01928 56.2
3 1 -5 2 1.56383 59.01928 73
0 -2 13 2 1.56371 59.02428 37.1
0 2 13 2 1.56371 59.02428 56.1
1 -5 5 2 1.56308 59.05054 95.9
1 5 5 2 1.56308 59.05054 88
3 0 5 2 1.56067 59.15070 74.3
3 -2 2 2 1.55772 59.27400 95.6
3 2 2 2 1.55772 59.27400 22.8
2 -3 8 2 1.55699 59.30444 15.5
2 3 8 2 1.55699 59.30444 50.2
0 -4 10 2 1.55467 59.40209 116
0 4 10 2 1.55467 59.40209 27.8
```

```
1 -3 11 2 1.55367 59.44405 12.7
1 3 11 2 1.55367 59.44405 24.4
2 1 -11 2 1.55305 59.47029 9.63
2 -1 -11 2 1.55305 59.47029 9.87
2 -4 5 2 1.55214 59.50866 26.9
2 4 5 2 1.55214 59.50866 25.9
3 -2 -3 2 1.55118 59.54892 24.5
3 2 -3 2 1.55118 59.54892 6.99
0 0 14 2 1.55069 59.56960 10.7
1 -1 13 2 1.54991 59.60275 50.3
1 1 13 2 1.54991 59.60275 18.8
1 -4 9 2 1.54926 59.63057 168
1 4 9 2 1.54926 59.63057 12.2
3 0 -6 2 1.54632 59.75528 40.1
0 -5 7 2 1.54504 59.80973 92.6
0 5 7 2 1.54504 59.80973 169
0 -3 12 2 1.54504 59.80979 506
0 3 12 2 1.54504 59.80979 114
2 0 11 2 1.53771 60.12415 139
3 -1 5 2 1.53727 60.14334 11.2
3 1 5 2 1.53727 60.14334 3.13
3 -2 3 2 1.53546 60.22127 64.6
3 2 3 2 1.53546 60.22127 278
1 5 -6 2 1.52960 60.47600 27.1
1 -5 -6 2 1.52960 60.47600 39.7
2 -2 10 2 1.52891 60.50641 7.13
2 2 10 2 1.52891 60.50641 79.9
2 -4 -6 2 1.52859 60.52014 11.5
2 4 -6 2 1.52859 60.52014 9.73
0 -1 14 2 1.52773 60.55806 100
0 1 14 2 1.52773 60.55806 11.9
3 -2 -4 2 1.52672 60.60229 115
3 2 -4 2 1.52672 60.60229 115
3 -1 -6 2 1.52354 60.74191 46.8
3 1 -6 2 1.52354 60.74191 46.8
2 3 -9 2 1.52072 60.86654 64.3
2 -3 -9 2 1.52072 60.86654 31.2
1 -5 6 2 1.51950 60.92062 159
1 5 6 2 1.51950 60.92062 440
3 0 6 2 1.51563 61.09276 11.6
```

```
2 -1 11 2 1.51531 61.10720 273
2 1 11 2 1.51531 61.10720 99.4
2 -4 6 2 1.50863 61.40708 27.7
2 4 6 2 1.50863 61.40708 143
3 -2 4 2 1.50682 61.48853 82.2
3 2 4 2 1.50682 61.48853 496
1 2 -13 2 1.50462 61.58826 81.2
1 -2 -13 2 1.50462 61.58826 78.3
3 0 -7 2 1.50012 61.79332 296
3 -2 -5 2 1.49622 61.97222 29.4
3 2 -5 2 1.49622 61.97222 2.23
1 4 -10 2 1.49417 62.06640 2.25
1 -4 -10 2 1.49417 62.06640 14.8
3 -1 6 2 1.49417 62.06672 2.4
3 1 6 2 1.49417 62.06672 2.49
1 0 -14 2 1.49380 62.08345 0.977
2 -3 9 2 1.49150 62.18980 1.01
2 3 9 2 1.49150 62.18980 3.09
2 0 -12 2 1.49096 62.21525 2.42
0 -5 8 2 1.48950 62.28301 35.2
0 5 8 2 1.48950 62.28301 9.72
1 3 -12 2 1.48718 62.39081 101
1 -3 -12 2 1.48718 62.39081 336
2 2 -11 2 1.48676 62.41040 4.77
2 -2 -11 2 1.48676 62.41040 9.73
```
**0 6 0 2 1.48492 62.49665 10.7**
```
1 -2 13 2 1.48401 62.53915 42.2
1 2 13 2 1.48401 62.53915 16.9
1 5 -7 2 1.48329 62.57293 111
1 -5 -7 2 1.48329 62.57293 151
2 -4 -7 2 1.48314 62.57980 167
2 4 -7 2 1.48314 62.57980 64.4
0 -6 1 2 1.48146 62.65918 115
0 6 1 2 1.48146 62.65918 1.41e+003
3 -1 -7 2 1.47930 62.76099 11.5
3 1 -7 2 1.47930 62.76099 29
1 -4 10 2 1.47857 62.79539 47.8
1 4 10 2 1.47857 62.79539 165
0 -4 11 2 1.47716 62.86207 11.2
0 4 11 2 1.47716 62.86207 26.3
```

```
1 1 -14 2 1.47324 63.04857 18.9
1 -1 -14 2 1.47324 63.04857 7.12
3 -2 5 2 1.47290 63.06485 0.118
3 2 5 2 1.47290 63.06485 0.371
1 -5 7 2 1.47255 63.08139 10.5
1 5 7 2 1.47255 63.08139 35.5
1 0 14 2 1.47211 63.10255 2.26
0 -6 2 2 1.47121 63.14534 14
0 6 2 2 1.47121 63.14534 16.5
2 1 -12 2 1.47051 63.17922 41.9
2 -1 -12 2 1.47051 63.17922 7.96
1 -3 12 2 1.46877 63.26248 74
1 3 12 2 1.46877 63.26248 3.94
3 -3 0 2 1.46842 63.27952 5.18
3 3 0 2 1.46842 63.27952 24.9
3 0 7 2 1.46753 63.32247 13.1
3 -3 -1 2 1.46732 63.33250 162
3 3 -1 2 1.46732 63.33250 8.07
0 -2 14 2 1.46450 63.46840 5.11
0 2 14 2 1.46450 63.46840 18
3 -3 1 2 1.46283 63.54924 12.4
3 3 1 2 1.46283 63.54924 32.5
2 -4 7 2 1.46190 63.59439 23
2 4 7 2 1.46190 63.59439 13.2
3 -2 -6 2 1.46081 63.64737 0.00783
3 2 -6 2 1.46081 63.64737 84
3 -3 -2 2 1.45958 63.70773 17
3 3 -2 2 1.45958 63.70773 3.67
2 -5 0 2 1.45761 63.80389 5.7
2 5 0 2 1.45761 63.80389 0.0246
2 3 -10 2 1.45590 63.88762 26.3
2 -3 -10 2 1.45590 63.88762 9.59
2 -5 -1 2 1.45580 63.89261 46.5
2 5 -1 2 1.45580 63.89261 15.6
0 -3 13 2 1.45563 63.90092 447
0 3 13 2 1.45563 63.90092 8.14
0 -6 3 2 1.45461 63.95102 52.2
0 6 3 2 1.45461 63.95102 65.8
2 0 12 2 1.45454 63.95463 11.1
2 -2 11 2 1.45355 64.00311 15.8
```

```
2 2 11 2 1.45355 64.00311 78.3
2 -5 1 2 1.45287 64.03645 47.8
2 5 1 2 1.45287 64.03645 50.2
1 -1 14 2 1.45242 64.05902 7
1 1 14 2 1.45242 64.05902 235
3 0 -8 2 1.45130 64.11433 7.64
3 -3 2 2 1.45079 64.13940 0.0327
3 3 2 2 1.45079 64.13940 121
3 -1 7 2 1.44801 64.27714 117
3 1 7 2 1.44801 64.27714 134
2 -5 -2 2 1.44752 64.30190 61.5
2 5 -2 2 1.44752 64.30190 204
0 0 15 2 1.44732 64.31188 0.624
3 -3 -3 2 1.44551 64.40211 4.95
3 3 -3 2 1.44551 64.40211 16
2 -5 2 2 1.44178 64.58842 92.4
2 5 2 2 1.44178 64.58842 21.1
2 -1 12 2 1.43553 64.90422 17.9
2 1 12 2 1.43553 64.90422 2.69
2 -4 -8 2 1.43521 64.92071 1.36
2 4 -8 2 1.43521 64.92071 385
3 -2 6 2 1.43486 64.93835 87.3
3 2 6 2 1.43486 64.93835 155
1 5 -8 2 1.43464 64.94964 37.8
1 -5 -8 2 1.43464 64.94964 48.5
0 -5 9 2 1.43325 65.02010 67.2
0 5 9 2 1.43325 65.02010 2.34
2 -5 -3 2 1.43309 65.02850 1.84
2 5 -3 2 1.43309 65.02850 2.91
3 -3 3 2 1.43276 65.04529 6.73
3 3 3 2 1.43276 65.04529 3.23
3 -1 -8 2 1.43242 65.06267 178
3 1 -8 2 1.43242 65.06267 0.0187
0 -6 4 2 1.43228 65.06979 0.0131
0 6 4 2 1.43228 65.06979 0.285
0 -1 15 2 1.42859 65.25867 0.0579
0 1 15 2 1.42859 65.25867 0.958
2 -3 10 2 1.42743 65.31834 5.44
2 3 10 2 1.42743 65.31834 9.91
1 4 -11 2 1.42567 65.40913 137
```

```
1 -4 -11 2 1.42567 65.40913 23.9
3 -3 -4 2 1.42565 65.41019 185
3 3 -4 2 1.42565 65.41019 79.5
1 -6 0 2 1.42501 65.44296 9.71
1 6 0 2 1.42501 65.44296 35.2
2 -5 3 2 1.42477 65.45547 2.6
2 5 3 2 1.42477 65.45547 31.5
1 -5 8 2 1.42354 65.51897 184
1 5 8 2 1.42354 65.51897 122
1 -6 -1 2 1.42263 65.56598 51.3
1 6 -1 2 1.42263 65.56598 20.9
3 -2 -7 2 1.42168 65.61578 9.12
3 2 -7 2 1.42168 65.61578 64.6
1 -6 1 2 1.42127 65.63694 34.7
1 6 1 2 1.42127 65.63694 21.6
3 0 8 2 1.41764 65.82605 92.7
1 2 -14 2 1.41630 65.89658 45.5
1 -2 -14 2 1.41630 65.89658 22.1
1 -6 -2 2 1.41423 66.00510 89.4
1 6 -2 2 1.41423 66.00510 29.5
2 2 -12 2 1.41387 66.02417 39.1
2 -2 -12 2 1.41387 66.02417 28.6
2 -4 8 2 1.41324 66.05708 97.3
2 4 8 2 1.41324 66.05708 193
2 -5 -4 2 1.41306 66.06688 2.06
2 5 -4 2 1.41306 66.06688 62.1
1 -6 2 2 1.41155 66.14649 45.2
1 6 2 2 1.41155 66.14649 2.82
2 0 -13 2 1.41147 66.15076 51.8
1 -4 11 2 1.41076 66.18845 7.81
1 4 11 2 1.41076 66.18845 9.37
3 -3 4 2 1.40940 66.26014 8.6
3 3 4 2 1.40940 66.26014 82
1 3 -13 2 1.40760 66.35588 34.3
1 -3 -13 2 1.40760 66.35588 17.5
0 -6 5 2 1.40502 66.49352 1.87
0 6 5 2 1.40502 66.49352 5.6
0 -4 12 2 1.40429 66.53290 7.57
0 4 12 2 1.40429 66.53290 90.7
2 -5 4 2 1.40245 66.63126 60.1
```

```
2 5 4 2 1.40245 66.63126 27.8
1 0 -15 2 1.40139 66.68850 115
3 0 -9 2 1.40108 66.70507 31.2
3 -3 -5 2 1.40071 66.72469 107
3 3 -5 2 1.40071 66.72469 0.0789
1 -6 -3 2 1.40011 66.75712 4.18
1 6 -3 2 1.40011 66.75712 165
3 -1 8 2 1.40003 66.76157 105
3 1 8 2 1.40003 66.76157 0.0138
1 -2 14 2 1.39777 66.88393 38.8
1 2 14 2 1.39777 66.88393 12.2
1 -6 3 2 1.39622 66.96793 58.9
1 6 3 2 1.39622 66.96793 14.9
2 1 -13 2 1.39408 67.08398 0.514
2 -1 -13 2 1.39408 67.08398 28.1
3 -2 7 2 1.39384 67.09722 86.4
3 2 7 2 1.39384 67.09722 8.01
2 3 -11 2 1.39295 67.14594 78.9
2 -3 -11 2 1.39295 67.14594 8.14
1 -3 13 2 1.39068 67.26979 2.24
1 3 13 2 1.39068 67.26979 33.7
2 -5 -5 2 1.38813 67.40984 27.7
2 5 -5 2 1.38813 67.40984 26.6
2 -4 -9 2 1.38595 67.53025 24.7
2 4 -9 2 1.38595 67.53025 27.6
1 5 -9 2 1.38481 67.59356 18.5
1 -5 -9 2 1.38481 67.59356 60.4
1 1 -15 2 1.38437 67.61800 15
1 -1 -15 2 1.38437 67.61800 92.1
3 -1 -9 2 1.38407 67.63446 1.75
3 1 -9 2 1.38407 67.63446 1.12
2 -2 12 2 1.38270 67.71074 4.23
2 2 12 2 1.38270 67.71074 24
1 0 15 2 1.38217 67.73988 26.7
3 -3 5 2 1.38153 67.77579 50.1
3 3 5 2 1.38153 67.77579 84.5
1 -6 -4 2 1.38079 67.81686 9.92
1 6 -4 2 1.38079 67.81686 175
3 -2 -8 2 1.37991 67.86583 171
3 2 -8 2 1.37991 67.86583 142
```

```
2 0 13 2 1.37796 67.97523 55
0 -5 10 2 1.37736 68.00905 34.9
0 5 10 2 1.37736 68.00905 61.8
0 -2 15 2 1.37649 68.05772 172
0 2 15 2 1.37649 68.05772 69.9
1 -6 4 2 1.37581 68.09573 22.7
1 6 4 2 1.37581 68.09573 31.9
2 -5 5 2 1.37560 68.10800 0.649
2 5 5 2 1.37560 68.10800 0.0366
0 -3 14 2 1.37459 68.16460 6.67
0 3 14 2 1.37459 68.16460 0.0757
0 -6 6 2 1.37373 68.21307 12.4
0 6 6 2 1.37373 68.21307 9.6
1 -5 9 2 1.37359 68.22124 9.4
1 5 9 2 1.37359 68.22124 2.78
3 -3 -6 2 1.37154 68.33714 12.6
3 3 -6 2 1.37154 68.33714 10.1
3 0 9 2 1.36707 68.59167 2.05e-007
1 -1 15 2 1.36583 68.66243 0.111
1 1 15 2 1.36583 68.66243 2.22e-006
2 -3 11 2 1.36552 68.68024 0.000127
2 3 11 2 1.36552 68.68024 0.355
2 -4 9 2 1.36373 68.78342 4.82
2 4 9 2 1.36373 68.78342 147
2 -1 13 2 1.36177 68.89628 4.36e-005
2 1 13 2 1.36177 68.89628 0.00078
1 4 -12 2 1.36042 68.97421 0.013
1 -4 -12 2 1.36042 68.97421 10
2 -5 -6 2 1.35913 69.04910 0.000151
2 5 -6 2 1.35913 69.04910 0.000159
1 6 -5 2 1.35691 69.17767 4.78
1 -6 -5 2 1.35691 69.17767 334
0 0 16 2 1.35686 69.18098 4.42
3 -1 9 2 1.35126 69.50888 53.5
3 1 9 2 1.35126 69.50888 451
1 -6 5 2 1.35102 69.52296 0.0186
1 6 5 2 1.35102 69.52296 55.5
3 -2 8 2 1.35089 69.53053 0.0137
3 2 8 2 1.35089 69.53053 0.797
3 0 -10 2 1.35048 69.55453 35.2
```

```
3 -3 6 2 1.34999 69.58343 0.17
3 3 6 2 1.34999 69.58343 22.4
1 -4 12 2 1.34629 69.80270 0.19
1 4 12 2 1.34629 69.80270 0.463
3 -4 0 2 1.34601 69.81892 70.3
3 4 0 2 1.34601 69.81892 0.204
2 2 -13 2 1.34554 69.84679 0.0681
2 -2 -13 2 1.34554 69.84679 27.6
3 -4 -1 2 1.34517 69.86934 1.66
3 4 -1 2 1.34517 69.86934 0.0175
2 -5 6 2 1.34503 69.87720 0.0332
2 5 6 2 1.34503 69.87720 1.12
3 -4 1 2 1.34171 70.07568 0.000123
3 4 1 2 1.34171 70.07568 0.319
0 -1 16 2 1.34139 70.09465 0.00378
0 1 16 2 1.34139 70.09465 0.000171
0 -6 7 2 1.33932 70.21916 0.109
0 6 7 2 1.33932 70.21916 0.000792
3 -4 -2 2 1.33919 70.22665 2.58e-007
3 4 -2 2 1.33919 70.22665 0.192
3 -3 -7 2 1.33899 70.23862 7.92e-005
3 3 -7 2 1.33899 70.23862 0.0351
2 0 -14 2 1.33836 70.27682 0.000791
1 2 -15 2 1.33680 70.37091 6.31e-007
1 -2 -15 2 1.33680 70.37091 0.0208
3 -2 -9 2 1.33653 70.38707 5.19e-005
3 2 -9 2 1.33653 70.38707 0.0328
2 4 -10 2 1.33635 70.39807 0.0103
2 -4 -10 2 1.33635 70.39807 4.2e-005
0 -4 13 2 1.33614 70.41074 3.58e-009
0 4 13 2 1.33614 70.41074 0.000102
3 -1 -10 2 1.33523 70.46602 1.75e-008
3 1 -10 2 1.33523 70.46602 0.000358
1 5 -10 2 1.33476 70.49445 2.55e-006
1 -5 -10 2 1.33476 70.49445 0.00607
1 3 -14 2 1.33450 70.51044 0.00203
1 -3 -14 2 1.33450 70.51044 0.00182
2 3 -12 2 1.33247 70.63400 2.15
2 -3 -12 2 1.33247 70.63400 0.024
3 -4 2 2 1.33240 70.63814 0.0237
```

```
3 4 2 2 1.33240 70.63814 0.0135
1 6 -6 2 1.32922 70.83206 2.38e-009
1 -6 -6 2 1.32922 70.83206 2.11e-006
2 -5 -7 2 1.32688 70.97608 7.09e-011
2 5 -7 2 1.32688 70.97608 7.09e-011
1 -5 10 2 1.32360 71.17858 4.8e-009
1 5 10 2 1.32360 71.17858 0.0514
2 1 -14 2 1.32351 71.18424 7.86e-006
2 -1 -14 2 1.32351 71.18424 0.0187
0 -5 11 2 1.32259 71.24124 0.126
0 5 11 2 1.32259 71.24124 1.29e-009
1 -6 6 2 1.32258 71.24203 0.0924
1 6 6 2 1.32258 71.24203 0.00823
1 -2 15 2 1.32009 71.39681 0.000957
1 2 15 2 1.32009 71.39681 0.000188
1 0 -16 2 1.31934 71.44355 4.62e-009
1 -3 14 2 1.31896 71.46734 1.4e-006
1 3 14 2 1.31896 71.46734 0.00238
3 0 10 2 1.31668 71.61019 1.64
2 -2 13 2 1.31642 71.62666 0.029
2 2 13 2 1.31642 71.62666 0.0357
3 -3 7 2 1.31566 71.67428 0.305
3 3 7 2 1.31566 71.67428 0.00187
2 -4 10 2 1.31423 71.76433 0.000939
2 4 10 2 1.31423 71.76433 0.00578
2 -5 7 2 1.31161 71.93035 0.425
2 5 7 2 1.31161 71.93035 0.422
2 0 14 2 1.30756 72.18791 5.59e-012
3 -2 9 2 1.30692 72.22907 0.00325
3 2 9 2 1.30692 72.22907 0.00226
2 -3 12 2 1.30628 72.26994 0.0273
2 3 12 2 1.30628 72.26994 1.22e-007
1 1 -16 2 1.30511 72.34476 7.22e-012
1 -1 -16 2 1.30511 72.34476 0.000117
3 -3 -8 2 1.30393 72.42062 0.000111
3 3 -8 2 1.30393 72.42062 4.21e-006
3 -1 10 2 1.30253 72.51054 0.0895
3 1 10 2 1.30253 72.51054 0.193
1 0 16 2 1.30222 72.53079 0.19
0 -3 15 2 1.30104 72.60712 0.0574
```

```
0 3 15 2 1.30104 72.60712 0.125
3 0 -11 2 1.30031 72.65458 1.3e-008
1 4 -13 2 1.29871 72.75822 2.28e-008
1 -4 -13 2 1.29871 72.75822 0.137
0 -2 16 2 1.29798 72.80544 8.67
0 2 16 2 1.29798 72.80544 0.0371
2 -1 14 2 1.29370 73.08539 0.0138
2 1 14 2 1.29370 73.08539 0.0218
3 -2 -10 2 1.29240 73.17103 0.0196
3 2 -10 2 1.29240 73.17103 6.28e-008
1 -1 16 2 1.28853 73.42661 2.31e-009
1 1 16 2 1.28853 73.42661 0.0124
2 4 -11 2 1.28717 73.51674 0.458
2 -4 -11 2 1.28717 73.51674 6.19e-009
3 1 -11 2 1.28668 73.54981 1.13
3 -1 -11 2 1.28668 73.54981 1.13
1 -4 13 2 1.28539 73.63577 1.76e-007
1 4 13 2 1.28539 73.63577 7.03e-007
1 5 -11 2 1.28525 73.64511 2.12e-008
1 -5 -11 2 1.28525 73.64511 1.97e-007
2 2 -14 2 1.28176 73.87845 0.00481
2 -2 -14 2 1.28176 73.87845 3.76e-007
0 0 17 2 1.27704 74.19724 0.142
2 3 -13 2 1.27482 74.34873 2.46e-008
2 -3 -13 2 1.27482 74.34873 0.0156
1 -5 11 2 1.27429 74.38454 2.39e-007
1 5 11 2 1.27429 74.38454 9.44e-007
0 -4 14 2 1.27265 74.49684 4.08e-007
0 4 14 2 1.27265 74.49684 4.06e-007
2 0 -15 2 1.27117 74.59830 1.47e-007
0 -5 12 2 1.26952 74.71191 1.11
0 5 12 2 1.26952 74.71191 2.86e-008
1 3 -15 2 1.26737 74.85992 0.0198
1 -3 -15 2 1.26737 74.85992 5.77e-008
1 2 -16 2 1.26503 75.02255 8.08e-008
1 -2 -16 2 1.26503 75.02255 4.76e-007
0 -1 17 2 1.26412 75.08555 5.87e-007
0 1 17 2 1.26412 75.08555 1.21e-005
2 1 -15 2 1.25842 75.48492 1.06e-005
2 -1 -15 2 1.25842 75.48492 3.03e-006
```

```
2 -2 14 2 1.25463 75.75337 5.41e-006
2 2 14 2 1.25463 75.75337 3.76e-007
1 -3 15 2 1.25311 75.86177 6e-007
1 3 15 2 1.25311 75.86177 5.43e-006
2 -3 13 2 1.24996 76.08646 2.01e-005
2 3 13 2 1.24996 76.08646 8.46e-006
1 -2 16 2 1.24991 76.09026 3e-007
1 2 16 2 1.24991 76.09026 2.52e-007
1 0 -17 2 1.24608 76.36640 1.08e-005
2 0 15 2 1.24286 76.59992 3.46e-007
0 -3 16 2 1.23415 77.24001 0.000216
0 3 16 2 1.23415 77.24001 2.2e-005
1 1 -17 2 1.23407 77.24621 1.78e-005
1 -1 -17 2 1.23407 77.24621 1.19e-005
2 -1 15 2 1.23094 77.47890 0.0004
2 1 15 2 1.23094 77.47890 6.03e-005
1 0 17 2 1.23074 77.49419 6.04e-005
0 -2 17 2 1.22760 77.72955 2.61e-005
0 2 17 2 1.22760 77.72955 0.000471
1 -1 17 2 1.21916 78.37013 0.000308
1 1 17 2 1.21916 78.37013 0.000353
0 0 18 2 1.20610 79.38551 0.000369
0 -1 18 2 1.19519 80.25578 0.000133
0 1 18 2 1.19519 80.25578 0.000133
```

# Appendix III. Rectorite-only films dataset

Table AIII-1. Sample ID and mechanical properties

| | | Clay | Interlayer | Film | | Tensile properties | |
|---|---|---|---|---|---|---|---|
| Test | Sample name | Cation | Charge index | Thickness | BET | Tensile strength | Young's modulus |
| # | | | Na=0/Ca=1 | mm | m²/g | MPa | GPa |
| 602 | F3191015-Ba 30OU 4h-2 | Ba | 1.00 | 18 | | 13.4 | 5.8 |
| 601 | F3191015-Ba 30OU4h-1 | Ba | 1.00 | 18 | | 9.6 | 5.1 |
| 600 | F3191015-Sr 30OU 4h-2 | Sr | 1.00 | 23 | | 0.7 | 0.4 |
| 599 | F3191015-Sr 30OU 4h -1 | Sr | 1.00 | 23 | | 1.9 | 1.5 |
| 598 | F3191015-Mg 30OU 4h-4 | Mg | 1.00 | 23 | | 4.4 | 3.0 |
| 597 | F3191015-Mg 30OU 4h-3 | Mg | 1.00 | 23 | | 9.6 | 3.9 |
| 596 | F3191015-Mg 30OU 4h-2 | Mg | 1.00 | 23 | | 10.4 | 4.4 |
| 595 | F3191015-Mg 30OU 4h-1 | Mg | 1.00 | 23 | | 4.7 | 2.4 |
| 594 | F3191015-K 30OU 4h -2 | K | 0.00 | 17 | 251 | 33.0 | 56.3 |
| 593 | F3191015-K 30OU 4h-1 | K | 0.00 | 17 | | 1.8 | 3.2 |
| 592 | F3191015-NH 30OU 4h-3 | NH | 0.00 | 22 | | 7.8 | 4.4 |
| 591 | F3191015-NH 30OU 4h-2 | NH | 0.00 | 22 | | 2.1 | 1.9 |
| 590 | F3191015-NH 30OU 4h-1 | NH | 0.00 | 22 | 354 | 43.7 | 47.3 |
| 589 | F1021115-RT1b 30OU NS-3 | RT1b | 0.75 | 20 | | 16.5 | 5.9 |
| 588 | F1021115-RT1b 30OU NS-2 | RT1b | 0.75 | 20 | | 12.6 | 2.2 |
| 587 | F1021115-RT1b 30OU NS-1 | RT1b | 0.75 | 20 | | 4.0 | 2.1 |
| 586 | F3021115-Ba 30OU NS top-3 | Ba | 1.00 | 30 | 176 | 14.9 | 25.4 |
| 585 | F3021115-Ba 30OU NS top-2 | Ba | 1.00 | 30 | | 11.2 | 8.8 |
| 584 | F3021115-Ba 30OU NS top-1 | Ba | 1.00 | 30 | | 8.4 | 16.9 |
| 583 | F3021115-Sr 30OU NS-3 | Sr | 1.00 | 23 | | 6.1 | 5.0 |
| 582 | F3021115-Sr 30OU NS-2 | Sr | 1.00 | 23 | | 2.1 | 2.2 |
| 581 | F3021115-Sr 30OU NS-1 | Sr | 1.00 | 23 | | 0.7 | 0.8 |
| 580 | F3021115-AAf 30OU NS-2 | RT3-AAf | 0.75 | 18 | | 11.3 | 1.5 |
| 579 | F3021115-AAf 30OU NS-1 | RT3-AAf | 0.75 | 18 | 208 | 15.6 | 2.3 |
| 578 | F3021115-AAf 30OU NS-1 | RT3-AAf | 0.75 | 18 | | 9.2 | 2.5 |
| 577 | F2021115-TH70 30OU NS-2 | RT2 | 0.75 | 26 | | 2.4 | 3.1 |
| 576 | F2021115-TH70 30OU NS-1 | RT2 | 0.75 | 26 | 115 | 7.7 | 8.5 |
| 575 | F3021115-AA13 30OU NS-3 | RT3-AA13 | 0.75 | 20 | | 24.6 | 13.3 |
| 574 | F3021115-AA13 30OU NS-2 | RT3-AA13 | 0.75 | 20 | | 7.4 | 11.8 |
| 573 | F3021115-AA13 30OU NS-1 | RT3-AA13 | 0.75 | 20 | | 5.5 | 4.2 |
| 572 | F3191015-Na 30OU 4h-3 | Na | 0.00 | 23 | 163 | 31.8 | 55.3 |
| 571 | F3191015-Na 30OU 4h-2 | Na | 0.00 | 23 | | 21.8 | 21.6 |
| 570 | F3191015-Na 30OU 4h-1 | Na | 0.00 | 23 | | 26.8 | 28.3 |

| Test | Sample name | Clay | Interlayer | Film | BET | Tensile properties | |
|---|---|---|---|---|---|---|---|
| | | Cation | Charge index | Thickness | | Tensile strength | Young's modulus |
| # | | | Na=0/Ca=1 | mm | m²/g | MPa | GPa |
| 569 | F3191015-Li 30OU 4h-3 | Li | 0.00 | 13 | | 8.6 | 3.4 |
| 568 | F3191015-Li 30OU 4h-2 | Li | 0.00 | 13 | | 10.1 | 3.6 |
| 567 | F3191015-Li 30OU 4h-1 | Li | 0.00 | 13 | | 2.5 | 1.6 |
| 566 | F3021115-Ca 5OU 4h-3 | Ca | 1.00 | 23 | | 14.7 | 20.2 |
| 565 | F3021115-Ca 5OU 4h-2 | Ca | 1.00 | 23 | | 22.9 | 18.1 |
| 564 | F3021115-Ca 5OU 4h-1 | Ca | 1.00 | 23 | | 1.4 | 0.9 |
| 563 | F3021115-Ca 30OU 4h-3 | Ca | 1.00 | 25 | | 6.1 | 2.6 |
| 562 | F3021115-Ca 30OU 4h-2 | Ca | 1.00 | 25 | | 5.5 | 15.1 |
| 561 | F3021115-Ca 30OU 4h-1 | Ca | 1.00 | 25 | | 8.3 | 15.4 |
| 560 | F3021115-Ca 30OU NS-3 | Ca | 1.00 | 30 | | 0.6 | 1.1 |
| 559 | F3021115-Ca 30OU NS-2 | Ca | 1.00 | 30 | | 8.7 | 6.1 |
| 558 | F3021115-Ca 30OU NS-1 | Ca | 1.00 | 30 | 128 | 8.0 | 3.0 |
| 557 | F3021115-Mg 30OU NS-1 | Mg | 1.00 | 13 | | 4.1 | 15.2 |
| 556 | F3021115-Cs 30OU NS-3 | Cs | 0.00 | 25 | | 4.0 | 9.4 |
| 555 | F3021115-Cs 30OU NS-2 | Cs | 0.00 | 25 | 139 | 9.8 | 5.3 |
| 554 | F3021115-Cs 30OU NS-1 | Cs | 0.00 | 25 | | 6.9 | 18.5 |
| 553 | F3021115-K 30OU NS-4 | K | 0.00 | 13 | | 35.7 | 11.4 |
| 552 | F3021115-K 30OU NS-3 | K | 0.00 | 13 | | 25.1 | 14.8 |
| 551 | F3021115-K 30OU NS-2 | K | 0.00 | 13 | | 20.1 | 42.2 |
| 550 | F3021115-K 30OU NS-1 | K | 0.00 | 13 | | 12.1 | 3.6 |
| 549 | F3021115-NH 30OU NS-3 | NH | 0.00 | 22 | | 13.8 | 3.5 |
| 548 | F3021115-NH 30OU NS-2 | NH | 0.00 | 22 | | 0.2 | 0.1 |
| 547 | F3021115-NH 30OU NS-1 | NH | 0.00 | 22 | | 15.7 | 4.2 |
| 546 | F3021115-Na 30OU NS-3 | Na | 0.00 | 22 | | 17.4 | 2.8 |
| 545 | F3021115-Na 30OU NS-2 | Na | 0.00 | 22 | | 14.3 | 4.6 |
| 544 | F3021115-Na 30OU NS -1 | Na | 0.00 | 22 | | 2.9 | 11.0 |
| 543 | F3021115-Li 30OU NS-2 | Li | 0.00 | 23 | 259 | 12.9 | 18.8 |
| 542 | F3021115-Li 30OU NS-1 | Li | 0.00 | 23 | | 5.7 | 5.6 |
| 541 | F3201213-Sr-3 | Sr | 1.00 | 26 | | 0.0 | 4.6 |
| 540 | F3201213-Sr-2 | Sr | 1.00 | 26 | 169 | 5.6 | 2.3 |
| 539 | F3201213-Sr-1 | Sr | 1.00 | 26 | | 6.7 | 18.0 |
| 350 | F1250615DE-MgRT-NU30-3 | Mg | 1.00 | 20 | | 13.9 | 20.6 |
| 349 | F1250615DE-MgRT-NU30-3 | Mg | 1.00 | 20 | | 0.0 | 0.8 |
| 348 | F1250615DE-MgRT-NU30-2 | Mg | 1.00 | 20 | 184 | 12.3 | 3.7 |
| 347 | F1250615DE-MgRT-NU30-1 | Mg | 1.00 | 20 | | 8.0 | 3.2 |
| 346 | F3250615DE-NH-NU5-2 | NH | 0.00 | 23 | | 0.5 | 0.8 |

| Test | Sample name | Clay | Interlayer | Film | BET | Tensile properties | |
|---|---|---|---|---|---|---|---|
| | | Cation | Charge index | Thickness | | Tensile strength | Young's modulus |
| # | | | Na=0/Ca=1 | mm | m²/g | MPa | GPa |
| 345 | F3250615DE-NH-NU5-1 | NH | 0.00 | 23 | | 10.7 | 6.9 |
| 344 | F3230615DE-RT3Na-NU30-3 | Na | 0.00 | 35 | | 11.3 | 5.4 |
| 343 | F3230615DE-RT3Na-NU30-2 | Na | 0.00 | 35 | | 9.8 | 2.9 |
| 342 | F3230615DE-RT3Na-NU30-1 | Na | 0.00 | 35 | | 16.1 | 6.0 |
| 341 | F3230615DE-RT3Na-NU5-3 | Na | 0.00 | 35 | | 1.9 | 10.2 |
| 340 | F3230615DE-RT3Na-NU5-2 | Na | 0.00 | 35 | | 4.9 | 3.0 |
| 339 | F3230615DE-RT3Na-NU5-1 | Na | 0.00 | 35 | | 3.4 | 4.1 |
| 338 | F3240615DE-RT3Li-NU5-3 | Li | 0.00 | 13 | | 7.3 | 2.5 |
| 337 | F3240615DE-RT3Li-NU5-2 | Li | 0.00 | 13 | | 2.9 | 1.7 |
| 336 | F3240615DE-RT3Li-NU5-1 | Li | 0.00 | 13 | | 10.6 | 50.7 |
| 335 | F3240615DE-AA13-NU5-3 | RT3-AA13 | 0.75 | 20 | | 14.8 | 6.6 |
| 334 | F3240615DE-AA13-NU5-2 | RT3-AA13 | 0.75 | 20 | | 0.5 | 0.4 |
| 333 | F3240615DE-AA13-NU5-1 | RT3-AA13 | 0.75 | 20 | | 4.6 | 1.5 |
| 332 | F3240615DE-RT3NH-OU30-3 | NH | 0.00 | 27 | | 21.7 | 10.6 |
| 331 | F1240615DE-RT1b-NU5s-3 | RT1b | 0.75 | 20 | 259 | 19.9 | 3.0 |
| 330 | F1240615DE-RT1b-NU5s-2 | RT1b | 0.75 | 20 | | 14.9 | 5.5 |
| 329 | F1240615DE-RT1b-NU5s-1 | RT1b | 0.75 | 20 | | 8.7 | 4.8 |
| 328 | F3240615DE-RT3Na-OU30-2 | Na | 0.00 | 13 | | 0.5 | 0.5 |
| 327 | F3240615DE-RT3NH-OU30-2 | NH | 0.00 | 27 | | 3.8 | 6.3 |
| 326 | F3240615DE-RT3NH-OU30-1 | NH | 0.00 | 27 | | 23.7 | 9.7 |
| 325 | F3240615DE-RT3NH-OU5-3 | NH | 0.00 | 27 | | 8.1 | 1.7 |
| 324 | F3240615DE-RT3NH-OU5-2 | NH | 0.00 | 27 | | 1.9 | 2.3 |
| 323 | F3230615DE-RT3Na-OU5-3 | Na | 0.00 | 18 | | 16.0 | 4.2 |
| 322 | F3240615DE-RT3NH-OU5-1 | NH | 0.00 | 10 | | 2.4 | 3.5 |
| 321 | F3230615DE-RT3Na-OU5-2 | Na | 0.00 | 18 | | 0.7 | 0.5 |
| 320 | F3240615DE-RT3Li-OU5-3 | Li | 0.00 | 13 | | 5.6 | 15.9 |
| 319 | F3240615DE-RT3Li-OU5-2 | Li | 0.00 | 13 | | 1.4 | 0.8 |
| 318 | F3240615DE-RT3Li-OU5-1 | Li | 0.00 | 13 | | 11.1 | 14.5 |
| 317 | F3240615DE-AAfOU5-3 | RT3-AAf | 0.75 | 12 | | 13.2 | 18.6 |
| 316 | F3240615DE-AAfOU5-2 | RT3-AAf | 0.75 | 12 | | 14.1 | 1.9 |
| 315 | F3240615DE-AAfOU5-1 | RT3-AAf | 0.75 | 12 | | 13.6 | 2.3 |
| 314 | F3230615DE-AA13OU30-3 | RT3-AA13 | 0.75 | 17 | | 0.2 | 0.0 |
| 313 | F3230615DE-AA13OU30-2 | RT3-AA13 | 0.75 | 17 | | 12.0 | 12.2 |
| 312 | F3230615DE-AA13OU30-1 | RT3-AA13 | 0.75 | 17 | | 1.0 | 2.3 |
| 311 | F3230615DE-AA13OU5-3 | RT3-AA13 | 0.75 | 15 | | 2.7 | 4.3 |
| 310 | F3230615DE-AA13OU5-2 | RT3-AA13 | 0.75 | 15 | | 1.2 | 2.1 |

| Test | Sample name | Clay | Interlayer | Film | BET | Tensile properties | |
|---|---|---|---|---|---|---|---|
| | | Cation | Charge index | Thickness | | Tensile strength | Young's modulus |
| # | | | Na=0/Ca=1 | mm | m²/g | MPa | GPa |
| 309 | F3230615DE-AA13OU5-1 | RT3-AA13 | 0.75 | 15 | | 6.9 | 7.5 |
| 308 | F1-061113-RT1b-P-3 | RT1b | 0.75 | 10 | | 2.1 | 0.6 |
| 307 | F1-061113-RT1b-P-2 | RT1b | 0.75 | 10 | | 20.0 | 44.3 |
| 306 | F1-061113-RT1b-P-1 | RT1b | 0.75 | 10 | | 12.7 | 19.3 |
| 304 | F2-121113-RT2pur-P-1 | RT2 | 0.75 | 20 | | 6.3 | 20.4 |
| 301 | F1-260415-RT1Li-2 | Li | 0.00 | 18 | | 6.6 | 0.7 |
| 300 | F1-260415-RT1Li-1 | Li | 0.00 | 18 | | 7.8 | 0.8 |
| 299 | F3-260415-RT3Li-1 | Li | 0.00 | 18 | | 7.0 | 10.2 |
| 298 | F3-260415-RT3NH4-15-3 | NH | 0.00 | 18 | | 11.5 | 1.6 |
| 297 | F3-260415-RT3NH4-15-2 | NH | 0.00 | 18 | | 17.3 | 2.8 |
| 296 | F3-260415-RT3NH4-15-1 | NH | 0.00 | 18 | | 12.8 | 16.8 |
| 295 | F3-260415-RT3Na-3 | Na | 0.00 | 18 | | 7.8 | 13.6 |
| 294 | F3-260415-RT3K-3 | K | 0.00 | 20 | | 8.9 | 1.2 |
| 293 | F3-260415-RT3K-2 | K | 0.00 | 20 | | 11.6 | 1.2 |
| 292 | F3-260415-RT3K-1 | K | 0.00 | 20 | | 9.6 | 0.8 |
| 291 | F3-230415-RT3AA13wT-2 | RT3-AA13 | 0.75 | 25 | | 1.2 | 0.4 |
| 290 | F3-230415-RT3AA13wT-1 | RT3-AA13 | 0.75 | 25 | | 3.3 | 6.2 |
| 289 | F2-230415-RT2TH70 wT-3 | RT2 | 0.75 | 20 | | 4.0 | 11.2 |
| 288 | F2-230415-RT2TH70 wT-2 | RT2 | 0.75 | 20 | | 7.8 | 49.8 |
| 287 | F2-230415-RT2TH70 wT-1 | RT2 | 0.75 | 20 | | 11.7 | 3.2 |
| 286 | F1-230415-RT1b wT-3 | RT1b | 0.75 | 25 | | 14.8 | 3.6 |
| 285 | F1-230415-RT1b wT-2 | RT1b | 0.75 | 25 | | 23.9 | 4.3 |
| 284 | F1-230415-RT1b wT-1 | RT1b | 0.75 | 25 | | 12.4 | 4.3 |
| 283 | F3-270115-NH4-14-3 | NH | 0.00 | 15 | | 9.8 | 1.7 |
| 282 | F3-270115-NH4-14-2 | NH | 0.00 | 15 | | 5.5 | 1.7 |
| 281 | F3-270115-NH4-14-1 | NH | 0.00 | 15 | | 19.9 | 2.8 |
| 280 | F3-200114-NH4-14-3 | NH | 0.00 | 100 | | 3.6 | 0.5 |
| 279 | F3-200114-NH4-14-2 | NH | 0.00 | 100 | | 3.4 | 1.1 |
| 278 | F3-200114-NH4-14-1 | NH | 0.00 | 100 | | 3.7 | 1.3 |
| 277 | F3-200114-Li13-3 | Li | 0.00 | 15 | | 3.2 | 1.9 |
| 276 | F3-200114-Li13-2 | Li | 0.00 | 15 | | 3.1 | 24.9 |
| 275 | F3-200114-Li13-1 | Li | 0.00 | 15 | | 9.7 | 3.8 |
| 274 | F3-070414AAf4-3 | RT3-AAf | 0.75 | 54 | | 16.4 | 1.5 |
| 273 | F3-070414AAf4-2 | RT3-AAf | 0.75 | 54 | | 10.8 | 1.3 |
| 272 | F3-070414AAf4-1 | RT3-AAf | 0.75 | 54 | | 11.9 | 1.9 |
| 271 | F3-070414AAf3-3 | RT3-AAf | 0.75 | 67 | | 4.5 | 2.4 |

| Test | Sample name | Clay Cation | Interlayer Charge index Na=0/Ca=1 | Film Thickness mm | BET m²/g | Tensile properties Tensile strength MPa | Young's modulus GPa |
|---|---|---|---|---|---|---|---|
| 270 | F3-070414AAf3-2b | RT3-AAf | 0.75 | 67 | | 11.7 | 2.5 |
| 269 | F3-070414AAf3-2 | RT3-AAf | 0.75 | 67 | | 11.1 | 2.0 |
| 268 | F3-070414AAf3-1 | RT3-AAf | 0.75 | 67 | | 10.7 | 2.9 |
| 267 | F3-070414AAf2-2 | RT3-AAf | 0.75 | 90 | | 3.9 | 1.4 |
| 266 | F3-070414AAf2-2 | RT3-AAf | 0.75 | 90 | | 3.9 | 1.4 |
| 265 | F3-070414AAf2-1 | RT3-AAf | 0.75 | 90 | | 6.4 | 1.7 |
| 264 | F3-070414AAf1-3 | RT3-AAf | 0.75 | 27 | | 3.0 | 0.9 |
| 263 | F3-070414AAf1-2 | RT3-AAf | 0.75 | 27 | | 10.2 | 2.5 |
| 262 | F3-070414AAf1-1 | RT3-AAf | 0.75 | 27 | | 5.5 | 1.5 |
| 261 | F3-201213-Cs-last1 | Cs | 0.00 | 31 | | 15.5 | 43.4 |
| 260 | F3-201213-NH4-13-2-3 | NH | 0.00 | 155 | | 4.5 | 0.9 |
| 259 | F3-201213-NH4-13-2-2b | NH | 0.00 | 155 | | 7.0 | 1.4 |
| 258 | F3-201213-NH4-13-2-2 | NH | 0.00 | 155 | | 6.7 | 1.0 |
| 257 | F3-201213-NH4-13-2-1 | NH | 0.00 | 155 | | 6.3 | 1.3 |
| 256 | F3-201213-NH4-13-1-3 | NH | 0.00 | 155 | | 4.6 | 0.9 |
| 253 | F3-201213-NH4-13-1-2 | NH | 0.00 | 155 | | 3.3 | 0.9 |
| 252 | F3-201213-NH4-13-1 | NH | 0.00 | 155 | | 3.3 | 0.9 |
| 251 | F3-201213-Sr3-last2 | Sr | 1.00 | 30 | | 8.0 | 11.1 |
| 250 | F3-201213-Sr3-last1 | Sr | 1.00 | 30 | | 4.0 | 3.1 |
| 249 | F3201213-43-K-last3 | K | 0.00 | 117 | | 5.4 | 2.6 |
| 248 | F3201213-43-K-last2 | K | 0.00 | 117 | | 0.4 | 3.6 |
| 247 | F3201213-43-K-last1 | K | 0.00 | 117 | | 4.7 | 1.3 |
| 246 | F3201213-42-NH4-12last3 | NH | 0.00 | 70 | | 9.2 | 1.6 |
| 245 | F3201213-42-NH4-12last2 | NH | 0.00 | 60 | | 6.0 | 1.6 |
| 244 | F3201213-42-NH4-12last1 | NH | 0.00 | 60 | | 11.8 | 2.9 |
| 243 | F3201213-41-2-Na2last3 | Na | 0.00 | 75 | | 9.6 | 1.5 |
| 242 | F3201213-41-2-Na2last2 | Na | 0.00 | 75 | | 9.9 | 1.7 |
| 241 | F3201213-41-2-Na2last1 | Na | 0.00 | 75 | | 9.5 | 1.3 |
| 240 | F3201213-41-Na2last3 | Na | 0.00 | 75 | | 5.5 | 1.6 |
| 239 | F3201213-41-Na2last2 | Na | 0.00 | 75 | | 8.7 | 1.0 |
| 238 | F3201213-40-Na1last1 | Na | 0.00 | 64 | | 8.1 | 1.4 |
| 237 | F3201213-40-Na1last3 | Na | 0.00 | 64 | | 7.3 | 1.7 |
| 236 | F3201213-40-Na1last2 | Na | 0.00 | 64 | | 6.4 | 1.2 |
| 235 | F3201213-40-Na1last | Na | 0.00 | 64 | | 7.5 | 1.4 |
| 215 | F2121113RT2TH70-3 | RT2 | 0.75 | 16 | | 11.1 | 34.0 |
| 214 | F2121113RT2TH70-2 | RT2 | 0.75 | 16 | | 9.8 | 7.7 |

| Test | Sample name | Clay Cation | Interlayer Charge index | Film Thickness | BET | Tensile properties Tensile strength | Young's modulus |
|------|-------------|------|-----------|-----------|-----|-----------|---------|
| # | | | Na=0/Ca=1 | mm | m²/g | MPa | GPa |
| 213 | F2121113RT2TH70-1 | RT2 | 0.75 | 16 | | 11.7 | 39.4 |
| 209 | F1061113RT1m-3 | RT1m | 0.75 | 22 | | 7.8 | 6.1 |
| 208 | F1061113RT1m-2 | RT1m | 0.75 | 22 | | 13.7 | 4.6 |
| 207 | F1061113RT1m-1 | RT1m | 0.75 | 22 | | 17.4 | 5.1 |
| 202 | F1061113RT1b-3 | RT1b | 0.75 | 26 | | 17.2 | 6.4 |
| 201 | F1061113RT1b-2 | RT1b | 0.75 | 26 | | 7.1 | 5.2 |
| 200 | F1061113RT1b-1 | RT1b | 0.75 | 26 | | 15.7 | 5.7 |
| 182 | F3180913RT3 100-3 | RT3-OWE | 0.75 | 20 | | 6.8 | 4.0 |
| 181 | F3180913RT3 100-2 | RT3-OWE | 0.75 | 20 | | 16.6 | 10.5 |
| 180 | F3180913RT3 100 | RT3-OWE | 0.75 | 20 | | 5.2 | 3.7 |
| 179 | F3-49-OWF-P3 | RT3-OWF | 0.75 | 151 | | 8.0 | 3.6 |
| 178 | F3-49-OWF-P2 | RT3-OWF | 0.75 | 151 | | 15.2 | 4.1 |
| 177 | F3-49-OWF-P1 | RT3-OWF | 0.75 | 151 | | 10.3 | 3.1 |
| 176 | F3-48-Sr-P3 | Sr | 1.00 | 70 | | 7.7 | 2.4 |
| 175 | F3-48-Sr-P2 | Sr | 1.00 | 55 | | 5.0 | 2.0 |
| 174 | F3-48-Sr-P1 | Sr | 1.00 | 52 | | 3.9 | 9.9 |
| 173 | F3-41-Na2-P4 | Na | 0.00 | 66 | | 5.9 | 1.4 |
| 172 | F3-41-Na2-P3 | Na | 0.00 | 66 | | 5.3 | 1.3 |
| 171 | F3-41-Na2-P2 | Na | 0.00 | 65 | | 6.5 | 0.9 |
| 170 | F3-41-Na2-P1 | Na | 0.00 | 60 | | 4.8 | 1.0 |
| 97 | F3-49-OWF 2i3 | RT3-OWF | 0.75 | 137 | | 8.3 | 2.4 |
| 96 | F3-49-OWF 2 i2 | RT3-OWF | 0.75 | 137 | | 7.3 | 2.4 |
| 95 | F3-49-OWF 2 i1 | RT3-OWF | 0.75 | 137 | | 8.5 | 3.6 |
| 94 | F3-49-OWF i3 | RT3-OWF | 0.75 | 137 | | 4.5 | 1.4 |
| 93 | F3-49-OWF i2 | RT3-OWF | 0.75 | 137 | | 6.3 | 2.0 |
| 92 | F3-49-OWF i1 | RT3-OWF | 0.75 | 137 | | 7.1 | 2.2 |
| 91 | F3-48-Sr-i3 | Sr | 1.00 | 67 | | 5.9 | 2.0 |
| 90 | F3-48-Sr-i2 | Sr | 1.00 | 67 | | 5.3 | 3.6 |
| 89 | F3-48-Sr-i1 | Sr | 1.00 | 67 | | 0.7 | 0.8 |
| 88 | F3-46-Ba-i3 | Ba | 1.00 | 170 | | 7.2 | 1.6 |
| 86 | F3-46-Ba-i2 | Ba | 1.00 | 170 | | 7.9 | 3.2 |
| 85 | F3-46-Ba-i1 | Ba | 1.00 | 170 | | 7.6 | 2.9 |
| 84 | F3-45-Cs-i3 | Cs | 0.00 | 130 | | 4.4 | 2.3 |
| 83 | F3-45-Cs-i2 | Cs | 0.00 | 110 | | 0.5 | 0.8 |
| 82 | F3-45-Cs-i1 | Cs | 0.00 | 90 | | 1.0 | 1.4 |
| 58 | F3-32-Na1-i7 | Na | 0.00 | 100 | | 3.0 | 0.5 |

| Test | Sample name | Clay Cation | Interlayer Charge index | Film Thickness | BET | Tensile properties Tensile strength | Young's modulus |
|------|-------------|-------------|-------------------------|----------------|-----|-------------------------------------|-----------------|
| # | | | Na=0/Ca=1 | mm | m²/g | MPa | GPa |
| 57 | F3-31-Li-i7 | Li | 0.00 | 58 | | 3.0 | 0.7 |
| 56 | F3-31-Li-i8 | Li | 0.00 | 58 | | 3.8 | 1.4 |
| 55 | F3-47-Sr-i4 | Sr | 1.00 | 53 | | 4.3 | 3.3 |
| 54 | F3-47-Sr-i2 | Sr | 1.00 | 53 | | 5.4 | 1.6 |
| 53 | F3-44-Mg-i4 | Mg | 1.00 | 60 | | 1.9 | 1.6 |
| 52 | F3-44-Mg-i3 | Mg | 1.00 | 60 | | 1.4 | 1.1 |
| 51 | F3-44-Mg-i2 | Mg | 1.00 | 60 | | 2.9 | 1.4 |
| 50 | F3-44-Mg-i1 | Mg | 1.00 | 60 | | 1.2 | 1.3 |
| 49 | F3-43-K-i4 | K | 0.00 | 72 | | 5.6 | 1.4 |
| 48 | F3-43-K-i3 | K | 0.00 | 40 | | 7.4 | 2.7 |
| 47 | F3-43-K-i2 | K | 0.00 | 88 | | 4.5 | 1.1 |
| 46 | F3-43-K-i1 | K | 0.00 | 107 | | 3.8 | 0.8 |
| 45 | F3-38-OWE i9 | RT3-OWE | 0.75 | 61 | | 14.0 | 6.1 |
| 44 | F3-38-OWE i8 | RT3-OWE | 0.75 | 61 | | 12.7 | 6.4 |
| 43 | F3-38-OWE i7 | RT3-OWE | 0.75 | 61 | | 11.4 | 5.8 |
| 42 | F3-38-OWE i6 | RT3-OWE | 0.75 | 61 | | 3.6 | 14.6 |
| 40 | F3-38-OWE i6 | RT3-OWE | 0.75 | 61 | | 4.3 | 6.1 |
| 39 | F3-42 NH4 4i | NH | 0.00 | 70 | | 5.9 | 1.8 |
| 38 | F3-42 NH4 3i | NH | 0.00 | 70 | | 6.0 | 0.9 |
| 37 | F3-42 NH4 2i | NH | 0.00 | 70 | | 6.1 | 1.0 |
| 36 | F3-42 NH4 1i | NH | 0.00 | 70 | | 6.0 | 1.2 |
| 35 | F3-41 Na2 4i | Na | 0.00 | 100 | | 2.8 | 0.8 |
| 34 | F3-41 Na2 3i | Na | 0.00 | 100 | | 2.7 | 0.8 |
| 33 | F3-41 Na2 2i | Na | 0.00 | 100 | | 3.2 | 1.0 |
| 32 | F3-41 Na2 1i | Na | 0.00 | 100 | | 2.9 | 0.9 |
| 31 | F3-40 Na1 5i | Na | 0.00 | 138 | | 2.5 | 0.5 |
| 30 | F3-40 Na1 4i | Na | 0.00 | 138 | | 2.4 | 0.4 |
| 29 | F3-40 Na1 3i | Na | 0.00 | 138 | | 2.6 | 0.4 |
| 28 | F3-40 Na1 2i | Na | 0.00 | 138 | | 2.4 | 0.5 |
| 27 | F3-40 Na1 1i | Na | 0.00 | 138 | | 2.6 | 0.4 |
| 17 | F3-Li-39o6 | Li | 0.00 | 113 | | 2.9 | 0.7 |
| 16 | F3-Li-39i5 | Li | 0.00 | 113 | | 3.1 | 0.5 |
| 15 | F3-Li-39i4 | Li | 0.00 | 113 | | 3.1 | 0.6 |
| 14 | F3-Li-39i3 | Li | 0.00 | 113 | | 2.9 | 0.4 |

## Table AIII-2. Slurry processing conditions

| Test | Sample name | Clay Cation | Concentration | Sonication time | Stirring time | pH |
|---|---|---|---|---|---|---|
| # | | | clay g/100 ml UPW | min | h | |
| 602 | F3191015-Ba 30OU 4h-2 | Ba | 1.00 | 30 | 4 | 6.80 |
| 601 | F3191015-Ba 30OU4h-1 | Ba | 1.00 | 30 | 4 | 6.80 |
| 600 | F3191015-Sr 30OU 4h-2 | Sr | 1.00 | 30 | 4 | 6.20 |
| 599 | F3191015-Sr 30OU 4h -1 | Sr | 1.00 | 30 | 4 | 6.20 |
| 598 | F3191015-Mg 30OU 4h-4 | Mg | 1.00 | 30 | 4 | 7.06 |
| 597 | F3191015-Mg 30OU 4h-3 | Mg | 1.00 | 30 | 4 | 7.06 |
| 596 | F3191015-Mg 30OU 4h-2 | Mg | 1.00 | 30 | 4 | 7.06 |
| 595 | F3191015-Mg 30OU 4h-1 | Mg | 1.00 | 30 | 4 | 7.06 |
| 594 | F3191015-K 30OU 4h -2 | K | 1.00 | 30 | 4 | 8.80 |
| 593 | F3191015-K 30OU 4h-1 | K | 1.00 | 30 | 4 | 8.80 |
| 592 | F3191015-NH 30OU 4h-3 | NH | 1.00 | 30 | 4 | 7.10 |
| 591 | F3191015-NH 30OU 4h-2 | NH | 1.00 | 30 | 4 | 7.10 |
| 590 | F3191015-NH 30OU 4h-1 | NH | 1.00 | 30 | 4 | 7.10 |
| 589 | F1021115-RT1b 30OU NS-3 | RT1b | 1.00 | 30 | 0 | 8.23 |
| 588 | F1021115-RT1b 30OU NS-2 | RT1b | 1.00 | 30 | 0 | 8.23 |
| 587 | F1021115-RT1b 30OU NS-1 | RT1b | 1.00 | 30 | 0 | 8.23 |
| 586 | F3021115-Ba 30OU NS top-3 | Ba | 1.00 | 30 | 0 | 6.80 |
| 585 | F3021115-Ba 30OU NS top-2 | Ba | 1.00 | 30 | 0 | 6.80 |
| 584 | F3021115-Ba 30OU NS top-1 | Ba | 1.00 | 30 | 0 | 6.80 |
| 583 | F3021115-Sr 30OU NS-3 | Sr | 1.00 | 30 | 0 | 6.20 |
| 582 | F3021115-Sr 30OU NS-2 | Sr | 1.00 | 30 | 0 | 6.20 |
| 581 | F3021115-Sr 30OU NS-1 | Sr | 1.00 | 30 | 0 | 6.20 |
| 580 | F3021115-AAf 30OU NS-2 | RT3-AAf | 1.00 | 30 | 0 | 6.85 |
| 579 | F3021115-AAf 30OU NS-1 | RT3-AAf | 1.00 | 30 | 0 | 6.85 |
| 578 | F3021115-AAf 30OU NS-1 | RT3-AAf | 1.00 | 30 | 0 | 6.85 |
| 577 | F2021115-TH70 30OU NS-2 | RT2 | 1.00 | 30 | 0 | 6.80 |
| 576 | F2021115-TH70 30OU NS-1 | RT2 | 1.00 | 30 | 0 | 6.80 |
| 575 | F3021115-AA13 30OU NS-3 | RT3-AA13 | 1.00 | 30 | 0 | 7.00 |
| 574 | F3021115-AA13 30OU NS-2 | RT3-AA13 | 1.00 | 30 | 0 | 7.00 |
| 573 | F3021115-AA13 30OU NS-1 | RT3-AA13 | 1.00 | 30 | 0 | 7.00 |
| 572 | F3191015-Na 30OU 4h-3 | Na | 1.00 | 30 | 4 | 8.58 |
| 571 | F3191015-Na 30OU 4h-2 | Na | 1.00 | 30 | 4 | 8.58 |
| 570 | F3191015-Na 30OU 4h-1 | Na | 1.00 | 30 | 4 | 8.58 |
| 569 | F3191015-Li 30OU 4h-3 | Li | 1.00 | 30 | 4 | 9.62 |
| 568 | F3191015-Li 30OU 4h-2 | Li | 1.00 | 30 | 4 | 9.62 |

| Test | Sample name | Clay Cation | Slurry processing conditions | | | |
| --- | --- | --- | --- | --- | --- | --- |
| | | | Concentration | Sonication time | Stirring time | pH |
| # | | | clay g/100 ml UPW | min | h | |
| 567 | F3191015-Li 30OU 4h-1 | Li | 1.00 | 30 | 4 | 9.62 |
| 566 | F3021115-Ca 5OU 4h-3 | Ca | 1.00 | 30 | 4 | 6.10 |
| 565 | F3021115-Ca 5OU 4h-2 | Ca | 1.00 | 30 | 4 | 6.10 |
| 564 | F3021115-Ca 5OU 4h-1 | Ca | 1.00 | 30 | 4 | 6.10 |
| 563 | F3021115-Ca 30OU 4h-3 | Ca | 1.00 | 30 | 4 | 6.30 |
| 562 | F3021115-Ca 30OU 4h-2 | Ca | 1.00 | 30 | 4 | 6.30 |
| 561 | F3021115-Ca 30OU 4h-1 | Ca | 1.00 | 30 | 4 | 6.30 |
| 560 | F3021115-Ca 30OU NS-3 | Ca | 1.00 | 30 | 0 | 6.30 |
| 559 | F3021115-Ca 30OU NS-2 | Ca | 1.00 | 30 | 0 | 6.30 |
| 558 | F3021115-Ca 30OU NS-1 | Ca | 1.00 | 30 | 0 | 6.30 |
| 557 | F3021115-Mg 30OU NS-1 | Mg | 1.00 | 30 | 0 | 7.06 |
| 556 | F3021115-Cs 30OU NS-3 | Cs | 1.00 | 30 | 0 | 5.50 |
| 555 | F3021115-Cs 30OU NS-2 | Cs | 1.00 | 30 | 0 | 5.50 |
| 554 | F3021115-Cs 30OU NS-1 | Cs | 1.00 | 30 | 0 | 5.50 |
| 553 | F3021115-K 30OU NS-4 | K | 1.00 | 30 | 0 | 8.80 |
| 552 | F3021115-K 30OU NS-3 | K | 1.00 | 30 | 0 | 8.80 |
| 551 | F3021115-K 30OU NS-2 | K | 1.00 | 30 | 0 | 8.80 |
| 550 | F3021115-K 30OU NS-1 | K | 1.00 | 30 | 0 | 8.80 |
| 549 | F3021115-NH 30OU NS-3 | NH | 1.00 | 30 | 0 | 7.10 |
| 548 | F3021115-NH 30OU NS-2 | NH | 1.00 | 30 | 0 | 7.10 |
| 547 | F3021115-NH 30OU NS-1 | NH | 1.00 | 30 | 0 | 7.10 |
| 546 | F3021115-Na 30OU NS-3 | Na | 1.00 | 30 | 0 | 8.58 |
| 545 | F3021115-Na 30OU NS-2 | Na | 1.00 | 30 | 0 | 8.58 |
| 544 | F3021115-Na 30OU NS -1 | Na | 1.00 | 30 | 0 | 8.58 |
| 543 | F3021115-Li 30OU NS-2 | Li | 1.00 | 30 | 0 | 9.62 |
| 542 | F3021115-Li 30OU NS-1 | Li | 1.00 | 30 | 0 | 9.62 |
| 541 | F3201213-Sr-3 | Sr | 1.00 | 30 | 0 | 6.20 |
| 540 | F3201213-Sr-2 | Sr | 1.00 | 30 | 0 | 6.20 |
| 539 | F3201213-Sr-1 | Sr | 1.00 | 30 | 0 | 6.20 |
| 350 | F1250615DE-MgRT-NU30-3 | Mg | 1.00 | 30 | 24 | 8.22 |
| 349 | F1250615DE-MgRT-NU30-3 | Mg | 1.00 | 30 | 24 | 8.22 |
| 348 | F1250615DE-MgRT-NU30-2 | Mg | 1.00 | 30 | 24 | 8.22 |
| 347 | F1250615DE-MgRT-NU30-1 | Mg | 1.00 | 30 | 24 | 8.22 |
| 346 | F3250615DE-NH-NU5-2 | NH | 1.00 | 5 | 24 | 7.10 |
| 345 | F3250615DE-NH-NU5-1 | NH | 1.00 | 5 | 24 | 7.10 |
| 344 | F3230615DE-RT3Na-NU30-3 | Na | 1.00 | 30 | 24 | 8.58 |

202

| Test | Sample name | Clay Cation | Slurry processing conditions | | | |
|---|---|---|---|---|---|---|
| | | | Concentration | Sonication time | Stirring time | pH |
| # | | | clay g/100 ml UPW | min | h | |
| 343 | F3230615DE-RT3Na-NU30-2 | Na | 1.00 | 30 | 24 | 8.58 |
| 342 | F3230615DE-RT3Na-NU30-1 | Na | 1.00 | 30 | 24 | 8.58 |
| 341 | F3230615DE-RT3Na-NU5-3 | Na | 1.00 | 5 | 24 | 8.58 |
| 340 | F3230615DE-RT3Na-NU5-2 | Na | 1.00 | 5 | 24 | 8.58 |
| 339 | F3230615DE-RT3Na-NU5-1 | Na | 1.00 | 5 | 24 | 8.58 |
| 338 | F3240615DE-RT3Li-NU5-3 | Li | 1.00 | 5 | 24 | 9.62 |
| 337 | F3240615DE-RT3Li-NU5-2 | Li | 1.00 | 5 | 24 | 9.62 |
| 336 | F3240615DE-RT3Li-NU5-1 | Li | 1.00 | 5 | 24 | 9.62 |
| 335 | F3240615DE-AA13-NU5-3 | RT3-AA13 | 1.00 | 5 | 24 | 7.00 |
| 334 | F3240615DE-AA13-NU5-2 | RT3-AA13 | 1.00 | 5 | 24 | 7.00 |
| 333 | F3240615DE-AA13-NU5-1 | RT3-AA13 | 1.00 | 5 | 24 | 7.00 |
| 332 | F3240615DE-RT3NH-OU30-3 | NH | 1.00 | 30 | 24 | 7.10 |
| 331 | F1240615DE-RT1b-NU5s-3 | RT1b | 1.00 | 5 | 24 | 8.85 |
| 330 | F1240615DE-RT1b-NU5s-2 | RT1b | 1.00 | 5 | 24 | 8.85 |
| 329 | F1240615DE-RT1b-NU5s-1 | RT1b | 1.00 | 5 | 24 | 8.85 |
| 328 | F3240615DE-RT3Na-OU30-2 | Na | 1.00 | 30 | 24 | 8.58 |
| 327 | F3240615DE-RT3NH-OU30-2 | NH | 1.00 | 30 | 24 | 7.10 |
| 326 | F3240615DE-RT3NH-OU30-1 | NH | 1.00 | 30 | 24 | 7.10 |
| 325 | F3240615DE-RT3NH-OU5-3 | NH | 1.00 | 5 | 24 | 7.10 |
| 324 | F3240615DE-RT3NH-OU5-2 | NH | 1.00 | 5 | 24 | 7.10 |
| 323 | F3230615DE-RT3Na-OU5-3 | Na | 1.00 | 5 | 24 | 8.58 |
| 322 | F3240615DE-RT3NH-OU5-1 | NH | 1.00 | 5 | 24 | 7.10 |
| 321 | F3230615DE-RT3Na-OU5-2 | Na | 1.00 | 5 | 24 | 8.58 |
| 320 | F3240615DE-RT3Li-OU5-3 | Li | 1.00 | 5 | 24 | 9.62 |
| 319 | F3240615DE-RT3Li-OU5-2 | Li | 1.00 | 5 | 24 | 9.62 |
| 318 | F3240615DE-RT3Li-OU5-1 | Li | 1.00 | 5 | 24 | 9.62 |
| 317 | F3240615DE-AAfOU5-3 | RT3-AAf | 1.00 | 5 | 24 | 6.85 |
| 316 | F3240615DE-AAfOU5-2 | RT3-AAf | 1.00 | 5 | 24 | 6.85 |
| 315 | F3240615DE-AAfOU5-1 | RT3-AAf | 1.00 | 5 | 24 | 6.85 |
| 314 | F3230615DE-AA13OU30-3 | RT3-AA13 | 1.00 | 30 | 24 | 7.00 |
| 313 | F3230615DE-AA13OU30-2 | RT3-AA13 | 1.00 | 30 | 24 | 7.00 |
| 312 | F3230615DE-AA13OU30-1 | RT3-AA13 | 1.00 | 30 | 24 | 7.00 |
| 311 | F3230615DE-AA13OU5-3 | RT3-AA13 | 1.00 | 5 | 24 | 7.00 |
| 310 | F3230615DE-AA13OU5-2 | RT3-AA13 | 1.00 | 5 | 24 | 7.00 |
| 309 | F3230615DE-AA13OU5-1 | RT3-AA13 | 1.00 | 5 | 24 | 7.00 |
| 308 | F1-061113-RT1b-P-3 | RT1b | 1.00 | 5 | 24 | 8.50 |

| Test | Sample name | Clay Cation | Slurry processing conditions | | | |
|---|---|---|---|---|---|---|
| | | | Concentration | Sonication time | Stirring time | pH |
| # | | | clay g/100 ml UPW | min | h | |
| 307 | F1-061113-RT1b-P-2 | RT1b | 1.00 | 5 | 24 | 8.50 |
| 306 | F1-061113-RT1b-P-1 | RT1b | 1.00 | 5 | 24 | 8.50 |
| 304 | F2-121113-RT2pur-P-1 | RT2 | 1.00 | 5 | 24 | 6.70 |
| 301 | F1-260415-RT1Li-2 | Li | 1.00 | 30 | 24 | 9.62 |
| 300 | F1-260415-RT1Li-1 | Li | 1.00 | 30 | 24 | 9.62 |
| 299 | F3-260415-RT3Li-1 | Li | 1.00 | 30 | 24 | 9.62 |
| 298 | F3-260415-RT3NH4-15-3 | NH | 1.00 | 30 | 24 | 7.10 |
| 297 | F3-260415-RT3NH4-15-2 | NH | 1.00 | 30 | 24 | 7.10 |
| 296 | F3-260415-RT3NH4-15-1 | NH | 1.00 | 30 | 24 | 7.10 |
| 295 | F3-260415-RT3Na-3 | Na | 1.00 | 30 | 24 | 8.58 |
| 294 | F3-260415-RT3K-3 | K | 1.00 | 30 | 24 | 8.80 |
| 293 | F3-260415-RT3K-2 | K | 1.00 | 30 | 24 | 8.80 |
| 292 | F3-260415-RT3K-1 | K | 1.00 | 30 | 24 | 8.80 |
| 291 | F3-230415-RT3AA13wT-2 | RT3-AA13 | 1.00 | 30 | 24 | 7.00 |
| 290 | F3-230415-RT3AA13wT-1 | RT3-AA13 | 1.00 | 30 | 24 | 7.00 |
| 289 | F2-230415-RT2TH70 wT-3 | RT2 | 1.00 | 30 | 24 | 6.70 |
| 288 | F2-230415-RT2TH70 wT-2 | RT2 | 1.00 | 30 | 24 | 6.70 |
| 287 | F2-230415-RT2TH70 wT-1 | RT2 | 1.00 | 30 | 24 | 6.70 |
| 286 | F1-230415-RT1b wT-3 | RT1b | 1.00 | 30 | 24 | 8.50 |
| 285 | F1-230415-RT1b wT-2 | RT1b | 1.00 | 30 | 24 | 8.50 |
| 284 | F1-230415-RT1b wT-1 | RT1b | 1.00 | 30 | 24 | 8.50 |
| 283 | F3-270115-NH4-14-3 | NH | 1.00 | 30 | 24 | 7.10 |
| 282 | F3-270115-NH4-14-2 | NH | 1.00 | 30 | 24 | 7.10 |
| 281 | F3-270115-NH4-14-1 | NH | 1.00 | 30 | 24 | 7.10 |
| 280 | F3-200114-NH4-14-3 | NH | 1.00 | 30 | 0 | 7.10 |
| 279 | F3-200114-NH4-14-2 | NH | 1.00 | 30 | 0 | 7.10 |
| 278 | F3-200114-NH4-14-1 | NH | 1.00 | 30 | 0 | 7.10 |
| 277 | F3-200114-Li13-3 | Li | 1.00 | 30 | 0 | 9.62 |
| 276 | F3-200114-Li13-2 | Li | 1.00 | 30 | 0 | 9.62 |
| 275 | F3-200114-Li13-1 | Li | 1.00 | 30 | 0 | 9.62 |
| 274 | F3-070414AAf4-3 | RT3-AAf | 1.00 | 5 | 0 | 6.85 |
| 273 | F3-070414AAf4-2 | RT3-AAf | 1.00 | 5 | 0 | 6.85 |
| 272 | F3-070414AAf4-1 | RT3-AAf | 1.00 | 5 | 0 | 6.85 |
| 271 | F3-070414AAf3-3 | RT3-AAf | 1.00 | 5 | 0 | 6.85 |
| 270 | F3-070414AAf3-2b | RT3-AAf | 3.03 | 5 | 0 | 6.85 |
| 269 | F3-070414AAf3-2 | RT3-AAf | 3.03 | 5 | 0 | 6.85 |

| Test | Sample name | Clay | Slurry processing conditions | | | |
|------|-------------|------|------|------|------|------|
| | | Cation | Concentration | Sonication time | Stirring time | pH |
| # | | | clay g/100 ml UPW | min | h | |
| 268 | F3-070414AAf3-1 | RT3-AAf | 3.03 | 5 | 0 | 6.85 |
| 267 | F3-070414AAf2-2 | RT3-AAf | 2.92 | 5 | 0 | 6.85 |
| 266 | F3-070414AAf2-2 | RT3-AAf | 2.92 | 5 | 0 | 6.85 |
| 265 | F3-070414AAf2-1 | RT3-AAf | 2.92 | 5 | 0 | 6.85 |
| 264 | F3-070414AAf1-3 | RT3-AAf | 2.04 | 5 | 0 | 6.85 |
| 263 | F3-070414AAf1-2 | RT3-AAf | 2.04 | 5 | 0 | 6.85 |
| 262 | F3-070414AAf1-1 | RT3-AAf | 2.04 | 5 | 0 | 6.85 |
| 261 | F3-201213-Cs-last1 | Cs | 1.00 | 30 | 0 | 5.50 |
| 260 | F3-201213-NH4-13-2-3 | NH | 1.00 | 30 | 0 | 7.10 |
| 259 | F3-201213-NH4-13-2-2b | NH | 1.00 | 30 | 0 | 7.10 |
| 258 | F3-201213-NH4-13-2-2 | NH | 1.00 | 30 | 0 | 7.10 |
| 257 | F3-201213-NH4-13-2-1 | NH | 1.00 | 30 | 0 | 7.10 |
| 256 | F3-201213-NH4-13-1-3 | NH | 1.00 | 30 | 0 | 7.10 |
| 253 | F3-201213-NH4-13-1-2 | NH | 1.00 | 30 | 0 | 7.10 |
| 252 | F3-201213-NH4-13-1 | NH | 1.00 | 30 | 0 | 7.10 |
| 251 | F3-201213-Sr3-last2 | Sr | 1.00 | 30 | 0 | 6.20 |
| 250 | F3-201213-Sr3-last1 | Sr | 1.00 | 30 | 0 | 6.20 |
| 249 | F3201213-43-K-last3 | K | 3.67 | 30 | 0 | 8.80 |
| 248 | F3201213-43-K-last2 | K | 3.67 | 30 | 0 | 8.80 |
| 247 | F3201213-43-K-last1 | K | 3.67 | 30 | 0 | 8.80 |
| 246 | F3201213-42-NH4-12last3 | NH | 3.43 | 5 | 0 | 7.10 |
| 245 | F3201213-42-NH4-12last2 | NH | 3.43 | 5 | 0 | 7.10 |
| 244 | F3201213-42-NH4-12last1 | NH | 3.43 | 5 | 0 | 7.10 |
| 243 | F3201213-41-2-Na2last3 | Na | 2.60 | 5 | 0 | 8.58 |
| 242 | F3201213-41-2-Na2last2 | Na | 2.60 | 5 | 0 | 8.58 |
| 241 | F3201213-41-2-Na2last1 | Na | 2.60 | 5 | 0 | 8.58 |
| 240 | F3201213-41-Na2last3 | Na | 2.04 | 5 | 0 | 8.58 |
| 239 | F3201213-41-Na2last2 | Na | 2.04 | 5 | 0 | 8.58 |
| 238 | F3201213-40-Na1last1 | Na | 4.05 | 5 | 0 | 8.58 |
| 237 | F3201213-40-Na1last3 | Na | 4.05 | 5 | 0 | 8.58 |
| 236 | F3201213-40-Na1last2 | Na | 4.05 | 5 | 0 | 8.58 |
| 235 | F3201213-40-Na1last | Na | 4.05 | 5 | 0 | 8.58 |
| 215 | F2121113RT2TH70-3 | RT2 | 1.00 | 5 | 24 | 6.70 |
| 214 | F2121113RT2TH70-2 | RT2 | 1.00 | 5 | 24 | 6.70 |
| 213 | F2121113RT2TH70-1 | RT2 | 1.00 | 5 | 24 | 6.70 |
| 209 | F1061113RT1m-3 | RT1m | 1.00 | 5 | 24 | 8.50 |

| Test | Sample name | Clay Cation | Concentration | Sonication time | Stirring time | pH |
|---|---|---|---|---|---|---|
| # | | | clay g/100 ml UPW | min | h | |
| 208 | F1061113RT1m-2 | RT1m | 1.00 | 5 | 24 | 8.50 |
| 207 | F1061113RT1m-1 | RT1m | 1.00 | 5 | 24 | 8.50 |
| 202 | F1061113RT1b-3 | RT1b | 1.00 | 5 | 24 | 8.50 |
| 201 | F1061113RT1b-2 | RT1b | 1.00 | 5 | 24 | 8.50 |
| 200 | F1061113RT1b-1 | RT1b | 1.00 | 5 | 24 | 8.50 |
| 182 | F3180913RT3 100-3 | RT3-OWE | 2.30 | 5 | 0 | 6.60 |
| 181 | F3180913RT3 100-2 | RT3-OWE | 2.30 | 5 | 0 | 6.60 |
| 180 | F3180913RT3 100 | RT3-OWE | 2.30 | 5 | 0 | 6.60 |
| 179 | F3-49-OWF-P3 | RT3-OWF | 4.00 | 5 | 0 | 6.60 |
| 178 | F3-49-OWF-P2 | RT3-OWF | 4.00 | 5 | 0 | 6.60 |
| 177 | F3-49-OWF-P1 | RT3-OWF | 4.00 | 5 | 0 | 6.60 |
| 176 | F3-48-Sr-P3 | Sr | 2.22 | 30 | 0 | 6.20 |
| 175 | F3-48-Sr-P2 | Sr | 2.22 | 30 | 0 | 6.20 |
| 174 | F3-48-Sr-P1 | Sr | 2.22 | 30 | 0 | 6.20 |
| 173 | F3-41-Na2-P4 | Na | 3.70 | 5 | 0 | 8.58 |
| 172 | F3-41-Na2-P3 | Na | 3.70 | 5 | 0 | 8.58 |
| 171 | F3-41-Na2-P2 | Na | 3.70 | 5 | 0 | 8.58 |
| 170 | F3-41-Na2-P1 | Na | 3.70 | 5 | 0 | 8.58 |
| 97 | F3-49-OWF 2i3 | RT3-OWF | 4.00 | 5 | 0 | 6.60 |
| 96 | F3-49-OWF 2 i2 | RT3-OWF | 4.00 | 5 | 0 | 6.60 |
| 95 | F3-49-OWF 2 i1 | RT3-OWF | 4.00 | 5 | 0 | 6.60 |
| 94 | F3-49-OWF i3 | RT3-OWF | 4.00 | 5 | 0 | 6.60 |
| 93 | F3-49-OWF i2 | RT3-OWF | 4.00 | 5 | 0 | 6.60 |
| 92 | F3-49-OWF i1 | RT3-OWF | 4.00 | 5 | 0 | 6.60 |
| 91 | F3-48-Sr-i3 | Sr | 2.22 | 30 | 0 | 6.20 |
| 90 | F3-48-Sr-i2 | Sr | 2.22 | 30 | 0 | 6.20 |
| 89 | F3-48-Sr-i1 | Sr | 2.22 | 30 | 0 | 6.20 |
| 88 | F3-46-Ba-i3 | Ba | 5.82 | 30 | 0 | 6.80 |
| 86 | F3-46-Ba-i2 | Ba | 5.82 | 30 | 0 | 6.80 |
| 85 | F3-46-Ba-i1 | Ba | 5.82 | 30 | 0 | 6.80 |
| 84 | F3-45-Cs-i3 | Cs | 4.76 | 30 | 0 | 5.50 |
| 83 | F3-45-Cs-i2 | Cs | 4.76 | 30 | 0 | 5.50 |
| 82 | F3-45-Cs-i1 | Cs | 4.76 | 30 | 0 | 5.50 |
| 58 | F3-32-Na1-i7 | Na | 3.12 | 5 | 0 | 8.58 |
| 57 | F3-31-Li-i7 | Li | 3.28 | 5 | 0 | 9.62 |
| 56 | F3-31-Li-i8 | Li | 3.28 | 5 | 0 | 9.62 |

| Test | Sample name | Clay Cation | Slurry processing conditions | | | |
|------|-------------|-------------|------------------------------|--|--|--|
| | | | Concentration | Sonication time | Stirring time | pH |
| # | | | clay g/100 ml UPW | min | h | |
| 55 | F3-47-Sr-i4 | Sr | 3.82 | 5 | 0 | 6.20 |
| 54 | F3-47-Sr-i2 | Sr | 3.82 | 5 | 0 | 6.20 |
| 53 | F3-44-Mg-i4 | Mg | 2.70 | 5 | 0 | 7.06 |
| 52 | F3-44-Mg-i3 | Mg | 2.70 | 5 | 0 | 7.06 |
| 51 | F3-44-Mg-i2 | Mg | 2.70 | 5 | 0 | 7.06 |
| 50 | F3-44-Mg-i1 | Mg | 2.70 | 5 | 0 | 7.06 |
| 49 | F3-43-K-i4 | K | 3.34 | 30 | 0 | 8.80 |
| 48 | F3-43-K-i3 | K | 3.34 | 30 | 0 | 8.80 |
| 47 | F3-43-K-i2 | K | 3.34 | 30 | 0 | 8.80 |
| 46 | F3-43-K-i1 | K | 3.34 | 30 | 0 | 8.80 |
| 45 | F3-38-OWE i9 | RT3-OWE | 4.24 | 5 | 0 | 6.60 |
| 44 | F3-38-OWE i8 | RT3-OWE | 4.24 | 5 | 0 | 6.60 |
| 43 | F3-38-OWE i7 | RT3-OWE | 4.24 | 5 | 0 | 6.60 |
| 42 | F3-38-OWE i6 | RT3-OWE | 4.24 | 5 | 0 | 6.60 |
| 40 | F3-38-OWE i6 | RT3-OWE | 4.24 | 5 | 0 | 6.60 |
| 39 | F3-42 NH4 4i | NH | 3.10 | 5 | 0 | 7.10 |
| 38 | F3-42 NH4 3i | NH | 3.10 | 5 | 0 | 7.10 |
| 37 | F3-42 NH4 2i | NH | 3.10 | 5 | 0 | 7.10 |
| 36 | F3-42 NH4 1i | NH | 3.10 | 5 | 0 | 7.10 |
| 35 | F3-41 Na2 4i | Na | 3.70 | 5 | 0 | 8.58 |
| 34 | F3-41 Na2 3i | Na | 3.70 | 5 | 0 | 8.58 |
| 33 | F3-41 Na2 2i | Na | 3.70 | 5 | 0 | 8.58 |
| 32 | F3-41 Na2 1i | Na | 3.70 | 5 | 0 | 8.58 |
| 31 | F3-40 Na1 5i | Na | 3.12 | 5 | 0 | 8.58 |
| 30 | F3-40 Na1 4i | Na | 3.12 | 5 | 0 | 8.58 |
| 29 | F3-40 Na1 3i | Na | 3.12 | 5 | 0 | 8.58 |
| 28 | F3-40 Na1 2i | Na | 3.12 | 5 | 0 | 8.58 |
| 27 | F3-40 Na1 1i | Na | 3.12 | 5 | 0 | 8.58 |
| 17 | F3-Li-39o6 | Li | 3.12 | 5 | 0 | 9.62 |
| 16 | F3-Li-39i5 | Li | 3.28 | 5 | 0 | 9.62 |
| 15 | F3-Li-39i4 | Li | 3.28 | 5 | 0 | 9.62 |
| 14 | F3-Li-39i3 | Li | 3.28 | 5 | 0 | 9.62 |

Table AIII-3. Slurry characterisation

| Test | Sample name | Clay Cation | Slurry characterisation in Zetasizer | | | | | | | |
|------|-------------|-------------|-----------------|-------------------------|------------------|-----------------------|------------------|--------------------|---------------------------|--------------------------------|
| | | | $\zeta$-potential | $\zeta$-potential st. dev. | Number Mean (d) | Number Mean st. dev. | Z-average (d) | Z-average st. dev. | Polydispersity Index | Polydispersity Index st. dev. |
| # | | | mV | mV | nm | nm | nm | nm | | |
| 602 | F3191015-Ba 30OU 4h-2 | Ba | -27.1 | 0.4 | 2176 | 84 | 2194 | 44 | 0.16 | 0.10 |
| 601 | F3191015-Ba 30OU4h-1 | Ba | -27.1 | 0.4 | 2176 | 84 | 2194 | 44 | 0.16 | 0.10 |
| 600 | F3191015-Sr 30OU 4h-2 | Sr | -25.0 | 0.8 | 481 | 19 | 1636 | 14 | 0.25 | 0.03 |
| 599 | F3191015-Sr 30OU 4h -1 | Sr | -25.0 | 0.8 | 481 | 19 | 1636 | 14 | 0.25 | 0.03 |
| 598 | F3191015-Mg 30OU 4h-4 | Mg | -13.6 | 0.6 | 1184 | 123 | 1539 | 33 | 0.15 | 0.02 |
| 597 | F3191015-Mg 30OU 4h-3 | Mg | -13.6 | 0.6 | 1184 | 123 | 1539 | 33 | 0.15 | 0.02 |
| 596 | F3191015-Mg 30OU 4h-2 | Mg | -13.6 | 0.6 | 1184 | 123 | 1539 | 33 | 0.15 | 0.02 |
| 595 | F3191015-Mg 30OU 4h-1 | Mg | -13.6 | 0.6 | 1184 | 123 | 1539 | 33 | 0.15 | 0.02 |
| 594 | F3191015-K 30OU 4h -2 | K | -43.7 | 0.3 | 662 | 23 | 818 | 20 | 0.17 | 0.07 |
| 593 | F3191015-K 30OU 4h-1 | K | -43.7 | 0.3 | 662 | 23 | 818 | 20 | 0.17 | 0.07 |
| 592 | F3191015-NH 30OU 4h-3 | NH | -38.7 | 1.8 | 622 | 172 | 1069 | 20 | 0.18 | 0.03 |
| 591 | F3191015-NH 30OU 4h-2 | NH | -38.7 | 1.8 | 622 | 172 | 1069 | 20 | 0.18 | 0.03 |
| 590 | F3191015-NH 30OU 4h-1 | NH | -38.7 | 1.8 | 622 | 172 | 1069 | 20 | 0.18 | 0.03 |
| 589 | F1021115-RT1b 30OU NS-3 | RT1b | -42.7 | 0.7 | 597 | 107 | 983 | 25 | 0.22 | 0.04 |
| 588 | F1021115-RT1b 30OU NS-2 | RT1b | -42.7 | 0.7 | 597 | 107 | 983 | 25 | 0.22 | 0.04 |
| 587 | F1021115-RT1b 30OU NS-1 | RT1b | -42.7 | 0.7 | 597 | 107 | 983 | 25 | 0.22 | 0.04 |
| 586 | F3021115-Ba 30OU NS top-3 | Ba | -30.8 | 0.8 | 1165 | 93 | 1413 | 49 | 0.83 | 0.24 |
| 585 | F3021115-Ba 30OU NS top-2 | Ba | -30.8 | 0.8 | 1165 | 93 | 1413 | 49 | 0.83 | 0.24 |
| 584 | F3021115-Ba 30OU NS top-1 | Ba | -30.8 | 0.8 | 1165 | 93 | 1413 | 49 | 0.83 | 0.24 |
| 583 | F3021115-Sr 30OU NS-3 | Sr | -27.2 | 0.3 | 886 | 129 | 1153 | 75 | 0.80 | 0.29 |
| 582 | F3021115-Sr 30OU NS-2 | Sr | -27.2 | 0.3 | 886 | 129 | 1153 | 75 | 0.80 | 0.29 |
| 581 | F3021115-Sr 30OU NS-1 | Sr | -27.2 | 0.3 | 886 | 129 | 1153 | 75 | 0.80 | 0.29 |
| 580 | F3021115-AAf 30OU NS-2 | RT3-AAf | -47.6 | 0.2 | 211 | 49 | 624 | 13 | 0.42 | 0.01 |
| 579 | F3021115-AAf 30OU NS-1 | RT3-AAf | -47.6 | 0.2 | 211 | 49 | 624 | 13 | 0.42 | 0.01 |
| 578 | F3021115-AAf 30OU NS-1 | RT3-AAf | -47.6 | 0.2 | 211 | 49 | 624 | 13 | 0.42 | 0.01 |
| 577 | F2021115-TH70 30OU NS-2 | RT2 | -46.5 | 1.7 | 189 | 13 | 627 | 7 | 0.30 | 0.01 |
| 576 | F2021115-TH70 30OU NS-1 | RT2 | -46.5 | 1.7 | 189 | 13 | 627 | 7 | 0.30 | 0.01 |
| 575 | F3021115-AA13 30OU NS-3 | RT3-AA13 | -32.7 | 0.9 | 778 | 19 | 1043 | 33 | 0.12 | 0.06 |
| 574 | F3021115-AA13 30OU NS-2 | RT3-AA13 | -32.7 | 0.9 | 778 | 19 | 1043 | 33 | 0.12 | 0.06 |
| 573 | F3021115-AA13 30OU NS-1 | RT3-AA13 | -32.7 | 0.9 | 778 | 19 | 1043 | 33 | 0.12 | 0.06 |
| 572 | F3191015-Na 30OU 4h-3 | Na | -48.5 | 0.3 | 230 | 9 | 900 | 59 | 0.52 | 0.05 |
| 571 | F3191015-Na 30OU 4h-2 | Na | -48.5 | 0.3 | 230 | 9 | 900 | 59 | 0.52 | 0.05 |
| 570 | F3191015-Na 30OU 4h-1 | Na | -48.5 | 0.3 | 230 | 9 | 900 | 59 | 0.52 | 0.05 |
| 569 | F3191015-Li 30OU 4h-3 | Li | -52.3 | 0.9 | 306 | 159 | 628 | 10 | 0.45 | 0.09 |
| 568 | F3191015-Li 30OU 4h-2 | Li | -52.3 | 0.9 | 306 | 159 | 628 | 10 | 0.45 | 0.09 |

| Test | Sample name | Clay Cation | ζ-potential | ζ-potential st. dev. | Number Mean (d) | Number Mean st. dev. | Z-average (d) | Z-average st. dev. | Polydispersity Index | Polydispersity Index st. dev. |
|---|---|---|---|---|---|---|---|---|---|---|
| # | | | mV | mV | nm | nm | nm | nm | | |
| 567 | F3191015-Li 30OU 4h-1 | Li | -52.3 | 0.9 | 306 | 159 | 628 | 10 | 0.45 | 0.09 |
| 566 | F3021115-Ca 5OU 4h-3 | Ca | -25.2 | 0.2 | 2010 | 73 | 2096 | 81 | 0.06 | 0.01 |
| 565 | F3021115-Ca 5OU 4h-2 | Ca | -25.2 | 0.2 | 2010 | 73 | 2096 | 81 | 0.06 | 0.01 |
| 564 | F3021115-Ca 5OU 4h-1 | Ca | -25.2 | 0.2 | 2010 | 73 | 2096 | 81 | 0.06 | 0.01 |
| 563 | F3021115-Ca 30OU 4h-3 | Ca | -24.4 | 0.1 | 894 | 158 | 1471 | 15 | 0.17 | 0.00 |
| 562 | F3021115-Ca 30OU 4h-2 | Ca | -24.4 | 0.1 | 894 | 158 | 1471 | 15 | 0.17 | 0.00 |
| 561 | F3021115-Ca 30OU 4h-1 | Ca | -24.4 | 0.1 | 894 | 158 | 1471 | 15 | 0.17 | 0.00 |
| 560 | F3021115-Ca 30OU NS-3 | Ca | -25.9 | 0.9 | 1089 | 65 | 1344 | 37 | 0.87 | 0.19 |
| 559 | F3021115-Ca 30OU NS-2 | Ca | -25.9 | 0.9 | 1089 | 65 | 1344 | 37 | 0.87 | 0.19 |
| 558 | F3021115-Ca 30OU NS-1 | Ca | -25.9 | 0.9 | 1089 | 65 | 1344 | 37 | 0.87 | 0.19 |
| 557 | F3021115-Mg 30OU NS-1 | Mg | -20.8 | 0.1 | 1365 | 157 | 1468 | 91 | 0.25 | 0.07 |
| 556 | F3021115-Cs 30OU NS-3 | Cs | -31.4 | 1.6 | 699 | 37 | 1159 | 15 | 0.17 | 0.02 |
| 555 | F3021115-Cs 30OU NS-2 | Cs | -31.4 | 1.6 | 699 | 37 | 1159 | 15 | 0.17 | 0.02 |
| 554 | F3021115-Cs 30OU NS-1 | Cs | -31.4 | 1.6 | 699 | 37 | 1159 | 15 | 0.17 | 0.02 |
| 553 | F3021115-K 30OU NS-4 | K | -49.6 | 1.5 | 663 | 10 | 804 | 11 | 0.09 | 0.02 |
| 552 | F3021115-K 30OU NS-3 | K | -49.6 | 1.5 | 663 | 10 | 804 | 11 | 0.09 | 0.02 |
| 551 | F3021115-K 30OU NS-2 | K | -49.6 | 1.5 | 663 | 10 | 804 | 11 | 0.09 | 0.02 |
| 550 | F3021115-K 30OU NS-1 | K | -49.6 | 1.5 | 663 | 10 | 804 | 11 | 0.09 | 0.02 |
| 549 | F3021115-NH 30OU NS-3 | NH | -37.4 | 0.6 | 677 | 160 | 1028 | 78 | 0.21 | 0.17 |
| 548 | F3021115-NH 30OU NS-2 | NH | -37.4 | 0.6 | 677 | 160 | 1028 | 78 | 0.21 | 0.17 |
| 547 | F3021115-NH 30OU NS-1 | NH | -37.4 | 0.6 | 677 | 160 | 1028 | 78 | 0.21 | 0.17 |
| 546 | F3021115-Na 30OU NS-3 | Na | -46.2 | 0.8 | 219 | 62 | 876 | 27 | 0.54 | 0.03 |
| 545 | F3021115-Na 30OU NS-2 | Na | -46.2 | 0.8 | 219 | 62 | 876 | 27 | 0.54 | 0.03 |
| 544 | F3021115-Na 30OU NS -1 | Na | -46.2 | 0.8 | 219 | 62 | 876 | 27 | 0.54 | 0.03 |
| 543 | F3021115-Li 30OU NS-2 | Li | -52.3 | 0.9 | 306 | 159 | 628 | 10 | 0.45 | 0.09 |
| 542 | F3021115-Li 30OU NS-1 | Li | -52.3 | 0.9 | 306 | 159 | 628 | 10 | 0.45 | 0.09 |
| 541 | F3201213-Sr-3 | Sr | -27.2 | 0.3 | 886 | 129 | 1153 | 75 | 0.80 | 0.29 |
| 540 | F3201213-Sr-2 | Sr | -27.2 | 0.3 | 886 | 129 | 1153 | 75 | 0.80 | 0.29 |
| 539 | F3201213-Sr-1 | Sr | -27.2 | 0.3 | 886 | 129 | 1153 | 75 | 0.80 | 0.29 |
| 350 | F1250615DE-MgRT-NU30-3 | Mg | -20.6 | 2.5 | 1125 | 601 | 1728 | 137 | 0.30 | 0.09 |
| 349 | F1250615DE-MgRT-NU30-3 | Mg | -20.6 | 2.5 | 1125 | 601 | 1728 | 137 | 0.30 | 0.09 |
| 348 | F1250615DE-MgRT-NU30-2 | Mg | -20.6 | 2.5 | 1125 | 601 | 1728 | 137 | 0.30 | 0.09 |
| 347 | F1250615DE-MgRT-NU30-1 | Mg | -20.6 | 2.5 | 1125 | 601 | 1728 | 137 | 0.30 | 0.09 |
| 346 | F3250615DE-NH-NU5-2 | NH | -38.2 | 0.2 | 1126 | 76 | 2650 | 199 | 1.00 | 0.00 |
| 345 | F3250615DE-NH-NU5-1 | NH | -38.2 | 0.2 | 1126 | 76 | 2650 | 199 | 1.00 | 0.00 |
| 344 | F3230615DE-RT3Na-NU30-3 | Na | -41.4 | 1.8 | 202 | 24 | 819 | 108 | 0.68 | 0.07 |
| 343 | F3230615DE-RT3Na-NU30-2 | Na | -41.4 | 1.8 | 202 | 24 | 819 | 108 | 0.68 | 0.07 |

| Test | Sample name | Clay Cation | Slurry characterisation in Zetasizer | | | | | | | |
|---|---|---|---|---|---|---|---|---|---|---|
| | | | ζ-potential | ζ-potential st. dev. | Number Mean (d) | Number Mean st. dev. | Z-average (d) | Z-average st. dev. | Polydispersity Index | Polydispersity Index st. dev. |
| # | | | mV | mV | nm | nm | nm | nm | | |
| 342 | F3230615DE-RT3Na-NU30-1 | Na | -41.4 | 1.8 | 202 | 24 | 819 | 108 | 0.68 | 0.07 |
| 341 | F3230615DE-RT3Na-NU5-3 | Na | -39.5 | 0.6 | 290 | 31 | 1080 | 54 | 0.63 | 0.03 |
| 340 | F3230615DE-RT3Na-NU5-2 | Na | -39.5 | 0.6 | 290 | 31 | 1080 | 54 | 0.63 | 0.03 |
| 339 | F3230615DE-RT3Na-NU5-1 | Na | -39.5 | 0.6 | 290 | 31 | 1080 | 54 | 0.63 | 0.03 |
| 338 | F3240615DE-RT3Li-NU5-3 | Li | -39.2 | 1.1 | 710 | 45 | 1235 | 50 | 0.33 | 0.18 |
| 337 | F3240615DE-RT3Li-NU5-2 | Li | -39.2 | 1.1 | 710 | 45 | 1235 | 50 | 0.33 | 0.18 |
| 336 | F3240615DE-RT3Li-NU5-1 | Li | -39.2 | 1.1 | 710 | 45 | 1235 | 50 | 0.33 | 0.18 |
| 335 | F3240615DE-AA13-NU5-3 | RT3-AA13 | -45.0 | 1.3 | 1064 | 88 | 2280 | 44 | 1.00 | 0.00 |
| 334 | F3240615DE-AA13-NU5-2 | RT3-AA13 | -45.0 | 1.3 | 1064 | 88 | 2280 | 44 | 1.00 | 0.00 |
| 333 | F3240615DE-AA13-NU5-1 | RT3-AA13 | -45.0 | 1.3 | 1064 | 88 | 2280 | 44 | 1.00 | 0.00 |
| 332 | F3240615DE-RT3NH-OU30-3 | NH | -41.3 | 0.2 | 886 | 157 | 1214 | 54 | 0.22 | 0.14 |
| 331 | F1240615DE-RT1b-NU5s-3 | RT1b | -34.8 | 0.4 | 566 | 230 | 1249 | 26 | 0.26 | 0.01 |
| 330 | F1240615DE-RT1b-NU5s-2 | RT1b | -34.8 | 0.4 | 566 | 230 | 1249 | 26 | 0.26 | 0.01 |
| 329 | F1240615DE-RT1b-NU5s-1 | RT1b | -34.8 | 0.4 | 566 | 230 | 1249 | 26 | 0.26 | 0.01 |
| 328 | F3240615DE-RT3Na-OU30-2 | Na | -46.2 | 1.6 | 236 | 20 | 868 | 101 | 0.64 | 0.04 |
| 327 | F3240615DE-RT3NH-OU30-2 | NH | -41.3 | 0.2 | 886 | 157 | 1214 | 54 | 0.22 | 0.14 |
| 326 | F3240615DE-RT3NH-OU30-1 | NH | -41.3 | 0.2 | 886 | 157 | 1214 | 54 | 0.22 | 0.14 |
| 325 | F3240615DE-RT3NH-OU5-3 | NH | -37.7 | 1.3 | 1344 | 216 | 1764 | 178 | 0.38 | 0.13 |
| 324 | F3240615DE-RT3NH-OU5-2 | NH | -37.7 | 1.3 | 1344 | 216 | 1764 | 178 | 0.38 | 0.13 |
| 323 | F3230615DE-RT3Na-OU5-3 | Na | -39.2 | 1.6 | 275 | 24 | 1337 | 111 | 0.69 | 0.02 |
| 322 | F3240615DE-RT3NH-OU5-1 | NH | -37.7 | 1.3 | 1344 | 216 | 1764 | 178 | 0.38 | 0.13 |
| 321 | F3230615DE-RT3Na-OU5-2 | Na | -39.2 | 1.6 | 275 | 24 | 1337 | 111 | 0.69 | 0.02 |
| 320 | F3240615DE-RT3Li-OU5-3 | Li | -39.2 | 1.1 | 238 | 44 | 1078 | 101 | 0.58 | 0.04 |
| 319 | F3240615DE-RT3Li-OU5-2 | Li | -39.2 | 1.1 | 238 | 44 | 1078 | 101 | 0.58 | 0.04 |
| 318 | F3240615DE-RT3Li-OU5-1 | Li | -39.2 | 1.1 | 238 | 44 | 1078 | 101 | 0.58 | 0.04 |
| 317 | F3240615DE-AAfOU5-3 | RT3-AAf | -45.1 | 2.4 | 523 | 12 | 785 | 18 | 0.27 | 0.02 |
| 316 | F3240615DE-AAfOU5-2 | RT3-AAf | -45.1 | 2.4 | 523 | 12 | 785 | 18 | 0.27 | 0.02 |
| 315 | F3240615DE-AAfOU5-1 | RT3-AAf | -45.1 | 2.4 | 523 | 12 | 785 | 18 | 0.27 | 0.02 |
| 314 | F3230615DE-AA13OU30-3 | RT3-AA13 | -39.3 | 0.6 | 812 | 148 | 1310 | 88 | 0.42 | 0.16 |
| 313 | F3230615DE-AA13OU30-2 | RT3-AA13 | -39.3 | 0.6 | 812 | 148 | 1310 | 88 | 0.42 | 0.16 |
| 312 | F3230615DE-AA13OU30-1 | RT3-AA13 | -39.3 | 0.6 | 812 | 148 | 1310 | 88 | 0.42 | 0.16 |
| 311 | F3230615DE-AA13OU5-3 | RT3-AA13 | -45.2 | 2.3 | 1169 | 101 | 2060 | 126 | 0.36 | 0.10 |
| 310 | F3230615DE-AA13OU5-2 | RT3-AA13 | -45.2 | 2.3 | 1169 | 101 | 2060 | 126 | 0.36 | 0.10 |
| 309 | F3230615DE-AA13OU5-1 | RT3-AA13 | -45.2 | 2.3 | 1169 | 101 | 2060 | 126 | 0.36 | 0.10 |
| 308 | F1-061113-RT1b-P-3 | RT1b | -38.3 | 1.5 | 440 | 122 | 1244 | 67 | 0.24 | 0.02 |
| 307 | F1-061113-RT1b-P-2 | RT1b | -38.3 | 1.5 | 440 | 122 | 1244 | 67 | 0.24 | 0.02 |
| 306 | F1-061113-RT1b-P-1 | RT1b | -38.3 | 1.5 | 440 | 122 | 1244 | 67 | 0.24 | 0.02 |

| Test | Sample name | Clay Cation | Slurry characterisation in Zetasizer | | | | | | | |
|---|---|---|---|---|---|---|---|---|---|---|
| | | | $\zeta$-potential | $\zeta$-potential st. dev. | Number Mean (d) | Number Mean st. dev. | Z-average (d) | Z-average st. dev. | Polydispersity Index | Polydispersity Index st. dev. |
| # | | | mV | mV | nm | nm | nm | nm | | |
| 304 | F2-121113-RT2pur-P-1 | RT2 | | | | | | | | |
| 301 | F1-260415-RT1Li-2 | Li | -47.2 | 1.5 | 204 | 11 | 850 | 28 | 0.56 | 0.04 |
| 300 | F1-260415-RT1Li-1 | Li | -47.2 | 1.5 | 204 | 11 | 850 | 28 | 0.56 | 0.04 |
| 299 | F3-260415-RT3Li-1 | Li | -47.2 | 1.5 | 204 | 11 | 850 | 28 | 0.56 | 0.04 |
| 298 | F3-260415-RT3NH4-15-3 | NH | -41.3 | 0.2 | 886 | 157 | 1214 | 54 | 0.22 | 0.14 |
| 297 | F3-260415-RT3NH4-15-2 | NH | -41.3 | 0.2 | 886 | 157 | 1214 | 54 | 0.22 | 0.14 |
| 296 | F3-260415-RT3NH4-15-1 | NH | -41.3 | 0.2 | 886 | 157 | 1214 | 54 | 0.22 | 0.14 |
| 295 | F3-260415-RT3Na-3 | Na | -46.2 | 1.6 | 236 | 20 | 868 | 101 | 0.64 | 0.04 |
| 294 | F3-260415-RT3K-3 | K | | | | | | | | |
| 293 | F3-260415-RT3K-2 | K | | | | | | | | |
| 292 | F3-260415-RT3K-1 | K | | | | | | | | |
| 291 | F3-230415-RT3AA13wT-2 | RT3-AA13 | -39.3 | 0.6 | 812 | 148 | 1310 | 88 | 0.42 | 0.16 |
| 290 | F3-230415-RT3AA13wT-1 | RT3-AA13 | -39.3 | 0.6 | 812 | 148 | 1310 | 88 | 0.42 | 0.16 |
| 289 | F2-230415-RT2TH70 wT-3 | RT2 | | | | | | | | |
| 288 | F2-230415-RT2TH70 wT-2 | RT2 | | | | | | | | |
| 287 | F2-230415-RT2TH70 wT-1 | RT2 | | | | | | | | |
| 286 | F1-230415-RT1b wT-3 | RT1b | -31.7 | 1.3 | 470 | 91 | 881 | 18 | 0.28 | 0.01 |
| 285 | F1-230415-RT1b wT-2 | RT1b | -31.7 | 1.3 | 470 | 91 | 881 | 18 | 0.28 | 0.01 |
| 284 | F1-230415-RT1b wT-1 | RT1b | -31.7 | 1.3 | 470 | 91 | 881 | 18 | 0.28 | 0.01 |
| 283 | F3-270115-NH4-14-3 | NH | -41.3 | 0.2 | 886 | 157 | 1214 | 54 | 0.22 | 0.14 |
| 282 | F3-270115-NH4-14-2 | NH | -41.3 | 0.2 | 886 | 157 | 1214 | 54 | 0.22 | 0.14 |
| 281 | F3-270115-NH4-14-1 | NH | -41.3 | 0.2 | 886 | 157 | 1214 | 54 | 0.22 | 0.14 |
| 280 | F3-200114-NH4-14-3 | NH | -37.4 | 0.6 | 677 | 160 | 1028 | 78 | 0.21 | 0.17 |
| 279 | F3-200114-NH4-14-2 | NH | -37.4 | 0.6 | 677 | 160 | 1028 | 78 | 0.21 | 0.17 |
| 278 | F3-200114-NH4-14-1 | NH | -37.4 | 0.6 | 677 | 160 | 1028 | 78 | 0.21 | 0.17 |
| 277 | F3-200114-Li13-3 | Li | -42.2 | 1.2 | 721 | 36 | 826 | 31 | 0.14 | 0.08 |
| 276 | F3-200114-Li13-2 | Li | -42.2 | 1.2 | 721 | 36 | 826 | 31 | 0.14 | 0.08 |
| 275 | F3-200114-Li13-1 | Li | -42.2 | 1.2 | 721 | 36 | 826 | 31 | 0.14 | 0.08 |
| 274 | F3-070414AAf4-3 | RT3-AAf | -49.0 | 0.6 | 444 | 177 | 908 | 16 | 0.28 | 0.02 |
| 273 | F3-070414AAf4-2 | RT3-AAf | -49.0 | 0.6 | 444 | 177 | 908 | 16 | 0.28 | 0.02 |
| 272 | F3-070414AAf4-1 | RT3-AAf | -49.0 | 0.6 | 444 | 177 | 908 | 16 | 0.28 | 0.02 |
| 271 | F3-070414AAf3-3 | RT3-AAf | -49.0 | 0.6 | 444 | 177 | 908 | 16 | 0.28 | 0.02 |
| 270 | F3-070414AAf3-2b | RT3-AAf | -49.0 | 0.6 | 444 | 177 | 908 | 16 | 0.28 | 0.02 |
| 269 | F3-070414AAf3-2 | RT3-AAf | -49.0 | 0.6 | 444 | 177 | 908 | 16 | 0.28 | 0.02 |
| 268 | F3-070414AAf3-1 | RT3-AAf | -49.0 | 0.6 | 444 | 177 | 908 | 16 | 0.28 | 0.02 |
| 267 | F3-070414AAf2-2 | RT3-AAf | -49.0 | 0.6 | 444 | 177 | 908 | 16 | 0.28 | 0.02 |
| 266 | F3-070414AAf2-2 | RT3-AAf | -49.0 | 0.6 | 444 | 177 | 908 | 16 | 0.28 | 0.02 |

| Test | Sample name | Clay Cation | Slurry characterisation in Zetasizer | | | | | | | |
|---|---|---|---|---|---|---|---|---|---|---|
| | | | ζ-potential | ζ-potential st. dev. | Number Mean (d) | Number Mean st. dev. | Z-average (d) | Z-average st. dev. | Polydispersity Index | Polydispersity Index st. dev. |
| # | | | mV | mV | nm | nm | nm | nm | | |
| 265 | F3-070414AAf2-1 | RT3-AAf | -49.0 | 0.6 | 444 | 177 | 908 | 16 | 0.28 | 0.02 |
| 264 | F3-070414AAf1-3 | RT3-AAf | -49.0 | 0.6 | 444 | 177 | 908 | 16 | 0.28 | 0.02 |
| 263 | F3-070414AAf1-2 | RT3-AAf | -49.0 | 0.6 | 444 | 177 | 908 | 16 | 0.28 | 0.02 |
| 262 | F3-070414AAf1-1 | RT3-AAf | -49.0 | 0.6 | 444 | 177 | 908 | 16 | 0.28 | 0.02 |
| 261 | F3-201213-Cs-last1 | Cs | -31.4 | 1.6 | 699 | 37 | 1159 | 15 | 0.17 | 0.02 |
| 260 | F3-201213-NH4-13-2-3 | NH | -37.4 | 0.6 | 677 | 160 | 1028 | 78 | 0.21 | 0.17 |
| 259 | F3-201213-NH4-13-2-2b | NH | -37.4 | 0.6 | 677 | 160 | 1028 | 78 | 0.21 | 0.17 |
| 258 | F3-201213-NH4-13-2-2 | NH | -37.4 | 0.6 | 677 | 160 | 1028 | 78 | 0.21 | 0.17 |
| 257 | F3-201213-NH4-13-2-1 | NH | -37.4 | 0.6 | 677 | 160 | 1028 | 78 | 0.21 | 0.17 |
| 256 | F3-201213-NH4-13-1-3 | NH | -37.4 | 0.6 | 677 | 160 | 1028 | 78 | 0.21 | 0.17 |
| 253 | F3-201213-NH4-13-1-2 | NH | -37.4 | 0.6 | 677 | 160 | 1028 | 78 | 0.21 | 0.17 |
| 252 | F3-201213-NH4-13-1 | NH | -37.4 | 0.6 | 677 | 160 | 1028 | 78 | 0.21 | 0.17 |
| 251 | F3-201213-Sr3-last2 | Sr | -27.2 | 0.3 | 886 | 129 | 1153 | 75 | 0.80 | 0.29 |
| 250 | F3-201213-Sr3-last1 | Sr | -27.2 | 0.3 | 886 | 129 | 1153 | 75 | 0.80 | 0.29 |
| 249 | F3201213-43-K-last3 | K | -49.6 | 1.5 | 663 | 10 | 804 | 11 | 0.09 | 0.02 |
| 248 | F3201213-43-K-last2 | K | -49.6 | 1.5 | 663 | 10 | 804 | 11 | 0.09 | 0.02 |
| 247 | F3201213-43-K-last1 | K | -49.6 | 1.5 | 663 | 10 | 804 | 11 | 0.09 | 0.02 |
| 246 | F3201213-42-NH4-12last3 | NH | -39.1 | 0.2 | 1223 | 53 | 1459 | 89 | 0.66 | 0.30 |
| 245 | F3201213-42-NH4-12last2 | NH | -39.1 | 0.2 | 1223 | 53 | 1459 | 89 | 0.66 | 0.30 |
| 244 | F3201213-42-NH4-12last1 | NH | -39.1 | 0.2 | 1223 | 53 | 1459 | 89 | 0.66 | 0.30 |
| 243 | F3201213-41-2-Na2last3 | Na | -37.7 | 0.3 | 381 | 364 | 1375 | 90 | 0.51 | 0.07 |
| 242 | F3201213-41-2-Na2last2 | Na | -37.7 | 0.3 | 381 | 364 | 1375 | 90 | 0.51 | 0.07 |
| 241 | F3201213-41-2-Na2last1 | Na | -37.7 | 0.3 | 381 | 364 | 1375 | 90 | 0.51 | 0.07 |
| 240 | F3201213-41-Na2last3 | Na | -37.7 | 0.3 | 381 | 364 | 1375 | 90 | 0.51 | 0.07 |
| 239 | F3201213-41-Na2last2 | Na | -37.7 | 0.3 | 381 | 364 | 1375 | 90 | 0.51 | 0.07 |
| 238 | F3201213-40-Na1last1 | Na | -37.7 | 0.3 | 381 | 364 | 1375 | 90 | 0.51 | 0.07 |
| 237 | F3201213-40-Na1last3 | Na | -37.7 | 0.3 | 381 | 364 | 1375 | 90 | 0.51 | 0.07 |
| 236 | F3201213-40-Na1last2 | Na | -37.7 | 0.3 | 381 | 364 | 1375 | 90 | 0.51 | 0.07 |
| 235 | F3201213-40-Na1last | Na | -37.7 | 0.3 | 381 | 364 | 1375 | 90 | 0.51 | 0.07 |
| 215 | F2121113RT2TH70-3 | RT2 | | | | | | | | |
| 214 | F2121113RT2TH70-2 | RT2 | | | | | | | | |
| 213 | F2121113RT2TH70-1 | RT2 | | | | | | | | |
| 209 | F1061113RT1m-3 | RT1m | -5.3 | 1.2 | 440 | 122 | 1197 | 17 | 0.26 | 0.03 |
| 208 | F1061113RT1m-2 | RT1m | -5.3 | 1.2 | 440 | 122 | 1197 | 17 | 0.26 | 0.03 |
| 207 | F1061113RT1m-1 | RT1m | -5.3 | 1.2 | 440 | 122 | 1197 | 17 | 0.26 | 0.03 |
| 202 | F1061113RT1b-3 | RT1b | -38.3 | 1.5 | 440 | 122 | 1244 | 67 | 0.24 | 0.02 |
| 201 | F1061113RT1b-2 | RT1b | -38.3 | 1.5 | 440 | 122 | 1244 | 67 | 0.24 | 0.02 |

| Test | Sample name | Clay Cation | Slurry characterisation in Zetasizer | | | | | | | |
|---|---|---|---|---|---|---|---|---|---|---|
| | | | $\zeta$-potential | $\zeta$-potential st. dev. | Number Mean (d) | Number Mean st. dev. | Z-average (d) | Z-average st. dev. | Polydispersity Index | Polydispersity Index st. dev. |
| # | | | mV | mV | nm | nm | nm | nm | | |
| 200 | F1061113RT1b-1 | RT1b | -38.3 | 1.5 | 440 | 122 | 1244 | 67 | 0.24 | 0.02 |
| 182 | F3180913RT3 100-3 | RT3-OWE | -44.7 | 0.7 | 1271 | 164 | 1631 | 61 | 0.19 | 0.16 |
| 181 | F3180913RT3 100-2 | RT3-OWE | -44.7 | 0.7 | 1271 | 164 | 1631 | 61 | 0.19 | 0.16 |
| 180 | F3180913RT3 100 | RT3-OWE | -44.7 | 0.7 | 1271 | 164 | 1631 | 61 | 0.19 | 0.16 |
| 179 | F3-49-OWF-P3 | RT3-OWF | -44.7 | 0.7 | 1271 | 164 | 1631 | 61 | 0.19 | 0.16 |
| 178 | F3-49-OWF-P2 | RT3-OWF | -44.7 | 0.7 | 1271 | 164 | 1631 | 61 | 0.19 | 0.16 |
| 177 | F3-49-OWF-P1 | RT3-OWF | -44.7 | 0.7 | 1271 | 164 | 1631 | 61 | 0.19 | 0.16 |
| 176 | F3-48-Sr-P3 | Sr | -27.2 | 0.3 | 886 | 129 | 1153 | 75 | 0.80 | 0.29 |
| 175 | F3-48-Sr-P2 | Sr | -27.2 | 0.3 | 886 | 129 | 1153 | 75 | 0.80 | 0.29 |
| 174 | F3-48-Sr-P1 | Sr | -27.2 | 0.3 | 886 | 129 | 1153 | 75 | 0.80 | 0.29 |
| 173 | F3-41-Na2-P4 | Na | -37.7 | 0.3 | 381 | 364 | 1375 | 90 | 0.51 | 0.07 |
| 172 | F3-41-Na2-P3 | Na | -37.7 | 0.3 | 381 | 364 | 1375 | 90 | 0.51 | 0.07 |
| 171 | F3-41-Na2-P2 | Na | -37.7 | 0.3 | 381 | 364 | 1375 | 90 | 0.51 | 0.07 |
| 170 | F3-41-Na2-P1 | Na | -37.7 | 0.3 | 381 | 364 | 1375 | 90 | 0.51 | 0.07 |
| 97 | F3-49-OWF 2i3 | RT3-OWF | -44.7 | 0.7 | 1271 | 164 | 1631 | 61 | 0.19 | 0.16 |
| 96 | F3-49-OWF 2 i2 | RT3-OWF | -44.7 | 0.7 | 1271 | 164 | 1631 | 61 | 0.19 | 0.16 |
| 95 | F3-49-OWF 2 i1 | RT3-OWF | -44.7 | 0.7 | 1271 | 164 | 1631 | 61 | 0.19 | 0.16 |
| 94 | F3-49-OWF i3 | RT3-OWF | -44.7 | 0.7 | 1271 | 164 | 1631 | 61 | 0.19 | 0.16 |
| 93 | F3-49-OWF i2 | RT3-OWF | -44.7 | 0.7 | 1271 | 164 | 1631 | 61 | 0.19 | 0.16 |
| 92 | F3-49-OWF i1 | RT3-OWF | -44.7 | 0.7 | 1271 | 164 | 1631 | 61 | 0.19 | 0.16 |
| 91 | F3-48-Sr-i3 | Sr | -27.2 | 0.3 | 886 | 129 | 1153 | 75 | 0.80 | 0.29 |
| 90 | F3-48-Sr-i2 | Sr | -27.2 | 0.3 | 886 | 129 | 1153 | 75 | 0.80 | 0.29 |
| 89 | F3-48-Sr-i1 | Sr | -27.2 | 0.3 | 886 | 129 | 1153 | 75 | 0.80 | 0.29 |
| 88 | F3-46-Ba-i3 | Ba | -30.8 | 0.8 | 1165 | 93 | 1413 | 49 | 0.83 | 0.24 |
| 86 | F3-46-Ba-i2 | Ba | -30.8 | 0.8 | 1165 | 93 | 1413 | 49 | 0.83 | 0.24 |
| 85 | F3-46-Ba-i1 | Ba | -30.8 | 0.8 | 1165 | 93 | 1413 | 49 | 0.83 | 0.24 |
| 84 | F3-45-Cs-i3 | Cs | -31.4 | 1.6 | 699 | 37 | 1159 | 15 | 0.17 | 0.02 |
| 83 | F3-45-Cs-i2 | Cs | -31.4 | 1.6 | 699 | 37 | 1159 | 15 | 0.17 | 0.02 |
| 82 | F3-45-Cs-i1 | Cs | -31.4 | 1.6 | 699 | 37 | 1159 | 15 | 0.17 | 0.02 |
| 58 | F3-32-Na1-i7 | Na | -37.7 | 0.3 | 381 | 364 | 1375 | 90 | 0.51 | 0.07 |
| 57 | F3-31-Li-i7 | Li | -38.7 | 1.2 | 388 | 256 | 1191 | 46 | 0.62 | 0.02 |
| 56 | F3-31-Li-i8 | Li | -38.7 | 1.2 | 388 | 256 | 1191 | 46 | 0.62 | 0.02 |
| 55 | F3-47-Sr-i4 | Sr | -27.2 | 0.3 | 886 | 129 | 1153 | 75 | 0.80 | 0.29 |
| 54 | F3-47-Sr-i2 | Sr | -27.2 | 0.3 | 886 | 129 | 1153 | 75 | 0.80 | 0.29 |
| 53 | F3-44-Mg-i4 | Mg | -20.3 | 0.6 | 431 | 74 | 1436 | 36 | 0.35 | 0.06 |
| 52 | F3-44-Mg-i3 | Mg | -20.3 | 0.6 | 431 | 74 | 1436 | 36 | 0.35 | 0.06 |
| 51 | F3-44-Mg-i2 | Mg | -20.3 | 0.6 | 431 | 74 | 1436 | 36 | 0.35 | 0.06 |

| Test | Sample name | Clay Cation | Slurry characterisation in Zetasizer | | | | | | | |
|---|---|---|---|---|---|---|---|---|---|---|
| | | | ζ-potential | ζ-potential st. dev. | Number Mean (d) | Number Mean st. dev. | Z-average (d) | Z-average st. dev. | Polydispersity Index | Polydispersity Index st. dev. |
| # | | | mV | mV | nm | nm | nm | nm | | |
| 50 | F3-44-Mg-i1 | Mg | -20.3 | 0.6 | 431 | 74 | 1436 | 36 | 0.35 | 0.06 |
| 49 | F3-43-K-i4 | K | -49.6 | 1.5 | 663 | 10 | 804 | 11 | 0.09 | 0.02 |
| 48 | F3-43-K-i3 | K | -49.6 | 1.5 | 663 | 10 | 804 | 11 | 0.09 | 0.02 |
| 47 | F3-43-K-i2 | K | -49.6 | 1.5 | 663 | 10 | 804 | 11 | 0.09 | 0.02 |
| 46 | F3-43-K-i1 | K | -49.6 | 1.5 | 663 | 10 | 804 | 11 | 0.09 | 0.02 |
| 45 | F3-38-OWE i9 | RT3-OWE | -44.7 | 0.7 | 1271 | 164 | 1631 | 61 | 0.19 | 0.16 |
| 44 | F3-38-OWE i8 | RT3-OWE | -44.7 | 0.7 | 1271 | 164 | 1631 | 61 | 0.19 | 0.16 |
| 43 | F3-38-OWE i7 | RT3-OWE | -44.7 | 0.7 | 1271 | 164 | 1631 | 61 | 0.19 | 0.16 |
| 42 | F3-38-OWE i6 | RT3-OWE | -44.7 | 0.7 | 1271 | 164 | 1631 | 61 | 0.19 | 0.16 |
| 40 | F3-38-OWE i6 | RT3-OWE | -44.7 | 0.7 | 1271 | 164 | 1631 | 61 | 0.19 | 0.16 |
| 39 | F3-42 NH4 4i | NH | -39.1 | 0.2 | 1223 | 53 | 1459 | 89 | 0.66 | 0.30 |
| 38 | F3-42 NH4 3i | NH | -39.1 | 0.2 | 1223 | 53 | 1459 | 89 | 0.66 | 0.30 |
| 37 | F3-42 NH4 2i | NH | -39.1 | 0.2 | 1223 | 53 | 1459 | 89 | 0.66 | 0.30 |
| 36 | F3-42 NH4 1i | NH | -39.1 | 0.2 | 1223 | 53 | 1459 | 89 | 0.66 | 0.30 |
| 35 | F3-41 Na2 4i | Na | -37.7 | 0.3 | 381 | 364 | 1375 | 90 | 0.51 | 0.07 |
| 34 | F3-41 Na2 3i | Na | -37.7 | 0.3 | 381 | 364 | 1375 | 90 | 0.51 | 0.07 |
| 33 | F3-41 Na2 2i | Na | -37.7 | 0.3 | 381 | 364 | 1375 | 90 | 0.51 | 0.07 |
| 32 | F3-41 Na2 1i | Na | -37.7 | 0.3 | 381 | 364 | 1375 | 90 | 0.51 | 0.07 |
| 31 | F3-40 Na1 5i | Na | -37.7 | 0.3 | 381 | 364 | 1375 | 90 | 0.51 | 0.07 |
| 30 | F3-40 Na1 4i | Na | -37.7 | 0.3 | 381 | 364 | 1375 | 90 | 0.51 | 0.07 |
| 29 | F3-40 Na1 3i | Na | -37.7 | 0.3 | 381 | 364 | 1375 | 90 | 0.51 | 0.07 |
| 28 | F3-40 Na1 2i | Na | -37.7 | 0.3 | 381 | 364 | 1375 | 90 | 0.51 | 0.07 |
| 27 | F3-40 Na1 1i | Na | -37.7 | 0.3 | 381 | 364 | 1375 | 90 | 0.51 | 0.07 |
| 17 | F3-Li-39o6 | Li | -42.6 | 6.8 | 388 | 256 | 1191 | 46 | 0.62 | 0.02 |
| 16 | F3-Li-39i5 | Li | -42.6 | 6.8 | 388 | 256 | 1191 | 46 | 0.62 | 0.02 |
| 15 | F3-Li-39i4 | Li | -42.6 | 6.8 | 388 | 256 | 1191 | 46 | 0.62 | 0.02 |
| 14 | F3-Li-39i3 | Li | -42.6 | 6.8 | 388 | 256 | 1191 | 46 | 0.62 | 0.02 |

Table AIII-4. Slurry characterisation in Malvern particle size analyser

| Test | Sample name | Clay Cation | Slurry characterisation in Malvern particle size analyser | | | | |
|---|---|---|---|---|---|---|---|
| | | | Particle Size (µm) | | | Surface weighted mean | Volume weighted mean |
| # | | | d (0.1) | d (0.5) | d (0.9) | d (3, 2) | d (4, 3) |
| 602 | F3191015-Ba 30OU 4h-2 | Ba | 2.74 | 5.71 | 14.35 | 5.07 | 43.99 |
| 601 | F3191015-Ba 30OU4h-1 | Ba | 2.74 | 5.71 | 14.35 | 5.07 | 43.99 |
| 600 | F3191015-Sr 30OU 4h-2 | Sr | 2.88 | 6.27 | 761.02 | 5.63 | 145.51 |
| 599 | F3191015-Sr 30OU 4h -1 | Sr | 2.88 | 6.27 | 761.02 | 5.63 | 145.51 |
| 598 | F3191015-Mg 30OU 4h-4 | Mg | 2.80 | 5.72 | 12.01 | 4.98 | 6.72 |
| 597 | F3191015-Mg 30OU 4h-3 | Mg | 2.80 | 5.72 | 12.01 | 4.98 | 6.72 |
| 596 | F3191015-Mg 30OU 4h-2 | Mg | 2.80 | 5.72 | 12.01 | 4.98 | 6.72 |
| 595 | F3191015-Mg 30OU 4h-1 | Mg | 2.80 | 5.72 | 12.01 | 4.98 | 6.72 |
| 594 | F3191015-K 30OU 4h -2 | K | 3.62 | 9.98 | 969.60 | 8.34 | 257.45 |
| 593 | F3191015-K 30OU 4h-1 | K | 3.62 | 9.98 | 969.60 | 8.34 | 257.45 |
| 592 | F3191015-NH 30OU 4h-3 | NH | 3.56 | 8.91 | 546.61 | 7.37 | 116.60 |
| 591 | F3191015-NH 30OU 4h-2 | NH | 3.56 | 8.91 | 546.61 | 7.37 | 116.60 |
| 590 | F3191015-NH 30OU 4h-1 | NH | 3.56 | 8.91 | 546.61 | 7.37 | 116.60 |
| 589 | F1021115-RT1b 30OU NS-3 | RT1b | 0.13 | 20.96 | 1324.14 | 0.50 | 478.46 |
| 588 | F1021115-RT1b 30OU NS-2 | RT1b | 0.13 | 20.96 | 1324.14 | 0.50 | 478.46 |
| 587 | F1021115-RT1b 30OU NS-1 | RT1b | 0.13 | 20.96 | 1324.14 | 0.50 | 478.46 |
| 586 | F3021115-Ba 30OU NS top-3 | Ba | 2.73 | 5.70 | 13.79 | 5.03 | 28.92 |
| 585 | F3021115-Ba 30OU NS top-2 | Ba | 2.73 | 5.70 | 13.79 | 5.03 | 28.92 |
| 584 | F3021115-Ba 30OU NS top-1 | Ba | 2.73 | 5.70 | 13.79 | 5.03 | 28.92 |
| 583 | F3021115-Sr 30OU NS-3 | Sr | 2.76 | 5.66 | 11.97 | 4.92 | 6.67 |
| 582 | F3021115-Sr 30OU NS-2 | Sr | 2.76 | 5.66 | 11.97 | 4.92 | 6.67 |
| 581 | F3021115-Sr 30OU NS-1 | Sr | 2.76 | 5.66 | 11.97 | 4.92 | 6.67 |
| 580 | F3021115-AAf 30OU NS-2 | RT3-AAf | 0.12 | 556.21 | 1074.91 | 0.44 | 482.18 |
| 579 | F3021115-AAf 30OU NS-1 | RT3-AAf | 0.12 | 556.21 | 1074.91 | 0.44 | 482.18 |
| 578 | F3021115-AAf 30OU NS-1 | RT3-AAf | 0.12 | 556.21 | 1074.91 | 0.44 | 482.18 |
| 577 | F2021115-TH70 30OU NS-2 | RT2 | 1.78 | 5.70 | 18.50 | 1.16 | 8.15 |
| 576 | F2021115-TH70 30OU NS-1 | RT2 | 1.78 | 5.70 | 18.50 | 1.16 | 8.15 |
| 575 | F3021115-AA13 30OU NS-3 | RT3-AA13 | 3.30 | 6.96 | 15.50 | 5.98 | 8.55 |
| 574 | F3021115-AA13 30OU NS-2 | RT3-AA13 | 3.295 | 6.96 | 15.499 | 5.975 | 8.547 |
| 573 | F3021115-AA13 30OU NS-1 | RT3-AA13 | 3.295 | 6.96 | 15.499 | 5.975 | 8.547 |
| 572 | F3191015-Na 30OU 4h-3 | Na | 2.705 | 5.825 | 17.903 | 5.147 | 47.267 |
| 571 | F3191015-Na 30OU 4h-2 | Na | 2.705 | 5.825 | 17.903 | 5.147 | 47.267 |
| 570 | F3191015-Na 30OU 4h-1 | Na | 2.705 | 5.825 | 17.903 | 5.147 | 47.267 |
| 569 | F3191015-Li 30OU 4h-3 | Li | 4.171 | 18.278 | 1078.051 | 10.98 | 291.418 |
| 568 | F3191015-Li 30OU 4h-2 | Li | 4.171 | 18.278 | 1078.051 | 10.98 | 291.418 |
| 567 | F3191015-Li 30OU 4h-1 | Li | 4.171 | 18.278 | 1078.051 | 10.98 | 291.418 |

| Test | Sample name | Clay Cation | Slurry characterisation in Malvern particle size analyser | | | | |
|---|---|---|---|---|---|---|---|
| | | | Particle Size (µm) | | | Surface weighted mean | Volume weighted mean |
| # | | | d (0.1) | d (0.5) | d (0.9) | d (3, 2) | d (4, 3) |
| 566 | F3021115-Ca 5OU 4h-3 | Ca | 3.238 | 7.267 | 17.404 | 6.106 | 9.149 |
| 565 | F3021115-Ca 5OU 4h-2 | Ca | 3.238 | 7.267 | 17.404 | 6.106 | 9.149 |
| 564 | F3021115-Ca 5OU 4h-1 | Ca | 3.238 | 7.267 | 17.404 | 6.106 | 9.149 |
| 563 | F3021115-Ca 30OU 4h-3 | Ca | 2.964 | 6.35 | 14.663 | 5.452 | 7.906 |
| 562 | F3021115-Ca 30OU 4h-2 | Ca | 2.964 | 6.35 | 14.663 | 5.452 | 7.906 |
| 561 | F3021115-Ca 30OU 4h-1 | Ca | 2.964 | 6.35 | 14.663 | 5.452 | 7.906 |
| 560 | F3021115-Ca 30OU NS-3 | Ca | 2.84 | 6.421 | 16.188 | 5.415 | 8.634 |
| 559 | F3021115-Ca 30OU NS-2 | Ca | 2.84 | 6.421 | 16.188 | 5.415 | 8.634 |
| 558 | F3021115-Ca 30OU NS-1 | Ca | 2.84 | 6.421 | 16.188 | 5.415 | 8.634 |
| 557 | F3021115-Mg 30OU NS-1 | Mg | 2.815 | 5.862 | 14.064 | 5.172 | 28.267 |
| 556 | F3021115-Cs 30OU NS-3 | Cs | 2.964 | 5.416 | 9.969 | 4.885 | 6.029 |
| 555 | F3021115-Cs 30OU NS-2 | Cs | 2.964 | 5.416 | 9.969 | 4.885 | 6.029 |
| 554 | F3021115-Cs 30OU NS-1 | Cs | 2.96 | 5.42 | 9.97 | 4.89 | 6.03 |
| 553 | F3021115-K 30OU NS-4 | K | 3.04 | 6.41 | 13.37 | 5.48 | 7.42 |
| 552 | F3021115-K 30OU NS-3 | K | 3.04 | 6.41 | 13.37 | 5.48 | 7.42 |
| 551 | F3021115-K 30OU NS-2 | K | 3.04 | 6.41 | 13.37 | 5.48 | 7.42 |
| 550 | F3021115-K 30OU NS-1 | K | 3.04 | 6.41 | 13.37 | 5.48 | 7.42 |
| 549 | F3021115-NH 30OU NS-3 | NH | 3.52 | 8.69 | 346.14 | 7.18 | 83.06 |
| 548 | F3021115-NH 30OU NS-2 | NH | 3.52 | 8.69 | 346.14 | 7.18 | 83.06 |
| 547 | F3021115-NH 30OU NS-1 | NH | 3.52 | 8.69 | 346.14 | 7.18 | 83.06 |
| 546 | F3021115-Na 30OU NS-3 | Na | 2.86 | 6.79 | 800.99 | 6.00 | 176.61 |
| 545 | F3021115-Na 30OU NS-2 | Na | 2.86 | 6.79 | 800.99 | 6.00 | 176.61 |
| 544 | F3021115-Na 30OU NS -1 | Na | 2.86 | 6.79 | 800.99 | 6.00 | 176.61 |
| 543 | F3021115-Li 30OU NS-2 | Li | 7.58 | 80.24 | 1156.30 | 22.45 | 372.24 |
| 542 | F3021115-Li 30OU NS-1 | Li | 7.58 | 80.24 | 1156.30 | 22.45 | 372.24 |
| 541 | F3201213-Sr-3 | Sr | 2.763 | 5.657 | 11.969 | 4.923 | 6.672 |
| 540 | F3201213-Sr-2 | Sr | 2.763 | 5.657 | 11.969 | 4.923 | 6.672 |
| 539 | F3201213-Sr-1 | Sr | 2.763 | 5.657 | 11.969 | 4.923 | 6.672 |
| 350 | F1250615DE-MgRT-NU30-3 | Mg | 0.11 | 3.21 | 20.42 | 0.34 | 13.92 |
| 349 | F1250615DE-MgRT-NU30-3 | Mg | 0.11 | 3.21 | 20.42 | 0.34 | 13.92 |
| 348 | F1250615DE-MgRT-NU30-2 | Mg | 0.11 | 3.214 | 20.424 | 0.344 | 13.917 |
| 347 | F1250615DE-MgRT-NU30-1 | Mg | 0.11 | 3.21 | 20.42 | 0.34 | 13.92 |
| 346 | F3250615DE-NH-NU5-2 | NH | 3.47 | 8.09 | 18.77 | 6.63 | 9.91 |
| 345 | F3250615DE-NH-NU5-1 | NH | 3.47 | 8.09 | 18.77 | 6.63 | 9.91 |
| 344 | F3230615DE-RT3Na-NU30-3 | Na | 2.66 | 6.40 | 40.29 | 5.42 | 45.83 |
| 343 | F3230615DE-RT3Na-NU30-2 | Na | 2.66 | 6.40 | 40.29 | 5.42 | 45.83 |
| 342 | F3230615DE-RT3Na-NU30-1 | Na | 2.66 | 6.40 | 40.29 | 5.42 | 45.83 |

| Test | Sample name | Clay Cation | Slurry characterisation in Malvern particle size analyser | | | | |
|---|---|---|---|---|---|---|---|
| | | | Particle Size (μm) | | | Surface weighted mean | Volume weighted mean |
| # | | | d (0.1) | d (0.5) | d (0.9) | d (3, 2) | d (4, 3) |
| 341 | F3230615DE-RT3Na-NU5-3 | Na | 3.46 | 11.70 | 36.93 | 7.90 | 18.61 |
| 340 | F3230615DE-RT3Na-NU5-2 | Na | 3.46 | 11.70 | 36.93 | 7.90 | 18.61 |
| 339 | F3230615DE-RT3Na-NU5-1 | Na | 3.46 | 11.70 | 36.93 | 7.90 | 18.61 |
| 338 | F3240615DE-RT3Li-NU5-3 | Li | 3.17 | 7.29 | 18.53 | 6.11 | 27.27 |
| 337 | F3240615DE-RT3Li-NU5-2 | Li | 3.17 | 7.29 | 18.53 | 6.11 | 27.27 |
| 336 | F3240615DE-RT3Li-NU5-1 | Li | 3.17 | 7.29 | 18.53 | 6.11 | 27.27 |
| 335 | F3240615DE-AA13-NU5-3 | RT3-AA13 | 3.43 | 7.96 | 19.36 | 6.57 | 10.09 |
| 334 | F3240615DE-AA13-NU5-2 | RT3-AA13 | 3.43 | 7.96 | 19.36 | 6.57 | 10.09 |
| 333 | F3240615DE-AA13-NU5-1 | RT3-AA13 | 3.43 | 7.96 | 19.36 | 6.57 | 10.09 |
| 332 | F3240615DE-RT3NH-OU30-3 | NH | 3.51 | 8.45 | 26.62 | 7.00 | 78.55 |
| 331 | F1240615DE-RT1b-NU5s-3 | RT1b | 0.16 | 17.98 | 1177.76 | 0.71 | 347.35 |
| 330 | F1240615DE-RT1b-NU5s-2 | RT1b | 0.16 | 17.98 | 1177.76 | 0.71 | 347.35 |
| 329 | F1240615DE-RT1b-NU5s-1 | RT1b | 0.16 | 17.98 | 1177.76 | 0.71 | 347.35 |
| 328 | F3240615DE-RT3Na-OU30-2 | Na | 2.73 | 6.99 | 814.91 | 5.92 | 171.81 |
| 327 | F3240615DE-RT3NH-OU30-2 | NH | 3.51 | 8.45 | 26.62 | 7.00 | 78.55 |
| 326 | F3240615DE-RT3NH-OU30-1 | NH | 3.51 | 8.45 | 26.62 | 7.00 | 78.55 |
| 325 | F3240615DE-RT3NH-OU5-3 | NH | 3.50 | 8.48 | 25.14 | 6.99 | 66.26 |
| 324 | F3240615DE-RT3NH-OU5-2 | NH | 3.50 | 8.48 | 25.14 | 6.99 | 66.26 |
| 323 | F3230615DE-RT3Na-OU5-3 | Na | 3.30 | 11.43 | 66.25 | 7.81 | 77.81 |
| 322 | F3240615DE-RT3NH-OU5-1 | NH | 3.38 | 6.98 | 14.85 | 6.07 | 26.74 |
| 321 | F3230615DE-RT3Na-OU5-2 | Na | 3.30 | 11.43 | 66.25 | 7.81 | 77.81 |
| 320 | F3240615DE-RT3Li-OU5-3 | Li | 3.07 | 8.41 | 774.63 | 6.82 | 163.20 |
| 319 | F3240615DE-RT3Li-OU5-2 | Li | 3.07 | 8.41 | 774.63 | 6.82 | 163.20 |
| 318 | F3240615DE-RT3Li-OU5-1 | Li | 3.07 | 8.41 | 774.63 | 6.82 | 163.20 |
| 317 | F3240615DE-AAfOU5-3 | RT3-AAf | 0.12 | 6.27 | 1136.00 | 0.39 | 325.26 |
| 316 | F3240615DE-AAfOU5-2 | RT3-AAf | 0.12 | 6.27 | 1136.00 | 0.39 | 325.26 |
| 315 | F3240615DE-AAfOU5-1 | RT3-AAf | 0.12 | 6.27 | 1136.00 | 0.39 | 325.26 |
| 314 | F3230615DE-AA13OU30-3 | RT3-AA13 | 3.37 | 8.25 | 31.55 | 6.84 | 86.04 |
| 313 | F3230615DE-AA13OU30-2 | RT3-AA13 | 3.37 | 8.25 | 31.55 | 6.84 | 86.04 |
| 312 | F3230615DE-AA13OU30-1 | RT3-AA13 | 3.37 | 8.25 | 31.55 | 6.84 | 86.04 |
| 311 | F3230615DE-AA13OU5-3 | RT3-AA13 | 3.27 | 7.99 | 21.59 | 6.50 | 22.39 |
| 310 | F3230615DE-AA13OU5-2 | RT3-AA13 | 3.27 | 7.99 | 21.59 | 6.50 | 22.39 |
| 309 | F3230615DE-AA13OU5-1 | RT3-AA13 | 3.27 | 7.99 | 21.59 | 6.50 | 22.39 |
| 308 | F1-061113-RT1b-P-3 | RT1b | 0.15 | 16.14 | 1183.63 | 0.65 | 355.05 |
| 307 | F1-061113-RT1b-P-2 | RT1b | 0.15 | 16.14 | 1183.63 | 0.65 | 355.05 |
| 306 | F1-061113-RT1b-P-1 | RT1b | 0.15 | 16.14 | 1183.63 | 0.65 | 355.05 |
| 304 | F2-121113-RT2pur-P-1 | RT2 | 3.11 | 6.99 | 17.25 | 5.90 | 9.83 |

| Test | Sample name | Clay Cation | Slurry characterisation in Malvern particle size analyser | | | Surface weighted mean | Volume weighted mean |
|---|---|---|---|---|---|---|---|
| | | | Particle Size (µm) | | | | |
| # | | | d (0.1) | d (0.5) | d (0.9) | d (3, 2) | d (4, 3) |
| 301 | F1-260415-RT1Li-2 | Li | 3.10 | 7.68 | 811.42 | 6.55 | 167.09 |
| 300 | F1-260415-RT1Li-1 | Li | 3.10 | 7.68 | 811.42 | 6.55 | 167.09 |
| 299 | F3-260415-RT3Li-1 | Li | 3.10 | 7.68 | 811.42 | 6.55 | 167.09 |
| 298 | F3-260415-RT3NH4-15-3 | NH | 3.51 | 8.45 | 26.62 | 7.00 | 78.55 |
| 297 | F3-260415-RT3NH4-15-2 | NH | 3.51 | 8.45 | 26.62 | 7.00 | 78.55 |
| 296 | F3-260415-RT3NH4-15-1 | NH | 3.51 | 8.45 | 26.62 | 7.00 | 78.55 |
| 295 | F3-260415-RT3Na-3 | Na | 2.73 | 6.99 | 814.91 | 5.92 | 171.81 |
| 294 | F3-260415-RT3K-3 | K | | | | | |
| 293 | F3-260415-RT3K-2 | K | | | | | |
| 292 | F3-260415-RT3K-1 | K | | | | | |
| 291 | F3-230415-RT3AA13wT-2 | RT3-AA13 | 3.37 | 8.25 | 31.55 | 6.84 | 86.04 |
| 290 | F3-230415-RT3AA13wT-1 | RT3-AA13 | 3.37 | 8.25 | 31.55 | 6.84 | 86.04 |
| 289 | F2-230415-RT2TH70 wT-3 | RT2 | 3.11 | 6.99 | 17.25 | 5.90 | 9.83 |
| 288 | F2-230415-RT2TH70 wT-2 | RT2 | 3.11 | 6.99 | 17.25 | 5.90 | 9.83 |
| 287 | F2-230415-RT2TH70 wT-1 | RT2 | 3.11 | 6.99 | 17.25 | 5.90 | 9.83 |
| 286 | F1-230415-RT1b wT-3 | RT1b | 0.12 | 10.83 | 1044.89 | 0.44 | 308.23 |
| 285 | F1-230415-RT1b wT-2 | RT1b | 0.12 | 10.83 | 1044.89 | 0.44 | 308.23 |
| 284 | F1-230415-RT1b wT-1 | RT1b | 0.12 | 10.83 | 1044.89 | 0.44 | 308.23 |
| 283 | F3-270115-NH4-14-3 | NH | 3.51 | 8.45 | 26.62 | 7.00 | 78.55 |
| 282 | F3-270115-NH4-14-2 | NH | 3.51 | 8.45 | 26.62 | 7.00 | 78.55 |
| 281 | F3-270115-NH4-14-1 | NH | 3.51 | 8.45 | 26.62 | 7.00 | 78.55 |
| 280 | F3-200114-NH4-14-3 | NH | 3.10 | 7.16 | 468.39 | 6.19 | 96.24 |
| 279 | F3-200114-NH4-14-2 | NH | 3.10 | 7.16 | 468.39 | 6.19 | 96.24 |
| 278 | F3-200114-NH4-14-1 | NH | 3.10 | 7.16 | 468.39 | 6.19 | 96.24 |
| 277 | F3-200114-Li13-3 | Li | 2.98 | 7.32 | 881.61 | 6.37 | 195.52 |
| 276 | F3-200114-Li13-2 | Li | 2.98 | 7.32 | 881.61 | 6.37 | 195.52 |
| 275 | F3-200114-Li13-1 | Li | 2.98 | 7.32 | 881.61 | 6.37 | 195.52 |
| 274 | F3-070414AAf4-3 | RT3-AAf | 0.11 | 6.70 | 912.29 | 0.37 | 200.44 |
| 273 | F3-070414AAf4-2 | RT3-AAf | 0.11 | 6.70 | 912.29 | 0.37 | 200.44 |
| 272 | F3-070414AAf4-1 | RT3-AAf | 0.11 | 6.70 | 912.29 | 0.37 | 200.44 |
| 271 | F3-070414AAf3-3 | RT3-AAf | 0.11 | 6.70 | 912.29 | 0.37 | 200.44 |
| 270 | F3-070414AAf3-2b | RT3-AAf | 0.11 | 6.70 | 912.29 | 0.37 | 200.44 |
| 269 | F3-070414AAf3-2 | RT3-AAf | 0.11 | 6.70 | 912.29 | 0.37 | 200.44 |
| 268 | F3-070414AAf3-1 | RT3-AAf | 0.11 | 6.70 | 912.29 | 0.37 | 200.44 |
| 267 | F3-070414AAf2-2 | RT3-AAf | 0.11 | 6.70 | 912.29 | 0.37 | 200.44 |
| 266 | F3-070414AAf2-2 | RT3-AAf | 0.11 | 6.70 | 912.29 | 0.37 | 200.44 |
| 265 | F3-070414AAf2-1 | RT3-AAf | 0.11 | 6.70 | 912.29 | 0.37 | 200.44 |

| Test | Sample name | Clay Cation | Slurry characterisation in Malvern particle size analyser | | | | |
|---|---|---|---|---|---|---|---|
| | | | Particle Size (µm) | | | Surface weighted mean | Volume weighted mean |
| # | | | d (0.1) | d (0.5) | d (0.9) | d (3, 2) | d (4, 3) |
| 264 | F3-070414AAf1-3 | RT3-AAf | 0.11 | 6.70 | 912.29 | 0.37 | 200.44 |
| 263 | F3-070414AAf1-2 | RT3-AAf | 0.11 | 6.70 | 912.29 | 0.37 | 200.44 |
| 262 | F3-070414AAf1-1 | RT3-AAf | 0.11 | 6.70 | 912.29 | 0.37 | 200.44 |
| 261 | F3-201213-Cs-last1 | Cs | 2.96 | 5.42 | 9.97 | 4.89 | 6.03 |
| 260 | F3-201213-NH4-13-2-3 | NH | 3.10 | 7.16 | 468.39 | 6.19 | 96.24 |
| 259 | F3-201213-NH4-13-2-2b | NH | 3.10 | 7.16 | 468.39 | 6.19 | 96.24 |
| 258 | F3-201213-NH4-13-2-2 | NH | 3.10 | 7.16 | 468.39 | 6.19 | 96.24 |
| 257 | F3-201213-NH4-13-2-1 | NH | 3.10 | 7.16 | 468.39 | 6.19 | 96.24 |
| 256 | F3-201213-NH4-13-1-3 | NH | 3.10 | 7.16 | 468.39 | 6.19 | 96.24 |
| 253 | F3-201213-NH4-13-1-2 | NH | 3.10 | 7.16 | 468.39 | 6.19 | 96.24 |
| 252 | F3-201213-NH4-13-1 | NH | 3.10 | 7.16 | 468.39 | 6.19 | 96.24 |
| 251 | F3-201213-Sr3-last2 | Sr | 2.76 | 5.66 | 11.97 | 4.92 | 6.67 |
| 250 | F3-201213-Sr3-last1 | Sr | 2.76 | 5.66 | 11.97 | 4.92 | 6.67 |
| 249 | F3201213-43-K-last3 | K | 3.04 | 6.41 | 13.37 | 5.48 | 7.42 |
| 248 | F3201213-43-K-last2 | K | 3.04 | 6.41 | 13.37 | 5.48 | 7.42 |
| 247 | F3201213-43-K-last1 | K | 3.04 | 6.41 | 13.37 | 5.48 | 7.42 |
| 246 | F3201213-42-NH4-12last3 | NH | 3.38 | 6.981 | 14.851 | 6.074 | 26.743 |
| 245 | F3201213-42-NH4-12last2 | NH | 3.38 | 6.981 | 14.851 | 6.074 | 26.743 |
| 244 | F3201213-42-NH4-12last1 | NH | 3.38 | 6.981 | 14.851 | 6.074 | 26.743 |
| 243 | F3201213-41-2-Na2last3 | Na | 3.91 | 17.626 | 55.709 | 9.843 | 36.919 |
| 242 | F3201213-41-2-Na2last2 | Na | 3.91 | 17.626 | 55.709 | 9.843 | 36.919 |
| 241 | F3201213-41-2-Na2last1 | Na | 3.91 | 17.626 | 55.709 | 9.843 | 36.919 |
| 240 | F3201213-41-Na2last3 | Na | 3.91 | 17.626 | 55.709 | 9.843 | 36.919 |
| 239 | F3201213-41-Na2last2 | Na | 3.91 | 17.626 | 55.709 | 9.843 | 36.919 |
| 238 | F3201213-40-Na1last1 | Na | 3.91 | 17.626 | 55.709 | 9.843 | 36.919 |
| 237 | F3201213-40-Na1last3 | Na | 3.91 | 17.626 | 55.709 | 9.843 | 36.919 |
| 236 | F3201213-40-Na1last2 | Na | 3.91 | 17.626 | 55.709 | 9.843 | 36.919 |
| 235 | F3201213-40-Na1last | Na | 3.91 | 17.626 | 55.709 | 9.843 | 36.919 |
| 215 | F2121113RT2TH70-3 | RT2 | 3.11 | 6.99 | 17.25 | 5.90 | 9.83 |
| 214 | F2121113RT2TH70-2 | RT2 | 3.11 | 6.99 | 17.25 | 5.90 | 9.83 |
| 213 | F2121113RT2TH70-1 | RT2 | 3.11 | 6.99 | 17.25 | 5.90 | 9.83 |
| 209 | F1061113RT1m-3 | RT1m | 2.70 | 6.19 | 23.23 | 5.32 | 16.74 |
| 208 | F1061113RT1m-2 | RT1m | 2.70 | 6.19 | 23.23 | 5.32 | 16.74 |
| 207 | F1061113RT1m-1 | RT1m | 2.70 | 6.19 | 23.23 | 5.32 | 16.74 |
| 202 | F1061113RT1b-3 | RT1b | 0.15 | 16.14 | 1183.63 | 0.65 | 355.05 |
| 201 | F1061113RT1b-2 | RT1b | 0.15 | 16.14 | 1183.63 | 0.65 | 355.05 |
| 200 | F1061113RT1b-1 | RT1b | 0.15 | 16.14 | 1183.63 | 0.65 | 355.05 |

| | | Clay | Slurry characterisation in Malvern particle size analyser | | | | |
|---|---|---|---|---|---|---|---|
| | | | | | | Surface weighted mean | Volume weighted mean |
| Test | Sample name | Cation | Particle Size (µm) | | | | |
| # | | | d (0.1) | d (0.5) | d (0.9) | d (3, 2) | d (4, 3) |
| 182 | F3180913RT3 100-3 | RT3-OWE | 11.52 | 6.97 | 3.53 | 8.69 | 23.12 |
| 181 | F3180913RT3 100-2 | RT3-OWE | 11.52 | 6.97 | 3.53 | 8.69 | 23.12 |
| 180 | F3180913RT3 100 | RT3-OWE | 11.52 | 6.97 | 3.53 | 8.69 | 23.12 |
| 179 | F3-49-OWF-P3 | RT3-OWF | 3.41 | 7.81 | 18.24 | 6.47 | 9.64 |
| 178 | F3-49-OWF-P2 | RT3-OWF | 3.41 | 7.81 | 18.24 | 6.47 | 9.64 |
| 177 | F3-49-OWF-P1 | RT3-OWF | 3.41 | 7.81 | 18.24 | 6.47 | 9.64 |
| 176 | F3-48-Sr-P3 | Sr | 2.76 | 5.66 | 11.97 | 4.92 | 6.67 |
| 175 | F3-48-Sr-P2 | Sr | 2.76 | 5.66 | 11.97 | 4.92 | 6.67 |
| 174 | F3-48-Sr-P1 | Sr | 2.76 | 5.66 | 11.97 | 4.92 | 6.67 |
| 173 | F3-41-Na2-P4 | Na | 3.91 | 17.626 | 55.709 | 9.843 | 36.919 |
| 172 | F3-41-Na2-P3 | Na | 3.91 | 17.626 | 55.709 | 9.843 | 36.919 |
| 171 | F3-41-Na2-P2 | Na | 3.91 | 17.626 | 55.709 | 9.843 | 36.919 |
| 170 | F3-41-Na2-P1 | Na | 3.91 | 17.626 | 55.709 | 9.843 | 36.919 |
| 97 | F3-49-OWF 2i3 | RT3-OWF | 3.41 | 7.81 | 18.24 | 6.47 | 9.64 |
| 96 | F3-49-OWF 2 i2 | RT3-OWF | 3.41 | 7.81 | 18.24 | 6.47 | 9.64 |
| 95 | F3-49-OWF 2 i1 | RT3-OWF | 3.41 | 7.81 | 18.24 | 6.47 | 9.64 |
| 94 | F3-49-OWF i3 | RT3-OWF | 3.41 | 7.81 | 18.24 | 6.47 | 9.64 |
| 93 | F3-49-OWF i2 | RT3-OWF | 3.41 | 7.81 | 18.24 | 6.47 | 9.64 |
| 92 | F3-49-OWF i1 | RT3-OWF | 3.41 | 7.81 | 18.24 | 6.47 | 9.64 |
| 91 | F3-48-Sr-i3 | Sr | 2.76 | 5.66 | 11.97 | 4.92 | 6.67 |
| 90 | F3-48-Sr-i2 | Sr | 2.76 | 5.66 | 11.97 | 4.92 | 6.67 |
| 89 | F3-48-Sr-i1 | Sr | 2.76 | 5.66 | 11.97 | 4.92 | 6.67 |
| 88 | F3-46-Ba-i3 | Ba | 2.73 | 5.70 | 13.79 | 5.03 | 28.92 |
| 86 | F3-46-Ba-i2 | Ba | 2.73 | 5.70 | 13.79 | 5.03 | 28.92 |
| 85 | F3-46-Ba-i1 | Ba | 2.73 | 5.70 | 13.79 | 5.03 | 28.92 |
| 84 | F3-45-Cs-i3 | Cs | 2.96 | 5.42 | 9.97 | 4.89 | 6.03 |
| 83 | F3-45-Cs-i2 | Cs | 2.96 | 5.42 | 9.97 | 4.89 | 6.03 |
| 82 | F3-45-Cs-i1 | Cs | 2.96 | 5.42 | 9.97 | 4.89 | 6.03 |
| 58 | F3-32-Na1-i7 | Na | 3.91 | 17.626 | 55.709 | 9.843 | 36.919 |
| 57 | F3-31-Li-i7 | Li | 3.16 | 7.81 | 896.64 | 6.70 | 188.86 |
| 56 | F3-31-Li-i8 | Li | 3.16 | 7.81 | 896.64 | 6.70 | 188.86 |
| 55 | F3-47-Sr-i4 | Sr | 2.76 | 5.66 | 11.97 | 4.92 | 6.67 |
| 54 | F3-47-Sr-i2 | Sr | 2.76 | 5.66 | 11.97 | 4.92 | 6.67 |
| 53 | F3-44-Mg-i4 | Mg | 0.11 | 2.73 | 31.12 | 0.33 | 19.64 |
| 52 | F3-44-Mg-i3 | Mg | 0.11 | 2.73 | 31.12 | 0.33 | 19.64 |
| 51 | F3-44-Mg-i2 | Mg | 0.11 | 2.73 | 31.12 | 0.33 | 19.64 |
| 50 | F3-44-Mg-i1 | Mg | 0.11 | 2.73 | 31.12 | 0.33 | 19.64 |

| Test | Sample name | Clay Cation | Slurry characterisation in Malvern particle size analyser | | | Surface weighted mean | Volume weighted mean |
|---|---|---|---|---|---|---|---|
| | | | Particle Size (µm) | | | | |
| # | | | d (0.1) | d (0.5) | d (0.9) | d (3, 2) | d (4, 3) |
| 49 | F3-43-K-i4 | K | 3.04 | 6.41 | 13.37 | 5.48 | 7.42 |
| 48 | F3-43-K-i3 | K | 3.04 | 6.41 | 13.37 | 5.48 | 7.42 |
| 47 | F3-43-K-i2 | K | 3.04 | 6.41 | 13.37 | 5.48 | 7.42 |
| 46 | F3-43-K-i1 | K | 3.04 | 6.41 | 13.37 | 5.48 | 7.42 |
| 45 | F3-38-OWE i9 | RT3-OWE | 11.52 | 6.97 | 3.53 | 8.69 | 23.12 |
| 44 | F3-38-OWE i8 | RT3-OWE | 11.52 | 6.97 | 3.53 | 8.69 | 23.12 |
| 43 | F3-38-OWE i7 | RT3-OWE | 11.52 | 6.97 | 3.53 | 8.69 | 23.12 |
| 42 | F3-38-OWE i6 | RT3-OWE | 11.52 | 6.97 | 3.53 | 8.69 | 23.12 |
| 40 | F3-38-OWE i6 | RT3-OWE | 11.52 | 6.97 | 3.53 | 8.69 | 23.12 |
| 39 | F3-42 NH4 4i | NH | 3.38 | 6.98 | 14.85 | 6.07 | 26.74 |
| 38 | F3-42 NH4 3i | NH | 3.38 | 6.98 | 14.85 | 6.07 | 26.74 |
| 37 | F3-42 NH4 2i | NH | 3.38 | 6.98 | 14.85 | 6.07 | 26.74 |
| 36 | F3-42 NH4 1i | NH | 3.38 | 6.98 | 14.85 | 6.07 | 26.74 |
| 35 | F3-41 Na2 4i | Na | 3.91 | 17.63 | 55.71 | 9.84 | 36.92 |
| 34 | F3-41 Na2 3i | Na | 3.91 | 17.63 | 55.71 | 9.84 | 36.92 |
| 33 | F3-41 Na2 2i | Na | 3.91 | 17.63 | 55.71 | 9.84 | 36.92 |
| 32 | F3-41 Na2 1i | Na | 3.91 | 17.63 | 55.71 | 9.84 | 36.92 |
| 31 | F3-40 Na1 5i | Na | 3.91 | 17.63 | 55.71 | 9.84 | 36.92 |
| 30 | F3-40 Na1 4i | Na | 3.91 | 17.63 | 55.71 | 9.84 | 36.92 |
| 29 | F3-40 Na1 3i | Na | 3.91 | 17.63 | 55.71 | 9.84 | 36.92 |
| 28 | F3-40 Na1 2i | Na | 3.91 | 17.63 | 55.71 | 9.84 | 36.92 |
| 27 | F3-40 Na1 1i | Na | 3.91 | 17.63 | 55.71 | 9.84 | 36.92 |
| 17 | F3-Li-39o6 | Li | 3.16 | 7.81 | 896.64 | 6.70 | 188.86 |
| 16 | F3-Li-39i5 | Li | 3.16 | 7.81 | 896.64 | 6.70 | 188.86 |
| 15 | F3-Li-39i4 | Li | 3.16 | 7.81 | 896.64 | 6.70 | 188.86 |
| 14 | F3-Li-39i3 | Li | 3.16 | 7.81 | 896.64 | 6.70 | 188.86 |

# Appendix IV. Publications emanating from this research

Atanasova, M.T., Vyalikh, A., Scheler, U., Focke, W.W., 2016. Characterisation of rectorite from the Beatrix Gold Mine in South Africa. *Applied Clay Science* 126, 7-16.

Atanasova, M.T., Focke, W.W., Loots, T., 2018. Self-assembled rectorite films with remarkable mechanical performance: preparation, structural characterisation and properties. Submitted for publication to Applied Clay Science, January 2018.

Atanasova, M.T., Focke, W.W., 2018. Flexible $NH_4$-rectorite-chitosan bionanocomposite films with enhanced mechanical performance. In preparation for publication, January 2018.